Doctoral theses at NTNU, 2015:217

Torodd Skjerve Nord

Force and response estimation on bottom-founded structures prone to ice-induced vibrations

Doctoral thesis

Torodd Skjerve Nord

NTNU
Norwegian University of
Science and Technology
Faculty of Engineering Science and Technology
Department of Civil and Transport Engineering

ISBN 978-82-326-1090-7 (printed ver.)
ISBN 978-82-326-1091-4 (electronic ver.)
ISSN 1503-8181

Doctoral theses at NTNU, 2015:217

NTNU
Norwegian University of
Science and Technology

NTNU
Norwegian University of
Science and Technology
Thesis for the degree of
Philosophiae Doctor

Torodd Skjerve Nord

Force and response estimation on bottom-founded structures prone to ice-induced vibrations

Thesis for the degree of Philosophiae Doctor

Trondheim, November 2015

Norwegian University of Science and Technology
Faculty of Engineering Science and Technology
Department of Civil and Transport Engineering

NTNU
Norwegian University of Science and Technology

UNIS
The University Centre in Svalbard

NTNU
Norwegian University of Science and Technology

Thesis for the degree of Philosophiae Doctor

Faculty of Engineering Science and Technology
Department of Civil and Transport Engineering

ISBN 978-82-326-1090-7 (printed ver.)
ISBN 978-82-326-1091-4 (electronic ver.)
ISSN 1503-8181

Doctoral theses at NTNU, 2015:217

Printed by NTNU Grafisk senter

To my family…

Abstract

Various types of bottom-founded structures, including lighthouses, quay structures, mono-pod platforms, multi-legged platforms, caisson-retained islands and bridges, are located in ice-infested waters. Level ice can interact with bottom-founded structures in various manners, and over fifty years of extensive measurement campaigns has brought attention to ice-induced vibrations. This phenomenon is caused by repeated ice crushing failures across the ice-structure interface and may entail violent vibrations of the structure, thereby potentially harming the structural integrity, secondary installations and operational safety. Such ice-induced vibrations are commonly divided into three regimes:

1) Intermittent crushing
2) Frequency lock-in
3) Continuous brittle crushing

in which the ice velocity increase from regime 1 to regime 3. The ice conditions leading to each of the three regimes are not yet fully understood. Therefore, measurement campaigns both in the field and in the laboratory must address these regimes, wherein two of the major ingredients are the ice force and the structural response.

A laboratory-scale ice-induced vibration measurement campaign was conducted at the Hamburg Ship Model Basin during August-September 2011, from which data were obtained for this thesis. Data measured at the Nordströmsgrund lighthouse in Sweden during the winter of 2003 and structural information on the Hanko-1 channel marker in Finland constitute the full-scale basis in this thesis.

The ice forces present during ice-induced vibrations are traditionally measured by load panels or inverse techniques. Load panels are expensive; thus, inverse techniques are favorable. This thesis assessed a deterministic-stochastic framework to identify both the ice forces and responses at both the model scale and full scale. All of the considered data were limited to scenarios of ice-induced vibrations, and the considered ice conditions were primarily level ice. The framework as it is applied in this thesis consists of a joint input-state estimation algorithm, a model of the structure and a set of response measurements. Both full-order finite element models and modally reduced order models were used in this thesis.

Using the laboratory measurements, the force and response identification was performed by employing two different full-order finite element models. One model was entirely based on the blueprints of the structure. The other model was tuned to more accurately reproduce the measured first natural frequency. The results were presented for two different regimes of ice-induced vibrations: the intermittent crushing regime and the continuous brittle crushing regime. The accuracy of the identified forces using the joint input-state estimation algorithm was assessed by comparing the forces with those obtained by a frequency-domain deconvolution method based on experimentally obtained frequency response functions. The results demonstrated the successful identification of the level-ice forces for both the intermittent and continuous brittle crushing regimes even when significant modeling errors were present. The responses (displacements) identified in conjunction with the forces were also compared to those measured during the experiment. Here, the estimated response was found to be sensitive

to the modeling errors in the blueprint model. Simple tuning of the model, however, enabled high-accuracy response estimation.
The joint input-state estimation algorithm was further used as a means to analyze the laboratory data, from which the global structural response was simultaneously identified with the forces. Novel insights into ice-induced vibration phenomena were obtained by comparing, on different time scales, measured and estimated response quantities and forces/pressures. First, the identified forces, ice velocities and time-frequency maps of the measured responses were presented for a series of ice-induced vibration tests. It was shown that the ice forces excited more than one mode of the structure and that the transition ice velocity at which the vibrations shifted from the first mode to the second mode increased with decreased foundation stiffness and superstructure mass. Second, a detailed analysis of the interaction between the structure and the ice edge was performed on a smaller time scale by comparing the locally measured pressures at the ice-structure interface to the identified structural responses and forces. It was shown that structural vibrations at a frequency that is higher than the dominant vibration frequency caused cyclic loading of the ice edge during intermittent crushing. These vibrations led to an increasing loading rate prior to ice failure. During an event that showed the tendencies of frequency lock-in vibrations, the structural response was dominated by a single vibration frequency.
At full scale, a comparison between the measured and identified dynamic ice forces acting on the Nordströmsgrund lighthouse is presented. The dynamic ice forces were identified from the measured responses using the joint input-state estimation algorithm in conjunction with a reduced-order finite element model. A convincing agreement between the measured and identified forces was found. The algorithm was further used to estimate the response of the structure at unmeasured locations, including the ice-action point. The structural velocity amplitudes when the structure was subject to frequency lock-in vibrations were occasionally higher than the ice velocity and within the range of observations for other structures.
A measurement campaign at the Hanko-1 channel marker in the Gulf of Finland is planned to monitor the forces leading to ice-induced vibrations via force identification. The ice forces are to be identified using the joint input-state estimation algorithm in conjunction with a modally reduced order model. Recently developed guidelines were used to determine the optimal response measurement types and locations that ensure the identifiability of the dynamic ice forces from only a limited number of sensors and a selection of vibration modes.

Preface

This thesis is submitted to the Norwegian University of Science and Technology (NTNU) for partial fulfillment of the requirements for the degree of philosophiae doctor.

This doctoral work was performed at the Department of Civil and Transport Engineering, NTNU, Trondheim and the Department of Arctic Technology of the University Centre in Svalbard, UNIS, with Professor Knut V. Høyland as the main supervisor and with co-supervisors Professor Emeritus Mauri Määttänen and Associate Professor Ole Øiseth. This work was also conducted in collaboration with Assistant Professor Eliz-Mari Lourens at the Faculty of Civil Engineering and Geosciences, Delft University of Technology, Delft, the Netherlands

This thesis was financed by the Research Council of Norway through NTNU's Research Centre for *Sustainable Arctic Marine and Coastal Technology* (SAMCoT CRI). The work described in this thesis was supported by the European Community's 7th Framework Programme through a grant from the budget of the Integrated Infrastructure Initiative HYDRALAB-IV, Contract no. 261520.

Acknowledgements

The first person I would like to thank is my main supervisor, Knut V. Høyland. He has always been available for discussions and has been a mentor in both ice-related issues and leadership guidance. Mauri Määttänen is a supervisor that I admire. He taught me the skills necessary to find structural design solutions, and we both share the unstoppable desire to develop new experimental designs. My third supervisor, Ole Øiseth, was always available for discussions and provided a wealth of knowledge in the field of structural dynamics and constructive supervision in critical phases close to deadlines and key decisions. This work is also a result of collaboration with Eliz-Mari Lourens, Hayo Hendrikse and Andrei Metrikine at TU Delft, the Netherlands. Eliz-Mari has been a true supervisor, assisted me in developing theoretical skills, and always been very helpful. Being the mother of the theory of joint force and state estimation, she educated me as I confronted the steep learning curve, which I am very grateful for today. Hayo has been a very good co-worker and friend during these years. Through his insight into the models for predicting ice-induced vibrations, he also helped generate physical interpretations of the results. Andrei has been a tactical and theoretical advisor and the brain behind the collaboration with Eliz-Mari. The aforementioned people constitute the core of the NTNU-TU Delft team on ice-induced vibrations, and I am grateful for all of the assistance that they provided. In addition, I am grateful for the assistance from Morten Bjerkås, who was a major contributor to discussions on ice-induced vibrations, Arctic structure design, and the history of Arctic offshore structures, especially Baltic Lighthouses.
I would like to thank Bjørn Haugen for the assistance with finite element modeling.
I would like to thank the leader of our research center, Sveinung Løset. He has been a tactical advisor and taught me leadership skills that I can use in the field. I would also like to thank the leader of the technology department at UNIS, Aleksey Marchenko. He has given me the opportunity to teach at UNIS and participate in a variety of experiments in the field and in the laboratory. I am also grateful for the assistance of and collaboration with Aleksey Shestov at UNIS. It has been a privilege to observe and learn from his theoretical knowledge and practical skills that are necessary to conducting successful tests in the field and in the laboratory. In addition, I would like to thank our center manager, Maria Azucena Gutierrez Gonzalez, for being a good advisor and supporter to me and all of the other PhD candidates in this center.
I would like to thank Devinder Sodhi for his comments on the introduction of this thesis.

I have also had the privilege to work with Erland Schulson, Øivind Asgeir Arntsen, Alf Tørum, Jukka Tuhkuri, Jaakko Heinonen, Kari Kolari, Evgeny Karulin, Anders Rønnquist, Arne Aalberg, Bjørn Haugen, Raed Lubbad, Nataly Marchenko, Anatoly Sinitsyn, Ivan Metrikin, Marat Kashafutdinov, Andrei Tsarau, Renat Yumetov, Farzad Farid-Afshin, Karl-Ulrich Evers, Sergey Kulyakhtin, Felix Breitschädel, Woflgang Kampel, Ekaterina Kim, Marit Reiso, Sergiy Sukhorukov, Anton Kulyakhtin, Christian Lønøy, Mayilvahanan Alagan Chella, Marat Kashafutdinov, David Wrangborg, Ole-Christian Ekeberg, Sergey Kulyakhtin, Arun Mulky Kamath, Hans Bihs, Anna Pustogvar, Vincent Vilamosa, Eleni Chatzi, Åse Ervik, Øyvind Wiig Petersen, Knut

Andreas Kvåle, Petter Nåvik, Marius Holtermann Andersen, Hongtao Lie, and Gesa Ziemer.
This work relied on my will to sacrifice time with friends and family. To my friends, I am very grateful for the effort that you spent to reduce the deterioration of my social presence, despite the fact that it sometimes appeared to be done in vain.
To my family, thank you for the endless support.

Contents

List of publications

This thesis contains a total of five papers (Appendices 1-5). Three papers have been submitted to journals; two have been published, and one is under review. Two papers have been published in conference proceedings.

1. Nord, T.S., Määttänen, M. and Øiseth, O., 2013. Frequency domain force identification in ice-structure interaction, Port and Ocean Engineering under Arctic Conditions, Espoo, Finland, ISBN 978-952-60-3635-9

2. Nord, T.S., Lourens, E.-M., Øiseth, O. and Metrikine, A., 2015. Model-based force and state estimation in experimental ice-induced vibrations by means of Kalman filtering. Cold Regions Science and Technology, 111(0): pp. 13-26

3. Nord, T.S., Lourens, E.-M., Määttänen, M., Øiseth, O. and Høyland, K.V., 2015. Laboratory experiments to study ice-induced vibrations of scaled model structures during their interaction with level ice at different ice velocities. Cold Regions Science and Technology, 119 :pp. 1-15

4. Nord, T.S., Lourens, E.-M., Øiseth, O. Ice force identification on the Nordströmsgrund lighthouse. Submitted to Computers and structures, under revision.

5. Nord, T.S., Øiseth, O. Petersen, Ø.W., Lourens, E., 2015b. Sensor network for dynamic ice-force identification: The Hanko-1 Channel Marker case study, Proceedings of the 23rd International Conference on Port and Ocean Engineering under Arctic Conditions (POAC), Trondheim, Norway, Paper no. 160.

Notations

Scalars, vectors and matrices

x, y, z	Scalar variables
$\mathbf{x}, \mathbf{y}, \mathbf{z}$	Vector variables
$\mathbf{X}, \mathbf{Y}, \mathbf{Z}$	Matrix variables
$\mathbf{I}$	Identity matrix
$\mathrm{diag}\{x\}$	Matrix with x on the diagonal
$\mathrm{diag}\{\mathbf{X}\}$	Vector formed from the elements of the diagonal of the matrix $\mathbf{X}$

Functions and operators

$\dot{x}, \ddot{x}$	First- and second-order derivatives of a variable x
x^*	Complex conjugate of a variable x
$\mathbf{X}^{-1}$	Inverse of a matrix $\mathbf{X}$
$\mathbf{X}^{\mathrm{T}}$	Transpose of a matrix $\mathbf{X}$
$\mathbf{X}^{\mathrm{H}}$	Hermitian transpose of a vector $\mathbf{X}$
$\mathbf{X}^{\dagger}$	Pseudo-inverse of a matrix $\mathbf{X}$

Random variables

$E\{\mathbf{x}\}$	Expected value of the random vector $\mathbf{x}$
$\hat{\mathbf{x}}$	Estimate of the random vector $\mathbf{x}$

Fixed symbols

Δt	Sampling period
t	Time
f	Frequency
$\mathbf{M}, \mathbf{C}, \mathbf{K}$	Mass, damping and stiffness matrix
ω_j	Angular eigenfrequency
ξ_j	Modal damping ratio
$\mathbf{\Omega}$	Diagonal matrix containing the angular eigenfrequencies, ω_j
$\mathbf{\Gamma}$	Matrix with $2\xi_j\omega_j$ on the diagonal
$\mathbf{\Phi}$	Real eigenvector matrix
$\mathbf{p}$	Force vector
$\mathbf{d}$	Data vector
$\mathbf{x}$	State vector
$\mathbf{S}_{\mathrm{p}}$	Force influence matrix
$\mathbf{S}_{\mathrm{d}}, \mathbf{S}_{\mathrm{v}}, \mathbf{S}_{\mathrm{a}}$	Selection matrices for displacement, velocity and acceleration
n_{d}	Number of measurements
n_{m}	Number of modes

n_{p}	Number of forces
n_{DOF}	Number of degrees of freedom
n_{s}	Number of states
$\mathbf{v}$	Measurement noise vector
$\mathbf{w}$	System noise vector
F_{EW}	Global force acting in the East-West direction
F_{NS}	Global force acting in the North-South direction
$\mathbf{u}$	Displacement vector
$\mathbf{z}$	Modal displacement vector
h	Ice thickness
ρ_i	Ice density
S_{ice}	Ice salinity
T_{ice}	Ice temperature
ψ	Force panel orientation angle
σ_f	Flexural strength of the ice
σ_c	Compressive strength of the ice
ε	Strain
α	Shear factor
η	Element shape function
L	Element length
$\mathbf{L}$	Gain matrix
$\mathbf{H}$	Frequency response function matrix
$\tilde{\mathbf{C}}$	Covariance matrix
$\boldsymbol{\rho}$	Correlation coefficient matrix

Sets

$\mathbb{R}^{\mathrm{n}}$	Set of n - dimensional real vectors
$\mathbb{R}^{\mathrm{m\times n}}$	Set of m×n real matrices
$\mathbb{C}^{\mathrm{n}}$	Set of n - dimensional complex vectors
$\mathbb{C}^{\mathrm{m\times n}}$	Set of m×n complex matrices

Abbreviations

DOF	Degree of freedom
SDOF	Single degree of freedom
MDOF	Multi degree of freedom
MVU	Minimum variance and unbiased
JIS	Joint input state
FRF	Frequency response function
FEM	Finite element method
RMS	Root mean square
PSD	Power spectral density
STRICE	Structures in ice
DIIV	Deciphering ice-induced vibrations
SAMCoT	Sustainable arctic marine and coastal technology
HSVA	Hamburg ship model basin
CRREL	Cold regions research and engineering laboratory
LOLEIF	Low-level ice forces
HSE	Health and safety executive
HPZ	High-pressure zone

Chapter 1 Introduction

1.1 Background

A large variety of man-made structures are located in ice-infested waters. The transport and exploitation of natural resources in the Arctic has led to increased demand for infrastructure that can withstand the harsh environment, including structures for hydrocarbon exploration and exploitation platforms, harbors, bridges, navigation markers and lighthouses.

Before 1941, shipping traffic through the seaway between the Swedish island Öland and the city of Kalmar on the mainland (Kalmarsund) that occurred during the winter months was inhibited by a combination of drifting ice and the absence of lighthouses (Frost, 1941). Maneuvering the ships in the ice-choked shallow water without lighthouses was unsafe; thus, in the 1870s, a naval officer suggested the construction of bottom-founded lighthouses to improve the safety of maritime navigation. This proposal and several that followed were intermittently downcasted by the Swedish parliament until 1938. The construction of five bottom-founded lighthouses that could withstand the ice actions was then approved. Limited knowledge about ice forces led the designers to conduct model-scale experiments, from which the model-scale ice forces and structural design were assessed. The model structure was fixed to a carriage that was accelerated to a target initial velocity. Thereafter, the structure indented water packed with wooden bricks, which simulated broken ice. The wooden bricks had a density that was similar to that of ice. The indentation distance was measured, and the force was estimated. It was assumed that the maximum force occurred at the beginning of the indentation and that the force linearly decreased to zero at the point where the indentation stopped. The maximum force was estimated from the linear assumption for the force history and by knowing the indentation length and the initial kinetic energy of the system. Scattered force estimates led the designers to refine the test setup, from which the design forces were determined. The five lighthouses were constructed on the basis of these experiments, and they remain in service today.

A review of the state of the lighthouses in the St. Lawrence waterway was presented by Danys (1977). The lighthouses constructed in the beginning of the early 1900s were also designed on basis of very limited knowledge about the ice forces. Danys reported the frequent occurrence of structural damage after years of service. Many substructures of timber cribwork were later replaced or upgraded with steel or concrete, which allowed the modern lighthouses of the 1970s to withstand the ice pressures. Under certain circumstances, it was claimed that the design pressures appeared to be excessively conservative (Neill, 1976). To support the selection of the appropriate design pressures, Frederking et al. (1986) conducted measurements of both static and dynamic ice forces acting on the Yamachiche Bend lightpier in the St. Lawrence river, Canada, in the time period of 1983-1986. Similar measurements were also conducted in the Baltic Sea, where the responses of the steel lighthouse Kemi 1 were measured during the first winter in service in 1973-1974 (Määttänen, 1975). Kemi 1 suffered from a fast degradation of its structural integrity and eventually collapsed during the same winter due to fatigue damage caused by ice-induced vibrations (Määttänen, 1975).

During the previous winter, the service staff at the Nordströmsgrund lighthouse reported large vibrations, and they suspected that this was a threat to the structural integrity (Engelbrektson, 1977). Response measurements confirmed the large vibrations, and observations of structural damage were made in 1973 (Bjørk, 1981).

Ice-induced vibrations are also a concern for Arctic petroleum production platforms. Observations of different structures in Cook Inlet, Alaska, revealed that the ice action produced considerably amounts of vibrations (Blenkarn, 1970; Peyton, 1967). The petroleum production platforms in Cook Inlet were designed for an ice crushing stress of 2.070 MPa (Croasdale, 1977) and sustained severe ice actions from both level ice and ridges. The measurements were further emphasized in a comprehensive survey on field measurements, model-scale tests and design considerations (Neill, 1976). Despite the fact that the new structural designs had greater ice resistance, the dynamic content of the ice action continued to pose a threat to the structural integrity. A summary of the literature on ice actions on offshore structures, including the Nordströmsgrund lighthouse, can be found in Bjerkås (2006).

The vibratory structural responses (ice-induced vibrations) accompanied by level-ice interaction represent one of the critical engineering design aspects of Arctic offshore structures. The Arctic guidelines for the design of structures, ISO 19906 (2010), divide ice-induced vibrations into three regimes: intermittent crushing (a), frequency lock-in (b) and continuous brittle crushing (c). Intermittent crushing is commonly associated with low ice velocities, frequency lock-in is commonly associated with intermediate ice velocities, and continuous brittle crushing is commonly associated with high ice velocities, typically greater than 100 mm s^{-1}. From a structural design perspective, frequency lock-in is the most unwanted regime due to its violent nature. The structure exhibits vibrations at or close to the natural frequency, and the shape of the repeated response cycles appears as periodic yet not necessarily entirely harmonic (sinusoidal).

Sodhi (2001) and Sodhi and Haehnel (2003) suggested three crushing modes, in which each mode depended on the ice indentation velocity and compliance of the structure. The modes serve as an invaluable tool for distinguishing physically different processes by force, response and pressure evolution at the interface; moreover, they serve as the theoretical basis for the three ice-induced vibration regimes in ISO 19906. At a low indentation velocity toward a rigid structure, the ice creeps and produces a gradually enlarging contact area between the ice and the structure. This mode is called creep deformation of ice. At high indentation velocities, the ice continuously fails in a brittle manner, thereby causing non-simultaneous contact. This mode is called brittle crushing (c). Joensuu and Riska (1988) indented ice toward a transparent plate at high indentation velocities, and when the ice failed by brittle flaking (spalling), they observed a narrow band of contact spots across the indenter width, i.e., the “line-like” contact. The contact spots within the line of contact were so-called high-pressure zones (HPZ), in which confined ice in the compressive failure region causes the contact pressure to be higher than elsewhere (Dempsey et al., 2001; Jordaan, 2001). Tuhkuri (1995) conducted various experiments to study the brittle failure process and observed that the ice-structure contact zone became wedge shaped, and the line contact was apparent. Using the terminology from Jordaan (2001), spalls are localized fractures from cracks that are initiated near a HPZ.

When ice sheets are indented to a vertical structure, the fractures causing the spalls/flaking propagate to the free edges, which are often the upper and lower surfaces

of the ice sheet. Indentation tests with freshwater ice and segmented indenters (Sodhi, 1998) showed that the spatial correlation of local ice forces across the width of a structure depends on the ice indentation speed: high correlation (or synchronization) at low speed and low correlation at high speed. During experiments on a flexible structure, Sodhi (2001) showed that the local pressures simultaneously increased during the load build-up at low indentation velocities. At the onset of ice failure, the indentation velocity increased by two orders of magnitude, and the pressure varied during the ice failure. This behavior is the third crushing mode, which he called ductile-brittle intermittent crushing, commonly associated with saw-tooth force and displacement signals (a). Despite colossal efforts to study the nature of frequency lock-in vibrations (b), their onset conditions are not yet fully understood. Synchronized local forces have been observed across the ice-structure interface during frequency lock-in vibrations both at full scale (Bjerkås et al., 2013) and in the laboratory (Ziemer and Deutsch, 2015). Nord et al. (2015) also observed a slight increase in the spatial correlation during an event that exhibited tendencies toward frequency lock-in, but the local forces were not fully synchronized. A review of the literature with a focus on the indentation of ice sheets was conducted by Sodhi et al. (1998). Recent small-scale indentation experiments by Wells et al. (2011), Taylor et al. (2013) and Browne et al. (2013) also linked the ice force and failure characteristics to the pressure. Browne et al. (2013) associated failures of HPZs to measured cyclic force patterns up to a frequency as high as 250 Hz. For literature reviews on crushing failure and the ice behavior adjacent to the indenter, see Jordaan (2001), Sodhi (2001), Sodhi et al. (1998) and Wells et al. (2011).

One of the most famous events caused by ice-induced vibrations dates back to the 12th of April, 1986, in the Beaufort Sea (Jefferies and Wright, 1988), wherein a multi-year ice floe interacted with the Molikpaq platform. The Molikpaq platform consists of a steel caisson filled with sand. Its base dimensions are 111 m by 111 m, with close-to-vertical exterior steel faces of the caisson. The ice loads exceeded the design capacity, and the vibrations resulted in fatigue damage to the sand core foundation, which is a key element in the platform's ice resistance. It remains a subject of debate as to which regime of ice-induced vibrations the event belong, namely, intermittent crushing or frequency lock-in (Määttänen, 2015). Molikpaq is currently one of the most extensively monitored Arctic offshore structures and is equipped with load panels and response measurement equipment (Weiss et al., 2001). For a summary on structures that have experienced frequency lock-in vibrations, see Määttänen (2008). For an overview of models used to predict ice-induced vibrations, see Hendrikse and Metrikine (2014).

Parallel or in front of the development of theory, numerical tools and guidelines was the development of field techniques to measure ice forces and responses. Because of the incomplete understanding of ice-structure interactions, Croasdale and Frederking (1986) stated that "Every opportunity must, therefore, be taken to use the techniques available to measure and observe ice/structure interaction phenomena". They surveyed experience with techniques that were applied (and often also developed) in the field in North America and categorized them into two fundamental approaches to obtain the ice forces: 1) in situ measurements on the ice and 2) structural response measurements. The second approach is preferred when a structure interacts with continuously moving ice. This approach consists of two fundamental methods for measuring forces: the direct method and the inverse method. Without using stringent definitions, the direct method measures the ice forces using load cells (in laboratory) or panels (full scale) at the ice-structure

interface, whereas the inverse method utilizes response measurements on the structure, e.g., strain measurements and/or accelerations. This method is called force identification.

Because extreme ice-induced vibration events are not fully understood, the in situ observation of ice conditions and the collection of ice properties and other environmental data are required in addition to the force and response measurements. Past measurement campaigns that facilitated the collection of this volume of information were extensive. Croasdale (1977) provided a table of the costs related to 'ice engineering' research projects; the cost to perform in situ ice pressure measurements during the winter of 1976-77 totaled $790,000. This was one of 130 projects in total that petroleum companies with interests in the Canadian Arctic had funded between 1969 and 1977 through the Arctic Petroleum Operators Association (APOA). Decreasing the costs of field measurements can be accomplished through reductions in instrument installations and maintenance needs. A debated reduction has been to omit the load panels in favor of force identification methods (see the comments at the end of Montgomery and Lipsett (1981)). The scientific loss by excluding load panels must be considered because the local processes across the ice-structure interface can be well captured with the panels. However, force identification is a cost-effective means of measuring the global ice forces.

Montgomery and Lipsett (1981) identified river-ice forces acting on a bridge pier in Alberta, Canada, using a frequency response function from a single-degree-of-freedom model in conjunction with acceleration measurements. A similar technique used to identify the ice forces was also used by Määttänen (1982), Brown (2007) and Frederking et al. (1986). Force identification has also been met with skepticism in the ice-research community (Kärnä and Turunen, 1989; Singh et al., 1990; Timco et al., 1989), where the criticism has been chiefly directed at inaccurate damping descriptions and nonlinearities not being accounted for in the frequency response function model. Among a wealth of force identification techniques, the deterministic frequency-domain deconvolution method (Ewins, 2000) is the most commonly applied technique in the ice-research community. This technique is easy to implement, and the frequency response function can either be obtained experimentally or from a numerical model. Its disadvantage is that it can be difficult to accurately determine the frequency response functions for large structures. For a literature review on force identification techniques, see Lourens (2012). Originally intended for input estimation problems in the field of optimal control (Gillijns and De Moor, 2007), the joint input-state (JIS) estimation algorithm was applied to structural dynamics by Lourens et al. (2012a), who also modified it for the use of modally reduced order systems. It is a recursive algorithm that estimates the forces (input) and response behavior (system states) simultaneously. The deterministic-stochastic nature of the algorithm allows for improved results when the model equations are inexact and the algorithm holds no prior assumption on the dynamic evolution of the forces.

1.2 Objectives and scope

The objective of this thesis is to assess a JIS estimation algorithm to simultaneously identify ice forces and responses on structures prone to ice-induced vibrations and to use the algorithm as a means to enhancing the understanding of ice-induced vibrations.

This study focuses on experimental work, the processing of experimental data and the theory of force identification. The scope of the work is the following:

- Conduct model-basin experiments on a multi-degree-of-freedom (MDOF) structure to study different regimes of ice-induced vibrations.
- Apply the JIS algorithm to identify ice forces and responses (at unmeasured locations) during ice-induced vibrations on both model-scale and full-scale structures using real response measurements.
- Use the identified forces and responses together with measured responses and ice velocities to understand the role of higher order structural vibration modes in ice-induced vibrations.
- Use the identified forces and responses from the model-basin experiments in conjunction with measured pressures at the ice-structure interface to study how the structural vibrations influence the pressures.
- Plan and execute full-scale measurements with optimal sensor locations for force identification on a channel marker.

The experimental data were limited to typical lighthouse-type, single-legged bottom-founded structures, although the discussion includes other types of bottom-founded structures considered to be relevant.

1.3 Research approach

The research was conducted by performing ice-induced vibration experiments on a model-scale structure and by utilizing available data from a measurement campaign on a full-scale structure. These data were used to assess the applicability of a JIS algorithm (Gillijns and De Moor, 2007) for force and response identification. At the model scale, the forces identified using the JIS algorithm were compared with forces identified using a frequency-domain deconvolution method. The algorithm was further used in conjunction with the measured data to enhance the understanding of ice-induced vibrations of bottom-founded structures. The JIS algorithm was used to identify forces on a full-scale structure. The identified forces were compared with measured forces from panels mounted to the structure. Recently developed guidelines that ensure the identifiability of forces using the JIS algorithm were followed to design a sensor network to identify dynamic ice forces on a channel edge marker. An illustration of the research approach with corresponding chapters is shown in Fig. 1.

1.4 Structure of the thesis

This thesis encompasses a collection of papers. Following the introduction (Chapter 1), the experimental basis is presented in Chapter 2. This is followed by the methods applied to identify the forces and states (Chapter 3). The main findings are summarized in Chapter 4, and the full-length papers are provided in Appendices 1-5, wherein Papers 1 to 3 discuss the work at the model scale and Papers 4 and 5 discuss the work at full scale.

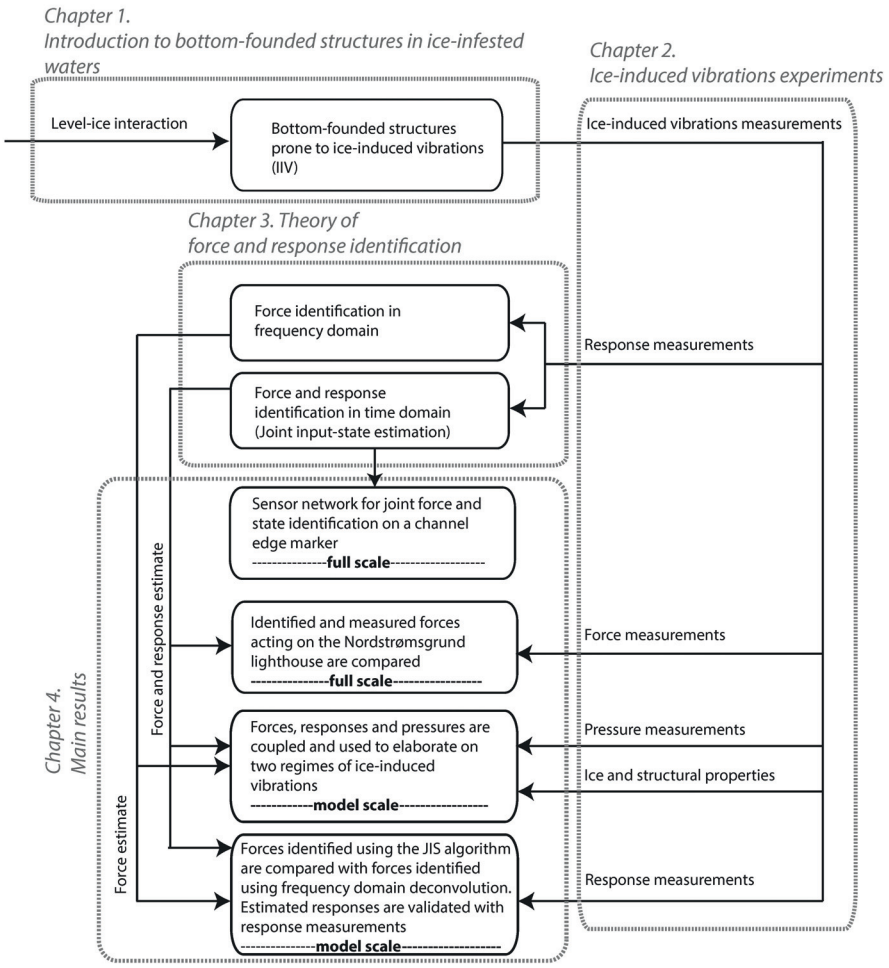

Figure 1. Illustration of the research approach.

Chapter 2 Ice-induced vibration measurements

This chapter summarizes the experimental component and is the basis for the following chapters. A brief summary of model-scale experiments is presented, leading up to a summary of our own experiments. Thereafter, a short introduction to a full-scale measurement campaign is presented followed by relevant structural information about a bottom-founded channel marker.

2.1 Model-scale experiments

The observations of the dynamic ice-structure interaction of vertical piers (Peyton, 1967) and the Cook Inlet platforms (Blenkarn, 1970) in the 1960s led the latter author to conclude that these vibrations were self-excited by nature. Määttänen (1978) noted that earlier laboratory tests concerning crushing failure mode were prone to vibrations, which he described as "*more of a by-product, (Määttänen, 1978)*". This led him to design a model-test campaign at the Cold Regions Research and Engineering Laboratory (CRREL) that systematically pursued the existence of ice-induced vibrations, similar to the vibrations observed in the Cook Inlet (Määttänen, 1979). Both fresh-water (Figs. 2 a and b) and urea ice sheets were forced onto a flexible pile that was pinned to a submerged foundation at two locations. The setup allowed a simple tuning of the first two natural frequencies by using adjustable pin points and mass of the superstructure. A report (Määttänen, 1983) summarized the results from that campaign and showed that the frequency of vibration increased with increasing ice velocity. At certain ice velocities, the response frequency remained close to the natural frequency, and the amplitudes became violent. These frequency lock-in vibrations were observed both in the first and second mode of the structure, in agreement with observations made in 1973 at the Kemi-1 steel lighthouse (Määttänen, 1975).

Numerous model-scale experiments were conducted, most of which with a single-degree-of-freedom (SDOF) oscillator (Barker et al., 2005; Finn et al., 1993; Gravesen et al., 2005; Huang et al., 2007; Izumiyama et al., 1994; Jordaan and Timco, 1988; Kärnä and Muhonen, 1990; Nakazawa and Sodhi, 1990; Singh et al., 1990; Sodhi, 1998; Timco et al., 1989; Toyama et al., 1983; Tsuchiya et al., 1985; Ziemer and Evers, 2014). Many features of the CRREL tests were adopted by an ice-induced vibration test campaign at the Hamburg ship model basin (HSVA) in 2002 (Kärnä et al., 2003). The natural frequencies were easily changed by adjusting the elastic foundation's torsional and bending stiffness. Additional masses and an active damper at the top could also be used to further tune the dynamic properties of the structure. Our own experimental campaign (Figs. 2 c and d), the Deciphering Ice Induced Vibrations (DIIV) campaign, was also conducted at HSVA in 2011 (Määttänen et al., 2012). The DIIV tests continued the MDOF research with a new flexible structure design and an additional forced vibration test setup (Hendrikse et al., 2012). The tests generated the laboratory data used in this thesis, and the experimental setup relevant to this thesis is summarized in the following section. Details are also given in Papers 1 to 3.

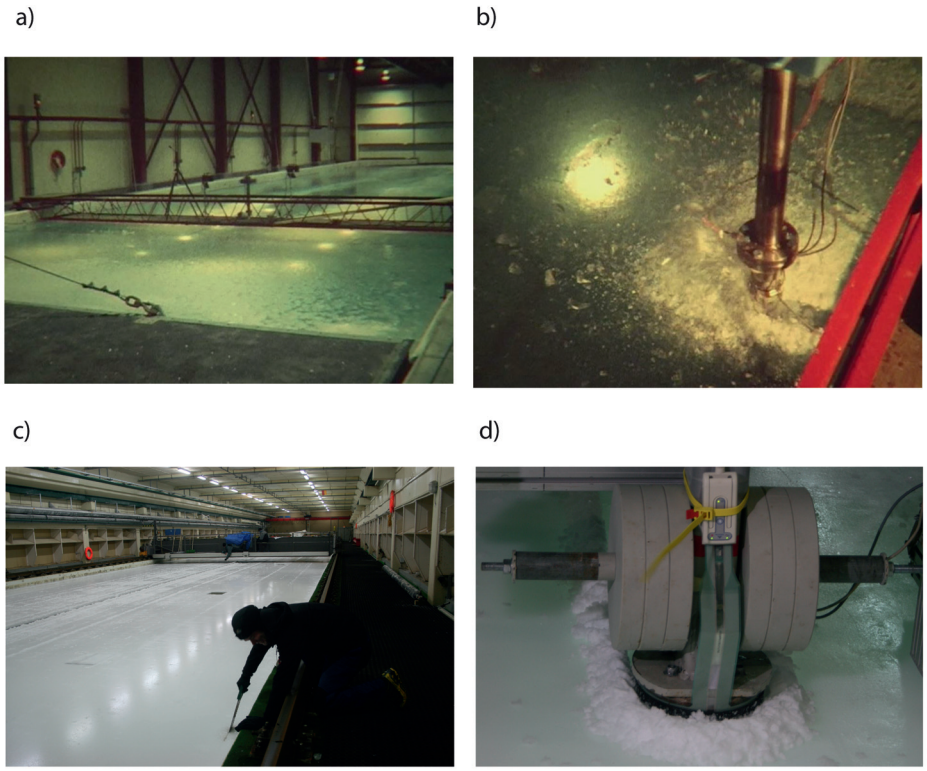

Figure 2. Ice-induced vibration test facilities: a) the Cold Regions Research Engineering Laboratory (CRREL) in Hanover, USA. Photo by Mauri Määttänen; b) Ice-induced vibrations tests in fresh-water ice. Photo by Mauri Määttänen; c) The Hamburg ship model basin (HSVA) ice tank, Germany; d) Ice-induced vibration tests in saline HSVA ice.

2.1.1 Deciphering ice-induced vibrations (DIIV) test setup

The structure (Fig. 3) was designed to have a scale ratio of 1:8-1:10 to a typical bottom-founded offshore structure. It was scaled to achieve modal similitude, meaning that the natural modes of the laboratory structure resembled the natural modes at full scale. This was achieved by scaling the natural frequency and ensuring that the lowest natural modes were easily excited at the ice-action point. Details about the dynamic scaling for this particular test setup can be found in Määttänen et al. (2012). The intention was to study different regimes of ice-induced vibrations and to allow the frequency of vibration to change from the first natural frequency to the second natural frequency with increasing ice velocity. The response measurement equipment consisted of one accelerometer, two lasers and three fully active strain gauge bridges, as shown in Fig. 3. A Tekscan tactile sensor 5530 was installed to measure the normal pressures at the ice-structure interface. Silicon glue (Fig. 4 a) on the cylinder and on the inside of the 0.5-mm-thick aluminum film protected the sensor (Fig. 4 b). The sensor included 2288 sensoring areas (sensels) within the perimeter, which was 416 mm wide and 157 mm

high. It covered an angle corresponding to 216 degrees, thereby enabling the full contact to be measured. Brackets on the backside of the indenter ensured that the aluminum film protection provided an evenly distributed pressure (Fig. 4 c). A sampling rate of 100 Hz was applied to all channels during both the dynamic calibration and ice action. The tests were conducted in the 78-m-long, 10-m-wide HSVA Large Ice Tank. Columnar-grained level-ice sheets were produced in NaCl-doped water by seeding. After the ice growth phase, the ice tank air temperature was increased to simultaneously reduce the ice strength to ensure that the ice force remained below the structural load capacity and attempt to achieve stress-rate similitude. Several issues related to scaling

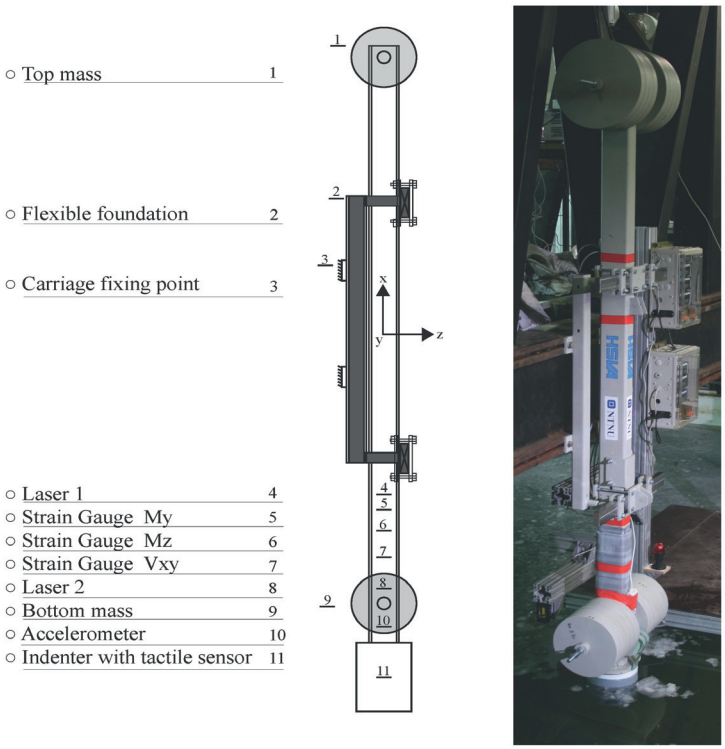

Figure 3. DIIV test structure and sensor locations.

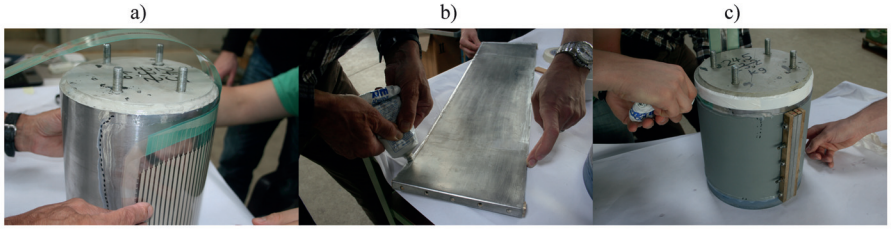

Figure 4. Tactile sensor installation: a) sensor glued to the indenter; b) protective film; c) brackets on the backside tightening the sensor protective film to the indenter.

of ice properties were demonstrated by Määttänen (1979) and further discussed by Timco (1984). Määttänen (1979) showed that compromises must be made among having similitude in the in-plane displacements and velocities of the ice sheet, the relative velocity between the ice and the structure, and the stress rate in the ice adjacent to the indenter. He showed that only similitude in the stress rate was achievable in practice when the ice strength was scaled. Because the HSVA ice has a lower ice strength and Young's modulus compared to sea ice, stress-rate similitude was attempted but not achieved because the ice strength was too low. A carriage forced the structure through the ice at velocities of between 10 mm s^{-1} and 350 mm s^{-1}. A set of different velocities, ice thicknesses, temperatures and structural configurations (adjustable mass and stiffness) provided a range of data sets for comparison (see table 1 in Paper 3). Data from this campaign are used in Papers 1, 2, and 3.

2.2 Full-scale measurements on the Nordströmsgrund lighthouse

The Nordströmsgrund lighthouse is located in the Gulf of Bothnia, 60 km southeast of the city of Luleå, Sweden. The structural response and ice forces during the winter seasons from 1999 to 2003 were monitored in the measurement projects, LOLEIF (LOw LEvel Ice Forces) and STRICE (STRuctures in ICE). The lighthouse (Fig. 5 a) is a gravity-based concrete structure with a wall thickness varying between 0.2 m at the top and 1.4 m at the mean water level. The submerged center structure and foundation caisson are filled with sand. Eight concrete bulkheads stiffen the main structure and a 0.7-m-thick concrete foundation plate that rests on a top layer of cement-grouted crushed stones and a lower layer of morainic soil.

Nine panels (Fig. 5 b) were installed across the outer surface at the mean water level at an elevation of +14.2 m to measure the ice forces. Two types of panels were installed on the lighthouse. One segmented panel faced directly east, in which eight segments enabled local force measurements through the ice thickness. The remaining eight panels each measured a single local force. In total, the nine panels covered the outer perimeter from 0 to 162^0. Two biaxial accelerometers and two biaxial inclinometers measured the structural response. The lowermost accelerometer was located close to the ice-action point at an elevation of +16.5 m, while the uppermost accelerometer was installed at an elevation of +37.1 m. The inclinometers were installed at +37.1 and +22.8 m. Because the signal from the uppermost inclinometer was low-pass filtered, the dynamic content was absent in the available data. The lowermost inclinometer was claimed to provide accurate measurements only up to 0.5 Hz (Frederking, 2005); thus, this sensor was not suitable for the dynamic application in Paper 4. The data recording frequency varied

between 1 and 100 Hz, selected high or low depending on the interaction and information sought. A summary of the STRICE project and earlier measurement campaigns can be found in Bjerkås (2006). Paper 4 utilizes the data collected in the STRICE project.

a) b)

Figure 5. The Nordströmsgrund lighthouse: a) picture of the concrete structure in ice-infested water; b) force panels mounted to the outer face.

2.3 The Hanko-1 channel marker

The Hanko-1 channel marker is located at N59 44.11 and E23 02.36 (WGS-84) offshore the city Hanko in Finland. A measurement campaign is planned to monitor the ice forces leading to ice-induced vibrations. The structure was chosen because of its location close to the mainland and because earlier measurements indicated frequency lock-in vibrations. The foundation pile is molded into a bedrock well via concrete casting (Fig. 6). A steel cone supports the 0.8-m-diameter circular-sectioned steel superstructure, which has a varying wall thickness from the mean water level up to the lantern at the top of the structure (Fig. 7). The structure exhibited frequency lock-in vibrations at the first natural frequency of 4.6 Hz on several occasions. For additional information about frequency lock-in vibrations on this channel marker and others, see Määttänen (2008), Kärnä and Turunen (1989) and Nordlund et al. (1988). Paper 5 discusses the optimal sensor network to identify the dynamic ice forces.

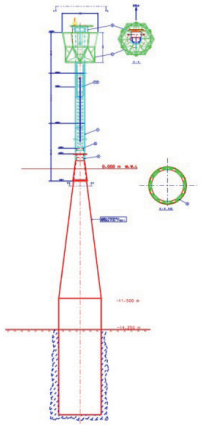

Figure 6. Hanko-1 Channel marker design.

Figure 7. Picture of a typical Channel marker, from Määttänen (2008).

Chapter 3 Force and state estimation

A wealth of methods exists to identify forces from measured responses. Lourens (2012) assessed several methods to identify dynamic forces in both the time and frequency domain. She divided the methods into two categories: deterministic and deterministic-stochastic. These are different in the sense that the latter includes stochastic uncertainties in the system model as well as the measurements. The two methods that are used in this thesis are outlined in the following sections, and a comprehensive literature review on different methods can be found in Lourens (2012).

Among the deterministic methods, we find the deconvolution methods in the time and frequency domain. The frequency-domain deconvolution method (Ewins, 2000) has been widely used within the ice community (Frederking et al., 1986; Montgomery and Lipsett, 1981; Määttänen, 1982). This method utilizes the frequency response function and a set of response measurements to identify the forces. Fabumni (1986) studied the number of forces that can be identified at an individual frequency dependent on the number of participating modes at that frequency. It was demonstrated that in the presence of measurement noise, only one force could be reconstructed with acceptable accuracy when only one mode was contributing to the response signal, as is the case around one of the natural frequencies. Doyle (1984) and Hillary and Ewins (1984) reconstructed the forces from strain measurements. The latter found that the forces were reconstructed with better accuracy when strain gauges were used instead of accelerometers. The advantage with the frequency-domain deconvolution method is that dynamic calibrations can be readily used to obtain the frequency response function matrix. The disadvantages are that accurate frequency response functions for large structures can be difficult to obtain, leakage errors occur during the transformation from the time to frequency domain, and the forces are solved for a specific length of a time signal. The last issue makes it difficult to address, for instance, a time-variant force location.

Unless the structural behavior can be obtained from dynamic calibrations, the forces must be identified with a limited amount of knowledge on the true structural behavior. This is often the case for civil engineering applications, including the Arctic structures. Measured data are often contaminated with noise; therefore, predicted states and data using a deterministic model will differ from the measured quantities. To better represent the measured data, stochastic uncertainties can be included in the model. In a force identification setting, the deterministic-stochastic approach estimates a deterministic force from the response measurements using a model with stochastic uncertainties. Within this branch, we find the Kalman filter methods, including the Augmented Kalman filter (Lourens et al., 2012b) and the JIS algorithm (Gillijns and De Moor, 2007). They are very similar, but only the latter can identify a force without any prior assumptions about its dynamic evolution. This becomes a great advantage for application to ice-structure interactions, namely because the ice conditions can rapidly evolve. The JIS algorithm was originally developed for use within the field of optimal control but was extended for applications to modally reduced order models as often used in structural dynamics by Lourens et al. (2012a). This modified algorithm allows for the forces and states to also be identified when the number of sensors and/or forces exceeds the number of structural modes used to construct the model. Another advantage with the JIS algorithm is that it also enables the prediction of responses at unmeasured

locations. For a literature overview on pure response (state) estimation techniques, in which the forces are either assumed known or assumed to be modeled as a zero mean stationary white process, see Lourens (2012).

3.1 Frequency-domain deconvolution method

The linear time-domain relationship between a unit impulse and the output can be written for a single-degree-of-freedom system:

$$d(\mathrm{t}) = \int_0^t h(t-\tau)\, p(\tau) d\tau \tag{1}$$

Here, $d(\mathrm{t})$ is the output, $p(\tau)$ is a unit impulse excitation, and $h(t-\tau)$ is the impulse response function. The Fourier transform applied to Eq. (1) transforms the system into the frequency domain as follows:

$$d(\omega) = H(\omega)\,\mathrm{p}(\omega) \tag{2}$$

Here, $H(\omega)$ is the complex frequency response function, and ω is the frequency in radians per second. In a system with n_p inputs (forces) and n_d outputs (response measurements), the relationship between the input and output reads

$$\mathbf{d}(\omega) = \mathbf{H}(\omega)\mathbf{p}(\omega) \tag{3}$$

where $\mathbf{d}(\omega) \in \mathbb{C}^{n_\mathrm{d}}$, $\mathbf{p}(\omega) \in \mathbb{C}^{n_\mathrm{p}}$ and $\mathbf{H}(\omega) \in \mathbb{C}^{n_\mathrm{d} \times n_\mathrm{p}}$. Each matrix component $H_{\mathrm{lk}}(\omega)$ can be calculated or obtained using dynamic calibrations. Refer to Ewins (2000) for the first case. In the latter case, each matrix column l is obtained by employing a controlled excitation at a point k. Four common types of excitations are hammer impacts, step relaxation, non-contact magnetic excitation and base excitation (Ewins, 2000).
When the frequency response function matrix is assembled, the force can be identified using the pseudo inverse as follows:

$$\mathbf{p}(\omega) = \left(\mathbf{H}^{\mathrm{H}}(\omega)\mathbf{H}(\omega)\right)^{-1}\mathbf{H}^{\mathrm{H}}(\omega)\mathbf{d}(\omega) \tag{4}$$

where $\mathbf{H}^{\mathrm{H}}(\omega)$ is the Hermitian transpose of the frequency response function matrix.

3.2 Model-based joint input-state estimation

This section explains the framework starting from model assembly, full and modally reduced order models, and the requirements for successful force identification using the presented JIS algorithm. Throughout this thesis, the word “state” refers to structural displacement and/or velocity.

3.2.1 State-space model assembly

The governing equations of motion for a linear system discretized in space and excited by an external force can be written as follows:

$$\mathbf{M}\ddot{\mathbf{u}}(t) + \mathbf{C}\dot{\mathbf{u}}(t) + \mathbf{K}\mathbf{u}(t) = \mathbf{f}(t) = \mathbf{S}_\mathrm{p}\mathbf{p}(t) \tag{5}$$

where $\mathbf{u} \in \mathbb{R}^{n_{\mathrm{DOF}}}$ is the displacement vector and the matrices $\mathbf{M}, \mathbf{C}, \mathbf{K} \in \mathbb{R}^{n_{\mathrm{DOF}} \times n_{\mathrm{DOF}}}$ denote the structural mass, damping and stiffness matrix, respectively. The excitation vector $\mathbf{p}(t) \in \mathbb{R}^{n_{\mathrm{p}}}$ is specified to act on the desired locations through the force influence matrix $\mathbf{S}_{\mathrm{p}} \in \mathbb{R}^{n_{\mathrm{DOF}} \times n_{\mathrm{p}}}$, where n_{p} is the number of force time histories.

The continuous-time state vector $\mathbf{x}(t) \in \mathbb{R}^{n_{\mathrm{s}}}$, $n_{\mathrm{s}} = 2n_{\mathrm{DOF}}$, is defined as

$$\mathbf{x}(t) = \begin{pmatrix} \mathbf{u}(t) \\ \dot{\mathbf{u}}(t) \end{pmatrix} \tag{6}$$

whereby the equation of motion of second order in Eq. (5) can be organized as a first-order continuous-time state equation

$$\dot{\mathbf{x}}(t) = \mathbf{A}_{\mathrm{c}}\mathbf{x}(t) + \mathbf{B}_{\mathrm{c}}\mathbf{p}(t) \tag{7}$$

where the system matrices $\mathbf{A}_{\mathrm{c}} \in \mathbb{R}^{n_{\mathrm{s}} \times n_{\mathrm{s}}}$ and $\mathbf{B}_{\mathrm{c}} \in \mathbb{R}^{n_{\mathrm{s}} \times n_{\mathrm{p}}}$ are defined as

$$\mathbf{A}_{\mathrm{c}} = \begin{bmatrix} \mathbf{0} & \mathbf{I} \\ -\mathbf{M}^{-1}\mathbf{K} & -\mathbf{M}^{-1}\mathbf{C} \end{bmatrix}, \mathbf{B}_{\mathrm{c}} = \begin{bmatrix} \mathbf{0} \\ \mathbf{M}^{-1}\mathbf{S}_{\mathrm{p}} \end{bmatrix} \tag{8}$$

The measurements are arranged in a data vector $\mathbf{d}(t) \in \mathbb{R}^{n_{\mathrm{d}}}$, in which the observations can be a linear combination of displacement, velocity and acceleration, with n_{d} being the number of data measurements. The data vector is constructed as follows:

$$\mathbf{d}(t) = \mathbf{S}_{\mathrm{a}}\ddot{\mathbf{u}}(t) + \mathbf{S}_{\mathrm{v}}\dot{\mathbf{u}}(t) + \mathbf{S}_{\mathrm{d}}\mathbf{u}(t) \tag{9}$$

where the selection matrices $\mathbf{S}_{\mathrm{a}}, \mathbf{S}_{\mathrm{v}}$ and $\mathbf{S}_{\mathrm{d}} \in \mathbb{R}^{n_{\mathrm{d}} \times n_{\mathrm{DOF}}}$ are populated according to the spatial location where the acceleration, velocity and/or displacement (strains) are measured. By premultiplying Eq. (5) by $\mathbf{M}^{-1}$, inserting the resulting expression into Eq. (9), and further utilizing the definition of the state vector, Eq. (9) can be transformed into the state-space form:

$$\mathbf{d}(t) = \mathbf{G}_{\mathrm{c}}\mathbf{x}(t) + \mathbf{J}_{\mathrm{c}}\mathbf{p}(t) \tag{10}$$

where the matrices $\mathbf{G}_{\mathrm{c}} \in \mathbb{R}^{n_{\mathrm{d}} \times n_{\mathrm{s}}}$ and $\mathbf{J}_{\mathrm{c}} \in \mathbb{R}^{n_{\mathrm{d}} \times n_{\mathrm{p}}}$ represent the output influence matrix and direct transmission matrix, respectively, defined as

$$\mathbf{G}_{\mathrm{c}} = [\mathbf{S}_{\mathrm{d}} - \mathbf{S}_{\mathrm{a}}\mathbf{M}^{-1}\mathbf{K} \quad \mathbf{S}_{\mathrm{v}} - \mathbf{S}_{\mathrm{a}}\mathbf{M}^{-1}\mathbf{C}], \qquad \mathbf{J}_{\mathrm{c}} = [\mathbf{S}_{\mathrm{a}}\mathbf{M}^{-1}\mathbf{S}_{\mathrm{p}}]$$

If modally reduced order models are used, the system matrices become (Lourens, 2012)

$$\mathbf{A}_{\mathrm{c}} = \begin{bmatrix} \mathbf{0} & \mathbf{I} \\ -\boldsymbol{\Omega}^2 & -\boldsymbol{\Gamma} \end{bmatrix}, \mathbf{B}_{\mathrm{c}} = \begin{bmatrix} \mathbf{0} \\ \boldsymbol{\Phi}^{\mathrm{T}}\mathbf{S}_{\mathrm{p}} \end{bmatrix} \tag{11}$$

and

$$\mathbf{G}_{\mathrm{c}} = [\mathbf{S}_{\mathrm{d}}\boldsymbol{\Phi} - \mathbf{S}_{\mathrm{a}}\boldsymbol{\Phi}\boldsymbol{\Omega}^2 \quad \mathbf{S}_{\mathrm{v}}\boldsymbol{\Phi} - \mathbf{S}_{\mathrm{a}}\boldsymbol{\Phi}\boldsymbol{\Gamma}], \qquad \mathbf{J}_{\mathrm{c}} = [\mathbf{S}_{\mathrm{a}}\boldsymbol{\Phi}\boldsymbol{\Phi}^{\mathrm{T}}\mathbf{S}_{\mathrm{p}}] \tag{12}$$

Here, $\boldsymbol{\Gamma} \in \mathbb{R}^{n_{\mathrm{m}} \times n_{\mathrm{m}}}$ is the diagonal damping matrix populated on the diagonal with the

terms $2\xi_j\omega_j$, where ω_j and ξ_j are the natural frequency and damping ratio, respectively, corresponding to mode j. $\mathbf{\Omega} \in \mathbb{R}^{n_m \times n_m}$ is a diagonal matrix containing the natural frequencies ω_j, and $\mathbf{\Phi} \in \mathbb{R}^{n_{DOF} \times n_m}$ is a matrix collecting the mass-normalized mode shapes.
In discrete time under a zero-order hold assumption and given a sampling rate of $1/\Delta t$, Eqs. (7) and (10) can be defined as follows:

$$\mathbf{x}_{k+1} = \mathbf{A}\mathbf{x}_k + \mathbf{B}\mathbf{p}_k \tag{13}$$

$$\mathbf{d}_k = \mathbf{G}\mathbf{x}_k + \mathbf{J}\mathbf{p}_k \tag{14}$$

where

$$\mathbf{x}_k = \mathbf{x}(k\Delta t),\ \mathbf{d}_k = \mathbf{d}(k\Delta t),\ \mathbf{p}_k = \mathbf{p}(k\Delta t),\ k = 1,...,N$$

and

$$\mathbf{A} = e^{\mathbf{A}_c \Delta t},\ \mathbf{B} = [\mathbf{A} - \mathbf{I}]\mathbf{A}_c^{-1}\mathbf{B}_c,\ \mathbf{G}_c = \mathbf{G},\ \mathbf{J}_c = \mathbf{J}$$

3.2.2 Requirements for successful force identification

The correct types and locations of response measurements are essential to successfully identify the forces. Maes et al. (2014) formulated a set of mathematical criteria that can be used to design sensor networks. The criteria ensure that the dynamic forces can be identified using the JIS estimation algorithm (Eqs. (18) – (27)) in conjunction with a modally reduced order model (Eqs. (11) – (12)). The first criterion ensures that the ice force can be estimated from the response measurements without a time delay. The second criterion ensures that the stability of the system inversion is maintained. The reader is recommended to read the reference for additional criteria that ensure the complete dynamic response to be identified.

3.2.2.1 Direct invertibility

The system input (the ice force) must be estimated from the output without a time delay. This is proven to hold if $\text{rank}(\mathbf{J}) = \text{rank}(\mathbf{S}_a\mathbf{\Phi}\mathbf{\Phi}^T\mathbf{S}_p) = n_p$ (= number of forces). To ensure this, the number of excited modes should be greater or equal to the number of forces, $\text{rank}\,(\mathbf{S}_p^T\mathbf{\Phi}) = n_p$. Moreover, at least n_p accelerations must be measured to secure a direct coupling between the acceleration responses and the estimated forces. Furthermore, the acceleration measurements should provide significant contributions from the modes excited by the forces.

3.2.2.2 Stability requirements

The stability of the system inversion can be verified by investigating the so-called transmission zeros. These zeros depend on the matrices $\mathbf{A}, \mathbf{B}, \mathbf{G}$ and $\mathbf{J}$ and are determined by solving the following eigenvalue problem (Emami-Naeini and Van Dooren, 1982):

$$\begin{bmatrix} \mathbf{A} - \lambda_j\mathbf{I} & \mathbf{B} \\ \mathbf{G} & \mathbf{J} \end{bmatrix} \begin{bmatrix} \mathbf{x}_{[0]} \\ \mathbf{p}_{[0]} \end{bmatrix} = \begin{bmatrix} \mathbf{0} \\ \mathbf{0} \end{bmatrix} \tag{15}$$

where $\lambda_j \in \mathbb{C}$ is a finite transmission zero for any selection of the corresponding initial conditions $\mathbf{x}_{[0]} \in \mathbb{C}^{n_s}$ and $\mathbf{p}_{[0]} \in \mathbb{C}^{n_p}$ for the state and force, respectively. If $|\lambda_j| < 1$, the system inversion is stable, whereas if $|\lambda_j| > 1$, the system inversion is unstable. When $|\lambda_j| = 1$, the system inversion is marginally stable. Maes et al. (2014) explained that the 0 Hz marginally stable transmission zero occurs because the acceleration and velocity measurements are insensitive to an excitation that is constant with time. The latter occurs if only acceleration data are included in the measurement setup. By including displacement/strain measurements, one can omit the marginally stable transmission zero at 0 Hz, and the inversion stability can be further checked from $\text{rank}(\mathbf{J} - \mathbf{G}(\mathbf{A} - \mathbf{I})^{-1}\mathbf{B}) = \min(n_p, n_d)$. This is demonstrated in section 4.3 (Paper 5).

3.2.3 The joint input-state (JIS) estimation algorithm

Assuming that the system matrices are known, the joint input-state estimation algorithm is used to jointly estimate the forces and states. By introducing the random variables $\mathbf{w}_k$ and $\mathbf{v}_k$, which represent the stochastic system (process noise) and measurement noise, respectively, the discrete-time state-space equations are defined as

$$\mathbf{x}_{k+1} = \mathbf{A}\mathbf{x}_k + \mathbf{B}\mathbf{p}_k + \mathbf{w}_k \tag{16}$$

$$\mathbf{d}_k = \mathbf{G}\mathbf{x}_k + \mathbf{J}\mathbf{p}_k + \mathbf{v}_k \tag{17}$$

Here, it is assumed that the vectors $\mathbf{w}_k$ and $\mathbf{v}_k$ are mutually uncorrelated, zero-mean, white-noise signals with known covariance matrices $\mathbf{Q} = E\{\mathbf{w}_k\mathbf{w}_k^T\}$ and $\mathbf{R} = E\{\mathbf{v}_k\mathbf{v}_k^T\}$. The process noise determines the confidence that we assign to the utilized model. The lower the process noise, the more we trust the system model. The measurement noise determines the confidence that we have in the measurements.

The algorithm predicts the forces and states in three steps: the minimum variance and unbiased (MVU) input estimation, the measurement update, and the time update. The first step calculates an optimal estimate of the force $\hat{\mathbf{p}}_{k|k}$ based on assumed covariances for the measurement errors, the system model, and the estimated states. The second step (measurement update) calculates an MVU state estimate $\hat{\mathbf{x}}_{k|k}$ using the measured data $\mathbf{d}_k$ and the gain matrix $\mathbf{L}_k$ from Eq. (22). Apart from the fact that the force is an estimated vector and not known, this step is the same as in the classical Kalman filter. In the final step, the state of the system is advanced in time using the system model.

To initialize the recursive algorithm, it is assumed that an unbiased estimate $\hat{\mathbf{x}}_{0|-1}$ of the initial state $\mathbf{x}_0$ is available. By unbiased estimate, we mean that the expectation of the error is zero, i.e., $E\{\mathbf{x}_0 - \hat{\mathbf{x}}_{0|-1}\} = 0$. The initial state error covariance matrix $\mathbf{P}_{0|-1} = E\{(\mathbf{x}_0 - \hat{\mathbf{x}}_{0|-1})(\mathbf{x}_0 - \hat{\mathbf{x}}_{0|-1})^T\}$ is also assumed to be known. The recursive algorithm can be implemented as follows:

Input estimation:

$$\tilde{\mathbf{R}}_k = \mathbf{G}\mathbf{P}_{k|k-1}\mathbf{G}^T + \mathbf{R} \tag{18}$$

$$\mathcal{M}_k = (\mathbf{J}^{\mathrm{T}}\tilde{\mathbf{R}}_k^{-1}\mathbf{J})^{-1}\mathbf{J}^{\mathrm{T}}\tilde{\mathbf{R}}_k^{-1} \tag{19}$$

$$\hat{\mathbf{p}}_{k|k} = \mathcal{M}_k(\mathbf{d}_k - \mathbf{G}\hat{\mathbf{x}}_{k|k-1}) \tag{20}$$

$$\mathbf{P}_{\mathrm{p}[k|k]} = (\mathbf{J}^{\mathrm{T}}\tilde{\mathbf{R}}_k^{-1}\mathbf{J})^{-1} \tag{21}$$

Measurement update:

$$\mathbf{L}_k = \mathbf{P}_{k|k-1}\mathbf{G}^{\mathrm{T}}\tilde{\mathbf{R}}_k^{-1} \tag{22}$$

$$\hat{\mathbf{x}}_{k|k} = \hat{\mathbf{x}}_{k|k-1} + \mathbf{L}_k(\mathbf{d}_k - \mathbf{G}\hat{\mathbf{x}}_{k|k-1} - \mathbf{J}\hat{\mathbf{p}}_{k|k}) \tag{23}$$

$$\mathbf{P}_{k|k} = \mathbf{P}_{k|k-1} - \mathbf{L}_k(\tilde{\mathbf{R}}_k - \mathbf{J}\,\mathbf{P}_{\mathrm{p}[k|k]}\mathbf{J}^{\mathrm{T}})\mathbf{L}_k^{\mathrm{T}} \tag{24}$$

$$\mathbf{P}_{\mathrm{xp}[k|k]} = \mathbf{P}_{\mathrm{px}[k|k]}^{\mathrm{T}} = -\mathbf{L}_k\mathbf{J}\,\mathbf{P}_{\mathrm{p}[k|k]} \tag{25}$$

Time update:

$$\hat{\mathbf{x}}_{k+1|k} = \mathbf{A}\hat{\mathbf{x}}_{k|k} + \mathbf{B}\hat{\mathbf{p}}_{k|k} \tag{26}$$

$$\mathbf{P}_{k+1|k} = \begin{bmatrix}\mathbf{A} & \mathbf{B}\end{bmatrix}\begin{bmatrix}\mathbf{P}_{k|k} & \mathbf{P}_{\mathrm{xp}[k|k]} \\ \mathbf{P}_{\mathrm{p}x[k|k]} & \mathbf{P}_{\mathrm{p}[k|k]}\end{bmatrix}\begin{bmatrix}\mathbf{A}^{\mathrm{T}} \\ \mathbf{B}^{\mathrm{T}}\end{bmatrix} + \mathbf{Q} \tag{27}$$

The force and state estimates are said to be optimal in the sense that the mean squared error estimate is made as small as possible, and no further mathematical manipulation will provide a better result (Brown and Hwang, 1997). The gain matrices $\mathcal{M}_k$ and $\mathbf{L}_k$ ensure that the force and state estimates are minimum variance and unbiased (Gillijns and De Moor, 2007). If the model used to construct the matrices $\mathbf{A}$ and $\mathbf{B}$ contains errors, the force and state estimates are no longer minimum variance and unbiased (Maes et al., 2015). When applied to a real structure, the modeling errors should therefore be minimized. The algorithm was recently extended by Maes et al. (2013) to address situations in which the system noise $\mathbf{w}_k$ and measurement noise $\mathbf{v}_k$ are correlated. This correlation is inherent when accelerations are measured, and the system and measurement noise are both affected by errors in the forcing (e.g., in the assumed positions of the forces). The errors can cause the assumption concerning the force location and number of forces to be violated, resulting in correlated measurement and process noise. The suggested method for identifying the correlation uses response measurements from a time window in which the excitation is assumed to be a stationary discrete-time white noise process. Thus, if the correlation is caused by unmodeled local ice forces, it is difficult to identify the correlation in practice because the local ice forces violate the white noise assumption. This study has not employed the algorithm with extensions to include correlated noise processes; this is left for future work. In a reduced order system setting, the above equations must be modified when the number of sensors n_{d} exceeds the number of forces n_{p} or when the number of forces n_{p} is larger than the number of modes n_{m}. This modification can be found in Lourens et al. (2012a).

Chapter 4 Results and discussion

Before presenting the main results, a brief description of each of the papers in Appendices 1-5 is given below:

Paper 1 describes the frequency-domain deconvolution method, the dynamic calibrations used to obtain frequency response functions, and the identified forces. Paper 2 describes how the ice forces were identified using the JIS algorithm in conjunction with a limited number of response measurements and finite element models. Here, the identified forces are compared with the forces obtained using the frequency-domain deconvolution method (Paper 1), and the accuracy of the jointly estimated responses are validated with displacement response measurements. Paper 3 couples force and response estimates to the measured tactile sensor pressures to demonstrate how the structural motion influences the ice pressure. Paper 4 compares, at full scale, identified versus measured ice forces on the Nordströmsgrund lighthouse. Paper 5 shows how a recently published technique can be used to decide upon an optimal sensor network for identifying ice forces on a channel marker by the JIS algorithm.

4.1 Joint input-state estimation at model scale

The objective was to assess the quality of the identified forces and states during ice-induced vibrations using a recently developed deterministic-stochastic framework and real measurements from the DIIV experiments in section 2.1.1. Second, it is used as a means to better understand ice-induced vibrations. To the author's knowledge, this framework has yet to be applied to ice-induced vibrations, and several papers (Frederking et al., 1986; Montgomery and Lipsett, 1981; Määttänen, 1982) used the deterministic frequency-domain deconvolution method.

The results in this section cover Papers 1 to 3. Using one accelerometer and one strain gauge response signal, the forces and responses were identified using the JIS algorithm (section 3.2). The forces were compared with those obtained using the frequency-domain deconvolution method with experimentally obtained frequency response functions (section 3.1), and the estimated response were validated with laser displacement measurements.

Before forces can be identified with the JIS algorithm, we must assign values to the covariance matrices for the process noise, $\mathbf{Q}$; the measurement noise, $\mathbf{R}$; the initial state error covariance matrix, $\mathbf{P}_{0|-1}$; and the initial state vector $\hat{\mathbf{x}}_{0|-1}$. The measurement noise determines the confidence that we have in the measurements and can be determined from the latent noise in the sensor. However, disturbances originating from second-order effects can cause difficulties when quantifying the noise magnitude. A practical solution is to choose the noise magnitude to be a small percentage of the measured data. For example, the diagonal elements of the matrix $\mathbf{R}$ can be assigned the square of a small percentage of the peak values or standard deviations of the data. Similar challenges are encountered when deciding upon the process noise, which determines the confidence that we assign to the utilized model. Model errors regarding natural frequencies and damping ratios, system non-linearities, and the accuracy of the time discretization contribute to the noise. The lower the errors, the more we trust the

system model. In practice, the diagonal elements of the matrix $\mathbf{Q}$ can be assigned the square of a small percentage of the values that they represent, i.e., displacements, velocities (full-order model), modal displacements and modal velocities (reduced-order model). The initial state error covariance matrix $\mathbf{P}_{0|-1}$ can usually be set as equal to the process noise $\mathbf{Q}$, and the initial state $\hat{\mathbf{x}}_{0|-1}$ can be effectively treated as an unknown by setting it to zero.

4.1.1 Forces

In Paper 2, ice forces during intermittent crushing and continuous brittle crushing were obtained using the JIS algorithm and compared with forces obtained using measured frequency response functions. The paper assessed the importance of applying accurate finite element models in conjunction with the JIS algorithm. The system matrices $\mathbf{A}, \mathbf{B}, \mathbf{G}$ and $\mathbf{J}$ were constructed according to Eqs. (8) and (10) by extracting the mass and stiffness matrices and by employing Rayleigh damping. The identification is performed by employing two different finite element models. The first model was based on limited knowledge of the true dynamic properties of the structure. This model was called the blueprint model. The second model was tuned so that the first natural frequency would be accurately described. This model was called the tuned model. The covariance matrices necessary for the JIS algorithm, $\mathbf{Q}$, $\mathbf{R}$ and $\mathbf{P}_{0|-1}$, were assigned values of 10^{-8}, 10^{-6} and 10^{-8}, respectively, on the diagonals. Two ice-induced vibration tests were used in this study: test 3300 and test 4300. The identified (JIS) force using the blueprint model versus the reference force (FRF) for test 3300 is shown in Fig. 8. Two different ice velocities were selected to show in detail the quality of the force identification. The time history and Fourier spectra are shown in Figs. 8c and d, respectively, for a velocity of approximately 90 mm s^{-1}. Minor differences were found at 11-12 Hz, and the overall estimation using JIS closely followed the reference force. At ~200 mm s^{-1}, the identified force (Fig. 8e) exhibits a somewhat larger deviation from the reference force. Regardless, the dominant frequencies below 10.2 Hz correlate well with the reference force (Fig. 8f). Only marginal improvements were seen using the tuned model, and the force identification results provided strong motivation for using the algorithm on full-scale applications.

4.1.2 Displacements

One of the advantages of the JIS algorithm is that the responses at any nodal location can be extracted. This enabled validation of the estimated displacements with the laser displacements (Paper 2).

The estimated displacements from test 3300 at the lowermost laser location (c.f. Fig. 3) using the blueprint model are displayed in Fig. 9. The displacements of the structure were overestimated throughout the test (Fig. 9 a). The estimated dominant response frequencies, however, were well correlated with the measured response (Fig. 9 b). At ~90 mm s^{-1} (Fig. 9 c), the average offset for the peaks is 2.41 mm, and at ~200 mm s^{-1} (Fig. 9 d), the average offset is 4.16 mm. This significant difference in the two offsets means that the response estimation becomes more prone to modeling errors at higher ice velocities. It was found that tuning the model significantly improved the estimated displacements, as shown in Fig. 10. The tuned model and the JIS algorithm predicted

the displacement to be almost identical to the measured displacement throughout the displacement time history (Figs. 10 (a) and (b)). The offset was below 1 mm at ~ 90 mm s^{-1} (Fig. 10 c), therein capturing both the first and second mode with high precision (Fig. 10 d). At ~200 mm s^{-1} (Fig. 10 e), the discrepancy remained limited to 1 mm, and an excellent reconstruction of both the first and second mode was obtained (Fig. 10 f). A similar trend was found for test 4300 (see Paper 2).

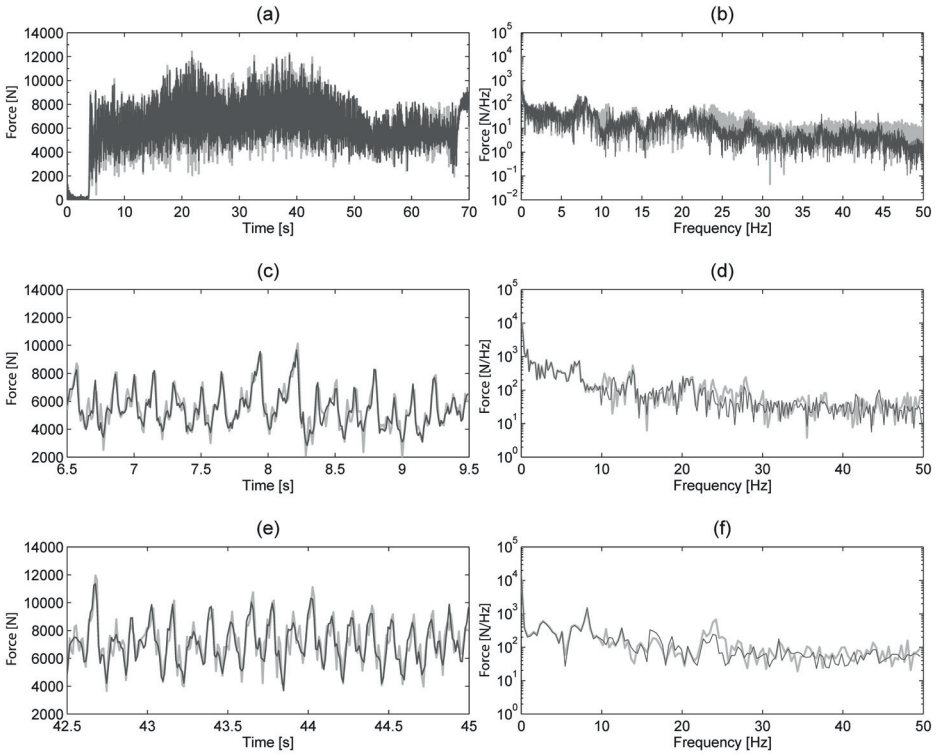

Figure 8. Identified force (light grey) versus reference force (black) (a) for the complete force time history, (b) for the frequency spectrum of the complete force time history, (c) at an ice velocity of ~90 mm s^{-1}, (d) for the frequency spectrum at an ice velocity of ~90 mm s^{-1}, (e) at an ice velocity of ~200 mm s^{-1} and (f) for the frequency spectrum at an ice velocity of ~200 mm s^{-1}.

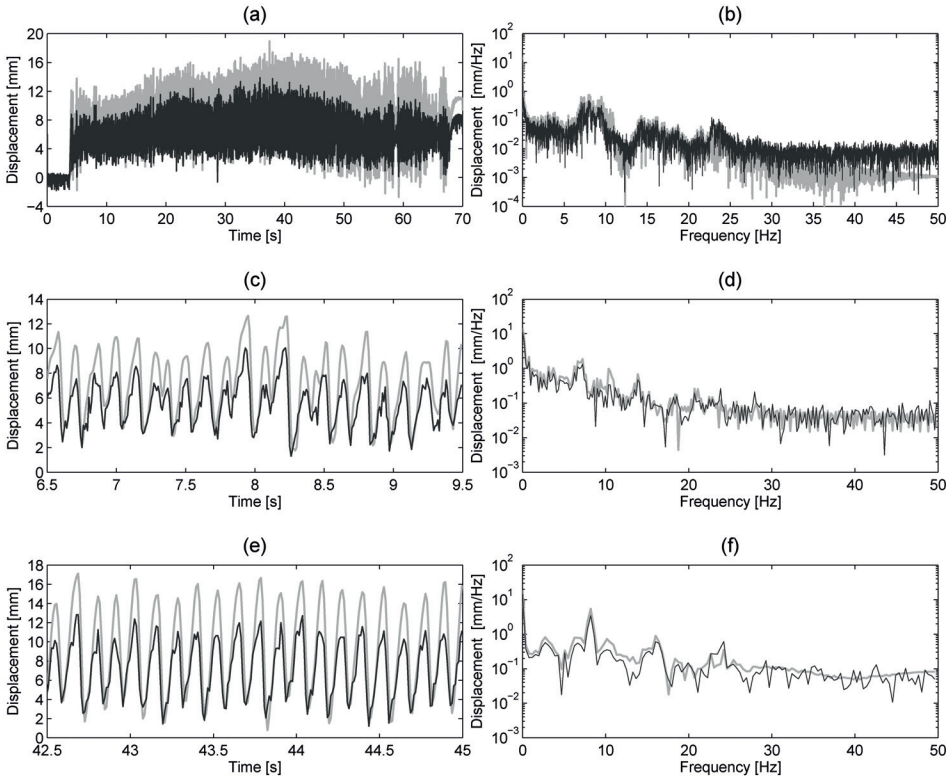

Figure 9. Estimated (light grey) versus measured (black) displacement (a) for the complete displacement time history, (b) for the frequency spectrum of the complete displacement time history, (c) at an ice velocity of ~90 mm s^{-1}, (d) for the frequency spectrum at an ice velocity of ~90 mm s^{-1}, (e) at an ice velocity of ~200 mm s^{-1} and (f) for the frequency spectrum at an ice velocity of ~200 mm s^{-1}.

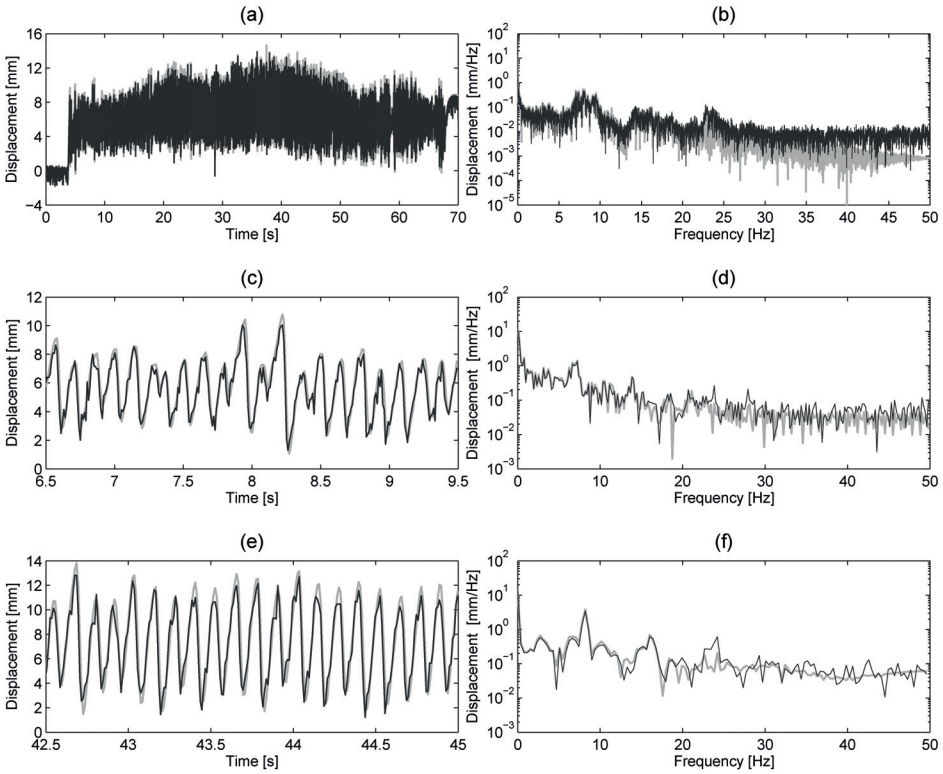

Figure 10. Estimated (light grey) versus measured (black) displacement (a) for the complete displacement time history, (b) for the frequency spectrum of the complete displacement time history, (c) at an ice velocity of ~90 mm s^{-1}, (d) for the frequency spectrum at an ice velocity of ~90 mm s^{-1}, (e) at an ice velocity of ~200 mm s^{-1} and (f) for the frequency spectrum at an ice velocity of ~200 mm s^{-1}.

4.1.3 Joint input-state estimation coupled with pressure measurements

The above application of the JIS algorithm showed that accurate forces and responses could be obtained if the model was sufficiently accurate. In Paper 3, the algorithm was used as a tool in conjunction with tuned finite element models to analyze the laboratory tests. The finite element models corresponded to the structural configurations during the measurements. One strain gauge and one accelerometer were used to identify the forces and states. Unlike Paper 2, which used full-order finite element models, Paper 3 reduced the model order by only retaining the first 30 eigenmodes and thereby greatly reduced the computational cost. These modes were used to assemble the matrices $\mathbf{A}, \mathbf{B}, \mathbf{G}$ and $\mathbf{J}$ according to Eqs. (11) and (12), therein assuming 2% proportional damping for all modes.

The identified forces were presented together with the measured responses and ice velocities in the first part of the paper, as shown in Fig. 11. Such figures were generated for five tests. The conclusions were formulated from the perspective of structural dynamics. The transition ice velocity at which the vibrations shifted from the first mode

to the second mode increased with decreased foundation stiffness and superstructure mass. Two examples of the transition from mode 1 to mode 2 are shown in Figs. 11 b and e. Here, the bright green band/trajectory represents the dominant strain gauge response, and the horizontal red lines are the natural frequencies of the structure. When the ice velocity increases, the transition is observed where the band displaces from being close to the first natural frequency to becoming close to the second natural frequency.

The reduction in both the superstructure mass and the foundation stiffness resulting in an increasing transition ice velocity suggests that the mode shapes should be considered; this is consistent with the instability criterion for frequency lock-in vibrations in ISO 19906 (2010), originally introduced by Määttänen (1978). Vibrations at a frequency other than the first natural frequency were often superimposed on the dominant vibration frequency, and the ice forces varied with changing ice velocity and frequency content of the response. These results are also in agreement with the results from ice-induced vibration experiments performed by Määttänen (1983).

With the tests presented in full in the first part of Paper 3, the second part coupled the structural motion estimates with the measured pressure at the ice-structure interface. When the forces and the spatially complete structural displacements were displayed together with the tactile sensor pressures, they showed how the structural motion influenced the pressure at the ice-structure interface. This analysis was performed for two regimes of ice-induced vibrations: the intermittent crushing regime and a regime that exhibited the tendencies of frequency lock-in vibrations. The forces were obtained in three ways: from the tactile sensor, from the JIS algorithm and from the frequency-domain deconvolution method. The tactile sensor force was calculated as the sum of local forces in the columns covering 0-180 degrees of the indenter, which was subsequently multiplied by a scaling factor to obtain a peak tactile sensor force that is close to the peak JIS-identified force. Undoubtedly, the tactile sensor sampling frequency of 100 Hz, time attenuation in the pressure signal and calibration pressures presented various constraints, as also discussed in Määttänen et al. (2011). Therefore, it was important to display the scaled tactile sensor force together with the identified forces to show that the measured interfacial pressures were responsible for the characteristics observed in the force time signal. Because the JIS-identified force was identified with the structural displacements simultaneously, we were able to study how the structural vibrations affected the pressure at the ice-structure interface.

The estimated displacement was compared with the measured displacement at the lowermost laser location.

The forces and the displacements during intermittent crushing at an ice velocity of 20 mm s^{-1} are shown in Fig. 12, and the estimated spatially complete structural motion and the pressure measurements are given in Fig. 13. Each (saw-tooth) cycle at the dominant frequency was attributed to a load build-up and ice failure, whereas a higher vibrational frequency was attributed to vibrations of the superstructure. It was found that the superstructure vibrations caused cyclic loading and unloading of the ice edge prior to each ice failure. It was further demonstrated that these vibrations can cause the loading rate to increase prior to ice failure; they may thus provoke a more brittle failure. The pressures increased when the superstructure motion direction was the same as the ice-drift direction (Fig. 13 c), and the pressures decreased when the superstructure motion direction was opposite to the ice-drift direction (Fig. 13 d). When the contours were

displayed frame by frame, in a movie-like manner, the contact area and pressure pulsated simultaneously across the interface during the load build-up. During ice failure, the relative velocity between the ice and the structure increased and the pressure developed non-simultaneously, in agreement with laboratory experiments by Sodhi (2001). At an ice velocity of 80 mm s^{-1}, the dominant frequency of vibration was higher than that at 20 mm s^{-1}, whereas the superstructure vibrations remained almost at the same frequency, approximately 14.8 Hz, which was slightly below the second natural frequency. Jordaan and Timco (1988) also measured two dominating frequencies in the force signal when they pushed a flat-faced indenter through S2 ice sheets at an indentation speed of 60 mm s^{-1}. The major crushing occurred at a frequency of 20 Hz, and a secondary frequency at approximately 50 Hz was attributed to further crushing or clearing events.

During test 3100, a time window (an event) in which the force and response showed tendencies of frequency lock-in vibrations was found. The ice velocity was approximately 180 mm s^{-1}, and the structure exhibited repeated, almost sinusoidal displacement cycles close to the ice-action point. In contrast to the intermittent crushing regime, the superstructure vibrations were also controlled at the dominant vibration frequency, and no cyclic loading of the ice edge was induced by the superstructure prior to each ice failure.

One method that can be used to determine if noticeable differences were present at the ice-structure interface during the event is to calculate the correlation coefficients between a set of local forces during the event and compare them to the correlation coefficients calculated prior to and after the event. To further investigate the measured pressures at the interface before, during and after the event, the indenter was divided into 13 equally spaced sectors (Fig. 14). Local forces were calculated for each sector and were subsequently used for a correlation analysis. The correlation coefficients between the sectors were calculated according to Eq. (28):

$$\boldsymbol{\rho}(i,j) = \frac{\tilde{\mathbf{C}}(i,j)}{\sqrt{\tilde{\mathbf{C}}(i,i)\tilde{\mathbf{C}}(j,j)}} \tag{28}$$

where $\boldsymbol{\rho}(i,j) \in \mathbb{R}^{n_p \times n_p}$ is the correlation coefficient matrix, $\tilde{\mathbf{C}} \in \mathbb{R}^{n_p \times n_p}$ is the covariance matrix of the local forces, and $n_p = 13$ is the number of local forces. Figs. 15 b-d show the correlation coefficients calculated for three intervals: b) before the event, c) during the event, and d) after the event. Note that sectors 1 and 13 and, in part, 2 and 12 are outside of the 0-180 degree angle range (i.e., on the backside of the indenter). The cross correlation coefficients between the local forces before the event (Fig. 15b) were less than 0.5, and there was almost no correlation after the event (Fig. 15d). During the event (Fig. 15c), the elements closest to the diagonal had cross correlation coefficients in the range of 0.3-0.6. Furthermore, the overall cross-diagonal elements were in the range of 0.2-0.4.

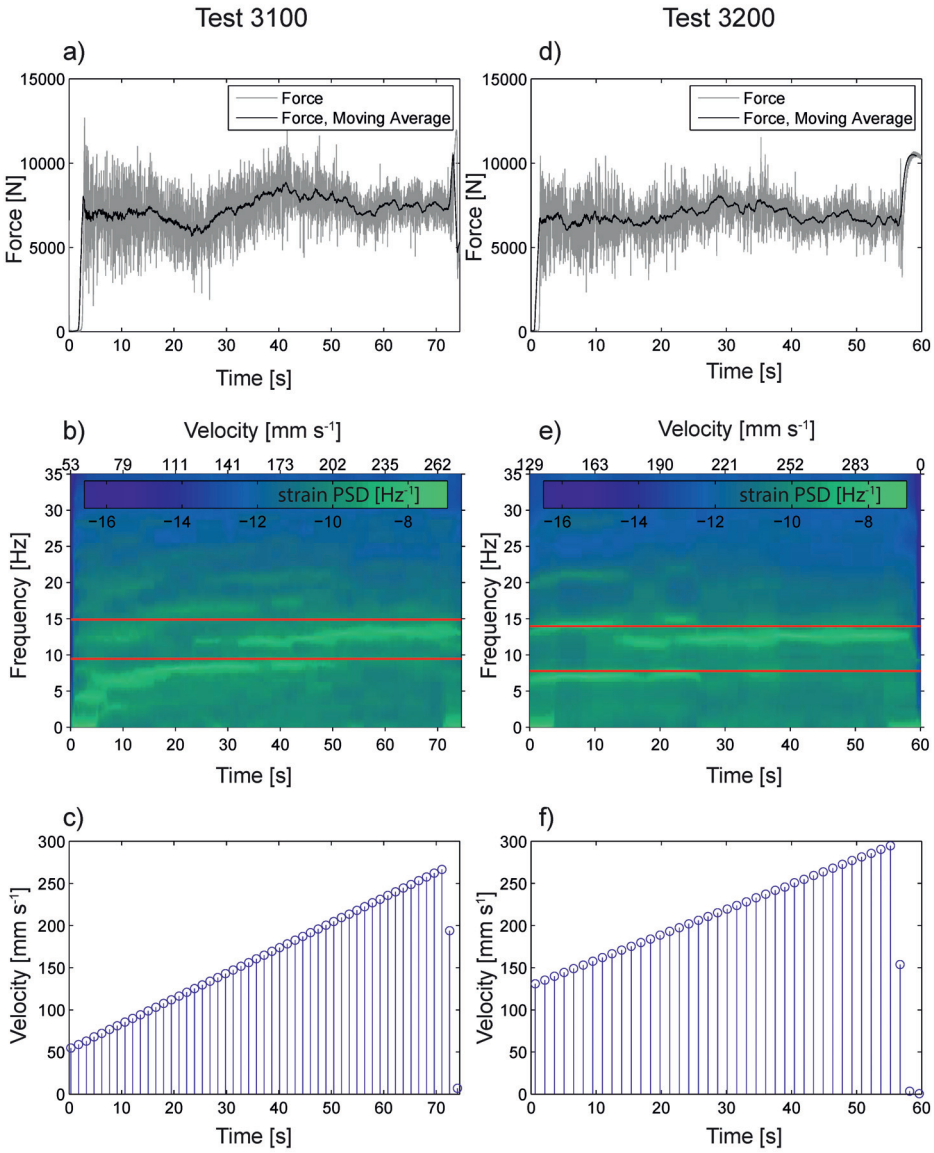

Figure 11. Test results for a) force test 3100, b) strain gauge response test 3100, c) ice velocity profile test 3100, d) force test 3200, e) strain gauge response test 3200, and f) ice velocity profile test 3200.

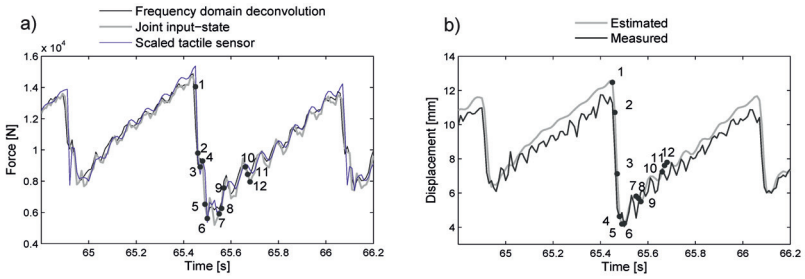

Figure 12. Intermittent crushing for test 4300 at an ice velocity of 20 mm s^{-1}: a) ice force; b) estimated and measured displacements.

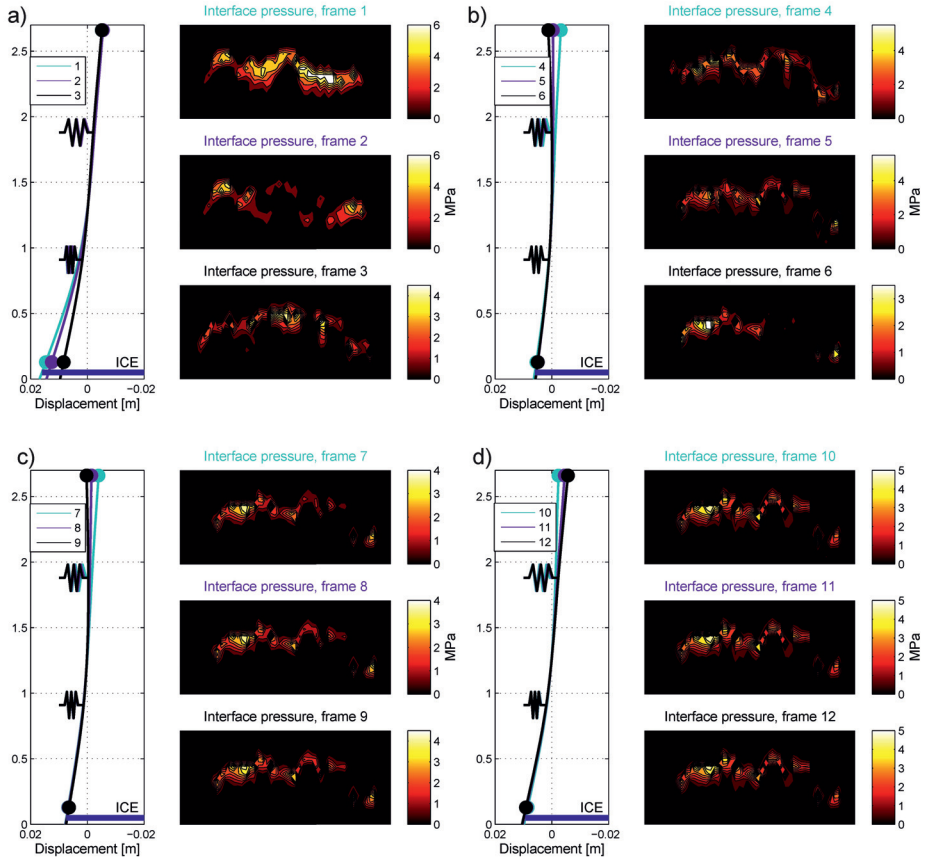

Figure 13. State of the structure and interface pressure during intermittent crushing for test 4300 at an ice velocity of 20 mm s^{-1}: a) ice failure, b) second mode extrusion, c) superstructure loading, and d) superstructure unloading.

Negative cross correlation coefficients were found when one of the sectors exceeded the 180 degree angle. Negative cross correlations may also occur when the structure experiences a lateral motion perpendicular to the ice-velocity direction. However, the strain gauge installed to detect any motion in that direction revealed that the strains were small. The correlation coefficients were in the range of those found in laboratory with fresh-water ice (Sodhi, 1998) and in medium-scale indentation tests (Sodhi et al., 1998; Taylor, 2009).

The correlation between the local peak forces during the "tendency to frequency lock-in event" were, however, much lower than what Bjerkås et al. (2013) observed during a full-scale frequency lock-in event at the Nordströmsgrund lighthouse, where they described the local peak forces as fully synchronized. Based on our model-scale results, it is suggested that only a small increase in the correlation coefficient may provoke such repeated vibration cycle events and that fully synchronized local peak forces are not a general requirement for such an event to occur.

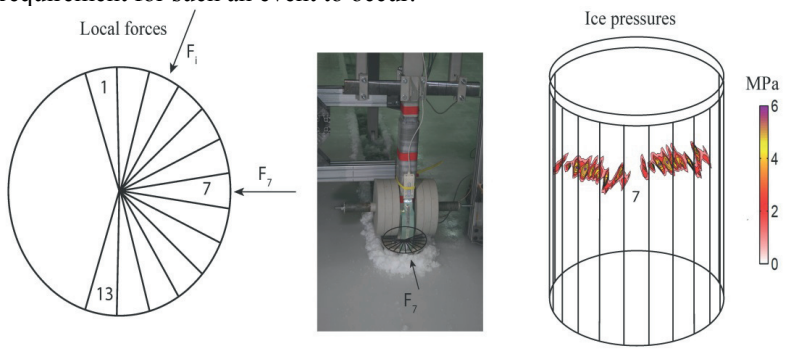

Figure 14. Division of the tactile sensor into local sectors, where F_7 is in the ice-drift direction.

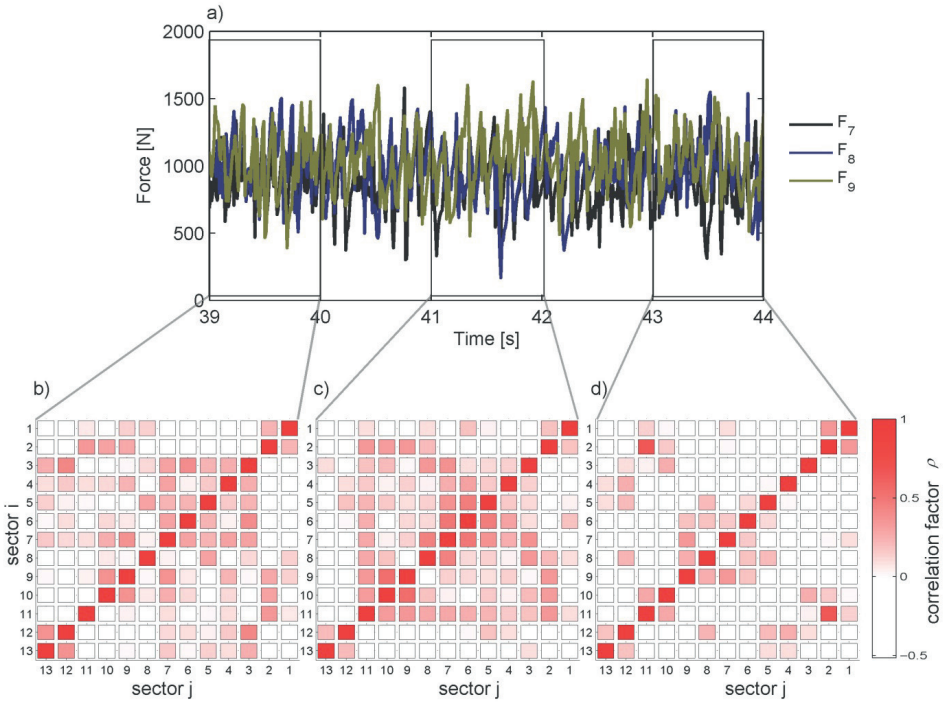

Figure 15. Local forces measured by the tactile sensor in test 3100: a) time history of three local forces, b) correlation map of the full set of local forces before the event, c) correlation map of the full set of local forces during the event, and d) correlation map of the full set of local forces after the event.

4.2 Full-scale comparison of identified and measured dynamic ice forces

The use of the JIS algorithm for identifying dynamic ice forces on a full-scale structure is demonstrated in this section (Paper 4). The data that were measured during the winter seasons of 1999-2003 at the Nordströmsgrund lighthouse enabled both the identification of forces and their comparison with global forces obtained from panel force measurements.

Two ice-induced vibration events, both occurring on the 30th of March, 2003, were selected for the study. A combination of ice conditions and measurement configurations on that particular day made the events suitable for the current study. The force panels covered a substantial portion of the ice-structure interface, the data were measured with a high sampling frequency, visual information was logged in daily reports, and the interaction was desired in the sense that it led to severe ice-induced vibrations. The events were governed by simultaneously (event 1) and non-simultaneously (event 2) occurring local peak forces across the ice-structure interface. The sampling frequency was 84 Hz for both events, which was higher than the usual sampling frequency. The

onset mechanisms for event 1 were studied by Bjerkås et al. (2013) and Bjerkås and Skiple (2005).

At 12.25 pm on the 30th of March, 2003, approximately 0.7-m-thick level ice approached from the northeast and interacted with the structure at an ice velocity of 0.06-0.065 ms^{-1}. The event was initiated at one load panel and spread to the sides. Subsequent ice failures were initiated simultaneously and quasi-simultaneously across the interface, causing large global forces and vibrational responses lasting for approximately 80 s. The vibration cycles repeated close to the lowest natural frequency, thereby producing frequency lock-in vibrations.

During the evening on the 30th of March, the ice drift changed direction from northeast (N-E) to north of northeast (NN-E). The structural vibrations during event 2 were caused by an ice field of primarily deformed ice that interacted with the structure at an ice velocity of approximately 0.18 ms^{-1}. The ice field was composed of reconsolidated ice-breaker-managed ice and naturally deformed ice. This caused the ice thickness profile to range between 1.3 and 1.6 m, as measured by an electromagnetic system (Haas et al., 2003).

A friction coefficient of 0.15 was used to obtain the measured global forces for both events. This assumption was based on a combination of earlier force measurements in which biaxial load cells were used for the load panels (Wessels et al., 1989) and on a study concerning sea ice friction on different construction materials (Frederking and Barker, 2001). Wind loads were neglected for both events. Despite the fact that the lighthouse had been a subject of numerous vibration studies, its dynamical properties in terms of the natural frequency values are fraught with scatters, from which the first natural frequency has been reported to be 2.3 Hz (Engelbrektson, 1977) and 2.8 Hz (Bjerkås et al., 2013). The finite element model used to identify the ice forces was built based on a dynamic soil structure interaction report by Heinonen et al. (2003). The model is displayed in Fig. 16, and the accelerometers were located at the floor level, where the blue markers have been added. A total of 24 eigenmodes were used to assemble the matrices $\mathbf{A}, \mathbf{B}, \mathbf{G}$ and $\mathbf{J}$ according to Eqs. (11) and (12), assuming 3% proportional damping for all modes.

Two biaxial accelerometers were used to identify the ice forces. Because only accelerometers were used, the system inversion is characterized by marginally stable transmission zeros at 0 Hz, as described in section (3.2.2.2). The marginally stable transmission zeros cause a drift in the identified forces and states, which can be removed using a high-pass filter. Recently, Eftekhar Azam et al. (2015) proposed a new Kalman filter approach to address low-frequency drift problems when only accelerometer measurements are used for the identification. A comparison with the results obtained using this algorithm is, however, considered to be beyond the scope of this thesis. The raw data were used for the identification, and the identified forces and states were filtered with a Butterworth high-pass filter with a cut-off frequency of 0.5 Hz, which is well below both the dominant dynamic response frequency and the first natural frequency of the structure. The signals from the inclinometers could also be used to eliminate the marginally stable transmission zeros; however, they were avoided because of uncertainties related to their dynamic contents.

The identified versus measured forces for event 1 with the simultaneous occurrence of peak forces are shown in Fig. 17. The identified forces in the E-W and N-S directions exhibit somewhat larger amplitudes compared to the measured forces (Figs. 17 a and b).

The identified dominant frequency contents coincide well, being at the same frequencies as those that were measured (Figs. 17 c and d). Considering the combined uncertainty of the force measurements and the modeling errors, the overall agreement is satisfactory.
The identified forces for the second event are shown in Fig. 18. Certain peaks of the identified forces are in agreement with the measured force (Figs. 18 a and b), whereas other peaks differ considerably. Dynamic local forces acting non-simultaneously can either decrease or amplify the global force summation. The unmeasured peaks in the force-time histories may be explained by significant local forces acting outside of the area covered by the force panels. The peaks that appear in the measured forces, but that are absent in the identified forces, may be explained as the result of unmeasured local forces that cancel out the measured forces.
The velocity and displacement at the ice-action point cannot be obtained by integration of the non-collocated accelerometer time histories. The JIS algorithm can, however, be used to identify the response at all unmeasured locations. The structural velocity amplitudes during frequency lock-in (event 1) were often slightly higher than the ice velocity, thereby agreeing with previous observations (Kärnä and Turunen, 1990). The structural motions were primarily in the ice-drift direction, with dynamic amplitudes in the range of 1 to 3 mm at the ice-action point. By estimating the time history of the displacement response on each floor, the horizontal motion was found to deviate slightly from a perfect line and to enter an elliptic motion (Fig. 19). The vibrations that exhibited an elliptic behavior in the horizontal plane were more pronounced during event 2 than during event 1. However, the vibrations were sustained for a few cycles only during event 1 with an approximately identical shape and amplitude. The only difference between event 1 and event 2 is the ice conditions. Therefore, the ice conditions likely provoke individual vibration cycles to enter this elliptic motion. Recent ice-induced vibration model-scale experiments by Ziemer and Evers (2014) showed similar in-plane vibratory displacements. They found that circular in-plane vibrations occurred with lower ice thicknesses and higher ice velocities compared to straight in-plane frequency lock-in vibrations.

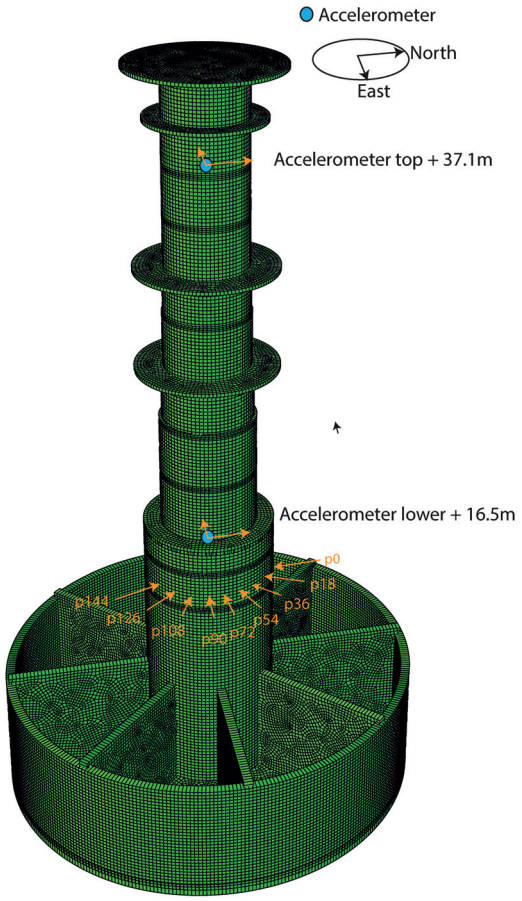

Figure 16. Finite element model and sensor locations.

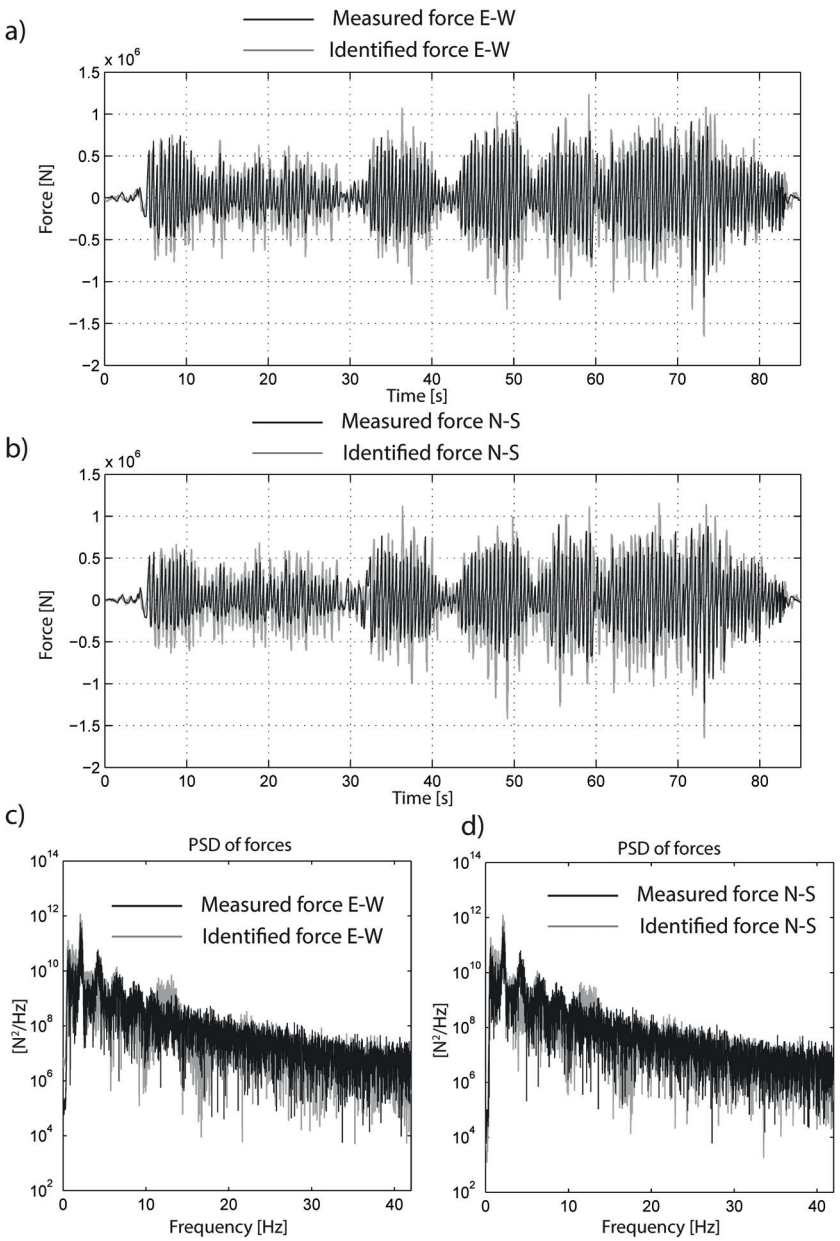

Figure 17. Identified versus measured forces: a) time history in the E-W direction, b) time history in the N-S direction, c) power spectral density of forces in the E-W direction, and d) power spectral density of forces in the N-S direction.

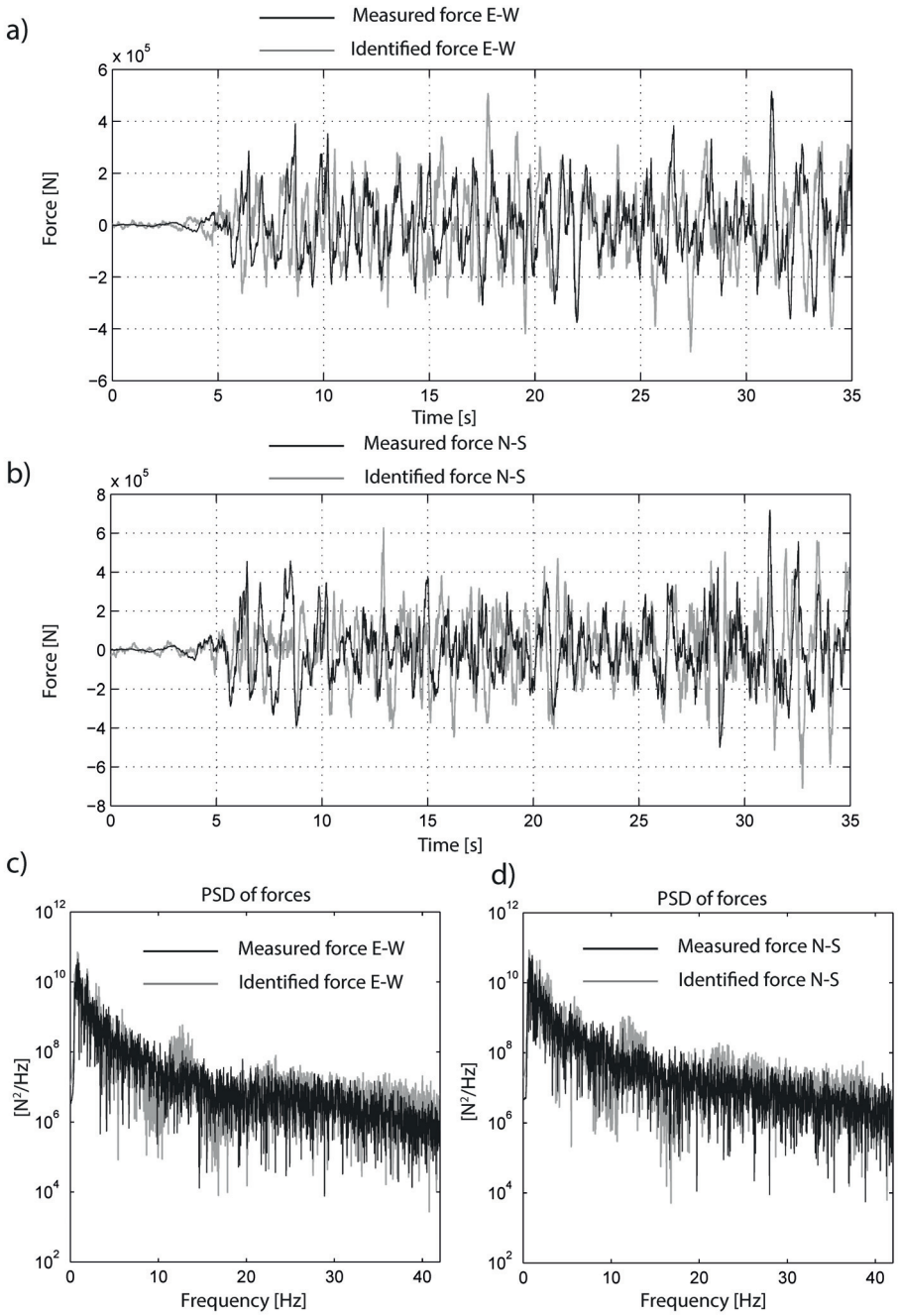

Figure 18. Identified (grey) versus measured (black) forces: a) time history in the E-W direction, b) time history in the N-S direction, c) frequency contents of forces in the E-W direction, and d) frequency contents of forces in the N-S direction.

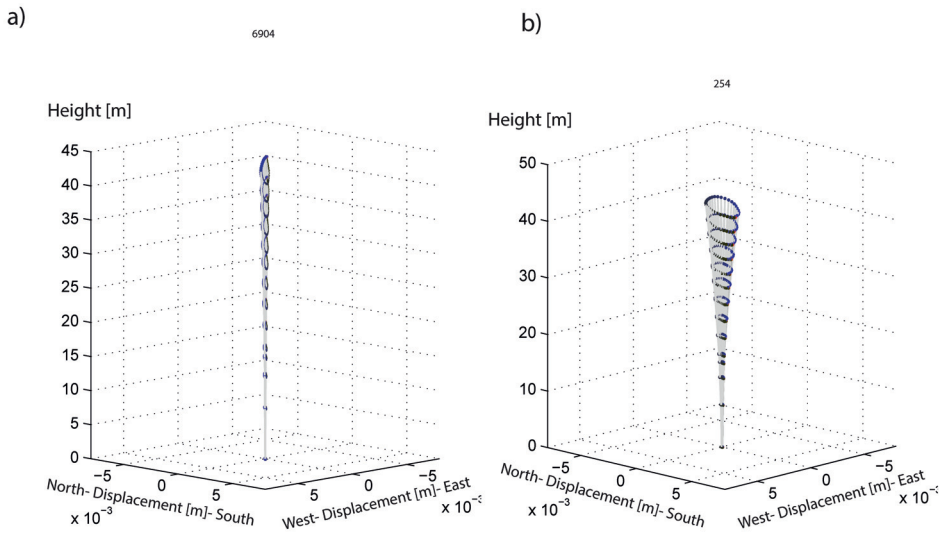

Figure 19. Time history of the structural response during one cycle of elliptic vibrations: a) estimated displacement at each building floor during event 1 and b) estimated displacement at each building floor during event 2.

4.3 Optimal sensor locations for force identification

A new measurement campaign was planned to monitor ice forces and responses of the Hanko-1 channel marker. Initially, this campaign was scheduled to be launched in the winter seasons of 2013-2014; however, two unusually mild winter seasons caused the Hanko-1 location to be ice free. The plan is to identify the ice forces using a joint input-state estimation algorithm in conjunction with a modally reduced order model. This section summarizes a case study in which the requirements in section 3.2.2 are used to determine the optimal sensor network for dynamic force identification (Paper 5).

The structure was modeled using quadrilateral shell elements with reduced integration (S4R) in ABAQUS. Construction blueprints were used to define the model properties. All of the shell degrees of freedom of the model are constrained to the rock well (cf. Fig. 6). The lantern/radar reflector plates were simplified from the true geometry, with the total mass kept similar to the real value, namely, ~ 1400 kilograms. The added mass of the displaced water was accounted for through the density of the steel below the mean water level. Several of the vibration modes were symmetric in the x-z direction, with the corresponding natural frequencies up to 40 Hz given in Paper 5. Circumferential modes were found in the substructure as a result of the high material density used to account for the displaced water. The bending modes are displayed in Fig. 20. It was important to include these bending modes in the modally reduced order model to obtain sufficient influence from the force on the modes and to obtain a sufficient number of modes contributing to the response at the sensor locations.

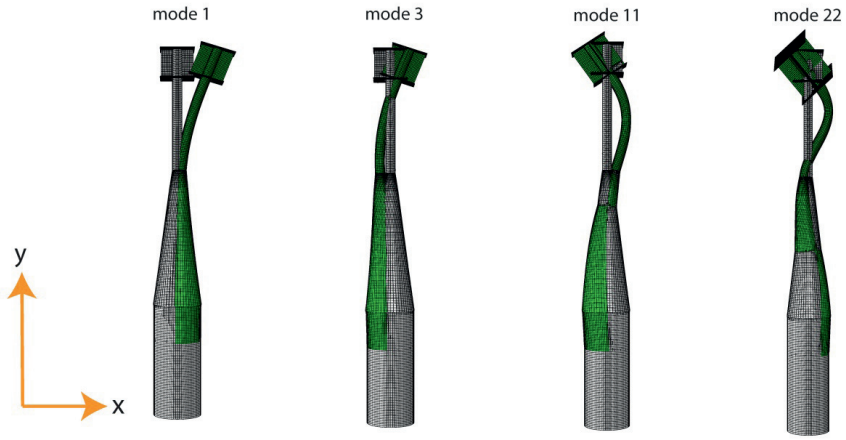

Figure 20. Bending vibration modes of Hanko-1.

To determine which locations were preferable for the installation of the accelerometers, the direct invertibility requirement in section 3.2.2.1 was used. To ensure direct invertibility, the number of excited modes should be greater than or equal to the number of forces, rank $(\mathbf{S}_p^T\mathbf{\Phi}) = n_p$. Second, at least n_p accelerations must be measured to secure a direct coupling between the acceleration responses and the estimated forces. Furthermore, the acceleration measurements should provide significant contributions from the modes excited by the forces.

The modal influences, $\mathbf{S}_p^T\mathbf{\Phi}$, of the two assumed force locations in Fig. 21 a are shown in Fig. 21 b (top). The force locations have a significant influence on modes 1, 2, 3, 4, 11, 12, 22 and 23, which means that if the global forces in the x and z directions are sought, $n_p = 2$, and $\mathbf{S}_p^T\mathbf{\Phi}$ will be of full rank.

The modal influences for thirteen possible sensor locations (Fig. 21 a) were simulated. The contributions from the modes to each of the possible accelerometer locations, $\mathbf{S}_a\mathbf{\Phi}$, are displayed in Fig. 21 b (bottom). The possible sensor locations capture a significant influence through all the bending modes.

At least two accelerometers are required to assure that $\text{rank}(\mathbf{J}) = n_p = 2$. The preferred sensor locations should have a large direct transmission value ($\mathbf{J} = \mathbf{S}_a\mathbf{\Phi}\mathbf{\Phi}^T\mathbf{S}_p$). This value determines the strength of the input-output (force-to-acceleration) coupling. Furthermore, the preferred sensor locations should be sheltered from ice actions and be practical for installation and maintenance. Therefore, it was assumed that the sensors could not be mounted closer than 1 m from the ice-action point. It was found that if three biaxial accelerometers were available, locations d_3, d_8 and d_10 were preferred locations for installation. Location d_10 was the lowermost location and provided the best input-output coupling, and locations below that level were not practical alternatives despite their strong input-output coupling. Location d_8 was selected to maintain a strong input-output coupling if the sensor at location d_10 failed. Location d_3 provided

redundancy to the measurement campaign and was suitable for response estimation validation.

Analysis of a map similar to that of Fig. 21 b (See Paper 5) suggested that two strain gauges at location d_4 should be installed to eliminate marginally stable transmission zeros at 0 Hz. This was confirmed by calculating the singular values of the matrix $\mathbf{J}-\mathbf{G}(\mathbf{A}-\mathbf{I})^{-1}\mathbf{B}$ (section 3.2.2.2). Two positive singular values, $1.5773\cdot10^{-11}$ and $1.5773\cdot10^{-12}$, were found, indicating that $\text{rank}(\mathbf{J}-\mathbf{G}(\mathbf{A}-\mathbf{I})^{-1}\mathbf{B})=2=n_p$. In summary, this sensor network guarantees the identifiability of dynamic ice forces using the JIS algorithm in conjunction with a modally reduced order model.

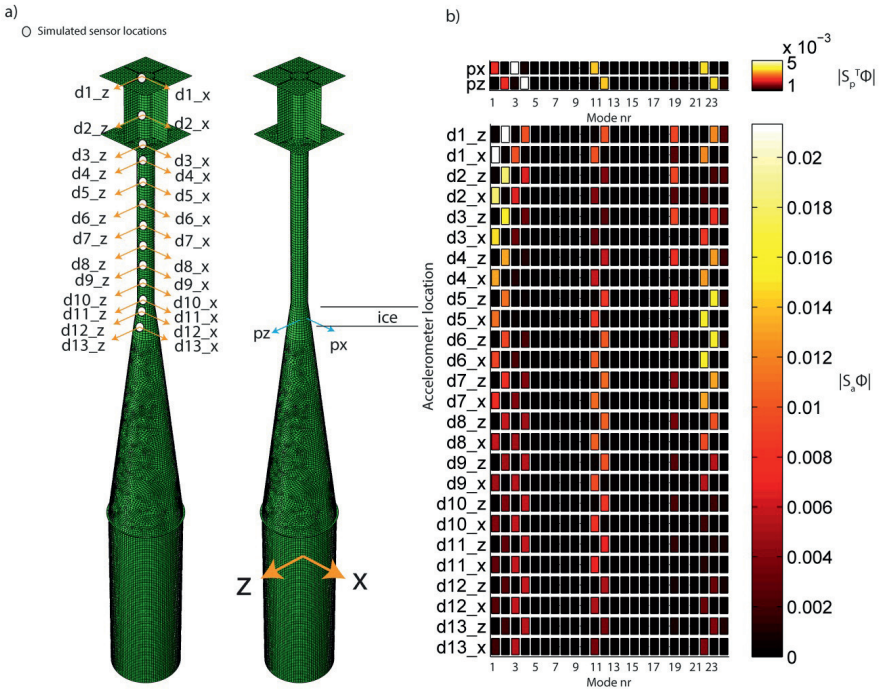

Figure 21. a) Simulated sensor locations and b) modal influences of forces and accelerations at simulated locations.

Chapter 5 Conclusions and recommendations for further work

5.1 Conclusions

This thesis discussed the analysis of both model-scale and full-scale experimental data. A joint input-state estimation algorithm was assessed and used to identify forces and responses during ice-induced vibrations of bottom-founded structures. The algorithm was further used as a key tool in the analysis of the data.
The main findings of this thesis are the following:

1) The joint input-state estimation algorithm is an effective and suitable tool for the force and state estimation of bottom-founded structures that exhibit ice-induced vibrations. Convincing results were obtained with both full-order finite element models and modally reduced finite element models, both used in conjunction with a limited number of response measurements (Papers 2, 3, 4, and 5). For the continuous monitoring of ice forces, the algorithm's main advantage is that its decision regarding the force and response is taken at the same time increment as it receives a measurement. The algorithm enabled the simultaneous study of the spatially complete responses of the structure with the ice forces. This was used to better understand ice-induced vibrations and resulted in the following conclusions.

2) The model basin results showed that each cycle at the dominant frequency of vibration during intermittent crushing was attributed to a load build-up and ice failure, whereas higher frequencies were attributed to the superstructure vibrations. At an ice velocity of 80 mm s^{-1}, the dominant frequency was higher than that at an ice velocity of 20 mm s^{-1}, whereas the superstructure vibrations remained at almost the same frequency, namely, approximately 14.8 Hz, which was slightly below the second natural frequency. By combining the identified forces and states with the tactile sensor pressure measurements, it was found that the superstructure vibrations caused cyclic loading and unloading of the ice edge prior to each ice failure. It was further demonstrated that these vibrations can cause the loading rate to increase prior to ice failure, thereby possibly provoking a more brittle failure (Paper 3).

3) The model basin results suggest that only a small increase in the correlation coefficient between local forces may provoke repeated vibration cycle events in the vicinity of the natural frequency and that fully synchronized local peak forces are not a general requirement for frequency lock-in vibration events to occur (Paper 3).

4) The identified forces on the Nordströmsgrund lighthouse exhibited convincing agreement with the measured dynamic forces from the panels. The dynamic ice

forces leading to ice-induced vibrations can now be assessed for many events that the force panels did not cover (Paper 4). However, the results depend on the accuracy of the finite element model.

5) Recently developed guidelines for sensor networks that ensure the identifiability of dynamic forces using the joint-input state estimation algorithm were applied to a case study of the Hanko-1 channel marker in the Gulf of Finland. Accelerometer and strain gauge locations that fulfill the requirements for identifying dynamic ice forces were suggested (Paper 5). Two winters with unusually high temperatures resulted in ice-free waters in the Gulf of Finland, and hence, the measurement campaign must be postponed until the winter of 2015-2016.

5.2 Recommendations for further work

This work demonstrated that the understanding of ice-induced vibrations can be enhanced using available techniques to identify ice forces and responses. This understanding, however, remains incomplete. The general recommendation for further work is repeated from the introduction, as stated by Croasdale and Frederking (1986); "Every opportunity must be taken to use the techniques available to measure and observe ice/structure interaction phenomena". More specific recommendations for further work are separated into four categories, under which each category contains subtasks.

1) *Structural considerations:* In this thesis, only single-legged structures prone to ice-induced vibrations were considered. For a complete evaluation of the JIS algorithm to identify ice forces, multi-legged structures, bridges and wide structures should also be considered. Wide structures can have large distances between the ice-action point(s) and the acceleration measurements (non-collocation distances), and the ice-action points can further be unknown and time variant. The identification of multiple ice forces acting on wide and multi-legged structures should be studied further.

2) *Ice-structure contact zone:* New laboratory tests with multi-degree-of-freedom structures would benefit from having a means for direct force measurements such that the identified forces can be compared with the measured forces. Pressure measurements with higher sampling rates enable the study of dynamic processes at the interface in the frequency range of higher structural modes. Determining which dynamic mechanism(s) in the ice that are responsible for the higher mode excitations deserve further investigation as well.

3) *Ice properties:* It is unclear how the cyclic loading of the ice edge caused by higher vibration modes affect the ice. These vibrations often occur at a frequency beyond the loading frequency traditionally used in unconfined and confined cyclic tests of ice specimens. Additional experiments are needed to study this topic.

4) *Numerical techniques:* The results are dependent on the accuracy of the finite element models. Improved results can be obtained using finite element model updating techniques before the force and state estimation are performed. Existing methods should be assessed to obtain the noise covariance matrices for when the measurement noise and process noise are correlated, in particular their applicability to Arctic offshore structures and their effect on the identified ice forces. A newly developed algorithm (the dual Kalman filter) can avoid the zero frequency drift in the identified forces and responses when only accelerations are measured. This algorithm should be assessed for use in Arctic engineering.
When considering (known) time-variant ice-action points or changing ice-drift directions (point 1), the JIS algorithm can be used to identify the forces with time-variant system matrices, e.g., replacing the system matrices $\mathbf{A}, \mathbf{B}, \mathbf{G}$ and $\mathbf{J}$ with time-variant matrices $\mathbf{A}_k, \mathbf{B}_k, \mathbf{G}_k$ and $\mathbf{J}_k$.

References

Barker, A., Timco, G., Gravesen, H. and Vølund, P., 2005. Ice loading on Danish wind turbines: Part 1: Dynamic model tests. Cold Regions Science and Technology, 41(1): pp.1-23.

Bjerkås, M., 2006. Ice action on offshore structures. PhD Thesis, NTNU, ISBN 82-471-7756-0, 173 pp.

Bjerkås, M., Meese, A. and Alsos, H.S., 2013. Ice Induced Vibrations- Observations of a Full-Scale Lock-in Event, Proceedings of the Twenty-third International Offshore and Polar Engineering International Society of Offshore and Polar Engineers (ISOPE), Anchorage, Alaska, pp. 1272-1279.

Bjerkås, M. and Skiple, A., 2005. Occurrence of intermittent and continuous crushing during ice-structure interaction, Proceedings of the 18th international Conference on Port and Ocean Engineering under Arctic conditions (POAC), Potsdam, NY, USA, pp. 1131-1141.

Bjørk, B., 1981. Ice-induced Vibration of Fixed Offshore Structures. Part 2: Experience with Baltic Lighthouses. Ship Research Institute of Norway, Information Department.

Blenkarn, K.A., 1970. Measurment and analysis of ice forces on Cook Inlet structure, Offshore Technology Conference, Houston, TX, pp. 365-378.

Brown, R.G. and Hwang, P.Y.C., 1997. Introduction to random signals and applied Kalman filtering: with MATLAB exercises and solutions. Wiley.

Brown, T.G., 2007. Analysis of ice event loads derived from structural response. Cold Regions Science and Technology, 47(3): 224-232.

Browne, T., Taylor, R., Jordaan, I. and Gürtner, A., 2013. Small-scale ice indentation tests with variable structural compliance. Cold Regions Science and Technology, 88(0): pp. 2-9.

Croasdale, K.R., 1977. Ice engineering for offshore exploration in Canada, Port and Ocean Engineering under Arctic Conditions, St. John's,Newfoundland, Canada, pp. 1-32.

Croasdale, K.R. and Frederking, R., 1986. Field techniques for ice force measurements, IAHR Symposium on Ice, Iowa City, Iowa, USA, pp. 443-482.

Danys, J.V., 1977. Ice forces on old and new offshore lighthouses in the St. Lawrence Waterway, Port and Ocean Engineering under Arctic Conditions (POAC), St. Johns, Newfoundland, Cananda, pp. 115-138.

Dempsey, J.P., Palmer, A.C. and Sodhi, D.S., 2001. High pressure zone formation during compressive ice failure. Engineering Fracture Mechanics, 68(17–18): 1961-1974.

Doyle, J., 1984. Further developments in determining the dynamic contact law. Experimental Mechanics, 24(4): 265-270.

Eftekhar Azam, S., Chatzi, E. and Papadimitriou, C., 2015. A dual Kalman filter approach for state estimation via output-only acceleration measurements. Mechanical Systems and Signal Processing, 60–61(0): 866-886.

Emami-Naeini, A. and Van Dooren, P., 1982. Computation of zeros of linear multivariable systems. Automatica, 18(4): 415-430.

Engelbrektson, A., 1977. Dynamic ice loads on a lighthouse structure, Fourth international conference on Port and Ocean engineering under Arctic Conditions (POAC), St. John's, Newfoundland, Canada, pp. 654-663.

Ewins, D.J., 2000. Modal Testing: Theory, Practice and Application, Second Edition.

Fabumni, J.A., 1986. Effects of structural modes on vibratory force determination by the pseudoinverse technique. AIAA Journal, 24(3): 504-509.

Finn, D.W., Jones, S.J. and Jordaan, I.J., 1993. Vertical and inclined edge-indentation of freshwater ice sheets. Cold Regions Science and Technology, 22(1): 1-18.

Frederking, R., 2005. Tiltmeter application at Nordströmsgrund lighthouse- Strice Project, 18th International Conference on Port and Ocean Engineering Under Arctic Conditions pp. 399-408.

Frederking, R. and Barker, A., 2001. Friction of Sea Ice on Various Construction Materials, Technical report, HYD-TR-67, PERD/CHC 3-49, National Research Council of Canada, Ottawa, Canada.

Frederking, R., Haynes, F.D., Hodgson, T.P. and Sayed, M., 1986. Static and dynamic ice loads on the Yamachiche lightpier, 1984-1986, 8th International Symposium on Ice, IAHR Iowa, USA, pp. 115-126.

Frost, R.V., 1941. Construction of five bottom-founded lighthouses by the deep water channel in Kalmarsund (Translated from Swedish)

Uppförandet av fem bottenfasta fyrar vid djuprännan i Kalmarsund, Lecture note for the Swedish union of concrete, 21st of February 1941, pp. 40.

Gillijns, S. and De Moor, B., 2007. Unbiased minimum-variance input and state estimation for linear discrete-time systems with direct feedthrough. Automatica, 43(5): pp. 934-937.

Gravesen, H., Sørensen, S.L., Vølund, P., Barker, A. and Timco, G., 2005. Ice loading on Danish wind turbines: Part 2. Analyses of dynamic model test results. Cold Regions Science and Technology, 41(1): pp. 25-47.

Haas, C., Jochmann, P., Gehrish, S., Kärnä, T., Kolari, K., Bjerkås, M., Bonnemaire, B. and Grösland, R., 2003. Full scale measurements at Lighthouse Norströmsgrund –winter 2003-Annex H2 EM ice thickness measurements.

Heinonen, J., Kärnä, T. and Luo, C., 2003. Dynamic Behavior of the Nordströmsgrund Lighthouse, STRICE- REPORT, VTT Technical Research Centre of Finland and Luleå University of Technology.

Hendrikse, H. and Metrikine, A., 2014. Interpretation and prediction of ice induced vibrations based on contact area variation. Submitted December 2014 to International Journal of Solids and Structures, Under revision.

Hendrikse, H., Metrikine, A. and Evers, K.-U., 2012. A method to measure the added mass and added damping in dynamic ice-structure interaction, "Ice Research for a Sustainable Environment"(IAHR). Dalian, China. Paper no. 094.

Hillary, B. and Ewins, D.J., 1984. The use of strain gauges in force determination and frequency response function measurements, Proceedings of IMAC 2 International Modal Analysis Conference, Orlando, USA, pp. 627-634.

Huang, Y., Shi, Q. and Song, A., 2007. Model test study of the interaction between ice and a compliant vertical narrow structure. Cold Regions Science and Technology, 49(2): pp. 151-160.

ISO, 2010. ISO/FDIS 19906, pp. 188.

Izumiyama, K., Irani, M.B. and Timco, G.W., 1994. Influence of compliance of structure on ice load, International symposium on Ice, IAHR, , Trondheim, Norway, pp. 229-238.

Jefferies, M.G. and Wright, W.H., 1988. DYNAMIC RESPONSE OF "MOLIQPAQ" to ice-structure interaction, Proc. 7th International conference on Offshore Mechanics and Arctic Engineering (OMAE 88), Houston, Texas, United States, pp. 201-220.

Joensuu, A. and Riska, K., 1988. Ice-structure contact, Report M88, ISBN 951-754-773-0, Helsinki University of Technology, Faculty of Mechanical Engineering, Laboratory of Naval Architecture and Marine Engineering.

Jordaan, I.J., 2001. Mechanics of ice–structure interaction. Engineering Fracture Mechanics, 68(17–18): pp.1923-1960.

Jordaan, I.J. and Timco, G.W., 1988. Dynamics of the ice-crushing process. Journal of Glaciology, 34(118).

Kärnä, T., Kolari, K., Jochmann, P., Evers, K.-U., Xiangjun, B., Määttänen, M. and Martonen, P., 2003. Ice action on compliant structures, VTT research notes 2223, VTT.

Kärnä, T. and Muhonen, A., 1990. Preliminary results from ice indentation tests using flexible and rigid indentors, IAHR Ice Symposium, Espoo, Finland, pp. 261-275.

Kärnä, T. and Turunen, R., 1989. Dynamic response of narrow structures to ice crushing. Cold Regions Science and Technology, 17(2): 173-187.

Kärnä, T. and Turunen, R., 1990. A straightforward technique for analysing structural response to dynamic ice-action. In: O.A. Ayorinde, N.K. Sinha and D.S. Sodhi (Editors), International Conference of Offshore Mechanics and Arctic Engineering.

Lourens, E., 2012. Force identification in structural dynamics PhD Thesis, KU Leuven.

Lourens, E., Papadimitriou, C., Gillijns, S., Reynders, E., De Roeck, G. and Lombaert, G., 2012a. Joint input-response estimation for structural systems based on reduced-order models and vibration data from a limited number of sensors. Mechanical Systems and Signal Processing, 29(0): pp. 310-327.

Lourens, E., Reynders, E., De Roeck, G., Degrande, G. and Lombaert, G., 2012b. An augmented Kalman filter for force identification in structural dynamics. Mechanical Systems and Signal Processing, 27(0): 446-460.

Maes, K., Lourens, E., Van Nimmen, K., Reynders, E., De Roeck, G. and Lombaert, G., 2014. Design of sensor networks for instantaneous inversion of modally reduced order models in structural dynamics. Mechanical Systems and Signal Processing(0).

Maes, K., Lourens, E., Van Nimmen, K., Van den Broeck, P., Guillaume, P., De Roeck, G. and Lombaert, G., 2013. Verification of joint input-state estimation by in situ measurements on a footbridge, Proceedings of the 9th International Workshop on Structural Health Monitoring, IWSHM, Stanford, CA, USA pp. 343-350.

Maes, K., Smyth, A.W., De Roeck, G. and Lombaert, G., 2015. Uncertainty quantification for joint input-state estimation in structural dynamics, 1st ECCOMAS Thematic conference on Uncertainty Quantification in Computational Sciences and Engineering, paper no. 548, Crete Island, Greece.

Montgomery, C.J. and Lipsett, A.W., 1981. Estimation of ice forces from dynamic response, International Symposium on Ice (IAHR), Quebec, P.Q. Canada, pp. 771-782.

Määttänen, M., 1975. Experiences of ice forces against a steel lighthouse mounted on the seabed, and proposed constructional refinements, Port and Ocean Engineering under Arctic conditions (POAC), Fairbanks, Alaska, pp. 857-867.

Määttänen, M., 1978. On conditions for the rise of self-excited ice induced autonomous oscillations in slender marine pile structures. PhD Thesis, UNIVERSITY OF OULU.

Määttänen, M., 1979. Laboratory tests for ice-structure interaction, Port and Ocean Engineering under Arctic Conditions(POAC), Trondheim, Norway, pp. 1139-1153.

Määttänen, M., 1982. True ice force by deconvolution, 1st International Modal Analysis Conference (IMAC), Orlando, FL, USA, pp. 556-590.

Määttänen, M., 1983. Dynamic ice-structure interaction during continous crushing, CRREL Report 83-5.

Määttänen, M., 2008. Ice velocity limit to frequency lock-in vibrations, International symposium on Ice, IAHR, Vancouver, Canada, pp. 1265-1276.

Määttänen, M., 2015. Ice induced frequency lock-in vibrations - Coverging towards concensus, Proceedings of the 23rd International Conference on Port and Ocean Engineering under Arctic Conditions, Trondheim, Norway.

Määttänen, M., Løset, S., Metrikine, A., Evers, K.-U., Hendrikse, H., Lønøy, C., Metrikin, I., Nord, T.S. and Sukhorukov, S., 2012. Novel ice induced vibration testing in a large-scale facility, "Ice Research for a Sustainable Environment"(IAHR), Dalian, China, paper no. 092.

Määttänen, M., Marjavaara, P., Saarinen, S. and Laakso, M., 2011. Ice crushing tests with variable structural flexibility. Cold Regions Science and Technology, 67(3): pp.120-128.

Nakazawa, N. and Sodhi, D., 1990. Ice forces on flat, vertical indentors pushed through floating ice sheets, CRREL REPORT 90-14.

Neill, C.R., 1976. Dynamic ice forces on piers and piles. An assessment of design guidelines in the light of recent research. Canadian Journal of Civil Engineering, 3(2): pp. 305-341.

Nord, T.S., Øiseth, O., Lourens, E., Määttanen, M. and Høyland, K.V., 2015. Laboratory experiments to study ice-induced vibrations of scaled model structures during their interactions with level ice at different ice velocities. Cold Regions Science and Technology(119): 1-15.

Nordlund, O.P., Tuomo, K. and Järvinen, E., 1988. Measurements of ice-induced vibrations of channel markers, IAHR Ice Symposium, Sapporo, Japan, pp. 537-548.

Peyton, H.R., 1967. Sea Ice Strength, University of Alaska.

Singh, S.K., Timco, G.W., Frederking, R. and Jordaan, I.J., 1990. Tests of ice crushing on a flexible structure, OMAE Houston TX. USA, pp. 89-94.

Sodhi, D., 1998. Nonsimultaneous crushing during edge indentation of freshwater ice sheets. Cold Regions Science and Technology, 27(3): 179-195.

Sodhi, D. and Haehnel, R., 2003. Crushing Ice Forces on Structures. Journal of Cold Regions Engineering, 17(4): pp.153-170.

Sodhi, D.S., 2001. Crushing failure during ice–structure interaction. Engineering Fracture Mechanics, 68(17–18): pp.1889-1921.

Sodhi, D.S., Takeuchi, T., Nakazawa, N., Akagawa, S. and Saeki, H., 1998. Medium-scale indentation tests on sea ice at various speeds. Cold Regions Science and Technology, 28(3): pp.161-182.

Taylor, R., 2009. Analysis of scale effect in compressive ice failure and implications for design. PhD Thesis, Memorial University, document ID, a3315266, Memorial University.

Taylor, R., Brown, T., Jordaan, I. and Gürtner, A., 2013. Fracture and damage during dynamic interactions between ice and compliant structures at laboratory scale, Proceedings of the ASME 2013 32nd International Conference on Ocean, Offshore and Arctic Engineering (OMAE), Nantes, France, pp. paper no. 11070.

Timco, G.W., 1984. Ice forces on structures: physical modelling techniques, International Symposium on Ice (IAHR), Hamburg, Germany, pp. 117-150.

Timco, G.W., Frederking, R. and Singh, S.K., 1989. The transfer function approach for a structure subjected to ice crushing, POAC, Luleå, Sweden, pp. 420-430.

Toyama, Y., Sensu, T., Minami, M. and Yashima, N., 1983. Model tests on self-excited vibration on cylindrical structures, Port and Ocean Under Arctic conditions (POAC), Helsinki, pp. 834-844.

Tsuchiya, M., Kanie, S., Ikejiri, K., Ikejiri, A. and Saeki, H., 1985. An Experimental Study on Ice-Structure Interaction. Offshore Technology Conference.

Tuhkuri, J., 1995. Experimental observations of the brittle failure process of ice and ice-structure contact. Cold Regions Science and Technology, 23(3): 265-278.

Weiss, R.T., Wright, B. and Rogers, B., 2001. In-ice performance of the Molikpaq off Sakhalin Island, Port and Ocean Engineering under Arctic Conditions (POAC), Ottawa, Canada.

Wells, J., Jordaan, I., Derradji-Aouat, A. and Taylor, R., 2011. Small-scale laboratory experiments on the indentation failure of polycrystalline ice in compression: Main results and pressure distribution. Cold Regions Science and Technology, 65(3): pp. 314-325.

Wessels, E., Jochmann, P. and Hoffmann, L., 1989. First results of ice force measurements with TIP - Panels at Norströmsgrund lighthouse, 10th International Conference on Port and Ocean Engineering under Arctic Conditions, Luleå, Sweden, pp. 1428-1439.

Ziemer, G. and Deutsch, C., 2015. Study of local pressure distribution and syncronization during frequency lock-in, Proceedings of the 23rdInternational Conference on Port and Ocean Engineering under Arctic Condition, Trondheim, Norway.

Ziemer, G. and Evers, K.-U., 2014. Ice model tests with a compliant cylindrical structure to investigate ice-induced vibrations, Proceedings of the ASME 2014 33rd International Conference on Ocean, Offshore and Arctic Engineering, OMAE, San Francisco, California, USA, paper no. 24011.

Appendix 1 Frequency domain force identification in ice-structure interaction

This appendix includes the paper presented at the 22nd Conference on Port and Ocean Engineering under Arctic Conditions, Espoo, Finland, in 2013.

- Nord, T.S., Määttänen, M. and Øiseth, O., 2013. Frequency domain force identification in ice-structure interaction, Port and Ocean Engineering under Arctic Conditions, Espoo, Finland, ISBN 978-952-60-3635-9

POAC'13
Espoo, Finland

Proceedings of the 22nd International Conference on
Port and Ocean Engineering under Arctic Conditions
June 9-13, 2013
Espoo, Finland

Frequency domain force identification in ice-structure interaction

Torodd S. Nord [1], Mauri Määttänen [2], Ole Øiseth [3]

[1, 2)] Sustainable Arctic Marine and Coastal Technology (SAMCoT), Centre for Research-based Innovation (CRI), Norwegian University of Science and Technology, Trondheim, Norway

[3] Norwegian University of Science and Technology (NTNU)/ Department of Structural Engineering, Trondheim, Norway.

ABSTRACT

A deterministic force identification method has been applied in ice-structure interaction. A compliant structure was forced through ice sheets in laboratory (EU-HYDRALAB DIIV test campaign at HSVA in 2011). Structural vibrations caused by crushing failure occurred over a range of velocities and frequencies. The experimentally obtained frequency response function (FRF) matrices and the measured responses were used to solve the inverse problem of identifying the forces at the ice action level.

The forces from two vibration tests are presented together with parametric Burg spectra of the responses. They indicate that forces drop on the transition between vibration frequencies, while maximum forces occur with presence of two dominating frequencies. No clear relationship between the natural frequencies, measured response and the peak forces was found.

INTRODUCTION

Pressure panels, tactile sensors and load cells are some of the direct measurement techniques which can estimate the loads on structures in different scales. Frederking et al. (2002) present a thorough review of load panels installed on the Molikpaq platform, after being deployed offshore Sakhalin. The evaluation of system performance and improvements suggested to enhance the ability to operate in arctic conditions provide a valuable insight to the challenges met in full-scale experimental testing.

The tactile sensors/panel sensors have been used in ice research by Takeuchi et al. (2000), Sodhi (2001), Taylor (2009), Määttänen et al. (2011) and Hendrikse et al. (2012). These sensors have the advantage that they can measure pressure with a high spatial resolution. They can be tailored to fit the indentor and enable extraction of both contact area and pressure. However, the sensors can only measure normal forces/stresses so that any shear forces/stresses have to be derived through assumed static and dynamic friction coefficients. When the stresses exceed elastic domain and material softening may be present, assuming a shear distribution becomes even more challenging.

The ice load survey carried out by Timco and Croasdale (2006) shows that there is considerable uncertainty, even within the ice research community, in prediction of ice loads on structures. Laboratory experiments are one of the ways that we can control to some extent both structure and ice conditions, aiming to adapt the knowledge into full scale. Different

laboratory studies on compliant structures (E.g. Määttänen (Määttänen, 1978; Määttänen, 1983; Määttänen et al., 2012), Kärnä (Kärnä, 1995; Kärnä et al., 2003), Toyama et al. (1983), Sodhi (2001) ,Gravesen et al. (2005) and Barker et al. (2005)) use different tehniques and measurement setups to derive the ice-forces. Many of the test-setups use direct measurement of the global ice force with load cells and dynamometers while others use indirect calculation of forces from structural response. The dynamometers give easy access to forces, still the added mass from water and model mass have to be dealt with. Load cells built into the indentor together with an accelerometer is possible in laboratory, but scarcely applicable on full-scale offshore structures.

Inverse force identification is a research topic adopted into structural dynamics and applied on systems where the forces are difficult to measure directly. For civil engineering purposes, bridges, piers, lighthouses and offshore structures interacting with ice are all examples where the ice force is difficult to quantify. The thesis by Lourens (2012) summarizes and qualitatively assess different linear approaches, while Kerschen et al. (2006) take the step further with a survey through nonlinear system identification methods. The classical book by Ewins (2000) explains vibratory experimental testing thoroughly, from the development of frequency response matrices to force identification. The frequency domain method was investigated by Fabumni (1986), who evaluated the effect of erroneous response signals, FRF matrix and number of forces to be identified. A general approach to establish a force-prediction model in the frequency domain is proposed by Wang (2002), who suggest an update of the analytical FRF from the measured response. Parloo et al. (2003) extend the framework to identify forces when the FRF matrix is not measurable anymore, which could be the scenario in ice-structure interaction.

In ice, the so far work on inverse force identification is limited, and restricted to deterministic frequency domain methods. Määttänen ((1983) ,(1982)) Singh et al. (1990), Timco et al. (1989) and Montgomery and Lipsett (1981) utilized the inverse force identification technique. Singh et al. (1990) emphasise the problems with what they refer to as a transfer function approach, and achieve interesting results by increasing the damping in the transfer function towards the damping observed during ice crushing in laboratory. Montgomery and Lipsett (1981) applied inverse force identification in full scale experiments. Accelerometers attached to bridge piers were set to measure the response during ice action and forces were solved inversely in the frequency domain.

The aim for this paper is to identify the ice force at different velocities acting on a compliant structure, solved in the frequency domain from measured responses. The force is solved solely based on measured FRF matrices in ice-free conditions, not modified with updated damping coefficients or added mass. The forces are sought at a location where no sensors measuring response are deployed, hence this is a so-called *non-collocated* problem (Nordström and Nordberg, 2004). A pseudo-inverse technique is used to invert the non-square FRF matrix, thus a least square solution of the forces is obtained. The response frequency components are presented in a Burg spectrum. That presentation enables direct comparison between forces and time-variant response frequency components. The attributes to both forces and measured responses are discussed and compared with the velocities and ice properties.

FORCE IDENTIFICATION IN THE FREQUENCY DOMAIN

The frequency domain deconvolution method belongs to the class of deterministic methods. Only a brief review of the method is presented here, but further details can be found in Ewins

(2000). For a single degree of freedom system, the dynamic response can be obtained by the following convolution integral in time domain:

$$u(t) = \int_0^t h(t-\tau)p(\tau)d\tau \tag{1}$$

Here, u(t) and p(τ) represent the response and the dynamic action respectively, while $h(t)$ is the response function for a unit impulse excitation. By applying the Fourier transform to the convolution integral in Eq.(1), the relation between response and applied excitation becomes:

$$\hat{u}(\omega) = \hat{H}(\omega)\hat{p}(\omega) \tag{2}$$

where $\hat{H}(\omega)$ is the complex frequency response function (FRF) of a system exited by a unit harmonic impulse. For multiple degree of freedom systems, the output $\hat{u}_i$ is a vector of n^d measured responses and $\hat{p}_j$ a vector of n^p unknown forces, hence we obtain the following system:

$$\hat{\mathbf{u}}(\omega)_{n^d\times 1} = \hat{\mathbf{H}}(\omega)_{n^d\times n^p}\hat{\mathbf{p}}(\omega)_{n^p\times 1} \tag{3}$$

The elements in the FRF matrix $\hat{H}_{ij}$ represents the response at a specific location *i* from an applied load at location *j*. It can either be determined experimentally or obtained numerically. If $n^d = n^p$, the FRF matrix is of full rank and the inverse problem can be solved by pre-multiplying Eq.(3) by $(\hat{H}_{ij})^{-1}$. In most cases, $n^d > n^p$, and use of an pseudo-inverse technique is necessary in order to solve the system. The pseudo-inverse of the non-square FRF matrix can be written in the following form:

$$\hat{\mathbf{H}}^{\dagger} = (\hat{\mathbf{H}}^H\hat{\mathbf{H}})^{-1}\hat{\mathbf{H}}^H, \tag{4}$$

where *H* is referring to the Hermitian transpose. The input forces are identified from the measured output responses and the pseudo-inverse of the FRF matrix:

$$\hat{\mathbf{p}}(\omega)_{n^p\times 1} = \hat{\mathbf{H}}^{\dagger}(\omega)_{n^d\times n^p}\hat{\mathbf{u}}(\omega)_{n^d\times 1} \tag{5}$$

After the complex forces $\hat{\mathbf{p}}(\omega)_{n^p\times 1}$ are identified, an inverse fast Fourier transform (FFT) can be applied to convert the forces into time domain.

EXPERIMENTAL SETUP

Structural properties

The identification method is applied on analysis of data from the *Deciphering Ice Induced vibration* (EU-HYDRALAB DIIV) test campaign at HSVA in 2011 (Määttänen et al. (2012), Hendrikse et al.(2012), Nord and Määttänen (2012)). A beam supported by horizontal leaf springs and vertical supports was constructed to vibrate with two dominant modes in the frequency range of interest. A cylindrical indentor with 220mm diameter was installed to the main beam at the ice action level. Figure 1 shows the set-up where the test structure is fixed to a 50 tonne carriage that drives with a predefined velocity (Figure 4, bottom row) through the ice-sheets while measuring responses. A set of different ice-thicknesses, temperatures and structural configurations (mass and stiffness adjustable) provided a range of comparable data-sets.

Data acquisition

Four response measurements were used firstly, to identify the FRF matrix and secondly to identify the force at the ice action level. Two lasers and two strain gauges were installed to measure the responses at locations on the lower part of the structure as shown in Figure 1. The sampling rate of 100Hz was applied to all channels, both during dynamic calibration and ice

action. The load cell was only used during the free vibration test to estimate the FRF matrix, thereby not used during ice interaction.

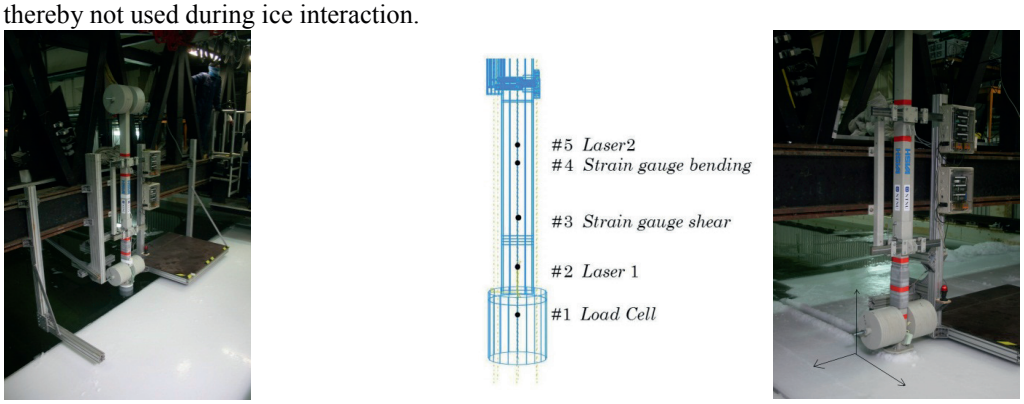

Figure 1. Test structure and sensor locations.

Ice properties

The ice sheets were homogeneous and columnar structured. Initial seeding and scraping the ice sheets from underneath controlled the grain size. Test 3300 had relatively warm ice, hence the compressive and flexural strength were low. Colder and thicker ice was present for the 4300 test, while the grain size was kept on similar level. A summary of the properties used in both tests is given in Table 1.

Table 1. Test setup properties.

Property	Test 3300	Test 4300	Property	Test 3300	Test 4300
Ice thickness, h_{ice} mm	58	60	Salinity, S ppt	3.2	3.2
Ice density, ρ kg/m^3	836.1	829.7	Indentor width,w mm	220	220
Flexural strength, σ_f N/mm^2	0.099	0.164	Aspect ratio, w/h_{ice}	3.79	3.67
Compr. Strength, σ_c N/mm^2	0.167	0.393	1st Nat. Frequency, f_1 Hz	10.2	12.2
Ice Temperature, T_{ice} ^{o}C	-0.8	-1.7	2nd Nat. Frequency, f_2 Hz	15.4	16.2

EXPERIMENTAL RESULTS

Experimentally determination of FRF matrix

In order to identify the ice actions, the FRF matrix of the system is needed. A survey of methods to determine the FRF matrix and their limitations have been thoroughly described by Ewins (2000). A step relaxation test in open water was chosen for the dynamic calibration. The response and applied load were measured when a steel rod connected to the ice action point was gradually loaded. In between the rod and the ice-action point there was a weak-link installed which went to failure with a certain applied load, typically 10kN. The FRF matrix elements can be determined from the applied load and measured response in the frequency domain:

$$\hat{H}_{ij}(\omega) = \frac{u_i(\omega)}{p_j(\omega)}, \tag{6}$$

where the complex $u_i(\omega)$ and $p_j(\omega)$ were determined by taking the fast Fourier transform (FFT) of the responses, $u_i(t)$, and applied excitations, $p_j(t)$. As outlined in Figure 1, four non-collocated responses were measured in DOF *i=2..5*. Element $\hat{H}_{11}$ is unknown since no measured response is available at the ice action point. Because of the missing measurement

DOF's, the FRF matrix is truncated. The real and imaginary parts of element $\hat{H}_{41}$ in the experimentally obtained FRF matrix are displayed in Figure 2. As expected, there are two frequencies that dominate the response, in this case about 12 and 16Hz. For every structural configuration, dynamic calibrations were performed such that the FRF could be obtained experimentally. All structural configurations were also compared with 3D FEM models for verification, see Nord and Määttänen (2012) for further details.

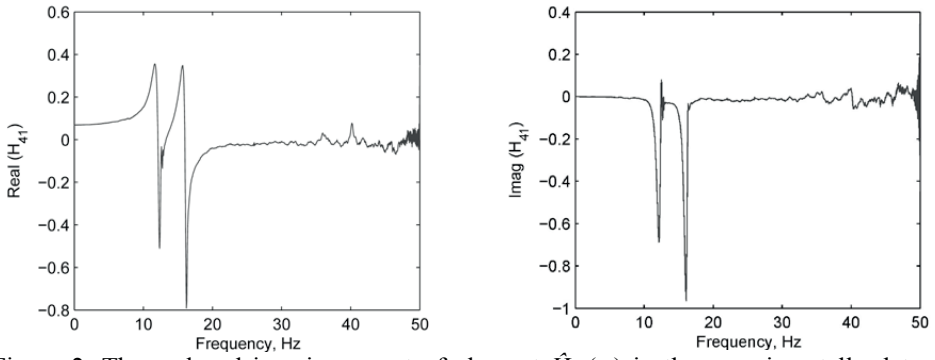

Figure 2. The real and imaginary part of element $\hat{H}_{41}(\omega)$ in the experimentally determined frequency response matrix.

Force identification

The forces were identified according to Eq. (5), with ¾ overlapping time segments of 2048 points. A statistical presentation of the forces is chosen to simplify the comparison between forces, responses and velocities. The data are processed by dividing the test series lengths into N=60 time intervals from $t_1 \ldots t_N$ illustrated in Figure 3. For every 2048pt force window that is identified, the forces are sorted into the corresponding time interval. The same procedure is used on the recorded carriage velocity (ice-sheet velocity). In each time interval, the mean (F_{av}), standard deviation (F_{std}) and peak forces are found. A threshold for selecting the peak forces is set equal to the mean value, and F_{maxav} denotes the average of the peak forces above this threshold value. The total length T for the analysed test-series 4300 and 3300 is chosen to be equal. However, the time before the structure hit the ice-edge is left out, which causes different lengths of the two time axes (Figure 4). The analysed data in this paper exclude most of the intermittent crushing, leaving the discussion to the continuous brittle crushing regime.

The forces, corresponding strain gauge responses and carriage velocities are shown in the upper, mid and bottom row of Figure 4, respectively. By comparison of the forces and the velocity intervals in test 4300, a repeated pattern can be observed in both the mean values, F_{av} and maximum values, F_{maxav} . Next to each velocity shift, the forces increase until they reach a local maximum. Thereafter the forces decrease until the transition to the next velocity interval. At the time when the global maximum occurs (t=270s, v=100mm/s), two dominating frequencies appear in the response spectrum. Subsequent response characteristics change both in number of active frequencies and their respective values. The forces decrease significantly when only one response frequency is present. The reductions are 25% and 24% in F_{av} and F_{maxav} respectively, calculated from the peak (t=270s) until the last interval (t=290s). Weaker and thinner ice in test 3300 explains the low forces. Two active frequency components are present at the instant of the global force maximum (t~108s). As seen from Figure 4, the velocity at that point is slightly above (v=180mm/s) the previous test. The force reductions

are now 28% and 32%, representing F_{av} and F_{maxav} respectively. These reductions depend on the point to represent the force after the decrease, selected to t=134s in this test.

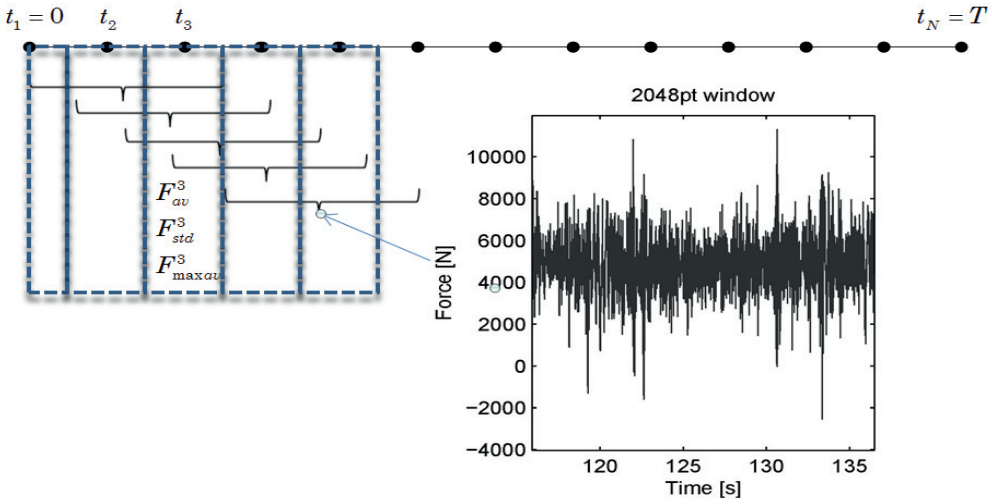

Figure 3. Post-processing routine for the identified forces.

Structural Response

The ice velocity was increased with time during both tests as displayed in Figure 4**.** In test 4300 the velocity was increased in steps, while a constant acceleration was applied in test 3300. At low velocities (v<80mm/s) in test 4300, the ice followed the deflection of the structure with ductile load build up, and the spring-back effect with brittle failure. This intermittent crushing event was only present for a few seconds before continuous brittle crushing dominated the failure process. Both tests had relatively warm ice, hence the ice was weak as seen from the measured compressive and flexural strength values in Table 1. Underwater-cameras revealed that the extrusion of crushed ice primarily consisted of small particles with some larger pieces spalling off. Radial cracks were occasionally observed, but they did not expand to the walls of the ice tank.

A Burg parametric filter was used to create the spectra of the strain gauge response signals. The response spectra of both tests are shown in the mid row of Figure 4, plotted with logarithmic scale pointing perpendicular to the plane. Horizontal red lines are added to the figures to represent the natural frequencies from open water calibration.

The analysed time-sequence in test 3300 covers the velocities between 70mm/s and 260mm/s. The red bands changing with time in the response spectra represent the presence of significant frequency components. While the dominating frequency components appear somewhat below the first and second natural frequencies at t<100s, respectively, they dislocate towards higher frequencies for t>100s. The highest frequency component crosses the second natural frequency as time exceeds 100s, while the lowest component occurs still below the first natural frequency. The frequency components seem to stabilize and the red bands in Figure 4 are kept almost constant prior to a second frequency shift at t~120s. After 120s, the energy in the second frequency component is gradually lost and subsequent crushing occurs with

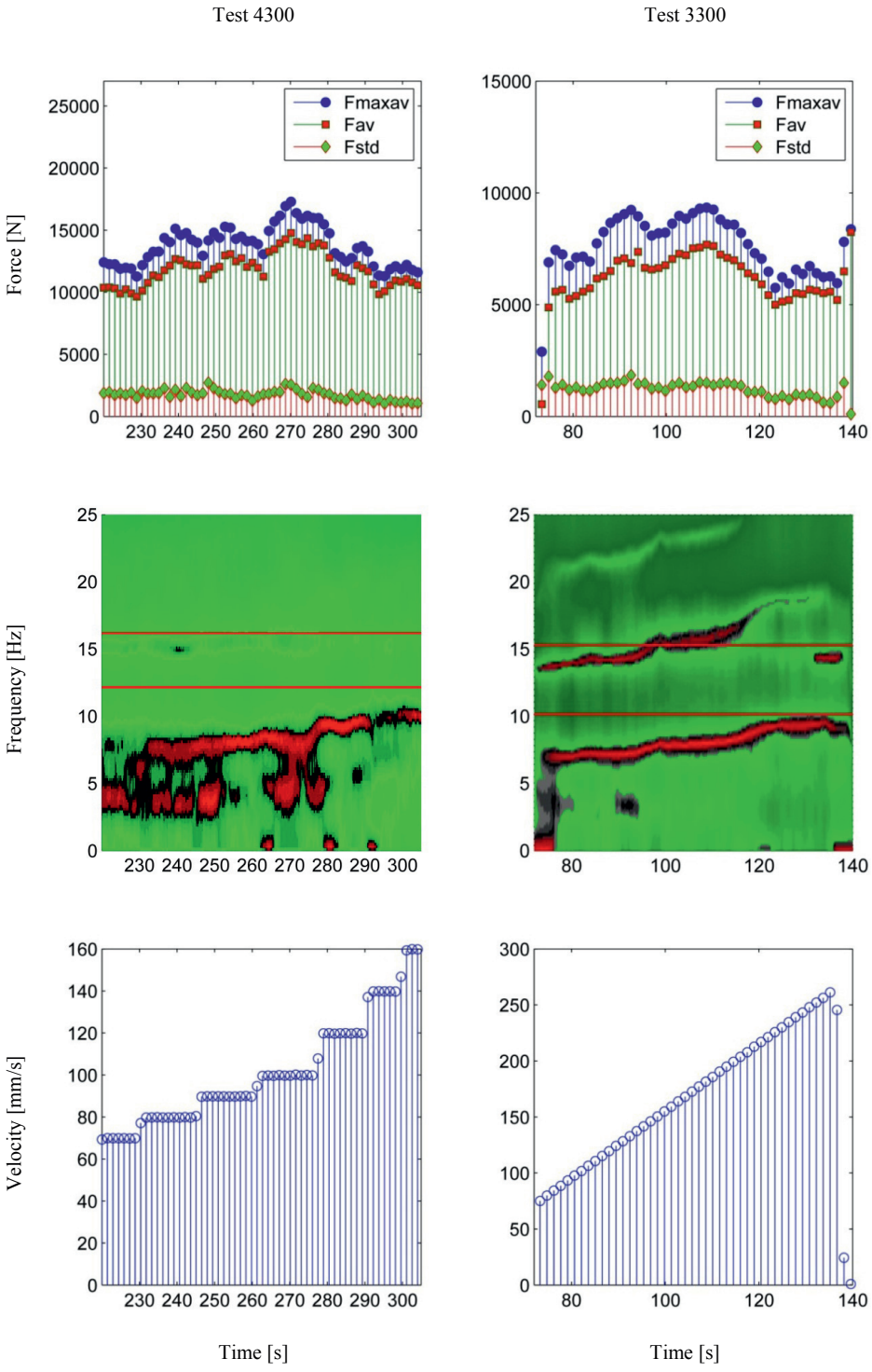

Figure 4. Top row: Identified forces. Mid row: Response spectra (Red color: High energy, green color: low energy) . Bottom row: Ice (carriage) velocity.

primarily one single vibration frequency close to the first natural frequency. Thereafter the carriage brakes down to zero velocity, hence the zero frequency component increases.

The significant response frequencies in test 4300 increased with time as the velocity increased for each interval. Evidently the response is not controlled in a single narrow band, but with smaller contributions spread at different frequencies. Still, the major vibration frequencies are possible to address in the spectrum. Minor contributions between 2-4Hz are recognized, and possibly related to that intermittent crushing occasionally controlled the interaction process. During the test, both the number of active frequencies and their content appear prone to velocity changes. At the time when the velocity shifts are doubled in magnitude ($v>100$mm/s) the frequency components displace more than what we observe at low velocity levels ($v<100$mm/s) when the velocity shifts were less.

DISCUSSION

Correlation of forces with response and ice properties

Apparently the intervals with constant velocities (4300) and constant acceleration (3300) have their distinct characteristics. The local force maxima occurred only for constant velocities. As the constant acceleration is low (~3mm/s^2), these rapid changes are not likely to occur, thus no local effects are identified for this configuration.

The low velocities in test 4300 may explain the low frequency contents (2-4Hz) to originate from the domain of intermittent crushing. At the time when the maximum force occurs, the two frequency components are both below the first natural frequency. For test 3300, the components below 5Hz are negligible and the frequency band close to the second natural frequency appears more dominant. Still, two frequency components located below each natural frequency are active at the time when the force reaches the maximum.

The results indicate that forces change both with the number of dominant vibration frequencies and their representative values. Despite that no force spectra are presented in this paper, both tests indicate that when the number of active frequencies is reduced from two to one, the forces decrease significantly. Noticeable the forces drop in the vicinity of a sudden frequency shift. It is not achieved to identify if the shift can be regarded as a change in the dynamic system. The identified dynamic component F_{maxav} appears low compared with F_{av}, whereas the study of Määttänen (1983) showed a more prominent dynamic contribution. The standard deviations of the forces, F_{std}, tend to decrease towards the end of both tests, implying a lower dynamic contribution in the forces at high velocities. The strikingly low dynamic force components may originate from the characteristics of the ice. Viscous behaviour of the ice could cause the material ahead of the indentor to dissipate more energy in the extrusion phase, causing additional damping of the vibration amplitudes.

Identification method

The classical paper by Fabumni (1986) explores the limitations by this method when random error is added to the response signal and the mobility matrix. Despite 15% random error introduced in the mobility matrix, one force could be determined on a cantilever beam with good accuracy. The number of forces, non-collocation of measurement sensors and the error are of importance, but also the general assumption that the forces can be identified from the experimentally obtained FRF without presence of ice. In the vicinity of the natural frequencies it is difficult to predict forces; however, the examples of forces given in this paper show those regions where the response is far from the natural frequencies. A paper by Hollandsworth (1989) demonstrates the effect of the non-collocation of the sensors, which

causes an underestimation of the applied forces. Hence the low maximum force level may not solely be explained by ice-properties, but also connected to the non-collocation of the sensors.

The discussion regarding which dynamic regimes the forces can be trusted has met low attention in ice-research besides the papers mentioned in the introduction. More sophisticated identification methods may bring new answers into the topic, whereas the research so far has been limited to the deterministic frequency domain methods.

CONCLUSION

In this work, the ice forces acting on a flexible structure were identified from experimentally obtained FRF matrices and measured responses from a set of non-collocated measurement transducers. The identified ice forces change with the number of active response frequencies and the corresponding frequency contents. The force maximum in both tests occurred when the responses had more than one major frequency component active.

ACKNOWLEDGEMENT

The authors wish to acknowledge the support from the Research Council of Norway through the Centre for Research-based Innovation SAMCoT and the support from all SAMCoT partners. The work described in this paper was supported by the European Community's 7th Framework Programme through the grant to the budget of the Integrated Infrastructure Initiative HYDRALAB-IV, Contract no. 261520. The authors would like to thank the Hamburg Ship Model Basin (HSVA), especially the ice tank crew, for the hospitality, technical and scientific support and the professional execution of the test programme in the Research Infrastructure ARCTECLAB.

REFERENCES

Barker, A., Timco, G., Gravesen, H. and Vølund, P., 2005. Ice loading on Danish wind turbines: Part 1: Dynamic model tests. Cold Regions Science and Technology, 41(1): 1-23.

Ewins, D.J., 2000. Modal Testing: Theory, Practice and Application, Second Edition.

Fabumni, J.A., 1986. Effects of structural modes on vibratory force determination by the pseudoinverse technique. AIAA Journal, 24(3): 504-509.

Frederking, R., D.Masterson, B.Wright and Spencer, P., 2002. ICE LOAD MEASURING PANELS – THE NEXT GENERATION, IAHR, New Zealand, pp. 450-457.

Gravesen, H., Sørensen, S.L., Vølund, P., Barker, A. and Timco, G., 2005. Ice loading on Danish wind turbines: Part 2. Analyses of dynamic model test results. Cold Regions Science and Technology, 41(1): 25-47.

Hendrikse, H., Metrikine, A. and Evers, K.-U., 2012. A method to measure the added mass and added damping in dynamic ice-structure interaction:, "Ice Research for a Sustainable Environment"(IAHR). Dalian, China.

Hollandsworth, P.E. and Busby, H.R., 1989. Impact force identification using the general inverse technique. International Journal of Impact Engineering, 8(4): 315-322.

Kerschen, G., Worden, K., Vakakis, A.F. and Golinval, J.-C., 2006. Past, present and future of nonlinear system identification in structural dynamics. Mechanical Systems and Signal Processing, 20(3): 505-592.

Kärnä, T., 1995. Finite ice failure depth in penetration of a vertical indentor into an ice edge : T. Karna, Annals of Glaciology, 19, 1994, pp 114–120. International Journal of Rock Mechanics and Mining Sciences & Geomechanics Abstracts, 32(2): A98.

Kärnä, T., Kolari, K., Jochmann, P., Evers, K.-U., Xiangjun, B., Määttänen, M. and Martonen, P., 2003. Ice action on compliant structures, VTT research notes 2223, VTT.

Lourens, E.-M., 2012. FORCE IDENTIFICATION IN STRUCTURAL DYNAMICS. PhD Thesis, Katholieke Universiteit Leuven.
Montgomery, C.J. and Lipsett, A.W., 1981. ESTIMATION OF ICE FORCES FROM DYNAMIC RESPONSE, International Symposium on Ice (IAHR), Quebec, P.Q. Canada, pp. 771-782.
Määttänen, M., 1978. ON CONDITIONS FOR THE RISE OF SELF-EXCITED ICE INDUCED AUTONOMOUS OSCILLATIONS IN SLENDER MARINE PILE STRUCTURES. PhD Thesis, UNIVERSITY OF OULU.
Määttänen, M., 1982. True ice force by deconvolution, 1st International Modal Analysis Conference (IMAC), Orlando, FL, USA, pp. 556-590.
Määttänen, M., 1983. DYNAMIC ICE-STRUCTURE INTERACTION DURING CONTINOUS CRUSHING, U.S. Army Cold Regions Research and Engineering Laboratory, Hanover, NH 03755. CRREL Report 83-5.
Määttänen, M., Løset, S., Metrikine, A., Evers, K.-U., Hendrikse, H., Lønøy, C., Metrikin, I., Nord, T.S. and Sukhorukov, S., 2012. Novel ice induced vibration testing in a large-scale facility, "Ice Research for a Sustainable Environment"(IAHR), Dalian, China.
Määttänen, M., Marjavaara, P., Saarinen, S. and Laakso, M., 2011. Ice crushing tests with variable structural flexibility. Cold Regions Science and Technology, 67(3): 120-128.
Nord, T.S. and Määttänen, M., 2012. Modal analysis in ice structure interaction, IAHR, Dalian, China.
Nordström, L.J.L. and Nordberg, T.P., 2004. A time delay method to solve non-collocated input estimation problems. Mechanical Systems and Signal Processing, 18(6): 1469-1483.
Parloo, E., Verboven, P., Guillaume, P. and Van Overmeire, M., 2003. Force identification by means of in-operation modal models. Journal of Sound and Vibration, 262(1): 161-173.
Singh, S.K., Timco, G.W., Frederking, R. and Jordaan, I.J., 1990. TESTS OF ICE CRUSHING ON A FLEXIBLE STRUCTURE, OMAE Houston TX. USA, pp. 89-94.
Sodhi, D.S., 2001. Crushing failure during ice–structure interaction. Engineering Fracture Mechanics, 68(17–18): 1889-1921.
Takeuchi, T., Sakai, M., Akagawa, S. and Saeki, H., 2000. On the Factors Influencing the Scaling of Ice Forces, IUATAM Symposium on Scaling Laws in Ice Mechanics and Ice Dynamics, Fairbanks, USA, pp. 149-160.
Taylor, R., 2009. Analysis of Scale Effect in Compressive Ice Failure. PhD Thesis.
Timco, G. and Croasdale, K.R., 2006. HOW WELL CAN WE PREDICT ICE LOADS?, IAHR, Sapporo, Japan, pp. 167-174.
Timco, G.W., Frederking, R. and Singh, S.K., 1989. THE TRANSFER FUNCTION APPROACH FOR A STRUCTURE SUBJECTED TO ICE CRUSHING, POAC, Luleå, Sweden, pp. 420-430.
Wang, B.T., 2002. PREDICTION OF IMPACT AND HARMONIC FORCES ACTING ON ARBITRARY STRUCTURES: THEORETICAL FORMULATION. Mechanical Systems and Signal Processing, 16(6): 935-953.
Y.Toyama, T.Sensu, M.Minami and N.Yashima, 1983. Model tests on self-excited vibration on cylindrical structures, Port and Ocean Under Arctic conditions (POAC), Helsinki, pp. 834-844.

Appendix 2 Model-based force and state estimation in experimental ice-induced vibrations

This appendix includes the paper published in the Journal of Cold Regions Science and Technology (see below).

- Nord, T.S., Lourens, E.-M., Øiseth, O. and Metrikine, A., 2015. Model-based force and state estimation in experimental ice-induced vibrations by means of Kalman filtering. Cold Regions Science and Technology, 111(0): pp. 13-26

Cold Regions Science and Technology 111 (2015) 13–26

Contents lists available at ScienceDirect

Cold Regions Science and Technology

journal homepage: www.elsevier.com/locate/coldregions

Model-based force and state estimation in experimental ice-induced vibrations by means of Kalman filtering

Torodd S. Nord [a,b,*], Eliz-Mari Lourens [c], Ole Øiseth [d], Andrei Metrikine [c]

[a] Sustainable Arctic Marine and Coastal Technology (SAMCoT), Centre for Research-based Innovation (CRI), Norwegian University of Science and Technology (NTNU), Trondheim, Norway
[b] The University Centre in Svalbard (UNIS), Longyearbyen, Spitsbergen, Norway
[c] Faculty of Civil Engineering and Geosciences, Delft University of Technology, Delft, The Netherlands
[d] Department of Structural Engineering, Norwegian University of Science and Technology, Trondheim, Norway

ARTICLE INFO

Article history:
Received 18 March 2014
Received in revised form 1 October 2014
Accepted 4 December 2014
Available online 11 December 2014

Keywords:
Dynamic ice-structure interaction
Inverse problems
Kalman filtering
Force identification
State estimation

ABSTRACT

Bottom-founded structures deployed in ice-choked waters may experience severe ice-induced vibrations. A direct monitoring of the level-ice forces requires installation and use of load panels. This is often cumbersome and costly. Indirect measurements interpreted by inverse techniques are therefore favourable since sensors for response measurements are easier to install, less expensive and provide information as to the structural motion. In this paper, the level-ice forces exerted on a scale model of a compliant bottom-founded structure are identified from non-collocated strain and acceleration measurements by means of a joint input-state estimation algorithm. The algorithm allows for uncertainty in the model equations, can be applied to full-scale structures and reconstructs forces without any prior assumptions on their dynamic evolution. The identification is performed employing two different finite element models. One is entirely based on the blueprints of the structure. The other is tuned to reproduce the measured first natural frequency more accurately. Results are presented for two different excitation scenarios characterized by the ice failure process and ice velocity. These scenarios are known as the intermittent crushing and the continuous brittle crushing regimes. The accuracy of the identified forces is assessed by comparing them with those obtained by a frequency domain deconvolution, on the basis of experimentally obtained frequency response functions. The results show successful identification of the level-ice forces for both the intermittent and continuous brittle crushing regimes even when significant modelling errors are present. The response (displacements) identified in conjunction with the forces is also compared to those measured during the experiment. Here the estimated response is found to be sensitive to the modelling errors in the blueprint model. Simple tuning of the model, however, enables high accuracy response estimation.

1. Introduction

Level-ice forces have been measured on bottom-founded structures since the very first oil platforms in the Cook Inlet, Alaska (Peyton, 1966). Bjerkås (2006) summarized the variety of methods used in field measurements to obtain the ice forces acting on fixed structures. Direct measurements of force–time histories (Interfacial methods (Bjerkås, 2006)) are often executed by means of load panels mounted on the structure. The Molikpaq platform was deployed at different sites in the Canadian Beaufort Sea in the 1980s. The platform was equipped with data acquisition systems for measuring ice forces and deformations of the structure. The measured ice forces from the so-called MEDOF panels have been widely used since then, but also questioned for their operational accuracy and reliability, reviewed by Frederking et al. (2002), Jefferies et al. (2011) and Spencer (2013).

Force identification by means of frequency domain deconvolution was performed by Montgomery and Lipsett (1981) to study the river-ice forces on the bridge crossing the Athabaska River in Alberta, Canada. They identified the forces from a single-degree-of-freedom model and the measured structural response using a frequency response function (FRF). Määttänen (1982) applied the same method to identify the ice forces on a lighthouse in the Gulf of Bothnia. An icebreaker, connected with a wire to the lighthouse, was used to perform a step relaxation test (Ewins, 2000) in order to obtain the FRF from the measured excitation and response. Unfortunately, a poor coherence function was found, such that the ice forces had to be identified using an FRF from modal decomposition instead. Määttänen (1983) identified the ice forces using the experimentally obtained FRF in a later report. Frederking et al. (1986) used the same approach to identify the dynamic ice forces on a lightpier in the St. Lawrence River, Canada, while the static force component was measured by load panels.

* Corresponding author at: Sustainable Arctic Marine and Coastal Technology (SAMCoT), Centre for Research-based Innovation (CRI), Norwegian University of Science and Technology (NTNU), Trondheim, Norway.
E-mail address: torodd.nord@ntnu.no (T.S. Nord).

http://dx.doi.org/10.1016/j.coldregions.2014.12.003
0165-232X/

The accuracy of the frequency domain deconvolution approach has been questioned by Timco et al. (1989) and Singh et al. (1990). They drew attention to the fact that the identified ice forces were overestimated, compared to the directly measured forces in regimes where the response was close to the natural frequency of the structure. In order to resolve the difference between the identified and measured forces, they suggested increasing the damping in the dynamic model. Fabumni (1986) studied the number of forces that can be identified at an individual frequency dependent on the number of participating modes at that frequency. It was demonstrated that in the presence of measurement noise only one force could be reconstructed with acceptable accuracy when only one mode is contributing to the response signal, as is the case around one of the natural frequencies.

The harsh environment affects the ability to deploy sensors on Arctic offshore structures. Unless the inner surface of the structure can be accessed, the ice-action point may be a challenging location to install a sensor since the ice is crushing against the outer surface. This implies that non-collocated sensors may be the only realistic option. Hollandsworth and Busby (1989) demonstrated the significance of sensor collocation, and found that if the sensors were deployed far from the excitation point, the forces were likely to be underestimated. Water level fluctuations or rafting of the ice causes variations in the location of the ice-action point on bottom-founded structures. This implies that perfect collocation of the sensors is in practice difficult to achieve.

Identification accuracy does not rely only on the sensor locations or modelling errors, but also on the structural design of the experiment, calibration procedures and noise levels. When using direct ice-force measurements, the internal damping and natural frequencies of the load panels or load cells may interfere with the ice failure. On occasions when the directly measured force signals include inertia from the measurement setup itself, subtraction of the undesired inertia is required to obtain the ice force (Barker et al.(2005)).

Another instrument that can be used to obtain the ice forces is tactile sensors (e.g., Sodhi (2001), Määttänen et al. (2011)). These sensors have the advantage of being able to measure pressure with high spatial resolution, and they can be tailored to fit any indenter and enable extraction of both contact area and pressure. However, tactile sensors can only measure stresses normal to the surface of the indenter, such that any shear stresses have to be derived through assumed static and dynamic friction coefficients. So far the application of the tactile sensor has been limited to small and medium-scale experiments.

Ice forces have traditionally been obtained by either direct force measurements or deterministic force identification in the frequency domain. A disadvantage of the latter method is that it is often problematic to accurately determine the FRFs of large structures. Since the offshore structures deployed in the Arctic are not an exception, in situ ice forces are difficult to obtain from frequency domain deconvolution and output only measurements. Direct measurement, on the other hand, implies heavy costs related to the load panels, installation and maintenance. Response measurements are therefore still a favourable means to obtain the forces. Furthermore, they provide additional important information about the structural motion.

In this contribution, we demonstrate a methodology to overcome the aforementioned difficulties. A recently developed deterministic–stochastic approach is used to jointly identify the ice forces and the states. The original algorithm, proposed by Gillijns and De Moor (2007), was intended for use in the field of optimal control. Lourens et al. (2012a) extended the algorithm for use with reduced-order systems, which are often encountered in structural dynamics. Niu et al. (2011) used the original algorithm to identify forces on a laboratory-scale structure. The deterministic–stochastic nature of the algorithm allows for improved results when the model equations are inexact. Since the algorithm requires no regularization, it can be applied online.

In what follows, the ice forces are identified in conjunction with the states, using the original algorithm (Gillijns and De Moor, 2007) and a limited number of response measurements on a laboratory test setup designed for studying ice-induced vibrations. The results are assessed by comparison with the forces obtained with frequency domain deconvolution, and the estimated displacements are compared with the ones measured.

2. Fundamentals

2.1. System equations

The governing equations of motion for a linear system discretized in space and excited by an external force can be written as follows:

$$\mathbf{M}\ddot{\mathbf{u}}(t) + \mathbf{C}\,\dot{\mathbf{u}}\,(t) + \mathbf{K}\mathbf{u}(t) = \mathbf{f}(t) = \mathbf{S}_p\mathbf{p}(t) \tag{1}$$

where $\mathbf{u} \in \mathbb{R}^{n_{DOF}}$ is the displacement vector, and the matrices $\mathbf{M}, \mathbf{C}, \mathbf{K} \in \mathbb{R}^{n_{DOF} \times n_{DOF}}$ denote the structural mass, damping and stiffness matrix, respectively. The excitation vector $\mathbf{p}(t) \in \mathbb{R}^{n_p}$ is specified to act on the desired locations through the force influence matrix $\mathbf{S}_p \in \mathbb{R}^{n_{DOF} \times n_p}$, where n_p is the number of force time histories. A step action table is provided below to communicate the governing elements to perform the force and state identification presented in this paper:

1. Model assembly and tuning; extract mass, damping and stiffness matrices ($\mathbf{M}, \mathbf{C}, \mathbf{K} \in \mathbb{R}^{n_{DOF} \times n_{DOF}}$).
2. Define force influence locations ($\mathbf{S}_p \in \mathbb{R}^{n_{DOF} \times n_p}$).
3. Define sensor locations and assemble the data vector (Section 2.2).
4. State-space transform (Section 2.2).
5. Perform joint state and input estimation (Section 2.3).

2.2. State-space description

The continuous-time state vector $\mathbf{x}(t) \in \mathbb{R}^{n_s}$, $n_s = 2n_{DOF}$ is defined as:

$$\mathbf{x}(t) = \begin{pmatrix} \mathbf{u}(t) \\ \dot{\mathbf{u}}(t) \end{pmatrix} \tag{2}$$

whereby the equation of motion of second order in (1) can be organized as a first-order continuous-time state equation

$$\dot{\mathbf{x}}\,(t) = \mathbf{A}_c\mathbf{x}(t) + \mathbf{B}_c\mathbf{p}(t) \tag{3}$$

where the system matrices $\mathbf{A}_c \in \mathbb{R}^{n_s \times n_s}$ and $\mathbf{B}_c \in \mathbb{R}^{n_s \times n_p}$ are defined as

$$\mathbf{A}_c = \begin{bmatrix} \mathbf{0} & \mathbf{I} \\ -\mathbf{M}^{-1}\mathbf{K} & -\mathbf{M}^{-1}\mathbf{C} \end{bmatrix}, \mathbf{B}_c = \begin{bmatrix} \mathbf{0} \\ \mathbf{M}^{-1}\mathbf{S}_p \end{bmatrix} \tag{4}$$

The measurements are arranged in a data vector $\mathbf{d}(t) \in \mathbb{R}^{n_d}$, in which the observations can be a linear combination of displacement, velocity and acceleration, with n_d the number of data measurements. The data vector is constructed as follows:

$$\mathbf{d}(t) = \mathbf{S}_a\ddot{\mathbf{u}}(t) + \mathbf{S}_v\,\dot{\mathbf{u}}\,(t) + \mathbf{S}_d\mathbf{u}(t) \tag{5}$$

where the selection matrices $\mathbf{S}_a$, $\mathbf{S}_v$ and $\mathbf{S}_d \in \mathbb{R}^{n_d \times n_{DOF}}$ are populated according to the spatial location where acceleration, velocity and/or displacement are measured. By premultiplying Eq. (1) with $\mathbf{M}^{-1}$, inserting the resulting expression into Eq. (5), and further utilizing the definition of the state vector, Eq. (5) can be transformed into the state-space form:

$$\mathbf{d}(t) = \mathbf{G}_c\mathbf{x}(t) + \mathbf{J}_c\mathbf{p}(t) \tag{6}$$

where the matrices $\mathbf{G}_c \in \mathbb{R}^{n_d \times n_s}$ and $\mathbf{J}_c \in \mathbb{R}^{n_d \times n_p}$ represent the output influence matrix and direct transmission matrix, respectively, defined as:

$$\mathbf{G}_c = \left[\mathbf{S}_d - \mathbf{S}_a\mathbf{M}^{-1}\mathbf{K} \quad \mathbf{S}_v - \mathbf{S}_a\mathbf{M}^{-1}\mathbf{C}\right], \mathbf{J}_c = \left[\mathbf{S}_a\mathbf{M}^{-1}\mathbf{S}_p\right]$$

In discrete time under a zero-order hold assumption and given a sampling rate of $1/\Delta t$, Eqs. (3) and (6) can be defined as follows:

$$\mathbf{x}_{k+1} = \mathbf{A}\mathbf{x}_k + \mathbf{B}\mathbf{p}_k \tag{7}$$

$$\mathbf{d}_k = \mathbf{G}\mathbf{x}_k + \mathbf{J}\mathbf{p}_k \tag{8}$$

where

$$\mathbf{x}_k = \mathbf{x}(k\Delta t),\ \mathbf{d}_k = \mathbf{d}(k\Delta t),\ \mathbf{p}_k = \mathbf{p}(k\Delta t),\ k = 1, \ldots, N$$

and

$$\mathbf{A} = e^{\mathbf{A}_c \Delta t},\ \mathbf{B} = [\mathbf{A} - \mathbf{I}]\mathbf{A}_c^{-1}\mathbf{B}_c$$
$$\mathbf{G}_c = \mathbf{G},\ \mathbf{J}_c = \mathbf{J}$$

2.3. Joint input-state estimation algorithm

Assuming the system matrices known, the algorithm developed by Gillijns and De Moor (2007) is used to jointly estimate the forces and states. It has the structure of a Kalman filter, but with the true force replaced with an optimal estimate. Unlike force identification using the traditional Kalman filter (see Lourens et al. (2012b)), no regularization parameter has to be calculated. This implies that no assumptions are made on the dynamic evolution of the forces. By introducing random variables $\mathbf{w}_k$ and $\mathbf{v}_k$, representing the stochastic system and measurement noise, respectively, the discrete-time state-space equations become

$$\mathbf{x}_{k+1} = \mathbf{A}\mathbf{x}_k + \mathbf{B}\mathbf{p}_k + \mathbf{w}_k \tag{9}$$

$$\mathbf{d}_k = \mathbf{G}\mathbf{x}_k + \mathbf{J}\mathbf{p}_k + \mathbf{v}_k \tag{10}$$

where it is assumed that the vectors $\mathbf{w}_k$ and $\mathbf{v}_k$ are mutually uncorrelated, zero-mean, white noise signals with known covariance matrices $\mathbf{Q} = E\{\mathbf{w}_k\mathbf{w}_l\}$ and $\mathbf{R} = E\{\mathbf{v}_k\mathbf{v}_l\}$. The algorithm predicts the forces and states in three steps: the unbiased minimum-variance input estimation (MVU), the measurement update, and the time update.

Input estimation:

$$\widetilde{\mathbf{R}}_k = \mathbf{G}\mathbf{P}_{k|k-1}\mathbf{G}^T + \mathbf{R} \tag{11}$$

$$\boldsymbol{M}_k = \left(\mathbf{J}^T\widetilde{\mathbf{R}}_k^{-1}\mathbf{J}\right)^{-1}\mathbf{J}^T\widetilde{\mathbf{R}}_k^{-1} \tag{12}$$

$$\hat{\mathbf{p}}_{k|k} = \mathrm{M}_k\left(\mathbf{d}_k - \mathbf{G}\hat{\mathbf{x}}_{k|k-1}\right) \tag{13}$$

$$\mathbf{P}_{p[k|k]} = \left(\mathbf{J}^T\widetilde{\mathbf{R}}_k^{-1}\mathbf{J}\right)^{-1} \tag{14}$$

Measurement update:

$$\mathbf{L}_k = \mathbf{P}_{k|k-1}\mathbf{G}^T\widetilde{\mathbf{R}}_k^{-1} \tag{15}$$

$$\hat{\mathbf{x}}_{k|k} = \hat{\mathbf{x}}_{k|k-1} + \mathbf{L}_k\left(\mathbf{d}_k - \mathbf{G}\hat{\mathbf{x}}_{k|k-1} - \mathbf{J}\mathbf{p}_{k|k}\right) \tag{16}$$

$$\mathbf{P}_{k|k} = \mathbf{P}_{k|k-1} - \mathbf{L}_k\left(\widetilde{\mathbf{R}}_k - \mathbf{J}\,\mathbf{P}_{p[k|k]}\mathbf{J}^T\right)\mathbf{L}_k^T \tag{17}$$

$$\mathbf{P}_{xp[k|k]} = \mathbf{P}_{px[k|k]}^T = -\mathbf{L}_k\mathbf{J}\,\mathbf{P}_{p[k|k]} \tag{18}$$

Time update:

$$\mathbf{x}_{k+1|k} = \mathbf{A}\hat{\mathbf{x}}_{k|k} + \mathbf{B}\hat{\mathbf{p}}_{k|k} \tag{19}$$

$$\mathbf{P}_{k+1|k} = [\mathbf{A} \quad \mathbf{B}]\begin{bmatrix}\mathbf{P}_{k|k} & \mathbf{P}_{xp[k|k]} \\ \mathbf{P}_{px[k|k]} & \mathbf{P}_{p[k|k]}\end{bmatrix}\begin{bmatrix}\mathbf{A}^T \\ \mathbf{B}^T\end{bmatrix} + \mathbf{Q} \tag{20}$$

For more details on the algorithm and the assumptions it is based upon, the reader is referred to Gillijns and De Moor (2007).

3. Laboratory experiment in ice-induced vibrations

The force identification algorithm outlined above is applied to data from the *Deciphering Ice-Induced Vibration* test campaign at the Hamburg Ice Basin (HSVA), carried out in 2011. See Määttänen et al. (2012), Hendrikse et al. (2012) and Nord and Määttänen (2012) for further details. Two tests from that campaign, referred to as test 4300 and 3300, are used in this study. The main components of the experimental setup are shown in Fig. 1. The ice sheet was floating on water, and the compliant test structure was fixed to a carriage. During testing the carriage forced the structure through the ice sheet, causing continuous ice failure at the indenter. The carriage velocity (ice velocity) was changed in order to investigate the different crushing regimes governing the interaction.

3.1. Test structure

The structure was designed to have a nominal scale ratio of 1:8–1:10 to a generic bottom-founded offshore structure. The structure was scaled to achieve modal similitude, meaning that the natural modes of the laboratory structure resemble the full-scale natural modes. More about the dynamic scaling for this particular test setup can be found in Määttänen et al. (2012). The frequency of vibration was expected to change from the first to the second natural frequency with increasing ice velocity.

To make the structure flexible the main beam was supported by two leaf springs attached to the two vertical support beams displayed in Fig. 1. The flexibility of the system could then be adjusted by changing the spacing between the vertical supports. In order to further tune the system towards the desired natural frequencies, the disc weights displayed in Fig. 1 could be added to the bottom and top of the structure. The bracings and joints were designed to retain low internal friction in order to avoid nonlinearities and to maintain low structural damping. At the location of the ice action, a cylindrical indenter with a 220 mm diameter was attached to the main shaft.

3.2. Sensoring and data acquisition

All sensors were located on the lower part of the structure (cf. Fig. 1). The accelerometer was installed close to the indenter, while the strain gauge was attached to the main beam, approximately 750 mm above the ice-action point. Two laser displacement sensors were installed on a separate frame to monitor the structural displacements at the lower part of the beam. The load cell installed at the ice-action point was only used to access the dynamic properties of the structure before it was subjected to ice forces. The data were sampled at 100 Hz.

3.3. Dynamic calibrations

A step relaxation test in open water prior to each ice test provided the static and dynamic properties of the structure (Ewins, 2000). A steel rod connected to the structure at the ice-action level was gradually loaded using a jack. Between the rod and the ice-action point a weak link was installed, which failed at a selected load level, causing transient vibrations. From the measured excitation and response, the FRF was calculated. This implies that an active load cell was installed only during

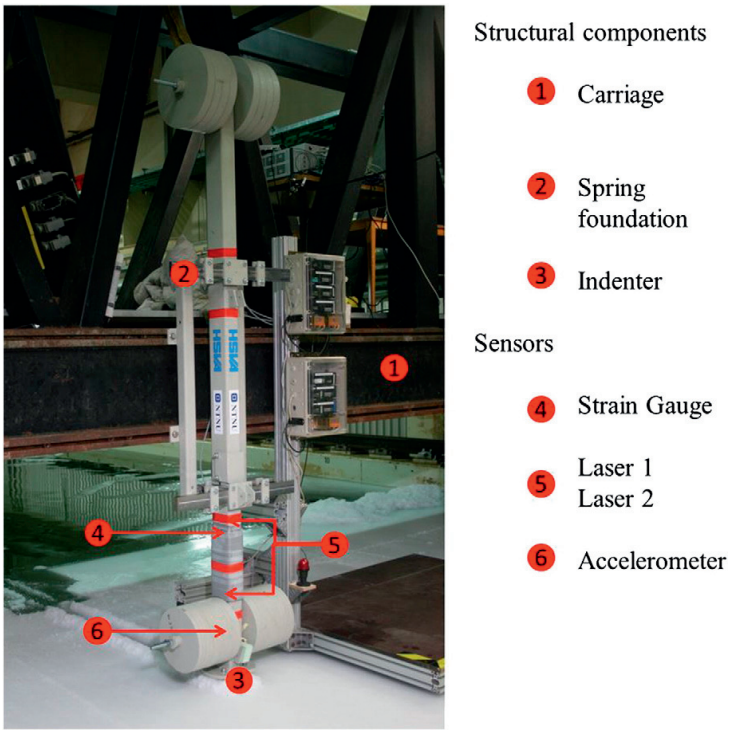

Fig. 1. Overview of the test setup: the compliant structure was mounted to the carriage that forced the structure through the ice sheet.

the dynamic calibrations, and not during ice action. Direct ice-force measurements for the MDOF structure would require a complex design with a comprehensive installation and calibration. The frequency domain deconvolution method on the basis of the experimentally obtained FRFs was used to extract the ice forces (see Section 5.2). At least one calibration test was performed for each structural configuration. The first and second natural frequencies were identified to be 12.2 and 16.2 Hz for test 4300 and 10.2 and 15.4 Hz for test 3300, respectively.

3.4. Ice-sheet properties

The tests were performed in the 78 m long and 10 m wide HSVA Large Ice Tank. The ice sheets were columnar-grained, produced in NaCl-doped water by seeding. The crystal size was controlled by scraping the ice from underneath. Gas bubbles were embedded in the growing ice sheet to ensure the brittle behaviour of the ice as described by Määttänen et al. (2012) and Evers and Jochmann (1993). Subsequent to the ice growth process at −22 °C, the temperature was raised to hit the target ice properties. The governing ice parameters can be found in Nord et al. (2013).

4. Fe model, strain observations and accelerometer location

4.1. FE model

To obtain the system matrices **A**, **B**, **G** and **J**, the structural properties in terms of the global **M**, **K** and **C** matrices must be known. These matrices can be obtained by discretization, using the finite element (FE) method. The FE model of the structure used in this work and the two first natural modes are displayed in Fig. 2(a) and (b). The structure

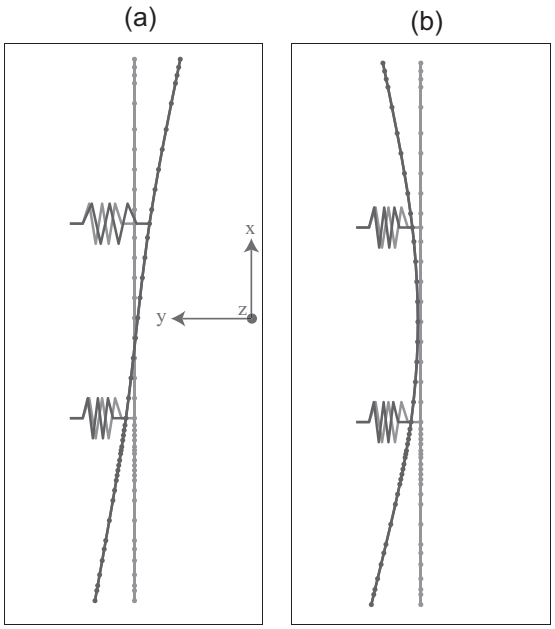

Fig. 2. Finite element model showing spring locations and vibration modes. First mode (a) and second mode (b).

Table 1
FE model properties.

Property	Lower spring stiffness	Upper spring stiffness	Natural frequencies	Damping ratios
Symbol	k_L	k_U	f_1/f_2	ζ_1/ζ_2
Dimension	[kN/mm]	[kN/mm]	[Hz]	[%]
Blueprint model 4300	7.10	4.62	11.17/16.84	2.0/2.0
Tuned model 4300	8.84	5.61	12.12/17.34	2.0/2.0
Blueprint model 3300	4.60	2.95	9.25/15.57	2.0/2.0
Tuned model 3300	6.90	3.50	10.27/16.50	2.0/2.0

is modelled as a beam supported by two linear springs. 42 beam elements are used for the hollow-section (RHS120 × 80 × 6) profile main beam, while the additional mass of the structure at discrete locations is modelled using lumped masses. First, a model based only on structural blueprints is used in the identification to assess how well the force can be reconstructed without any prior knowledge of the true (measured) dynamical properties. Second, a tuned model is assembled based on the knowledge obtained from the dynamic calibrations. The FE software was used to print the **M** and **K** matrices, while Rayleigh damping is used to construct the damping matrix.

4.1.1. Models based on structural blueprints

The stiffness of the linear springs is the combined stiffness of the vertical support beams and the leaf springs, where the combined stiffness relies on the accuracy of the simplistic beam formulas used for the structural design. The added masses from the weight discs were 120 kg in the top and bottom, while the indenter and foundation masses were 32 kg and 15 kg, respectively. The design was intended to provide low internal damping, so that Rayleigh damping coefficients are calculated based on an assumed damping ratio of 2% in the first and second mode.

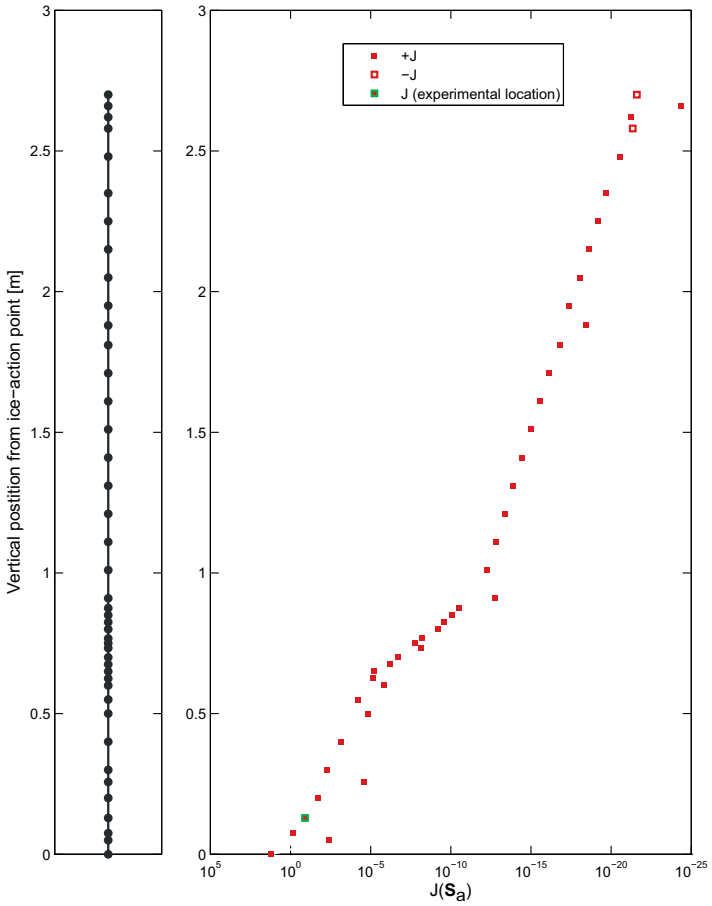

Fig. 3. Finite element model discretization (left). Direct transmission $\mathbf{J} = [\mathbf{S}_a\mathbf{M}^{-1}\mathbf{S}_p]$ as a function of accelerometer location, $\mathbf{S}_a$ (right).

4.1.2. Models tuned using dynamic calibrations

The modelling errors are assumed to originate mainly in the foundation (cf. Fig. 1). The boundary conditions used in the design calculation of the combined stiffness rendered less stiffness than observed. As a consequence, the tuning solely affects the model springs. The stiffness is tuned until the first natural frequency becomes close to the one found in the receptance plot from the dynamic calibrations. This limited number of tuning parameters is considered favourable for the comparative results presented in Section 5. The structural properties for both the blueprint and the tuned models are given in Table 1.

4.2. Strain observations

In order to use the measured strain data to identify the forces and states, the strains must be described through the linear relationship between the output influence matrix **G** and the states. When the shape functions used to establish the finite element are known, they can be readily used to establish the complete transformation from (predicted) states to strain. A two-node beam element has been used in this work. The element has six DOFs in each node and shear deformations have been taken into account—see Bell (2013) for further details.

The general relation between the transverse displacement field and the generalized degrees of freedom can be written as follows:

$$\eta(x) = \mathbf{N}_q \mathbf{q} \tag{21}$$

where $\mathbf{N}_q = \begin{bmatrix} 1 & x & x^2 & x^3 \end{bmatrix}$ and $\mathbf{q} = \mathbf{A}_{el}^{-1}\mathbf{a}$ are the generalized displacement patterns and the generalized DOFs, while **a** symbolizes the physical element DOFs. The $\mathbf{A}_{el}$ matrix must be given for deformations in both *xz* and *xy* planes (see coordinate system in Fig. 2) For lateral motion in the y direction and rotation about the z axis (*xy* plane), the matrix $\mathbf{A}_{el}$ is as follows:

$$\mathbf{a} = \mathbf{A}_{el}\mathbf{q}, \quad \begin{bmatrix} a_2 \\ a_6 \\ a_8 \\ a_{12} \end{bmatrix} = \begin{bmatrix} \eta(0) \\ -\eta_{,x}(0) - \dfrac{\alpha L^2}{12}\eta_{,xxx}(0) \\ \eta(L) \\ -\eta_{,x}(L) - \dfrac{\alpha L^2}{12}\eta_{,xxx}(L) \end{bmatrix} \tag{22}$$

$$= \begin{bmatrix} 1 & 0 & 0 & 0 \\ 0 & -1 & 0 & \dfrac{-\alpha L^2}{2} \\ 1 & L & L^2 & L^3 \\ 0 & -1 & -2L & \dfrac{-L^2(6+\alpha)}{2} \end{bmatrix} \mathbf{q}$$

where α is the dimensionless shear coefficient given in Bell (2013). Inserting the expression for the generalized DOFs into Eq. (21), the element shape functions are obtained as follows:

$$\eta_y(x) = \mathbf{N}_q \mathbf{q} = \mathbf{N}_q \mathbf{A}_{el}^{-1} \mathbf{a} = \mathbf{N}^{el} \mathbf{a} \tag{23}$$

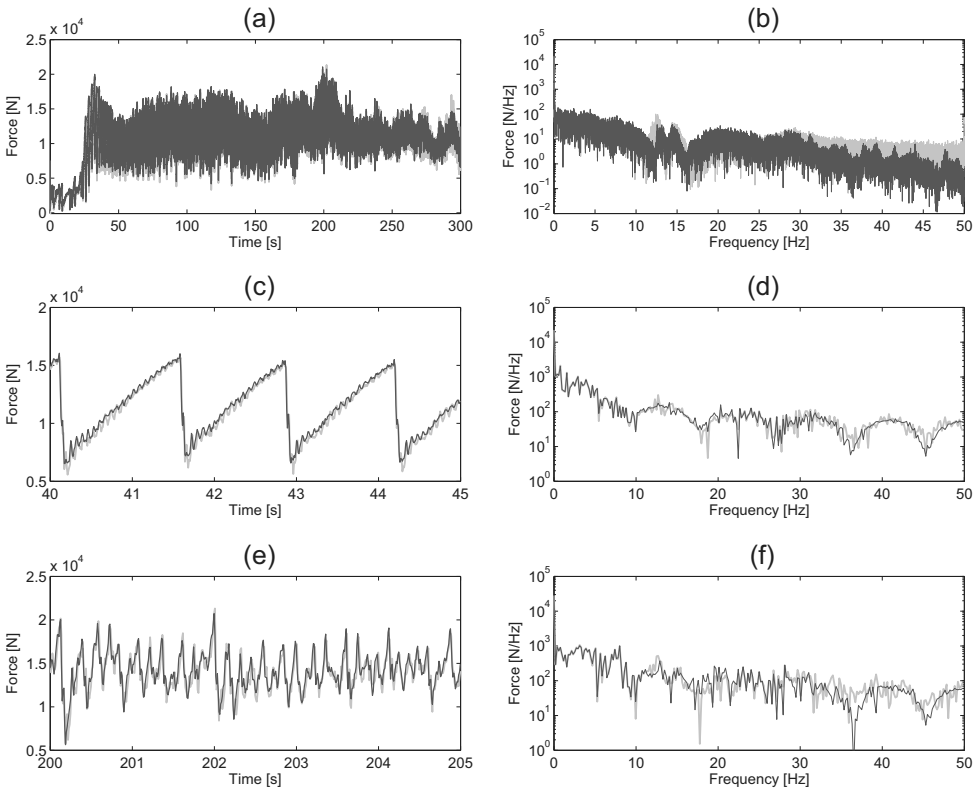

Fig. 4. Identified force (light grey) versus reference force (black) for: (a) complete force time history, (b) frequency spectrum of complete force time history, (c) intermittent crushing, (d) frequency spectrum of intermittent crushing, (e) continuous brittle crushing and (f) frequency spectrum of continuous brittle crushing.

When the shape-functions N^{el} are given through the relation in Eq. (23), the bending strain can be found as:

$$\begin{aligned}\varepsilon_b(x) &= -y\eta_{y,xx} = -y\mathbf{N}^{el}_{y,xx}\mathbf{a} \\ &= -y\left[-\frac{6}{L^2(1+\alpha)}+\frac{12x}{L^3(1+\alpha)}-\frac{4+\alpha}{L(1+\alpha)}+\frac{6x}{L^2(1+\alpha)}\right. \\ &\quad \left.\frac{6}{L^2(1+\alpha)}-\frac{12x}{L^3(1+\alpha)}-\frac{2+\alpha}{L(1+\alpha)}+\frac{6x}{L^2(1+\alpha)}\right]\mathbf{a}\end{aligned} \tag{24}$$

where y is the distance from the centroid to the point on the cross-section where the strain is measured. Since the strains are not continuous between the elements, the bending strain at the node of interest can be taken as the average over two neighbouring elements. The data influence matrix for strain (see Eq. (5)), denoted $\mathbf{S}_d$, has to be populated according to the global DOF vector, $\mathbf{u}$.

4.3. Optimal accelerometer location

As positioning an accelerometer at the ice-action point is difficult in practice, this section illustrates a simple, yet powerful methodology to determine the optimal location to install one accelerometer, given that the interest is to identify the force at ice-action level. The direct transmission matrix $\mathbf{J} = [\mathbf{S}_a\mathbf{M}^{-1}\mathbf{S}_p]$ gives an indication of the strength of the influence of the force on the measured accelerations. The global mass matrix $\mathbf{M}$ can be constructed for any type of structure and the selection matrix $\mathbf{S}_a$, and the force influence matrix $\mathbf{S}_p$ can simulate any accelerometer and force locations. The judgment of the best location will herein be designated as the point in which the highest direct transmission value is found. This methodology can also be used to optimize the locations of more than one accelerometer, also when identifying multiple forces. In a practical sense, it enables identification of the best accelerometer locations on offshore structures interacting with an icefloe at multiple locations. Note that the phenomenon of localized high-pressure areas ("high-pressure zones" (Jordaan, 2001)) at the interface between structure and ice is not considered in this paper. An important requirement for successful force identification is that Rank($\mathbf{J}$) $\geq n_p$ (Gillijns and De Moor, 2007). This can only be achieved by, first, including at least as many accelerometers as the number of forces sought for and, secondly, selecting their location carefully.

The blueprint model for test 3300 is used for the simulations. The nodal locations are displayed on the undeformed structure according to Fig. 3 (left), with the ice-action point being at the lowermost location. $\mathbf{S}_p$ is kept constant with influence on the ice-action point, while $\mathbf{S}_a$ changes as the accelerometer location is moved along the beam, starting from the ice-action point. For the current problem $n_p = n_d = 1$, therefore $\mathbf{J}$ becomes a scalar. The values of the direct transmission $\mathbf{J}$ as a function of accelerometer location are shown in Fig. 3 (right). As expected, the optimal location to install an accelerometer is at the collocated position at the ice-action point, for which the highest direct transmission value is obtained. The force influence decreases as the accelerometer location is simulated farther away from the ice-action point. The non-smoothness of the curve follows from the inverse of the mass matrix. All transmission values correspond to the same column of the inverse mass matrix, namely the vector $\mathbf{M}^{-1}\mathbf{S}_p$. The influence of the force on the acceleration data is vanishing as the distance from the

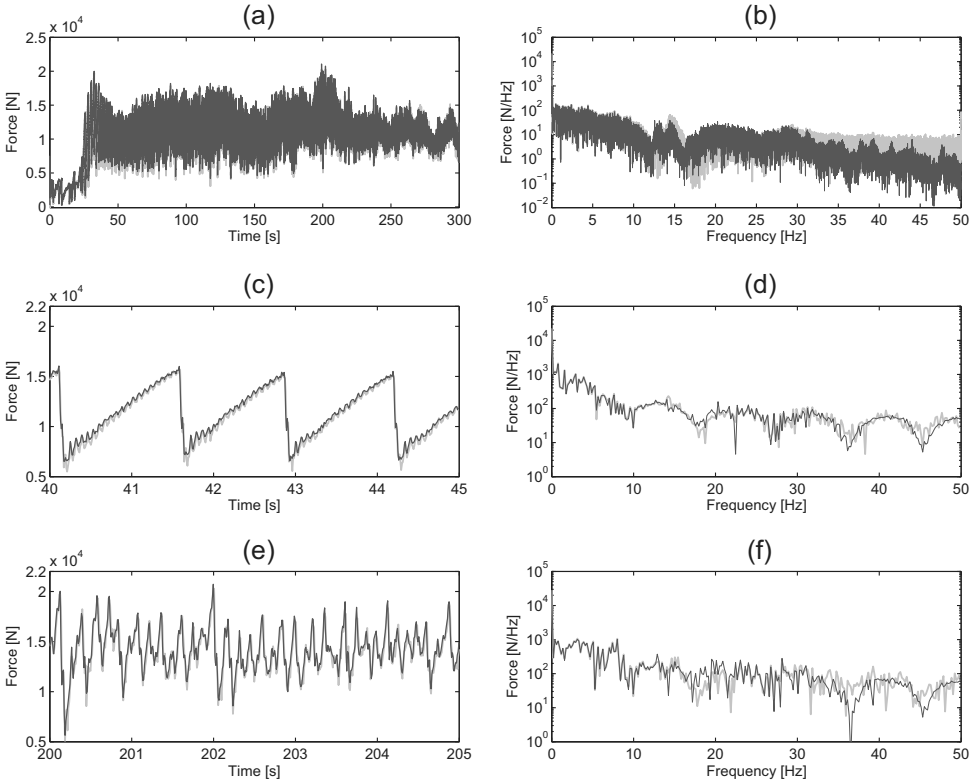

Fig. 5. Identified force (light grey) versus reference force (black) for: (a) complete force time history, (b) frequency spectrum of complete force time history, (c) intermittent crushing, (d) frequency spectrum of intermittent crushing, (e) continuous brittle crushing and (f) frequency spectrum of continuous brittle crushing.

accelerometer to the ice action point increases. Where the transmission value crosses the zero line, there exists a location in which the force has no influence on the data. As a result, the decreasing influence eventually causes numerical problems during force identification.

The numerical problems occur during the system inversion, where ill-conditioned matrices lead to numerical instabilities in the algorithm (Lourens et al., 2012a). Practical examples to illustrate conditions for a successful system inversion are shown in Maes et al. (2015). The decreasing direct transmission value ($\mathbf{J}$) due to non-collocation is explained by Lourens (2012) using the modally reduced system, where $\mathbf{J} = \mathbf{S}_a\boldsymbol{\varphi}\boldsymbol{\varphi}^T\mathbf{S}_p$ and $\boldsymbol{\varphi}$ collects the eigenvectors. When $\mathbf{J}$ becomes zero, the force has no influence on the data. This lack of influence can be attributed to either a sensor position that falls at a node of all modes or to the sensor being positioned such that the modal contributions at that location cancel each other out.

Since the ice thickness and hence the location of the ice action point were practically constant in this test campaign, one $\mathbf{S}_p$ value is sufficient. However, in situ measurements will often have an attack point influenced by water-level fluctuations or rafting of the ice. In order to find the optimal accelerometer locations and account for varying attack-point, one can effectively assemble a vector, $\mathbf{S}_p$, of all possible force locations and vary the sensor positions, $\mathbf{S}_a$. On structures where the insides of the legs are inaccessible, the sensors must be located on the outer surface. If the sensors are deployed too close to the ice-action point, they also become vulnerable to the ice floe. Whereas this example shows that the decreasing direct transmission correlates to the increase of non-collocation, the optimal location to ensure successful structural monitoring should be balanced somewhere between non-collocation and the harsh environment.

5. Results and discussion

5.1. Interaction characteristics

The ice velocity (recorded carriage velocity) in test 4300 was increased in steps, ranging from 10 to 300 mm/s. At low velocities the ice followed the deflection of the structure with a ductile load build-up and a subsequent spring-back deflection due to brittle failure. These response characteristics were only observed for a few seconds; thereafter, the failure process alternated between intermittent and continuous brittle crushing. Underwater cameras revealed that the extrusion of crushed ice primarily consisted of small particles with some larger pieces spalling off. Radial cracks were occasionally observed, but they did not expand to the walls of the ice tank. The ice velocity in test 3300 was increased linearly from ~65 mm/s to ~270 mm/s. The very first interaction alternated between intermittent and continuous brittle crushing. As the velocity increased, the structural response showed small amplifications in the vicinity of the natural frequencies. Because the amplifications were discontinuous and held small amplitudes, the characterization lends towards continuous brittle crushing rather than a frequency lock-in. As for 4300, the extruded particles were mainly pulverized ice with intermittent instances of larger ice pieces spalling off.

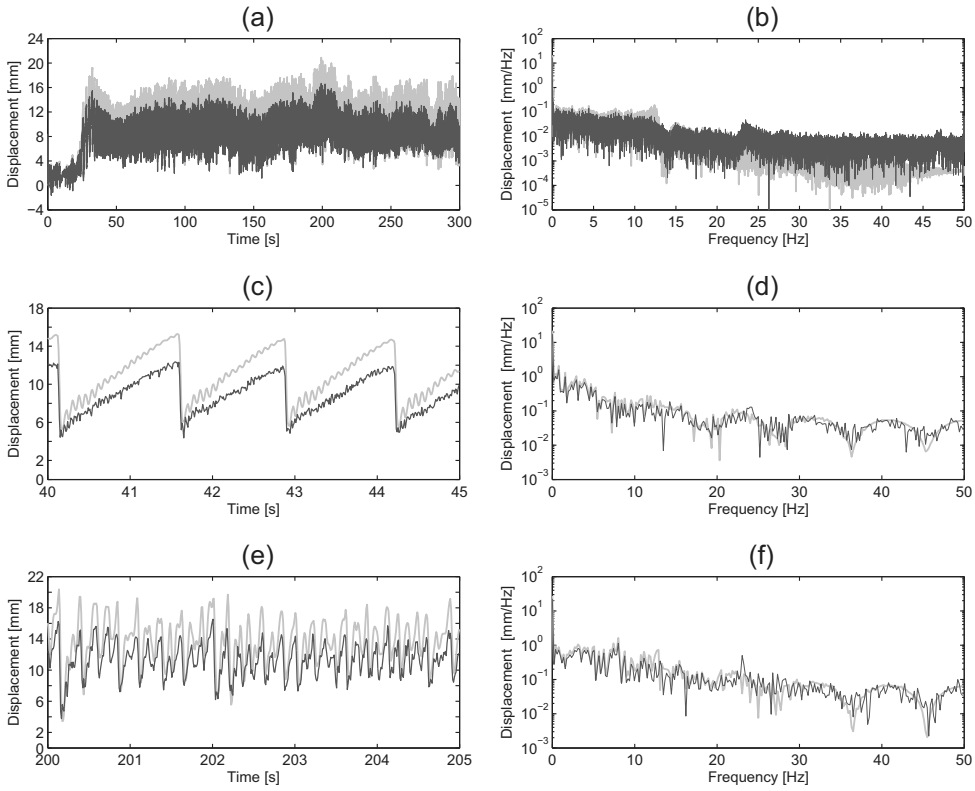

Fig. 6. Estimated (light grey) versus measured (black) displacement during: (a) complete displacement time history, (b) frequency spectrum of complete displacement time history, (c) intermittent crushing, (d) frequency spectrum of intermittent crushing, (e) continuous brittle crushing and (f) frequency spectrum of continuous brittle crushing.

5.2. Reference force

The FRF was obtained experimentally from the step-relaxation test as described in Section 3.3. The ice force used for validation was subsequently found by inverting the FRF as follows:

$$\hat{\mathbf{p}}(\omega) = \hat{\mathbf{H}}^{\dagger}(\omega)\ \hat{\mathbf{d}}(\omega) \tag{25}$$

where ω [rad/s] is frequency; $\hat{\mathbf{p}} \in \mathbb{C}^{n_p}$ is the force; $\hat{\mathbf{d}} \in \mathbb{C}^{n_d}$ is the measured response, and $\hat{\mathbf{H}}^{\dagger} \in \mathbb{C}^{n_d \times n_p}$ is the pseudo-inverse of the FRF matrix. A more detailed description of this procedure can be found in Nord et al. (2013). In what follows, due to the fact that the forces used for validation are obtained using the measured FRFs and not directly measured using a load cell, the validation forces will be referred to as the reference force. This is considered to be consistent with the limitation of not having a directly measured force, at the same time as it reflects the complexity of measuring ice forces.

5.3. Force identification test 4300

The ice force and the states are identified on the basis of one strain gauge and one accelerometer, both non-collocated as shown in Fig. 1. The values assigned to the diagonals of the covariance matrices $\mathbf{Q}$, $\mathbf{R}$, $\mathbf{P}_{0|-1}$ required by the joint input-state estimator (Section 2.3), namely $10e^{-8}$, $10e^{-6}$, and $10e^{-8}$, are chosen based on the peaks in the measured response and the identified states; see Lourens et al. (2012a) for details. The initial state $\hat{\mathbf{x}}_{0|-1}$ is assigned the value of $\mathbf{0}$, effectively treating it as an unknown.

5.3.1. Blueprint model

Fig. 4(a) and (b) displays the identified force for the full test series, compared with the reference force and its frequency spectrum, respectively. The identified force appears almost identical to the reference force (Fig. 4(a)), with the only discrepancy observed at the very end of the test. An initial crack was cut into the ice edge for this test, causing the small peaks in the force-history before full contact was initiated at ~25 s. In order to investigate whether the algorithm and an approximate model are able to reconstruct the forces in the two fundamental ice-crushing regimes, two short sequences representing each of these regimes are selected. The results for the intermittent crushing regime are shown in Fig. 4(c). The identified force exhibits the classical saw-toothed behaviour of intermittent crushing, as each cycle appears almost identical to the reference force. The corresponding Fourier spectrum is shown in Fig. 4(d). In the more dynamic, continuous brittle crushing regime (Fig. 4(e)), the force is also identified accurately. Only at higher frequencies (see Fig. 4(f)) does the difference become slightly more pronounced.

5.3.2. Tuned model

Fig. 5(a) and (b) shows an overall excellent reconstruction of the forces. Where a small discrepancy is observed at the end of the time series for the blueprint model (cf. Fig. 4), it is now almost absent in

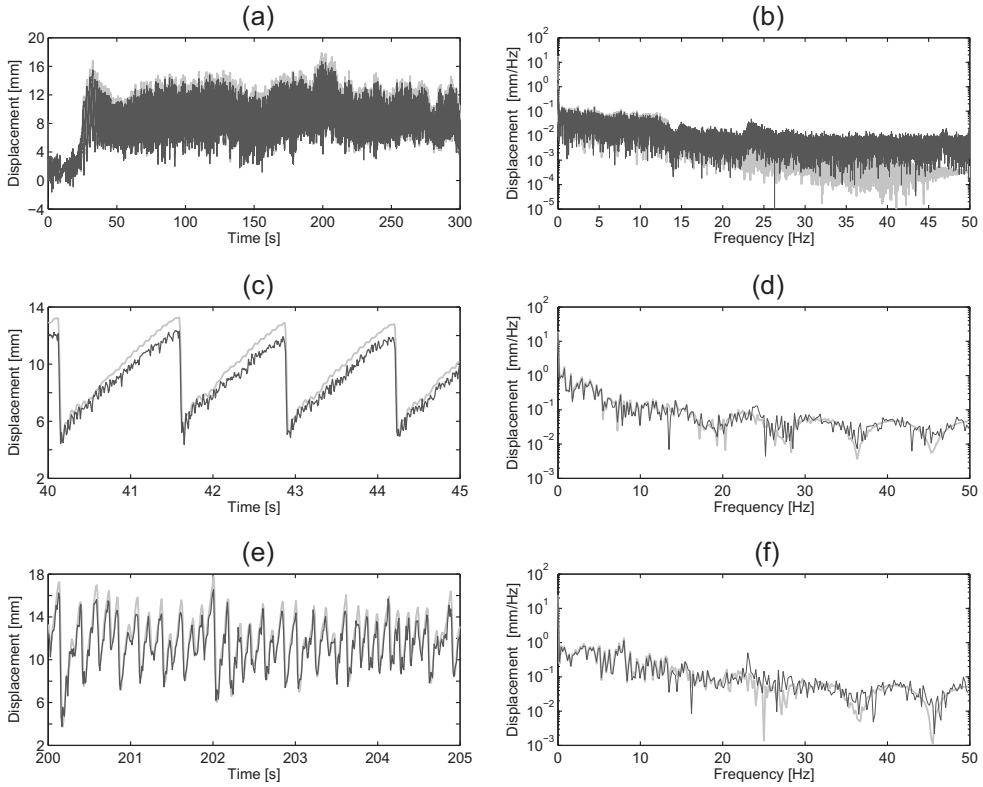

Fig. 7. Estimated (light grey) versus measured (black) displacement during: (a) complete displacement time history, (b) frequency spectrum of complete displacement time history, (c) intermittent crushing, (d) frequency spectrum of intermittent crushing, (e) continuous brittle crushing and (f) frequency spectrum of continuous brittle crushing.

the tuned model (Fig. 5(a)). The saw-toothed cycles governing the intermittent crushing regime (Fig. 5(b) and (c)) hold a similar quality to the blueprint model. The peaks and valleys in the continuous brittle crushing regime follow the reference force somewhat better with the tuned model (Fig. 5(e)) than the blueprint model (cf. Fig. 4(e)) although the improvements are limited to frequencies with low amplitudes beyond 10 Hz as seen in Fig. 5(f).

5.4. Response estimation test 4300

While the foregoing application of the algorithm focused on the identification of the forces, here the aim is to show the accuracy of the (jointly) estimated displacement at unmeasured locations. Recall that, in what follows, only the non-collocated acceleration and strain gauge are used to estimate the displacement at the location of the lowermost laser (cf. Fig. 1).

5.4.1. Blueprint model

The measured and estimated displacements are displayed in Fig. 6(a). The displacements are overestimated throughout the test, in particular around 11 to 12 Hz (Fig. 6(b)). In the intermittent crushing regime (Fig. 6(c)) the peak offsets remain constant, while for the continuous brittle crushing regime (Fig. 6(e)), some peaks differ less than others. The shape of each cycle is well captured for the intermittent regime, while for the brittle crushing regime the load build-up phase differs prior to the terminal ice failure. Despite the overestimation, the dominant Fourier amplitudes of the estimated displacements (Fig. 6(d) and (f)) are in good agreement with the measurements.

5.4.2. Tuned model

The overall agreement between measured and estimated response (Fig. 7(a)) improves significantly when tuning the foundation stiffness. The Fourier amplitudes for the estimated response at 11 to 12 Hz in Fig. 7(b) are now reduced and correspond well to the measured response. The constant peak offset in the intermittent regime (Fig. 7(c)) reduces to 1 mm, while in continuous brittle crushing (Fig. 7(e)) the difference ranges from 0 to 2 mm. Reducing the peak offset for intermittent crushing has limited effect on the higher frequencies displayed in Fig. 7(d). The improved accuracy is, as expected, more visible in the frequency domain during continuous brittle crushing (Fig. 7(f)). The light grey and dark lines correspond to each other well, and the major frequency components are well captured.

5.5. Force identification test 3300

The identification is performed with the same non-collocated sensors, covariance matrices and initial conditions as for test 4300.

5.5.1. Blueprint model

The identified and the reference force time histories are displayed in Fig. 8(a). The structure interacts with the ice edge after ~3 s. While the peaks are almost identical, the identified valleys are lower than in the reference force. As for test 4300, the largest discrepancy appears close to the end of the test, in both cases with ice velocity close to 250 mm/s. The frequency spectra (Fig. 8(b)) show that the major peaks below 10 Hz are captured accurately. Again two sequences are selected to more closely investigate the identification, herein representing

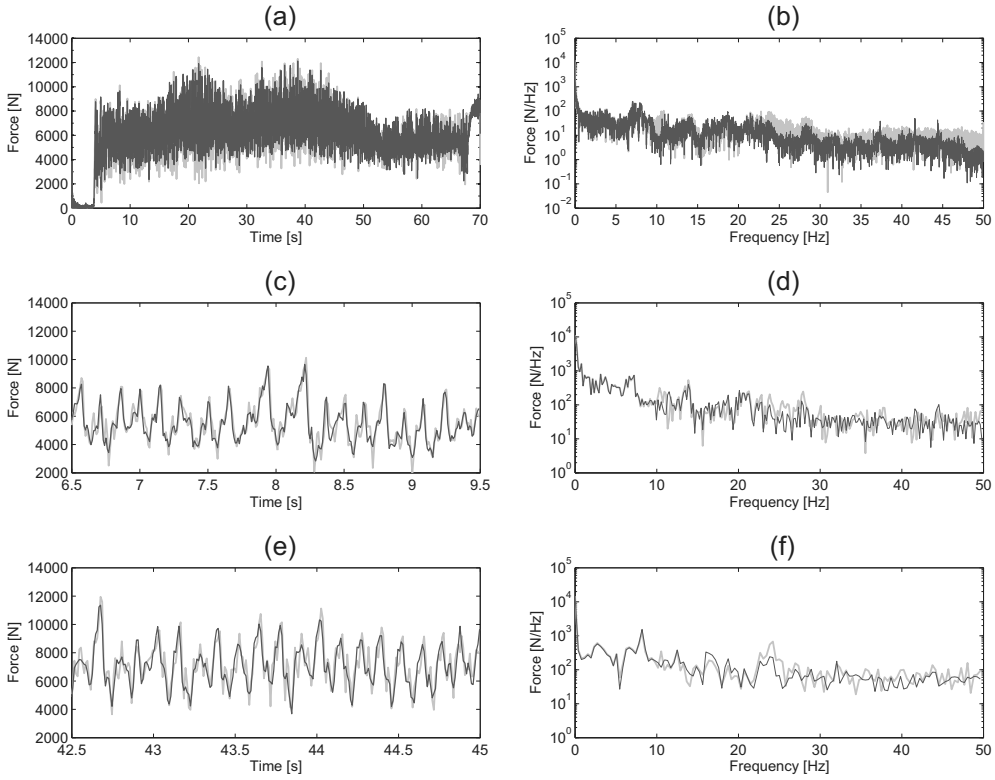

Fig. 8. Identified force (light grey) versus reference force (black) for: (a) complete force time history, (b) frequency spectrum of complete force time history, (c) at ice velocity ~90 mm/s, (d) frequency spectrum at ice velocity ~90 mm/s, (e) at ice velocity ~200 mm/s and (f) frequency spectrum at ice velocity ~200 mm/s.

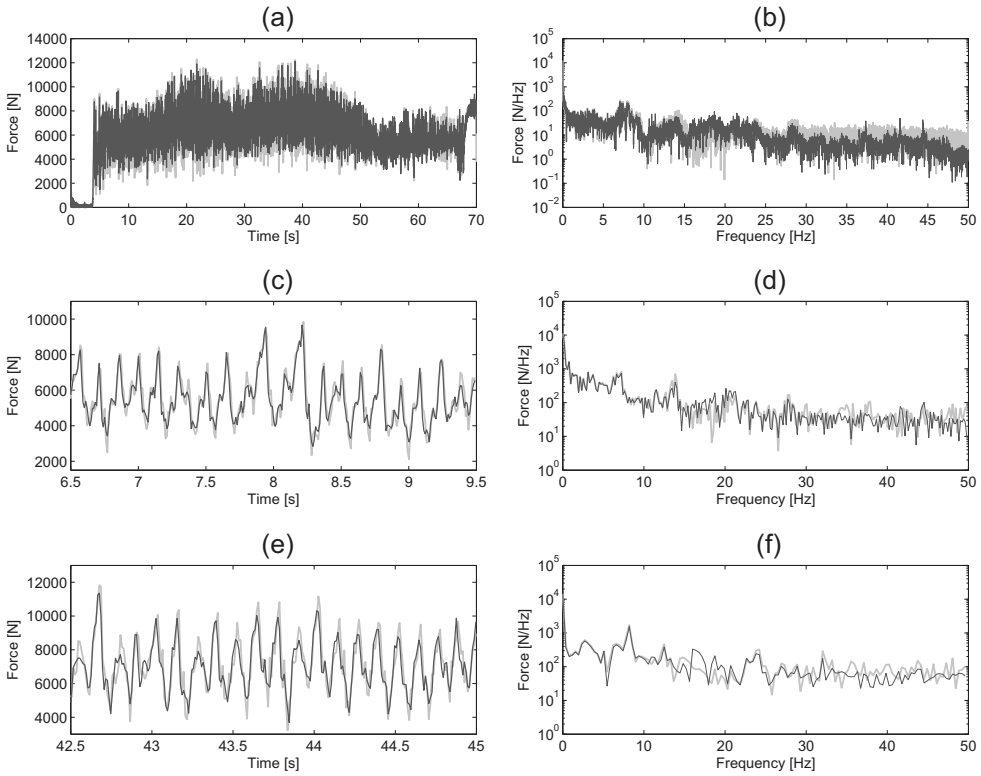

Fig. 9. Identified force (light grey) versus reference force (black) for: (a) complete force time history, (b) frequency spectrum of complete force time history, (c) at ice velocity ~90 mm/s, (d) frequency spectrum at ice velocity ~90 mm/s, (e) at ice velocity ~200 mm/s and (f) frequency spectrum at ice velocity ~200 mm/s.

ice velocities at ~90 mm/s and ~200 mm/s. The algorithm and the blueprint model capture the dominant force peaks at ice velocity of ~90 mm/s (Fig. 8(c)). The difference is primarily attributed to the frequencies above the first natural frequency (Fig. 8(d)), whereas the reconstruction up to 10.2 Hz is excellent. At ~200 mm/s, the identified force (Fig. 8(e)) deviates somewhat more from the reference force. Still, the frequencies with the most energy (below 10.2 Hz) correlate well with the reference force (Fig. 8(f)).

5.5.2. Tuned model

From the full force time history (Fig. 9(a)) and the corresponding Fourier amplitudes (Fig. 9(b)), it is difficult to point out distinct improvements compared to the results obtained using the blueprint model (cf. Fig. 8(a) and (b)). The identified force at ~90 mm/s (Fig. 9(c)) appears almost identical to the one using the blueprint model (cf. Fig. 8(c)), while a slightly more pronounced discrepancy is still seen at ~200 mm/s (Fig. 9(e)). While an accurate reconstruction was obtained up to 10.2 Hz using the blueprint model, Fig. 9(d) and (f) shows that the forces are identified with the same accuracy up to 13 Hz using the tuned model.

5.6. Response estimation test 3300

5.6.1. Blueprint model

Fig. 10(a) shows that the identified displacement is overestimated compared to the measured displacement throughout the test. The estimated dominant response frequencies, however, are well correlated with the measured response (Fig. 10(b)). At ~90 mm/s (Fig. 10(c)) the average offset for the peaks is 2.41 mm, while at ~200 mm/s (Fig. 10(d)) the average offset is 4.16 mm. This significant difference in the two offsets means that the response estimation becomes more prone to modelling errors at higher ice velocities. At higher velocities the influence of higher modes in the response increases. Similar structural response has been reported by Määttänen (1983), who also observed that the response changed from first to second vibration mode when the ice velocity increased. The corresponding Fourier amplitudes in Fig. 10(d) and (f) show that the dominant frequency components are successfully captured, despite the modelling errors.

5.6.2. Tuned model

The tuned model and the joint input-state algorithm predict the displacement to be almost identical to the measured displacement throughout the displacement time history (Fig. 11(a) and (b)). The offset is below 1 mm at ~ 90 mm/s (Fig. 11(c)), capturing both the first and second mode with high precision (Fig. 11(d)). At ~200 mm/s (Fig. 11(e)) the discrepancy is still limited to 1 mm, and an excellent reconstruction of both the first and second mode is obtained (Fig. 11(f)).

The response prediction results in test 4300 and 3300 show that information about the first natural frequency and simple tuning of the model significantly improves the reconstruction. This precision is found to be maintained both when the ice sheet is moving with constant velocity intervals (4300), and when the ice sheet is accelerating towards the structure (3300). Because the predicted states can be extracted at any desired nodal location, the algorithm can be used to reconstruct displacements and velocities, for instance, at the ice-action point.

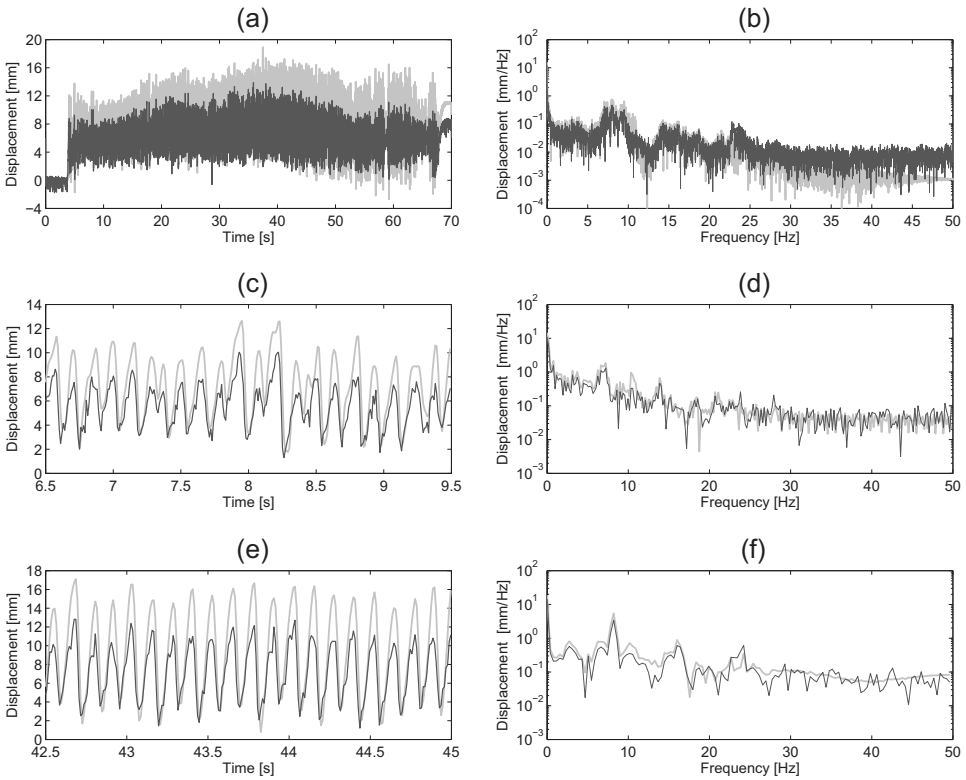

Fig. 10. Estimated (light grey) versus measured (black) displacement during: (a) complete displacement time history, (b) frequency spectrum of complete displacement time history, (c) at ice velocity ~90 mm/s, (d) frequency spectrum at ice velocity ~90 mm/s, (e) at ice velocity ~200 mm/s and (f) frequency spectrum at ice velocity ~200 mm/s.

5.7. Application to full-scale structures

Ice forces have excited various types of extensively instrumented full-scale structures, making them interesting for force identification. The laboratory results have shown that ice forces can be well identified by the joint input-state estimator even in situations where the model properties are uncertain. The algorithm is generic in the sense that it can be applied to any structure described by a state-space model, where the state-space matrices can be constructed based on a FE model or experimentally identified. Being a model-based identification technique, the force estimation accuracy depends, however, on sufficient model details. For application on full-scale structures where a) larger modelling errors are often unavoidable and b) the local ice action point (s) may be inexact or unknown, the algorithm can be used to identify a set of equivalent forces acting at arbitrary positions. These forces will then be sufficient to accurately estimate the dynamic response of the structure to the ice forces at all (unmeasured) locations, even in the presence of modelling errors. This response predictive ability of the algorithm has been validated by Lourens et al. (2012a) using data from an in situ experiment on a footbridge. On wide structures such as the Molikpaq (Jefferies and Wright (1988)), for instance, the local ice-action point (s) may be inexact or unknown and the model may contain inaccuracies. Instead of identifying the local forces, the algorithm can then be applied to identify the total dynamic force on the structure, as well as its response to this force at all unmeasured locations (e.g. strains at locations vulnerable to fatigue).

6. Conclusions

The ice forces acting on a generic bottom-founded offshore structure have successfully been identified in conjunction with the states, using a joint input-state algorithm and a limited number of response measurements. The ice forces are well reconstructed in two important regimes governing the dynamic ice-structure interaction: the intermittent and continuous brittle crushing regimes. Convincing accuracy is maintained, regardless of whether the ice velocity is increased stepwise or with constant acceleration. Simple tuning of the model support stiffness improved the estimated response. The results shown in this contribution provide a strong motivation for online monitoring of full-scale structures in the Arctic region.

Acknowledgements

The authors wish to acknowledge the support of the Research Council of Norway (203471) through the Centre for Research-based Innovation SAMCoT, and the support of all SAMCoT partners. The work described in this paper was supported by the European Community's 7th Framework Program through a grant to the budget of the Integrated Infrastructure Initiative HYDRALAB-IV, Contract no. 261520. The authors would like to thank the Hamburg Ship Model Basin (HSVA), especially the ice tank crew, for the hospitality, technical and scientific support and the professional execution of the test program in the Research Infrastructure ARCTECLAB. In addition, the authors are grateful for the Finite Element support from Associate Professor Bjørn Haugen

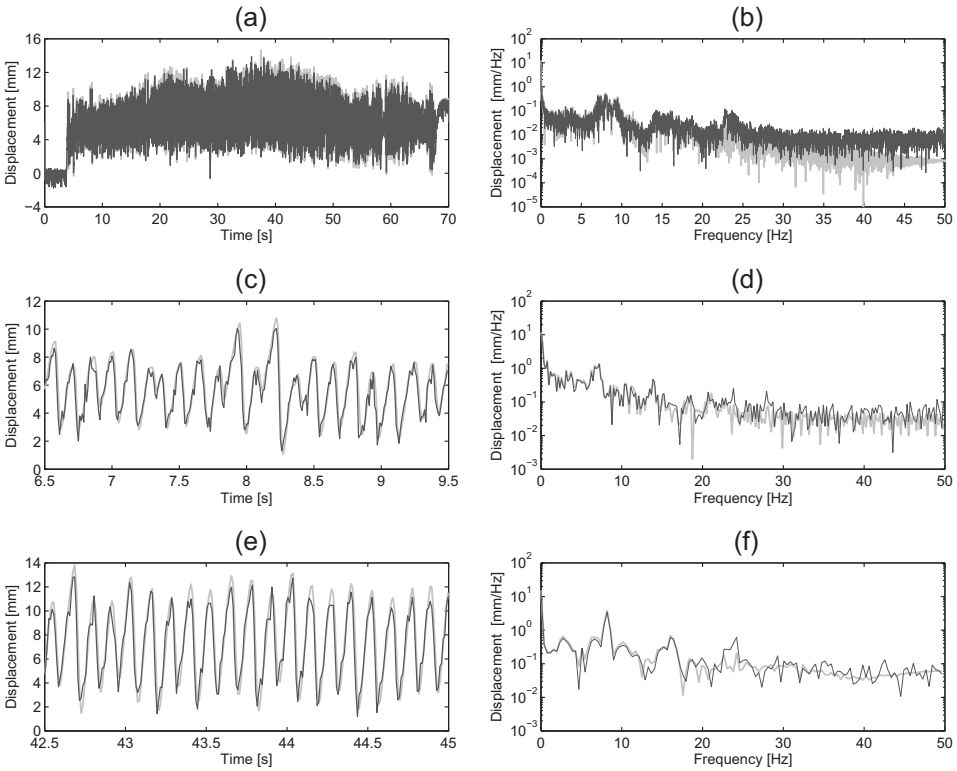

Fig. 11. Estimated (light grey) versus measured (black) displacement during: (a) complete displacement time history, (b) frequency spectrum of complete displacement time history, (c) at ice velocity ~90 mm/s, (d) frequency spectrum at ice velocity ~90 mm/s, (e) at ice velocity ~200 mm/s and (f) frequency spectrum at ice velocity ~200 mm/s.

at the Department of Engineering Design and Materials at the Norwegian University of Science and Technology.

References

Barker, A., Timco, G., Gravesen, H., Vølund, P., 2005. Ice loading on Danish wind turbines: Part 1: dynamic model tests. Cold Reg. Sci. Technol. 41 (1), 1–23.

Bell, K., 2013. An engineering approach to finite element analysis of linear structural mechanics problems. Akademika Publ. (Trondheim, XIX, 656 s.: ill. pp.).

Bjerkås, M., 2006. Ice action on offshore structures. (PhD Thesis), NTNU 82-471-7756-0 (173 pp.).

Evers, K.-U., Jochmann, P., 1993. An advanced technique to improve the mechanical properties of model ice developed at the HSVA ice tank. Port and Ocean Engineering under Arctic Conditions, Hamburg, Germany, pp. 877–888.

Ewins, D.J., 2000. Modal Testing: Theory, Practice and Application. Second edition.

Fabumni, J.A., 1986. Effects of structural modes on vibratory force determination by the pseudoinverse technique. AIAA J. 24 (3), 504–509.

Frederking, R., Haynes, F.D., Hodgson, T.P., Sayed, M., 1986. Static and Dynamic Ice Loads On The Yamachiche Lightpier, 1984–1986. 8th International Symposium on Ice. IAHR, Iowa, USA, pp. 115–126.

Frederking, R., Masterson, D., Wright, B., Spencer, P., 2002. Ice Load Measuring Panels—The Next Generation. IAHR, New Zealand, pp. 450–457.

Gillijns, S., De Moor, B., 2007. Unbiased minimum-variance input and state estimation for linear discrete-time systems with direct feedthrough. Automatica 43 (5), 934–937.

Hendrikse, H., Metrikine, A., Evers, K.-U., 2012. A method to measure the added mass and added damping in dynamic ice-structure interaction. Ice Research for a Sustainable Environment. IAHR, Dalian, China.

Hollandsworth, P.E., Busby, H.R., 1989. Impact force identification using the general inverse technique. Int. J. Impact Eng. 8 (4), 315–322.

Jefferies, M.G., Wright, W.H., 1988. Dynamic Response OF "MOLIQPAQ" to ice–structure interaction. Proc. 7th International conference on Offshore Mechanics and Arctic Engineering (OMAE 88), Houston, Texas, United States, pp. 201–220.

Jefferies, M., Rogers, B., Hardy, M., Wright, B., 2011. Ice Load Measurement on Molikpaq: Methodology and Accuracy. Port and Ocean Engineering under Arctic Conditions, Montréal, Canada.

Jordaan, I.J., 2001. Mechanics of ice–structure interaction. Eng. Fract. Mech. 68 (17–18), 1923–1960.

Lourens, E., 2012. Force identification in structural dynamics. (PhD Thesis). KU Leuven ISBN 978-94-6018-522-9.

Lourens, E., Papadimitriou, C., Gillijns, S., Reynders, E., De Roeck, G., Lombaert, G., 2012a. Joint input-response estimation for structural systems based on reduced-order models and vibration data from a limited number of sensors. Mech. Syst. Signal Process. 29, 310–327.

Lourens, E., Reynders, E., De Roeck, G., Degrande, G., Lombaert, G., 2012b. An augmented Kalman filter for force identification in structural dynamics. Mech. Syst. Signal Process. 27, 446–460.

Määttänen, M., 1982. True ice force by deconvolution. 1st International Modal Analysis Conference (IMAC), Orlando, FL, USA, pp. 556–590.

Määttänen, M., 1983. Dynamic ice–structure interaction during continuous crushing. CRREL Reportpp. 83–85.

Määttänen, M., Marjavaara, P., Saarinen, S., Laakso, M., 2011. Ice crushing tests with variable structural flexibility. Cold Reg. Sci. Technol. 67 (3), 120–128.

Määttänen, M., Løset, S., Metrikine, A., Evers, K.-U., Hendrikse, H., Lønøy, C., Metrikin, I., Nord, T.S., Sukhorukov, S., 2012. Novel ice induced vibration testing in a large-scale facility. Ice Research for a Sustainable Environment. IAHR, Dalian, China.

Maes, K., Lourens, E., Van Nimmen, K., Reynders, E., De Roeck, G., Lombaert, G., 2015. Design of sensor networks for instantaneous inversion of modally reduced order models in structural dynamics. Mech. Syst. Signal Process. 52–53, 628–644.

Montgomery, C.J., Lipsett, A.W., 1981. Estimation of Ice Forces from Dynamic Response. International Symposium on Ice (IAHR), Quebec, P.Q. Canada, pp. 771–782.

Niu, Y., Klinkov, M., Fritzen, C.-P., 2011. Online force reconstruction using an unknown-input Kalman filter approach. International Conference on Structural Dynamics, Eurodyn 2011, Leuven, Belgium, pp. 2569–2576.

Nord, T.S., Määttänen, M., 2012. Modal analysis in ice structure interaction. 21st International Symposium on Ice. IAHR, Dalian, China.

Nord, T.S., Määttänen, M., Øiseth, O., 2013. Frequency domain force identification in ice–structure interaction. The proceedings of the 22nd International Conference on Port and Ocean Engineering under Arctic Conditions (POAC), Espoo, Finland.

Peyton, H.R., 1966. Sea Ice Strength, Office of Naval Research. Report UAG-182 from Geophysical Institute. University of Alaska.
Singh, S.K., Timco, G.W., Frederking, R., Jordaan, I.J., 1990. Tests of Ice Crushing on a Flexible Structure. OMAE, Houston TX. USA, pp. 89–94.
Sodhi, D.S., 2001. Crushing failure during ice–structure interaction. Eng. Fract. Mech. 68 (17–18), 1889–1921.
Spencer, P., 2013. A review of the MEDOF panels installed on the Molikpaq structure in the Canadian Beaufort sea. International Conference on Port and Ocean Engineering under Arctic Conditions (POAC), Espoo, Finland.
Timco, G.W., Frederking, R., Singh, S.K., 1989. The Transfer Function Approach for A Structure Subjected to Ice Crushing. POAC, Luleå, Sweden, pp. 420–430.

Appendix 3 Laboratory experiments to study ice-induced vibrations of scaled model structures during their interactions with level ice at different ice velocities

This appendix includes the paper published in the Journal of Cold Regions Science and Technology (see below).

- Nord, T.S., Lourens, E.-M., Määttänen, M., Øiseth, O. and Høyland, K.V., 2015. Laboratory experiments to study ice-induced vibrations of scaled model structures during their interactions with level ice at different ice velocities Cold Regions Science and Technology(119) :pp.1-15

Cold Regions Science and Technology 119 (2015) 1–15

Contents lists available at ScienceDirect

Cold Regions Science and Technology

journal homepage: www.elsevier.com/locate/coldregions

Laboratory experiments to study ice-induced vibrations of scaled model structures during their interaction with level ice at different ice velocities

Torodd S. Nord [a,b,*], Eliz-Mari Lourens [c], Mauri Määttänen [a], Ole Øiseth [d], Knut V. Høyland [a]

[a] Sustainable Arctic Marine and Coastal Technology (SAMCoT), Centre for Research-based Innovation (CRI), Norwegian University of Science and Technology, Trondheim, Norway
[b] The University Centre in Svalbard (UNIS), Longyearbyen, Spitsbergen, Norway
[c] Faculty of Civil Engineering and Geosciences, Delft University of Technology, Delft, the Netherlands
[d] Department of Structural Engineering, Norwegian University of Science and Technology, Trondheim, Norway

ARTICLE INFO

Article history:
Received 12 November 2014
Received in revised form 14 May 2015
Accepted 29 June 2015
Available online 4 July 2015

Keywords:
Ice-induced vibrations
Model-scale testing
Force and response characteristics
Contact-zone characteristics
Ice crushing

ABSTRACT

A simplified model of a typical bottom-founded structure was forced through ice sheets in a laboratory experiment to study ice-induced vibrations. The ice forces exerted on the structure are identified in conjunction with the response of the entire structure using a joint input-state estimation algorithm. Novel insights into ice-induced vibration phenomena are obtained by comparing, on different time scales, measured and estimated response quantities and forces/pressures. First, the identified forces, ice velocities and time-frequency maps of the measured responses are presented for a series of ice-induced vibration tests. It is shown that the ice forces excite more than one mode of the structure and that the transition ice velocity at which the vibrations shift from the first to the second mode increases with reduced foundation stiffness and reduced superstructure mass. Second, a detailed analysis of the interaction between the structure and the ice edge is performed on a smaller time scale by comparing the locally measured pressures at the ice-structure interface to the identified structural responses and forces. It is shown that structural vibrations at a frequency higher than the dominant vibration frequency cause cyclic loading of the ice edge during intermittent crushing. These vibrations led to an increasing loading rate prior to ice failure. During an event that shows the tendencies of frequency lock-in vibrations, the structural response was dominated by a single vibration frequency.

1. Introduction

Ice crushing on bottom-founded structures may induce severe vibrations, potentially threatening operational reliability and structural integrity. Over the past 50 years, considerable effort has been spent on investigating the phenomenon of ice-induced vibrations. The physics remains, however, not yet fully understood.

The characteristics of the ice crushing forces differ depending on the structural compliance and velocity of the ice (Sodhi and Haehnel, 2003). As ice-induced vibrations are determined by the crushing failure, different laboratory studies have been performed to explain the crushing failure in relation to ice-induced vibrations; see e.g., Määttänen (Määttänen, 1979; Määttänen et al., 2012), Kärnä (Kärnä, 1995; Kärnä et al., 2003a, 2003b), Toyama et al. (1983), Sodhi (2001), Gravesen et al. (2005), Barker et al. (2005) and Huang et al. (2007).

At low ice velocities and with the interaction governed by intermittent crushing, the dominant vibration frequency was found to be proportional to the structural stiffness (Browne et al., 2013; Määttänen, 1975; Nakazawa and Sodhi, 1990). At higher velocities, the dominant vibration frequency tends towards one of the natural frequencies, and lock-in vibrations may occur. Single degree of freedom (SDOF)-oscillators have dominated the research in laboratory experiments in recent decades. In principle, ice forces may excite all modes of a structure depending on the location of the ice-action point and the frequency content of the ice forces. Määttänen measured a great contribution of the second mode both in full scale (Määttänen, 1975) and laboratory experiments (Määttänen, 1983), revealing that it is inadequate to consider only the first mode. A limited number of studies have subsequently been published on bottom-founded multi degree of freedom (MDOF) laboratory structures; see e.g. Kärnä et al. (2003a).

The discovery of the line-like contact (Joensuu and Riska, 1988) brought a new dimension to the fundamentals of ice crushing and drew more attention towards the ice–structure interface. When the ice failed by brittle flaking against a transparent plate, they saw a narrow band of contact spots across the indenter width, the “line-like” contact. During experiments on a flexible structure, Sodhi (2001)

* Corresponding author at: Sustainable Arctic Marine and Coastal Technology (SAMCoT), Centre for Research-based Innovation (CRI), Norwegian University of Science and Technology, Trondheim, Norway.
E-mail address: torodd.nord@ntnu.no (T.S. Nord).

http://dx.doi.org/10.1016/j.coldregions.2015.06.017
0165-232X/

showed that the local pressures grew simultaneously during the load build-up at low indentation speeds. At the onset of ice failure, the indentation speed increased by two orders of magnitude, and the pressure changed progressively during the ice failure. Recent small-scale indentation experiments by Wells et al. (2011), Taylor et al. (2013) and Browne et al. (2013) also link the ice force and failure characteristics to the pressure. The latter associated failures of high pressure zones to measured cyclic force patterns up to a frequency as high as 250 Hz. For a literature review on crushing failure and the ice behavior adjacent to the indenter, see Jordaan (2001), Sodhi (2001), Sodhi et al. (1998) and Wells et al. (2011).

In this contribution, we use a novel approach to elucidate the influence of the structural state on ice-induced vibrations. Using a set of response measurements, linear filtering theory is applied to estimate the interaction. Both the states and the forces are treated as unknowns and jointly estimated using a finite element model and a joint input-state estimation algorithm (Gillijns and De Moor, 2007). This algorithm has been modified (Lourens et al., 2012) for application to reduced-order models, where the modification enabled force and state estimation also when the number of forces and/or response measurements exceeded the number of structural modes used to construct the model. The algorithm requires no prior assumptions on the dynamic evolution of the forces, allows for uncertainty in the model equations as well as the measurements, and requires only a limited number of response measurements. The estimated states and forces are optimal in the sense that they are linear minimum-variance unbiased estimates. Recently Nord et al. (2015) applied the original algorithm (Gillijns and De Moor, 2007) to ice-induced vibrations. They demonstrated that the force and response estimates were of acceptable accuracy when information about the first natural frequency was accessible. The computational effort is significantly reduced with the reduced-order models, allowing real-time estimation of the forces and states, a great advantage for monitoring also full-scale arctic structures. While Nord et al. (2015) demonstrated that the framework was applicable to ice force identification, this paper further utilizes the advantage of simultaneous force and response identification to explain how the structural motion affects the ice pressure at the indenter.

In what follows, the identified forces, velocities, and time-frequency maps of the responses of the Deciphering Ice-Induced Vibrations (DIIV) test campaign are presented first. Secondly, the interaction during two different ice-induced vibration regimes is studied in detail by means of the jointly estimated response and ice force in combination with the measured local pressures acting on a cylindrical indenter. When these data are presented together, they provide novel insights into the influence of the modal contributions on the ice–structure interface.

2. Dual force and state estimation

2.1. System equations

The force is treated as an unknown concentrated load acting on a linear time-invariant structure that is represented by a finite element model consisting of a limited number of structural modes:

$$\ddot{\mathbf{z}}(t) + \mathbf{\Gamma}\,\dot{\mathbf{z}}\,(t) + \mathbf{\Omega}^2\mathbf{z}(t) = \mathbf{\Phi}^{\mathrm{T}}\mathbf{S}_p\mathbf{p}(t) \tag{1}$$

where $\mathbf{z}(t) \in \mathbb{R}^{n_m}$ is the vector of modal coordinates and n_m the number of modes used to assemble the model. The excitation vector $\mathbf{p}(t) \in \mathbb{R}^{n_p}$ is specified to act on the desired locations through the force influence matrix $\mathbf{S}_p \in \mathbb{R}^{n_{DOF} \times n_p}$, where n_p is the number of force time histories and n_{DOF} is the number of degrees of freedom. $\mathbf{\Gamma} \in \mathbb{R}^{n_m \times n_m}$ is the diagonal damping matrix populated on the diagonal with the terms $2\xi_j\omega_j$ where ω_j and ξ_j are the natural frequency in rad s^{-1} and damping ratio corresponding to mode j, respectively. $\mathbf{\Omega} \in \mathbb{R}^{n_m \times n_m}$ is a diagonal matrix containing the natural frequencies ω_j and $\mathbf{\Phi} \in \mathbb{R}^{n_{DOF} \times n_m}$ is a matrix collecting the mass-normalized mode shapes.

2.2. State-space model

The continuous-time state vector $\mathbf{x}(t) \in \mathbb{R}^{n_s}$, $n_s = 2n_m$ is defined as follows:

$$\mathbf{x}(t) = \begin{pmatrix} \mathbf{z}(t) \\ \dot{\mathbf{z}}(t) \end{pmatrix} \tag{2}$$

whereby the equation of motion of second order in Eq. (1) can be organized as a first-order continuous-time state equation

$$\dot{\mathbf{x}}(t) = \mathbf{A}_c\mathbf{x}(t) + \mathbf{B}_c\mathbf{p}(t) \tag{3}$$

where the system matrices $\mathbf{A}_c \in \mathbb{R}^{n_s \times n_s}$ and $\mathbf{B}_c \in \mathbb{R}^{n_s \times n_p}$ are defined as

$$\mathbf{A}_c = \begin{bmatrix} \mathbf{0} & \mathbf{I} \\ -\mathbf{\Omega}^2 & -\mathbf{\Gamma} \end{bmatrix}, \mathbf{B}_c = \begin{bmatrix} \mathbf{0} \\ \mathbf{\Phi}^{\mathrm{T}}\mathbf{S}_p \end{bmatrix}. \tag{4}$$

The measurements are arranged in a data vector $\mathbf{d}(t) \in \mathbb{R}^{n_d}$, in which the observations can be a linear combination of displacement, velocity and acceleration, with n_d the number of data measurements. The data vector is constructed as follows:

$$\mathbf{d}(t) = \mathbf{S}_a\mathbf{\Phi}\,\ddot{\mathbf{z}}(t) + \mathbf{S}_v\mathbf{\Phi}\;\;\dot{\mathbf{z}}\,(t) + \mathbf{S}_d\mathbf{\Phi}\;\;\mathbf{z}(t) \tag{5}$$

where the selection matrices $\mathbf{S}_a$, $\mathbf{S}_v$ and $\mathbf{S}_d \in \mathbb{R}^{n_d \times n_{DOF}}$ are populated according to the spatial location at which acceleration, velocity, displacement and/or strain are measured. Eq. (5) can be transformed into state-space form using Eqs. (1) and (2):

$$\mathbf{d}(t) = \mathbf{G}_c\mathbf{x}(t) + \mathbf{J}_c\mathbf{p}(t) \tag{6}$$

where the matrices $\mathbf{G}_c \in \mathbb{R}^{n_d \times n_s}$ and $\mathbf{J}_c \in \mathbb{R}^{n_d \times n_p}$ represent the output influence matrix and direct transmission matrix, respectively, defined as follows:

$$\begin{aligned} \mathbf{G}_c &= \begin{bmatrix} \mathbf{S}_d\mathbf{\Phi} - \mathbf{S}_a\mathbf{\Phi}\mathbf{\Omega}^2 & \mathbf{S}_v\mathbf{\Phi} - \mathbf{S}_a\mathbf{\Phi}\mathbf{\Gamma} \end{bmatrix} \\ \mathbf{J}_c &= \begin{bmatrix} \mathbf{S}_a\mathbf{\Phi}\mathbf{\Phi}^{\mathrm{T}}\mathbf{S}_p \end{bmatrix}. \end{aligned} \tag{7}$$

In discrete time under a zero-order hold assumption and given a sampling rate of $1/\Delta t$, Eqs. (3) and (6) become:

$$\mathbf{x}_{k+1} = \mathbf{A}\mathbf{x}_k + \mathbf{B}\mathbf{p}_k \tag{8}$$

$$\mathbf{d}_k = \mathbf{G}\mathbf{x}_k + \mathbf{J}\mathbf{p}_k \tag{9}$$

where

$$\mathbf{x}_k = \mathbf{x}(k\Delta t),\ \mathbf{d}_k = \mathbf{d}(k\Delta t),\ \mathbf{p}_k = \mathbf{p}(k\Delta t),\ k = 1, \ldots, N$$

and

$$\mathbf{A} = e^{\mathbf{A}_c\Delta t},\ \mathbf{B} = [\mathbf{A} - \mathbf{I}]\mathbf{A}_c^{-1}\mathbf{B}_c$$

$$\mathbf{G}_c = \mathbf{G},\ \mathbf{J}_c = \mathbf{J}.$$

2.3. Joint input-state (JIS) estimation algorithm

Assuming that the system matrices are known, the joint input-state estimation algorithm can be used to jointly estimate the forces and states from a limited number of response measurements. By introducing the random variables $\mathbf{w}_k$ and $\mathbf{v}_k$, which represent the stochastic system and measurement noise, respectively, the discrete-time state-space equations become the following:

$$\mathbf{x}_{k+1} = \mathbf{A}\mathbf{x}_k + \mathbf{B}\mathbf{p}_k + \mathbf{w}_k \tag{10}$$

$$\mathbf{d}_k = \mathbf{G}\mathbf{x}_k + \mathbf{J}\mathbf{p}_k + \mathbf{v}_k \tag{11}$$

where it is assumed that the vectors $\mathbf{w}_k$ and $\mathbf{v}_k$ are mutually uncorrelated, zero-mean, white-noise signals with known covariance matrices $\mathbf{Q} = E\{\mathbf{w}_k\mathbf{w}_k^T\}$ and $\mathbf{R} = E\{\mathbf{v}_k\mathbf{v}_k^T\}$. The algorithm predicts the forces and states in three steps: the unbiased minimum-variance (MVU) input estimation, the measurement update, and the time update. The first step calculates an optimal estimate of the force $\hat{\mathbf{p}}_{k|k}$ based on assumed covariances for the measurement errors, the system model, and the estimated states. The second step (measurement update) calculates a MVU state estimate $\hat{\mathbf{x}}_{k|k}$ using the measured data $\mathbf{d}_k$ and the gain matrix $\mathbf{L}_k$ from Eq. (16), where the gain is dependent on assumed state error covariances. Apart from the fact that the force is an estimated vector and not known, this step is the same as in the classical Kalman filter. In the final step, the state of the system is advanced in time using the system model. For more details on the derivation of this recursive algorithm, see Gillijns and De Moor (2007).

Input estimation:

$$\tilde{\mathbf{R}}_k = \mathbf{G}\mathbf{P}_{k|k-1}\mathbf{G}^T + \mathbf{R} \tag{12}$$

$$\mathbf{M}_k = \left(\mathbf{J}^T\tilde{\mathbf{R}}_k^{-1}\mathbf{J}\right)^{-1}\mathbf{J}^T\tilde{\mathbf{R}}_k^{-1} \tag{13}$$

$$\hat{\mathbf{p}}_{k|k} = \mathbf{M}_k\left(\mathbf{d}_k - \mathbf{G}\hat{\mathbf{x}}_{k|k-1}\right) \tag{14}$$

$$\mathbf{P}_{p[k|k]} = \left(\mathbf{J}^T\tilde{\mathbf{R}}_k^{-1}\mathbf{J}\right)^{-1}. \tag{15}$$

Measurement update:

$$\mathbf{L}_k = \mathbf{P}_{k|k-1}\mathbf{G}^T\tilde{\mathbf{R}}_k^{-1} \tag{16}$$

$$\hat{\mathbf{x}}_{k|k} = \hat{\mathbf{x}}_{k|k-1} + \mathbf{L}_k\left(\mathbf{d}_k - \mathbf{G}\hat{\mathbf{x}}_{k|k-1} - \mathbf{J}\hat{\mathbf{p}}_{k|k}\right) \tag{17}$$

$$\mathbf{P}_{k|k} = \mathbf{P}_{k|k-1} - \mathbf{L}_k\left(\tilde{\mathbf{R}}_k - \mathbf{J}\ \mathbf{P}_{p[k|k]}\mathbf{J}^T\right)\mathbf{L}_k^T \tag{18}$$

$$\mathbf{P}_{xp[k|k]} = \mathbf{P}_{px[k|k]}^T = -\mathbf{L}_k\mathbf{J}\ \mathbf{P}_{p[k|k]}. \tag{19}$$

Time update:

$$\hat{\mathbf{x}}_{k+1|k} = \mathbf{A}\hat{\mathbf{x}}_{k|k} + \mathbf{B}\hat{\mathbf{p}}_{k|k} \tag{20}$$

$$\mathbf{P}_{k+1|k} = [\mathbf{A}\quad\mathbf{B}]\begin{bmatrix}\mathbf{P}_{k|k} & \mathbf{P}_{xp[k|k]}\\ \mathbf{P}_{px[k|k]} & \mathbf{P}_{p[k|k]}\end{bmatrix}\begin{bmatrix}\mathbf{A}^T\\ \mathbf{B}^T\end{bmatrix} + \mathbf{Q}. \tag{21}$$

3. Ice-induced vibrations, experimental

The Deciphering Ice-Induced Vibrations (EU-HYDRALAB DIIV) test campaign was conducted at the HSVA large ice-tank facility in Hamburg, Germany (Hendrikse et al., 2012; Määttänen et al., 2012; Nord and Määttänen, 2012).

3.1. Test structure

The structure (Fig. 1) was designed to have a scale ratio of 1:8–1:10 with respect to a typical bottom-founded offshore structure. The structure was scaled to achieve modal similitude, meaning that the natural modes of the laboratory structure resembled the full-scale natural modes. This was achieved by scaling the natural frequencies and ensuring that the lowest natural modes were easily excited at the ice-action point. The first natural frequency of bottom-founded structures in the Baltic Sea and Cook Inlet is typically in the range 0.3–4.6 Hz (Blenkarn, 1970; Määttänen, 2008; Neill, 1976). Additional details about the dynamic scaling for this particular test setup can be found in Määttänen et al. (2012). The intention was also to construct a system that allowed

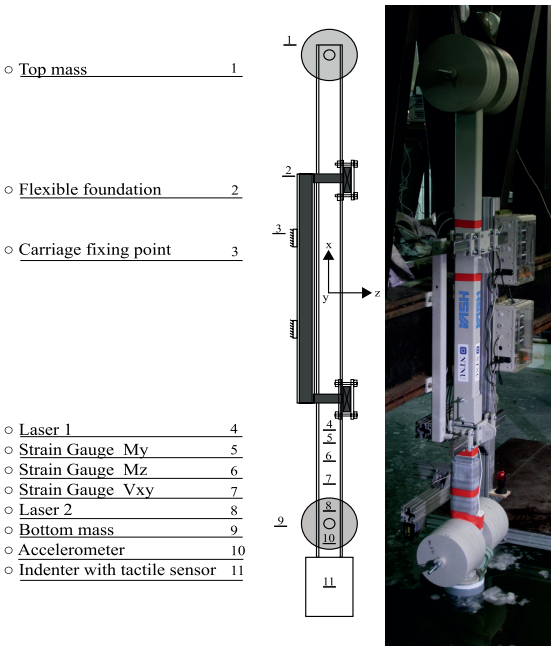

Fig. 1. Test structure overview and sensor locations.

the frequency of vibration to change from the first to the second natural frequency with increasing ice velocity.

To create a flexible structure, the main beam was supported by two leaf springs attached to two vertical support beams. The flexibility of the system could then be adjusted by changing the spacing between the vertical supports. To further tune the system toward the desired natural frequencies, disc weights could be added to the bottom and top of the structure. The bracings and joints were designed to retain low internal friction to avoid nonlinearities and maintain low structural damping. At the location of the ice action, a cylindrical indenter with a diameter of 220 mm was attached to the main shaft. The elastic modes in the test rig consist of both the main shaft bending and support fixture spring action (Fig. 2). The support was fixed to a 50 ton carriage, housing also the data logging system. A set of different velocities, ice thicknesses, temperatures and structural configurations (adjustable mass and stiffness) provided a range of data sets for comparison.

3.2. Sensor types, positions, and data acquisition

One accelerometer, two lasers and three fully active strain gauge bridges were installed to measure the response at locations on the lower part of the structure, as shown in Fig. 1. Dynamic calibration tests were conducted to obtain the static and dynamic properties of the structure, see Nord et al. (2015) for further details. At the waterline, a Tecscan tactile sensor 5530 was installed to measure the normal pressures at the interface between the cylindrical indenter and the ice edge. The sensor was glued around the edges with silicon (Fig. 3a), both on the cylinder and the inside of the 0.5 mm thick aluminum film protecting the sensor (Fig. 3b). The sensor had 2288 sensels inside the 416 mm width and 157 mm height. It covered a 216 degree angle, enabling the full contact to be measured. Prior experience with this instrumentation ensured that the local pressures were not smeared out beyond the sensel area (Määttänen et al., 2011). Brackets on the backside of the indenter were used to distribute the pressure (Fig. 3c). A

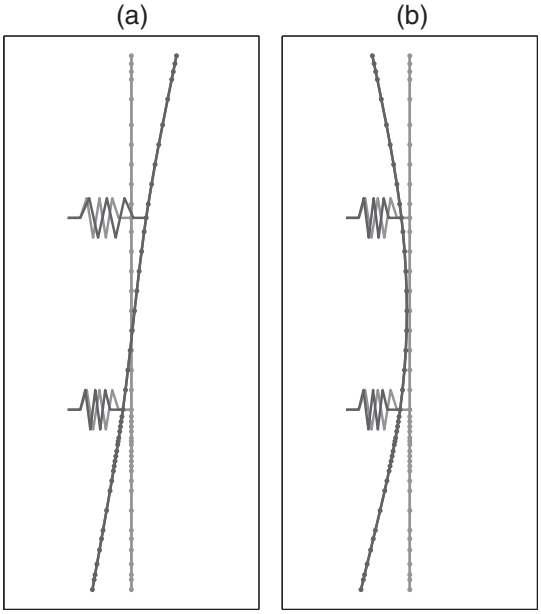

Fig. 2. Finite element vibration modes: a) mode 1; b) mode 2.

sampling rate of 100 Hz was applied to all channels, both during the dynamic calibration and ice action.

3.3. Ice properties

The tests were conducted in the 78 m long, 10 m wide HSVA Large Ice Tank. The water depth was 2.5 m with a deep section of 5 m at the end of the basin (10 × 12 m). Columnar-grained level ice sheets were produced in NaCl-doped water (water salinity, 6.8‰) by seeding. During the ice growth process at an air temperature of −22 °C, water saturated with air was charged under high pressure through perforated tubes fixed at the bottom of the ice tank. When the pressure dropped, tiny air bubbles with diameters of 200–500 μm rose upwards and were embedded in the growing ice sheet. Typically, the upper granular layer was more transparent and stronger than the columnar layer (Fig. 4a). Vertical (Fig. 4b) and horizontal (Fig. 4c) thin sections of the model ice under polarized light showed the columnar crystal structure. After the ice growth phase, the ice tank air temperature was raised to reduce the ice strength sufficiently for the ice force to remain below the structural load capacity while simultaneously attempting to achieve stress-rate similitude. Several issues related to the scaling of ice properties were demonstrated by Määttänen (1979) and further discussed by Timco (1984). When the structure is scaled with modal similitude as described in Section 3.1, it follows from Määttänen (1979) that compromises must be made between having similitude in the in-plane displacements and velocities of the ice sheet, the relative velocity between ice and structure, and the stress rate in the ice adjacent to the indenter. He showed that that only similitude in the stress rate was practically achievable when the ice strength was scaled. Because the HSVA ice has lower ice strength and Young's modulus as compared to sea ice, the stress rate similitude was attempted, but not fully achieved due to too low ice strength (see Table 1 for ice strength during the experiments). The ice property scaling is not further discussed in this paper. In every test, ice samples were collected for salinity, density, thin sections and uniaxial compression tests at a strain rate of 10^{-3} s^{-1}. The samples were collected from the sides and middle of the ice sheet every 10 m along its length. Flexural strength tests were also conducted at each site at which samples were collected.

3.4. Testing

In total, four ice sheets were tested (tests 1000–4000). Changing the structural configurations took less than 10 min, which enabled several structural configurations to be tested within one ice sheet. In this paper, we focus on the test-series 3000 and 4000. Test series 1000 and 2000 were considered trial tests and omitted from the analysis. Table 1 shows the configurations for the analyzed data sets. Test series 4000 was performed with slightly thicker, colder and stronger ice than the 3000-test series. The ice edge was formed to the indenter shape by an initial sweep for tests 3100 and 4100, and thus the initial conditions were the same as for the tests 3200 and 3300. An initial wedge shaped crack of approximately 1 m was cut in front of the indenter for test 4300 so that the first ice contact occurred only at the sides of the indenter. The carriage forced the structure through the ice at velocities between 10 mm s^{-1} and 350 mm s^{-1} (Table 1). The carriage velocity is referred to as ice velocity throughout this paper.

4. Ice forces and structural response

4.1. FE model

The FE model of the structure used in this work and the two first natural modes are displayed in Fig. 2 a–b. The structure was modelled as a beam supported by two linear springs. A total of 42 Timoshenko beam elements were used for the hollow-section (RHS120 × 80 × 6) profile main beam, while the additional mass of the structure at discrete locations was represented using lumped masses. The matrices collecting the eigenvectors ($\Phi \in \mathbb{R}^{n_{DOF} \times n_m}$) and natural frequencies ($\Omega \in \mathbb{R}^{n_m \times n_m}$) were constructed from the mass and stiffness matrices that were printed from the FE software. A constant damping ratio of 2% was assigned to each of the in total $n_m = 30$ eigenmodes. The reduced-order state-space matrices were constructed according to Eqs. (4) and (7). Four different finite element models corresponding to the structural

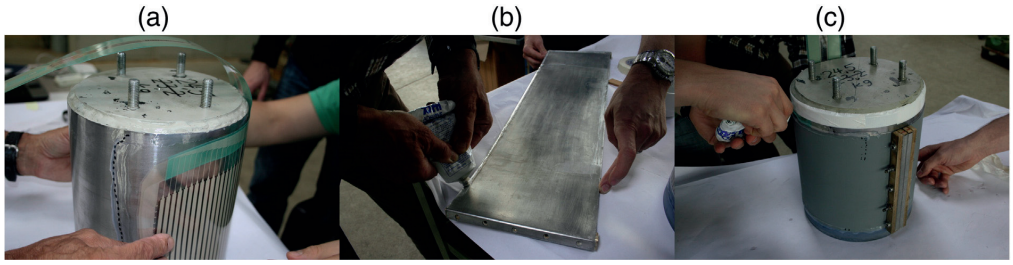

Fig. 3. Tactile sensor installation: a) glue to indenter; b) aluminum film; c) clamping brackets.

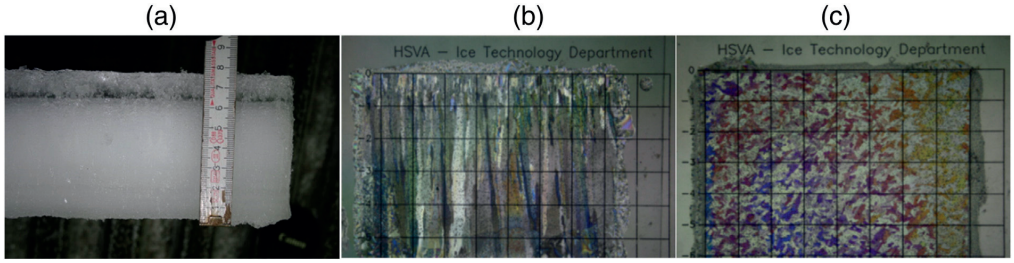

Fig. 4. HSVA ice: a) vertical profile; b) vertical thin section; c) horizontal thin section.

properties in Table 1 were used for the force and state identification. Each of these models was tuned to represent the first natural frequency accurately. The models' leaf spring stiffness was tuned based on the dynamic properties obtained from the dynamic calibrations of the structure. For more details on the finite element model and strain observations, see Nord et al. (2015).

4.2. Force and response

The forces were identified on the basis of one strain gauge and one accelerometer using the joint-input state algorithm and the reduced-order, tuned models of the structure, with the value of 10^{-8} assigned to the diagonals of the covariance matrices **Q**, **R** and $\mathbf{P}_{0|-1}$ (Section 2.3). For further details, see Nord et al. (2015). A moving average was added to the force time-histories to simplify the comparison between forces, responses and ice velocities (Figs. 5–7). A response time-frequency map was obtained using a parametric Burg method on a 500 point moving window, enabling a study of the evolution of the frequency content on the basis of the measured strain gauge response. Note that the Burg spectrum was only used to illustrate the dominant frequency components and has a smoother appearance compared to the Fourier spectrum. Red lines are added on top of the time-frequency map to show the first and second natural frequency of the structure. In what follows, the term *vibration frequency* refers to the strain gauge response (M_y in Fig. 1).

The forces, corresponding strain gauge response maps and ice velocities for tests 3100 and 3200 are shown in Fig. 5a–f. Tests 3100 and 3200 were conducted in the same ice with the same superstructure mass, but with different foundation stiffness. The ice velocity (Fig. 5c) in test 3100 was increased linearly starting from 50 mm s^{-1}. A few cycles of sawtooth brittle failure occurred due to the low ice velocity. The dominant vibration frequency stabilized slightly below the first natural frequency at ~130 mm s^{-1} (Fig. 5b). Between 135 to 185 mm s^{-1}, the state of the structure was in a transition between response in the first and second modes (Fig. 5b). The corresponding force reached a maximum in the same velocity interval. At an ice velocity of ~200 mm s^{-1}, the dominant vibrations were governed by the second mode at a frequency of ~13 Hz, slightly below the second natural frequency.

In Test 3200, the structure initiated contact with the ice at an ice velocity of 130 mm s^{-1} (Fig. 5f). The dominant vibration frequency was slightly below the first natural frequency up to ~175 mm s^{-1}. The transition range from the first to the second vibration mode (Fig. 5e) occurred between 175 and 215 mm s^{-1}. The force (Fig. 5d) increased next to the transition, but the increase was less pronounced than in test 3100 (Fig. 5a–b). When the ice velocity exceeded 245 mm s^{-1}, the force decreased and the dominant vibration frequency (Fig. 5e) became closer to the second natural frequency.

In test 3300, the upper mass was reduced from 240 to 120 kg compared to tests 3100 and 3200. The forces, corresponding strain gauge responses and ice velocities for test 3300 together with 4100 are shown in Fig. 6a–f. Test 3300 covered ice velocities between ~65 mm s^{-1} and ~265 mm s^{-1} (Fig. 6c). The dominant vibration frequencies appeared below the first and second natural frequencies at ice velocities of less than 150 mm s^{-1} (Fig. 6b). When the ice velocity increased, both frequency components displaced toward higher frequencies, observed as small bends in the two dominant frequency trajectories. The second frequency trajectory seems unaffected by the second natural frequency and follows the relation $f = 2f_0$, where f_0 is the first dominant response frequency trajectory. Traces of $f = 3f_0$ are also present, but this super-harmonic is less pronounced than the second. During the intervals in which the frequency bands dislocated, the force level decreased. At ~245 mm s^{-1}, the super-harmonics disappeared, the force decreased, and both the first and second mode were present in the response. The phenomenon of super-harmonics has also been reported in the ice force signals on the JZ20-2-1 platform by Duan et al. (2002). Kärnä et al. (2010) simulated the ice actions on an offshore wind turbine and found super-harmonics in the simulated force signal. They suggested that the super-harmonics appeared because of a small phase shift in the local forces across the interface. It is out of the scope of this paper to further investigate the super-harmonics.

The dominant vibration frequency was at 5 Hz during the first seconds of test 4100 (Fig. 6e) and slowly progressed toward the first natural frequency with increasing ice velocity. Traces of the second mode appeared at less than ~160 mm s^{-1} and greater than ~280 mm s^{-1}. Due to the stronger ice, the force level is higher compared to the 3000-tests. No transition from vibrations in the first to the second mode was found.

Table 1
Test scheme (Test is the test id number, V_{ice} is ice velocity, f_1 is first natural frequency, f_2 is second natural frequency, m_1 is the bottom mass, m_2 is the top mass, S_{spring} is leaf spring support distance, D is indenter diameter, h_{ice} is ice thickness, σ_c is uniaxial compressive ice strength, σ_f is flexural ice strength, T_{ice} is ice temperature and S is ice salinity).

Test	V_{ice}	f_1	f_2	m_1/m_2	S_{spring}	D	h_{ice}	σ_c	σ_f	T_{ice}	S
	[mm s^{-1}]	[Hz]	[Hz]	[kg]	[mm]	[mm]	[mm]	[MPa]	[MPa]	[°C]	[ppt]
3100	50–265	9.4	14.9	120/240	400	220	58	0.17	0.11	−0.8	3.2
3200	130–300	7.8	13.9	120/240	500	220	58	0.17	0.11	−0.8	3.2
3300	65–265	10.2	15.3	120/120	500	220	58	0.17	0.09	−0.8	3.2
4100	100–350	10.4	15.4	120/120	500	220	60	0.40	0.18	−1.7	3.2
4300	10–320	12.2	16.1	120/120	400	220	60	0.40	0.15	−1.7	3.2

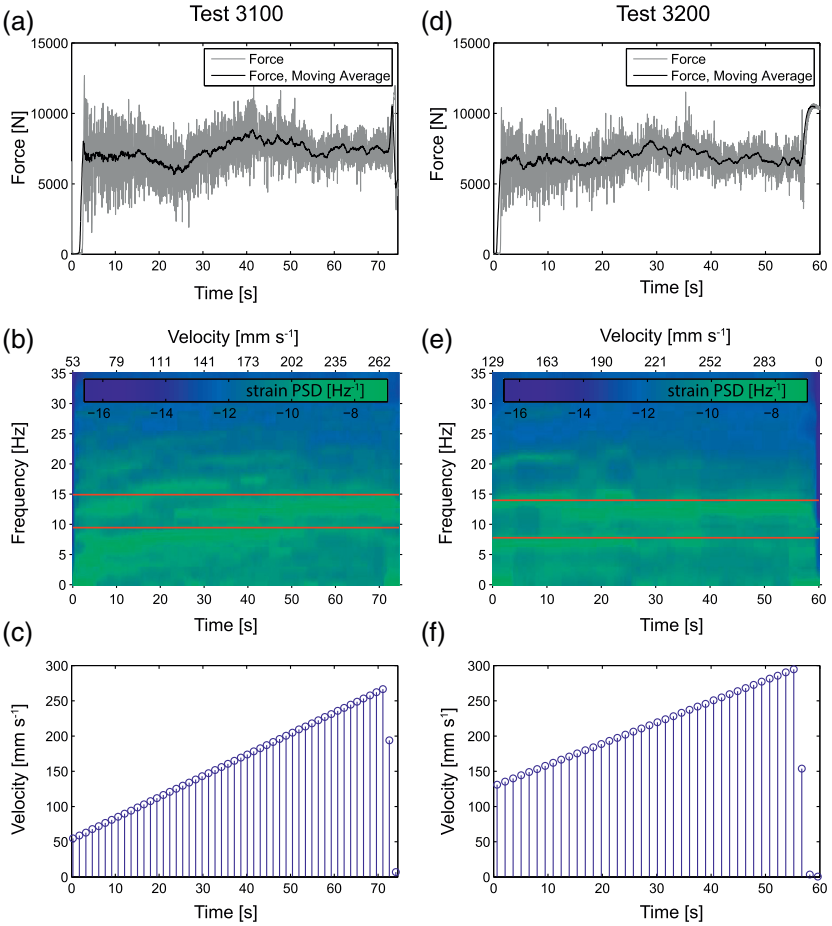

Fig. 5. Test results for a) force — test 3100; b) strain gauge response — test 3100; c) ice velocity — test 3100; d) force — test 3200; e) strain gauge response — test 3200; f) ice velocity — test 3200. (For interpretation of the references to color in this figure, the reader is referred to the web version of this article.)

In test 4300 (Fig. 7a–c), the ice velocity was increased in steps. The dominant response frequency in test 4300 increased as the ice velocity increased for each interval (Fig. 7b). At the time when the global force maximum occurred (t = 199 s), multiple frequencies appeared in the response spectrum (Fig. 7b). The force decreased significantly when frequency components less than ~7 Hz vanished. Moreover, the force amplitudes became smaller as the ice velocity increased.

The major observations from all the above tests can be summarized as follows:

The transition ice velocity at which the vibrations shifted from the first to the second mode increased with reduced foundation stiffness and reduced superstructure mass. This suggests that the mode shapes are important to consider, consistent with the instability criterion in ISO 19906 (2010), originally introduced by Määttänen (1978). Vibrations at a frequency other than the first natural frequency were often superimposed on the dominant vibration frequency and the ice forces varied with changing ice velocity and frequency content of the response. These results are also in agreement with the results from ice-induced vibrations experiments performed by Määttänen (1983).

5. Joint force, response and pressure analysis

The next sections will elaborate on the coupling between the structural state and the pressure at the interface. We will demonstrate the influence of multi-modal vibrations on the ice edge pressure in two different regimes of ice crushing using the response estimates obtained with the JIS in conjunction with the tactile sensor pressure measurements. The forces are reconstructed in three different ways: 1) using the JIS, 2) using the tactile pressure signals, and 3) by means of the frequency domain deconvolution method (Nord et al., 2013).

A shear stress distribution is necessary to reconstruct the true tactile sensor force on the cylindrical surface from the pressure measurements. To avoid having to make any assumptions on the shear forces, the sum of a set of local normal forces is simply scaled to have it correspond to the identified force amplitude. The scaled force facilitates a comparison of the physical processes captured by the tactile sensor and the identified force signals, similar to the approach presented by Sodhi (2001).

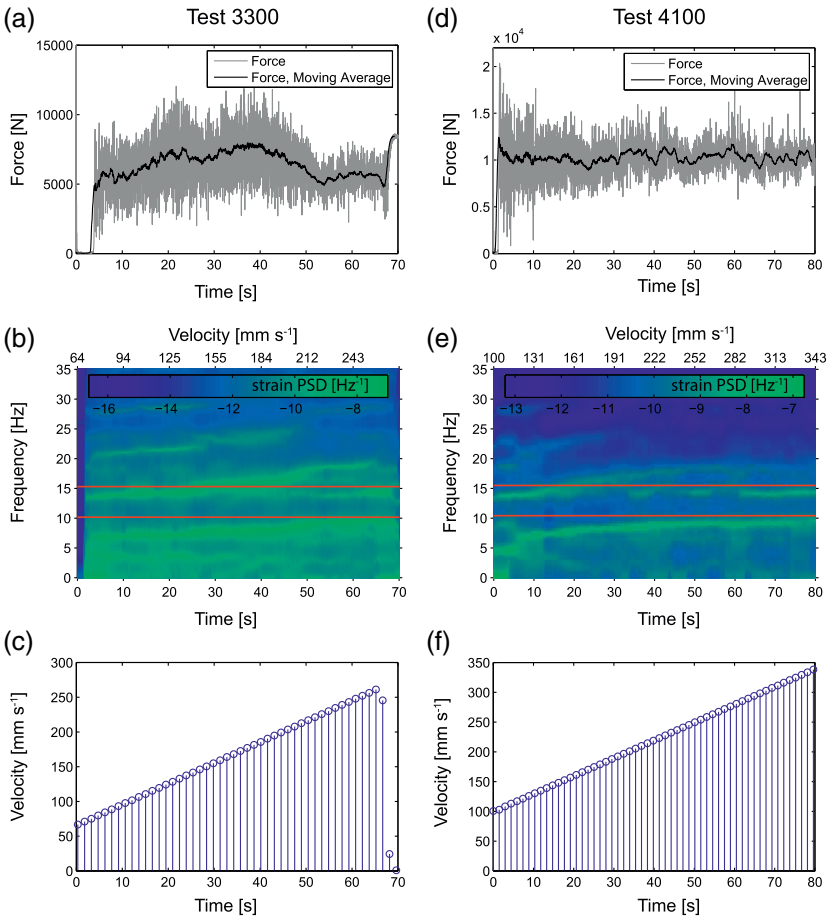

Fig. 6. Test results for a) force — test 3300; b) strain gauge response — test 3300; c) ice velocity — test 3300; d) force — test 4100; e) strain gauge response — test 4100; f) ice velocity — test 4100. (For interpretation of the references to color in this figure, the reader is referred to the web version of this article.)

The tactile sensor force is calculated as the sum of local forces in the columns covering 0–180° of the indenter, and subsequently multiplied by the scaling factor to have the peak tactile sensor force close to the peak JIS-identified force. The synchronization between the tactile sensor data and the response data (also the identified forces) has been executed manually because the tactile sensor had a separate data-logging system. The 100 Hz sampling frequency of the tactile sensor is a constraint in the sense that local, high-frequency processes at the ice-structure interface cannot be observed. Time attenuation is observed in the tactile sensor data, and the error seems to be velocity dependent during crushing; see Määttänen et al. (2011) for further discussion on the tactile sensor limitations. Despite the difficulties with the tactile sensor, the data and the optimal joint estimates provide a strong means of studying the dual state and interfacial process.

5.1. Intermittent crushing

In this section we consider two time intervals of intermittent crushing from test 4300. The first time interval starts after 64.8 s, in which the ice velocity was 20 mm s^{-1}. The reconstructed forces from the three methods described above and the measured versus estimated displacement at the lowermost laser location are displayed in Fig. 8a and b, respectively. The force time histories are similar (Fig. 8a), with the largest differences seen at the onset of a new load build-up. The laser noise is visible as the small teeth superposed upon the dominant vibration frequency (Fig. 8b), but the overall estimation of displacement in test 4300 is satisfactory as the root mean square (RMS) value of the error between the measured and estimated displacement is 1.1 mm. The numbered markers in Fig. 8 are selected to illustrate how the interplay between the structure and the ice edge develops and influences the ice pressure in Fig. 9.

The failure initialization covered a large portion across the indenter width, with only some minor residuals of the ice edge remaining (Fig. 9a). The pressure developments during intermittent crushing at an ice velocity of 20 mm s^{-1} are shown in Multimedia 1. A horizontal line of contact developed occasionally, but often the contact surface had a curved shape, as displayed in Fig. 9a, frame 1.

The fast disintegration during the next 10 ms induced a large spring-back of the lower structure (Fig. 9a, frames 2–3). The ice failure was initiated in the middle, and before new contact developed (Fig. 9a, frame 3), the failure spread to the sides. Both pulverized ice and larger pieces were extruded away from the indenter. The spring-back deflection at the ice-action point during the intermittent crushing was in the range of 10–15 mm.

The large release of strain energy in the lower structure excited the superstructure (Fig. 9b). When the superstructure advanced to the

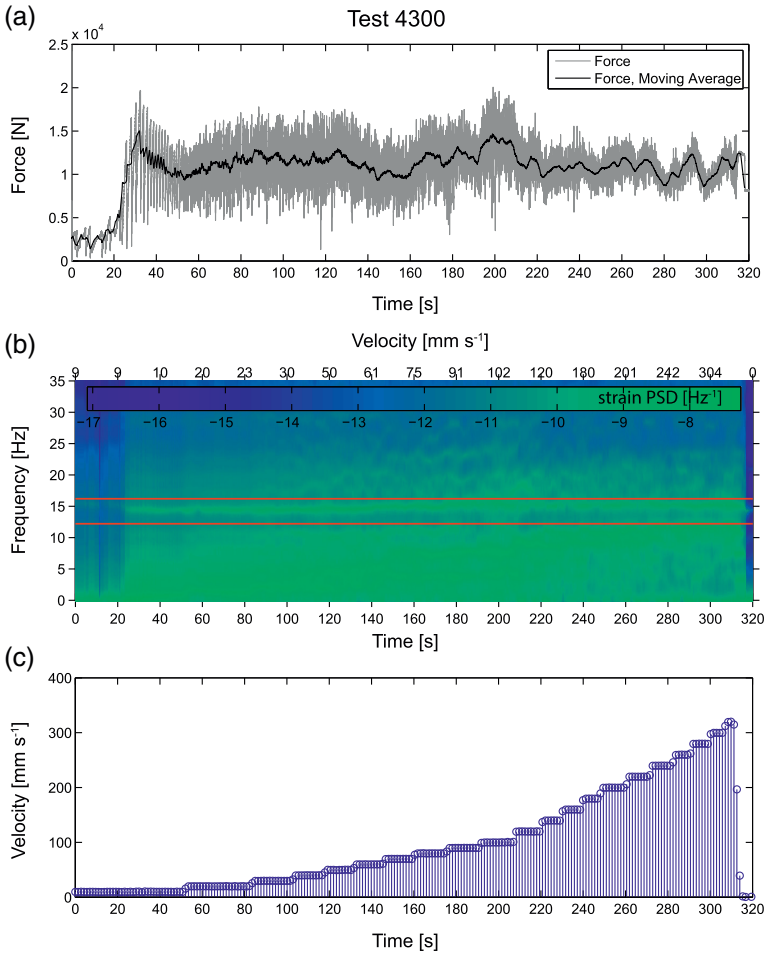

Fig. 7. Test results for a) force — test 4300; b) strain gauge response — test 4300; c) ice velocity — test 4300. (For interpretation of the references to color in this figure, the reader is referred to the web version of this article.)

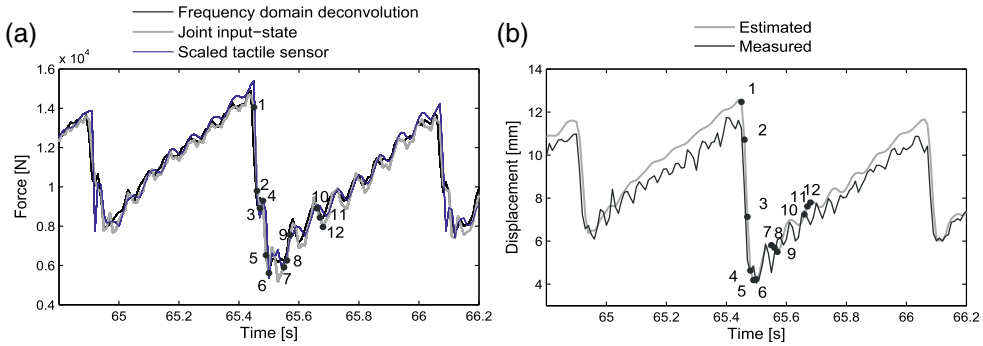

Fig. 8. Intermittent crushing in test 4300 at 20 mm s^{-1} ice velocity: a) ice force; b) estimated and measured displacements. (For interpretation of the references to color in this figure, the reader is referred to the web version of this article.)

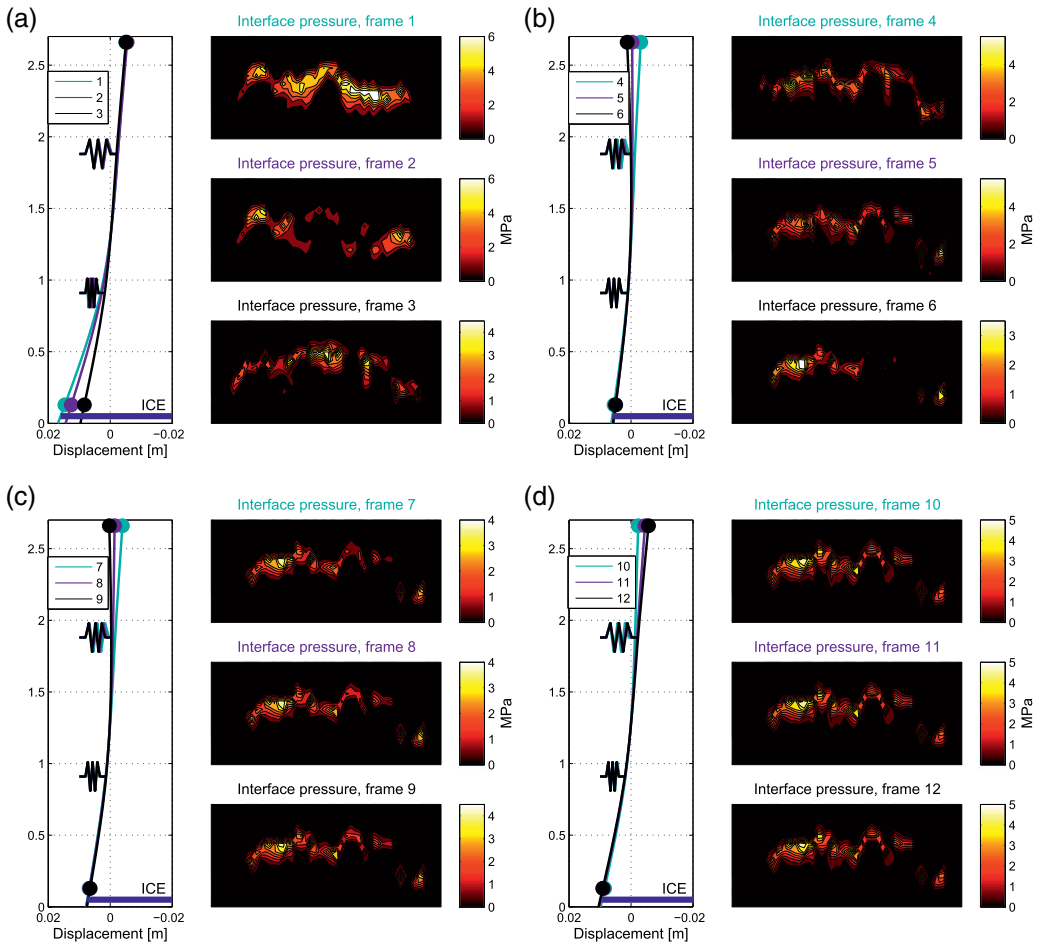

Fig. 9. State of the structure and interface pressure during intermittent crushing in test 4300 at 20 mm s^{-1} ice velocity: a) ice failure; b) second mode extrusion; c) superstructure loading; d) superstructure unloading. (For interpretation of the references to color in this figure, the reader is referred to the web version of this article.)

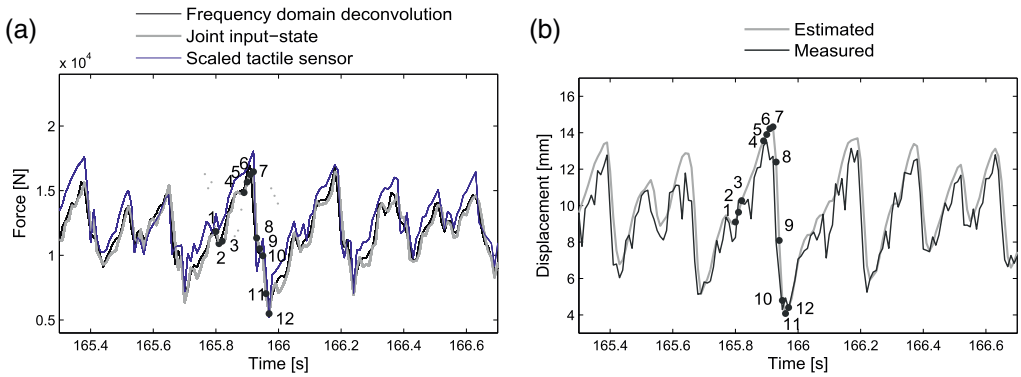

Fig. 10. Intermittent crushing in test 4300 at 80 mm s^{-1} ice velocity: a) ice force; b) estimated and measured displacements.

left, the structure entered the second mode shape (Fig. 9b, frames 4–6), and the ice edge was loaded. From frames 5 to 6, a secondary ice failure appeared to initiate on the right side of the indenter. But since the pressure evolved the same shape in Fig. 9c, frame 7, as for Fig. 9b, frame 5, likely the energy in the structure was insufficient to generate new failures.

When the new loading cycle was initiated, the first contact was not fully developed over the width at the first minor force peaks (Fig. 9c frames 8–9 and Fig. 8). The pressure was then significantly affected by the motion of the superstructure and increased as it advanced in the ice-drift direction (left), seen on the pressure color bar. As long as the superstructure is excited from the ice edge, the cyclic loading (Fig. 9c, frames 7–9) and unloading (Fig. 9d, frames 10–12) proceed.

The second time interval starts after 164.3 s, in which the ice velocity was 80 mm s^{-1}. The dominant vibration frequency was approximately 4 Hz while additional frequency contents were at ~7.2 and ~14.8 Hz (c.f. Fig. 7b). The forces and the corresponding estimated and measured displacement are displayed in Fig. 10a and b, respectively The force and response cycles have varying periods and amplitudes, being less saw-tooth shaped than at an ice velocity of 20 mm s^{-1} (c.f. Fig. 8). The dominant vibration frequency is still far below the natural frequency, such that this regime can also be regarded as intermittent crushing (ISO, 2010). As for intermittent crushing at an ice velocity of 20 mm s^{-1}, the superstructure also alternated its movement direction when the ice velocity was 80 mm s^{-1}, oscillating with a frequency of ~14.8 Hz. When the direction of the superstructure movement was opposite to the ice-drift direction (Fig. 11a, frames 1–2), a release of strain energy in the structure caused an unloading of pressure at the ice edge, apparent as the small load drop in the force curve (Fig. 10a). The effect can also be observed in the contours of the pressure at the interface. The darker left side of the interface indicates that the area was marginally unloaded. During the next frame (Fig. 11a, frames 2–3), the pressure seems to slightly increase on the right side. The increased pressure caused a small peak in the tactile sensor force (Fig. 10a), while the structural response and hence the identified forces did not manage to reconstruct this peak. This may be an effect of few sampling points or a pressure change so small that it did not influence the structure, and thus the structure "filtered" the information out.

An increasing loading rate prior to the terminal failure was caused by the superstructure movement (Fig. 11b frames 4–6), and the major

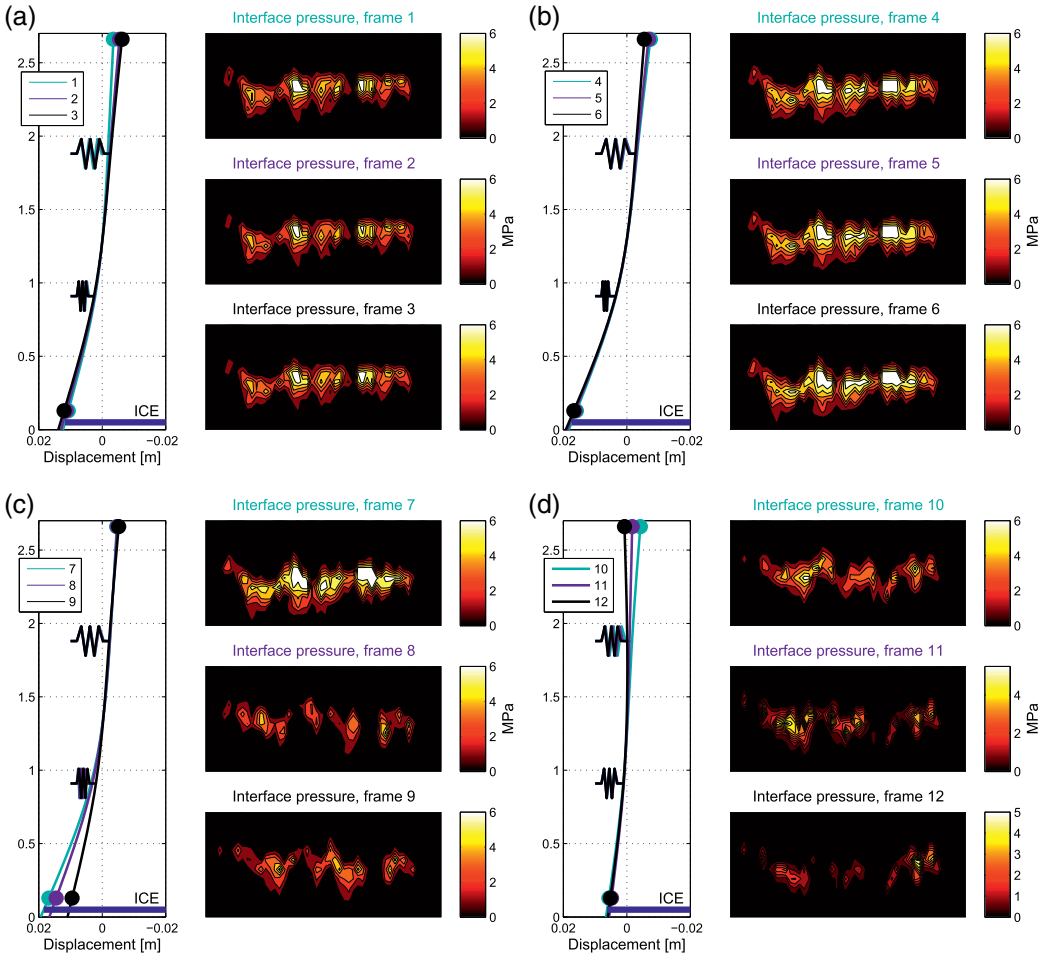

Fig. 11. State of the structure and interface pressure during intermittent crushing in test 4300 at 80 mm s^{-1} ice velocity: a) superstructure unloading; b) superstructure loading; c) ice failure; d) second mode initiation. (For interpretation of the references to color in this figure, the reader is referred to the web version of this article.)

contact spots at the interface grew. Within the next 10 ms (Fig. 11c, frames 7–8), the terminal failure occurred, and the contact changed nonsimultaneously as the ice force decreased. The superstructure advanced to the left during the ice failure (Fig. 11d, frames 10–12). The corresponding displacement close to the ice-action point was less than ~1 mm (c.f. Fig. 10b), hence the superstructure motion contributed insignificantly to the ice crushing.

Jordaan and Timco (1988) found two dominating frequencies in the measured force signal when they pushed a flat-faced indenter through S2 ice sheets at an indentation speed of 60 mm s^{-1}. The major crushing occurred at a frequency of 20 Hz, while a secondary frequency at approximately 50 Hz was attributed to further crushing or clearing events. Sodhi (2001) used a tactile sensor to study the intermittent crushing process on a flat indenter and used the following three phases to describe one loading cycle:

a) The loading phase: the ice force and the response increase gradually with high pressure zones growing simultaneously until terminal ice failure.
b) The ejection phase: fast release of strain energy in the structure causes extrusion of the ice particles and a nonsimultaneous failure.
c) The separation phase: no contact occurs between the structure and the ice, and hence the force level should be zero.

The results for the two time windows presented above indicate that loading and unloading induced by the vibrations of the superstructure took place during the load build-up. The pressure zones grew simultaneously during loading and they decreased simultaneously during unloading, seen as pulsating contact pressure and area (see also Multimedia 1). During the ice failure, the relative velocity between the ice and the structure increased and the pressure developed nonsimultaneously, in agreement with Sodhi's results. No separation phase was observed in the present tests. It should be noted that, for the same test, Nord et al. (2015) described the interaction at an ice velocity slightly above 100 mm s^{-1} as continuous brittle crushing. Because the frequency of the ice force was below the first natural frequency, stringent interpretation of ISO (2010) may argue that the interaction was intermittent crushing. However, the combination of high ice velocity and significant force frequency content(s) not far below the first natural frequency makes the correct regime difficult to define, and the interaction occasionally alternates between the regimes, being in a transition mode.

The dominant vibration frequency increased when the ice velocity increased. Each cycle at the dominant frequency was attributed to a load build-up and ice failure. A higher vibration frequency was attributed to the superstructure vibrations, which caused cyclic loading and unloading of the ice edge prior to each ice failure. This vibration frequency was slightly below the second natural frequency during intermittent crushing at both ice velocities of 20 and 80 mm s^{-1}. Hence the number of cycles that loaded and unloaded the ice edge prior to the terminal ice failure decreased when the ice velocity increased. It was further demonstrated that these vibrations can cause the loading rate to increase prior to ice failure, thereby they may provoke a more brittle failure. These processes are entirely dependent on a combination of the modal properties of the structure and the ice.

5.2. Susceptibility to "frequency lock-in" regime

The following event (Fig. 12) started after 41 s in test 3100 at an ice velocity of approximately 180 mm s^{-1}. The forces (Fig. 12a) and the displacements (Fig. 12b) exhibited repeated cycles that were slightly amplified for approximately 1–2 s. Unfortunately, the tactile sensor calibration for test 3100 was in disproportion to the ice strength. This caused the sensor to lose the high pressure zones, and the pressure cut-off value can be observed in Fig. 13 (a–d) as the plateau on the contours. Uniaxial compression strength tests demonstrated that test 3100 had nearly half the strength of the ice sheet used in test 4300. Hence the pressures in test 3100 are assumed to be lower than for test 4300. Despite the missing high pressure zones, the characteristic shape of the contact was captured.

The contact area increased during the entire loading phase (Fig. 13a–b, frames 1–6), as demonstrated by the expanding band of pressure of 2 MPa. At the onset of ice failure (Fig. 13c, frames 7–9), the superstructure strived to continue in the first mode. The failures generated discontinuities on the contours that were changing location with time, indicating nonsimultaneous failures. The states of the structure in the sequences in Fig. 13a–d reveal a key difference in this regime compared to intermittent crushing. The superstructure may oscillate back and forth several times during one full loading cycle in the intermittent regime, while during the vibration cycles in this event, the superstructure vibrations were also controlled by the dominant vibration frequency. This relationship is further supported by the estimated phase angle difference between the top and the bottom displacements of the structure of 185° for the given event. The second before and after the event, the phase differences were 169° and 145°, respectively. The modal displacement contributions from the first two modes were found to be almost in phase at the ice-action point during the event, while they were out of phase prior to and after the event.

One method to study if noticeable differences were present at the ice-structure interface during the event, was to calculate the correlation coefficients between a set of local forces during the event, and compare them to the correlation coefficients calculated prior to and after the event. To investigate the spatial correlations of pressures acting on a predefined area of the tactile sensor, local forces were reconstructed from thirteen sectors as displayed in Fig. 14. The local forces were

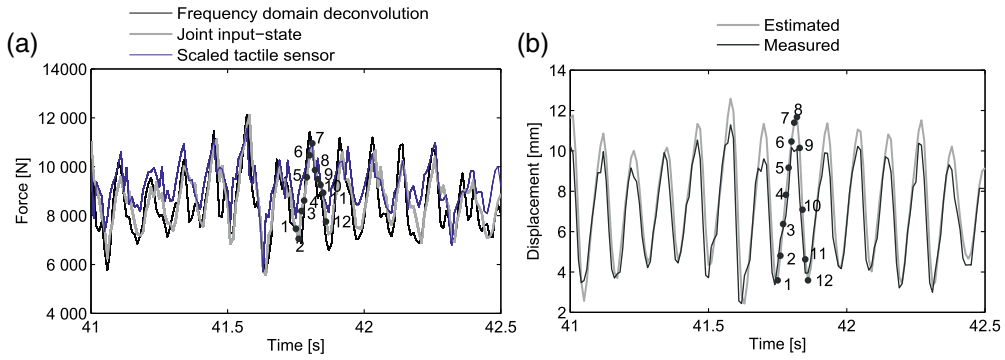

Fig. 12. Susceptibility to frequency lock-in event in test 3100: a) ice forces; b) measured versus estimated displacements.

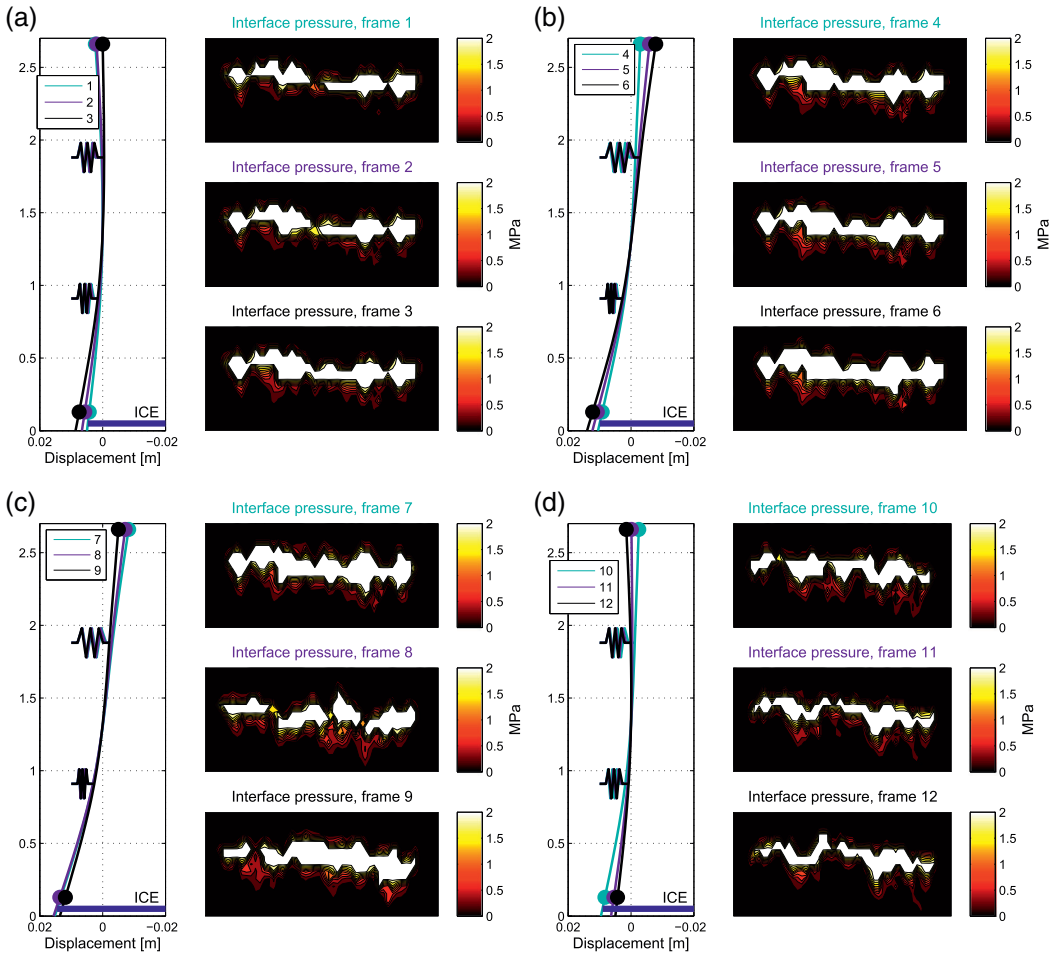

Fig. 13. State of the structure and interface pressure during the event in test 3100: a) cycle initiation; b) first mode loading; c) ice failure; d) ice failure and extrusion phase. (For interpretation of the references to color in this figure, the reader is referred to the web version of this article.)

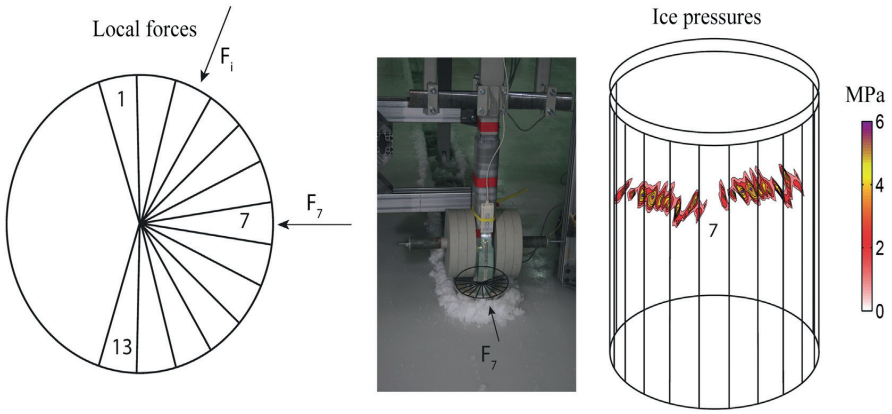

Fig. 14. Division of the tactile sensor into local sectors, where F_7 is in the ice-drift direction.

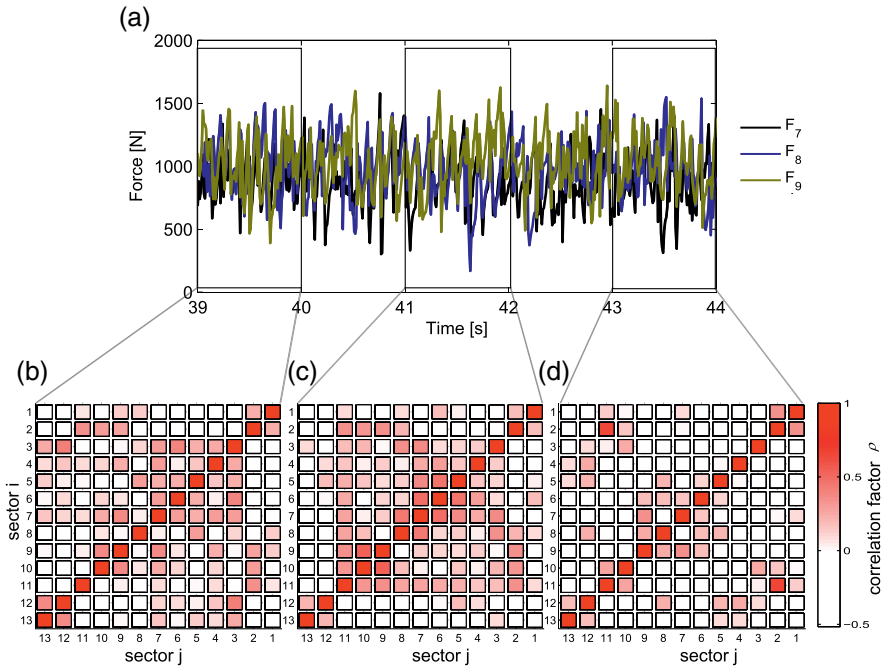

Fig. 15. Local forces from the tactile sensor in test 3100: a) time history of three local forces; b) correlation map of the full set of local forces before the event; c) correlation map of the full set of local forces during the event; d) correlation map of the full set of local forces after the event.

determined by multiplying the average pressure in each sector by the individual sector area. The shear forces derived from the normal forces add no information about the correlation and are therefore neglected. Each sector covers the full ice thickness, and the center distance between the individual neighbor sectors is 32 mm. The time histories (Fig. 15a) of the individual sectors only give indications that some ice failures occur simultaneously. To study the spatial correlation of the forces, maps of the correlation coefficients (Fig. 15b–d) were constructed from the set of local forces as follows:

$$\rho(i,j) = \frac{\tilde{C}(i,j)}{\sqrt{\tilde{C}(i,i)\tilde{C}(j,j)}} \tag{22}$$

where $\rho(i,j) \in \mathbb{R}^{n_p \times n_p}$ is the correlation coefficient matrix, $\tilde{C} \in \mathbb{R}^{n_p \times n_p}$ is the covariance matrix of the local forces and $n_p = 13$ is the number of local forces. Fig. 15b–d shows the correlation coefficient calculated for three intervals: b) before the event, c) during the event, and d) after the event. Note that sectors 1 and 13 and, in part, 2 and 12 are outside the 0–180 degree angle (on the backside of the indenter). The cross correlation coefficients between the local forces before the event (Fig. 15b) are below 0.5, and there is almost no correlation after the event (Fig. 15d). During the event (Fig. 15c), the closest elements to the diagonal have cross correlation coefficients in the range 0.3–0.6. Furthermore, the overall cross-diagonal elements are in the range 0.2–0.4. Negative cross correlation coefficients are found when one of the sectors exceeds the 180 degree angle. The negative cross correlations could possibly also occur when the structure has a lateral motion perpendicular to the ice velocity direction. However, the strain gauge installed to detect any motion in that direction revealed that the strains were small. In summary, the correlation coefficients were higher during the event in Fig. 15c, compared to before and after the event, but the event was still governed by local peak forces that occurred nonsimultaneously.

Sodhi (1998) found similar correlation coefficients in three out of four indentation tests in fresh-water ice, being approximately 0.38–0.47 at an indentation velocity of 100 mm s^{-1} and with a 50 mm sector spacing. At that indentation velocity, he found that there were instances when the local peak forces occurred simultaneously, while at higher ice velocities, the local peak forces occurred randomly. Taylor (2009) investigated the correlation between the 15 adjacent load panels used in the medium-scale JOIA test campaign: the results were distinguished by the indentation velocity, in which a fast event corresponded to 30 mm s^{-1}. Little correlation was found during the fast event when the separation was larger than one panel width (100 mm). Four pressure-sensing panels were also installed on the indenter face in that campaign. Sodhi et al. (1998) reported the correlation coefficient as a function of the distance between the columns in the pressure-sensing panel grid. At an indentation velocity of 30 mm s^{-1} (high indentation velocity), the interaction was governed by nonsimultaneous ice failures, and with a ~30 mm distance the correlation coefficient was approximately 0.15. Their results at a high indentation velocity correspond well to the correlation found after the event (Fig. 15d). The occurrence of the event with repeated vibration cycles may have been provoked by the small increase in the correlation coefficients between the local ice failures (Fig. 15c), while the increasing randomness of the local peak forces from the time interval 41–42 s to the time interval 43–44 s may have caused the structure to exit the event.

In full scale, Bjerkås et al. (2013) and Bjerkås and Skiple (2005) studied the ice forces during an event of frequency lock-in vibrations of the Nordströmsgrund lighthouse, and found that the local peak forces that were measured by individual panels were synchronized (simultaneous occurrence of local peak forces) during the event.

The synchronized local forces caused large global forces accompanied with violent vibrations close to the natural frequency. Simultaneous

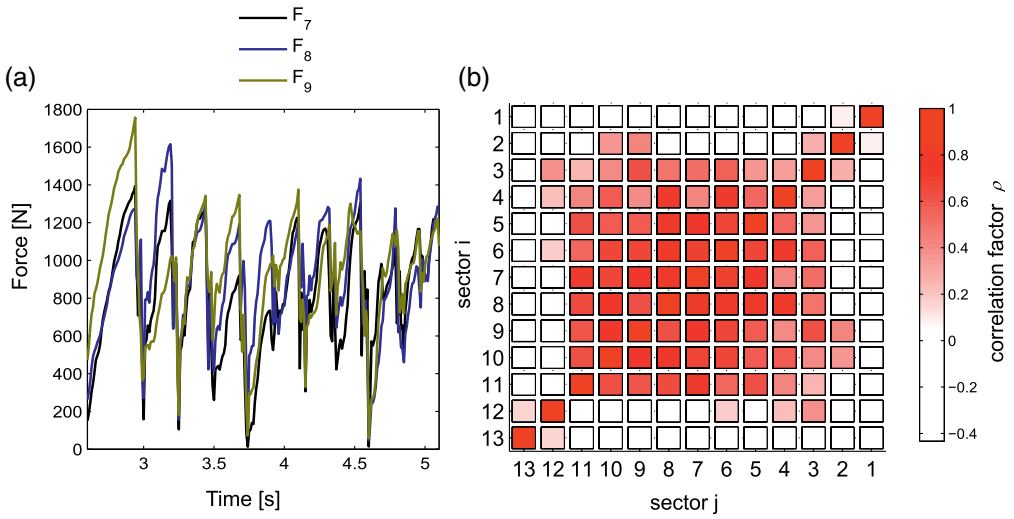

Fig. 16. Local forces from the first cycles after ice-edge contact in test 3100: a) local force in sectors 7–9; b) correlation map of all thirteen local forces.

occurrences of local peak forces were also observed when the ice initiated contact with the laboratory structure at the start of each test. The forces and correlation map during the first ice contact in test 3100 are shown in Fig. 16a and b, respectively. The dominant vibration frequency was then only approximately 5 Hz, hence the crushing regime can be regarded as intermittent crushing. The force time histories (Fig. 16a) and the correlation map (Fig. 16b) show that the correlation was significantly higher compared to the "lock-in" event at 180 mm s^{-1} (c.f. Fig. 15c).

In summary the structural response was found to be controlled by a single dominant vibration frequency during the event. Our model-scale results suggest that fully synchronized failures are not required to experience significant repeated cycles of ice-induced vibrations close to the natural frequency of the structure.

6. Conclusions

Measurements from a series of ice-induced vibration scale tests were used to identify the ice forces causing the structural vibrations as well as spatially complete information on the vibrations themselves. The dominant vibration frequency increased during intermittent crushing when the ice velocity increased. Each cycle at the dominant vibration frequency consisted of a load build-up and ice failure, while a higher vibration frequency was attributed to the higher-order superstructure vibrations within this cycle. The higher vibration frequency was slightly below the second natural frequency during intermittent crushing at ice velocities of 20 and 80 mm s^{-1}. These vibrations caused cyclic loading of the ice edge and increased the loading rate prior to ice failure. Two tests showed that the dominant vibration shape shifted from the first to the second mode when the ice velocity increased. The transition ice velocity at which the vibrations changed was found to depend on the structure's stiffness and mass properties.

Spatial correlations between local forces were calculated before, during and after an event that showed tendencies to frequency lock-in vibrations in the first mode. A slightly higher spatial correlation was found during the event, but the local peak forces were not fully synchronized across the indenter width.

The key tool that enabled the current analysis was the JIS estimation algorithm. It provided both the ice forces and spatially complete information on the structural behavior based on a limited number of response measurements. Given that the sensor types and sensor locations are carefully selected and the finite element model represents the structure well, this algorithm is promising in terms of full-scale force and response estimation.

To improve similar experimental test setups in the future, it is suggested that pressure sensors with a higher sampling frequency be used, such that the influence on the vibrations of local, higher-frequency processes at the ice–structure interface can be better understood.

Supplementary data to this article can be found online at http://dx.doi.org/10.1016/j.coldregions.2015.06.017.

Acknowledgements

The authors wish to acknowledge support from the Research Council of Norway (203471) through the Centre for Research-based Innovation SAMCoT and support from all SAMCoT partners. The work described in this paper was supported by the European Community's 7th Framework Programme through a grant to the budget of the Integrated Infrastructure Initiative HYDRALAB-IV, Contract no. 261520. The authors would like to thank the Hamburg Ship Model Basin (HSVA), particularly the ice tank crew, for their hospitality, technical and scientific support and the professional execution of the test program in the Research Infrastructure ARCTECLAB.

References

Barker, A., Timco, G., Gravesen, H., Vølund, P., 2005. Ice loading on Danish wind turbines: part 1: dynamic model tests. Cold Reg. Sci. Technol. 41 (1), 1–23.

Bjerkås, M., Skiple, A., 2005. Occurrence of intermittent and continuous crushing during ice-structure interaction. Proceedings of the 18th international Conference on Port and Ocean Engineering under Arctic conditions (POAC), Potsdam, NY, USA, pp. 1131–1141.

Bjerkås, M., Meese, A., Alsos, H.S., 2013. Ice induced vibrations–observations of a full-scale lock-in event. Proceedings of the Twenty-Third International Offshore and Polar Engineering International Society of Offshore and Polar Engineers (ISOPE), Anchorage, Alaska, pp. 1272–1279.

Blenkarn, K.A., 1970. Measurment and analysis of ice forces on Cook Inlet structure. Offshore Technology Conference, Houston, TX, pp. 365–378.

Browne, T., Taylor, R., Jordaan, I., Gürtner, A., 2013. Small-scale ice indentation tests with variable structural compliance. Cold Reg. Sci. Technol. 88, 2–9.

Duan, Z., Ou, J., Spencer, B.F., 2002. Investigation of ice forces on jacket platform structures: in-situ measured data on JZ-20-2-1 platform in the China Bohai Sea. ASCE Engineering Mechanics Conference, Colombia University, New York.

Gillijns, S., De Moor, B., 2007. Unbiased minimum-variance input and state estimation for linear discrete-time systems with direct feedthrough. Automatica 43 (5), 934–937.

Gravesen, H., Sørensen, S.L., Vølund, P., Barker, A., Timco, G., 2005. Ice loading on Danish wind turbines: part 2. Analyses of dynamic model test results. Cold Reg. Sci. Technol. 41 (1), 25–47.
Hendrikse, H., Metrikine, A., Evers, K.-U., 2012. A method to measure the added mass and added damping in dynamic ice–structure interaction. "Ice Research for a Sustainable Environment" (IAHR). Dalian, China (Paper no. 094).
Huang, Y., Shi, Q., Song, A., 2007. Model test study of the interaction between ice and a compliant vertical narrow structure. Cold Reg. Sci. Technol. 49 (2), 151–160.
ISO, 2010. ISO/FDIS 19906. p. 188.
Joensuu, A., Riska, K., 1988. Ice–structure contact. Report M88. Helsinki University of Technology, Faculty of Mechanical Engineering, Laboratory of Naval Architecture and Marine Engineering 951-754-773-0.
Jordaan, I.J., 2001. Mechanics of ice–structure interaction. Eng. Fract. Mech. 68 (17–18), 1923–1960.
Jordaan, I.J., Timco, G.W., 1988. Dynamics of the ice-crushing process. J. Glaciol. 34 (118).
Kärnä, T., 1995. Finite ice failure depth in penetration of a vertical indentor into an ice edge: T. Karna, Annals of Glaciology, 19, 1994. Int. J. Rock Mech. Min. Sci. Geomech. Abstr. 32 (2), A98 (pp. 114–120).
Kärnä, T., Kolari, K., Jochmann, P., Evers, K.-U., Bi, X., Mättänen, M., Martonen, P., 2003a. Tests on dynamic ice–structure interaction. 22ND International conference on Offshore Mechanics and Arctic Engineering (OMAE),Cancun, Mexico (paper no. 37397).
Kärnä, T., Kolari, K., Jochmann, P., Evers, K.-U., Xiangjun, B., Määttänen, M., Martonen, P., 2003b. Ice action on compliant structures. VTT Research Notes 2223. VTT.
Kärnä, T., Gravesen, H., Fransson, L., Løset, S., 2010. Simulation of multi-modal vibrations due to ice actions paper no. 136, 20th International Symposium on Ice, IAHR, Lahti, Finland (paper no. 136).
Lourens, E., Papadimitriou, C., Gillijns, S., Reynders, E., De Roeck, G., Lombaert, G., 2012. Joint input-response estimation for structural systems based on reduced-order models and vibration data from a limited number of sensors. Mech. Syst. Signal Process. 29, 310–327.
Määttänen, M., 1975. Experiences of ice forces against a steel lighthouse mounted on the seabed, and proposed constructional refinements. Port and Ocean Engineering Under Arctic conditions (POAC), Fairbanks, Alaska, pp. 857–867.
Määttänen, M., 1978. On Conditions for the Rise of Self-Excited Ice Induced Autonomous Oscillations in Slender Marine Pile Structures (PhD Thesis) University of Oulu.
Määttänen, M., 1979. Laboratory Tests for Ice–Structure Interaction. Port and Ocean Engineering Under Arctic Conditions (POAC), Trondheim, Norway, pp. 1139–1153.
Määttänen, M., 1983. Dynamic ice–structure interaction during continuous crushing. CRREL Report 83-5.
Määttänen, M., 2008. Ice velocity limit to frequency lock-in vibrations. International Symposium on Ice. IAHR, Vancouver, Canada, pp. 1265–1276.
Määttänen, M., Marjavaara, P., Saarinen, S., Laakso, M., 2011. Ice crushing tests with variable structural flexibility. Cold Reg. Sci. Technol. 67 (3), 120–128.
Määttänen, M., Løset, S., Metrikine, A., Evers, K.-U., Hendrikse, H., Lønøy, C., Metrikin, I., Nord, T.S., Sukhorukov, S., 2012. Novel ice induced vibration testing in a large-scale facility. "Ice Research for a Sustainable Environment" (IAHR), Dalian, China (paper no. 092).
Nakazawa, N., Sodhi, D.S., 1990. Ice forces on flat, vertical indentors pushed through floating ice sheets. CRREL Report 90-14.
Neill, C.R., 1976. Dynamic ice forces on piers and piles. An assessment of design guidelines in the light of recent research. Can. J. Civ. Eng. 3 (2), 305–341.
Nord, T.S., Määttänen, M., 2012. Modal analysis in ice structure interaction. 21st International Symposium on Ice, IAHR, Dalian, China (paper no. 093).
Nord, T.S., Määttänen, M., Øiseth, O., 2013. Frequency Domain Force Identification in Ice–Structure Interaction. Port and Ocean Engineering under Arctic Conditions, Espoo, Finland 978-952-60-3635-9.
Nord, T.S., Lourens, E.-M., Øiseth, O., Metrikine, A., 2015. Model-based force and state estimation in experimental ice-induced vibrations by means of Kalman filtering. Cold Reg. Sci. Technol. 111, 13–26.
Sodhi, D.S., 1998. Nonsimultaneous crushing during edge indentation of freshwater ice sheets. Cold Reg. Sci. Technol. 27 (3), 179–195.
Sodhi, D.S., 2001. Crushing failure during ice–structure interaction. Eng. Fract. Mech. 68 (17–18), 1889–1921.
Sodhi, D., Haehnel, R., 2003. Crushing ice forces on structures. J. Cold Reg. Eng. 17 (4), 153–170.
Sodhi, D.S., Takeuchi, T., Nakazawa, N., Akagawa, S., Saeki, H., 1998. Medium-scale indentation tests on sea ice at various speeds. Cold Reg. Sci. Technol. 28 (3), 161–182.
Taylor, R., 2009. Analysis of Scale Effect in Compressive Ice Failure and Implications for Design (PhD Thesis), Memorial University (document ID, a3315266).
Taylor, R., Brown, T., Jordaan, I., Gürtner, A., 2013. Fracture and damage during dynamic interactions between ice and compliant structures at laboratory scale. Proceedings of the ASME 2013 32nd International Conference on Ocean, Offshore and Arctic Engineering (OMAE), Nantes, France (paper no. 11070).
Timco, G.W., 1984. Ice forces on structures: physical modelling techniques. International Symposium on Ice (IAHR), Hamburg, Germany, pp. 117–150.
Toyama, Y., Sensu, T., Minami, M., Yashima, N., 1983. Model Tests on Self-Excited Vibration on Cylindrical Structures. Port and Ocean Under Arctic conditions (POAC), Helsinki, pp. 834–844.
Wells, J., Jordaan, I., Derradji-Aouat, A., Taylor, R., 2011. Small-scale laboratory experiments on the indentation failure of polycrystalline ice in compression: main results and pressure distribution. Cold Reg. Sci. Technol. 65 (3), 314–325.

Appendix 4 Ice force identification on the Nordströmsgrund lighthouse

This appendix includes the paper submitted to the Journal of Computers and Structures (see below).

- Nord, T.S., Lourens, E.-M., Øiseth, O. Ice force identification on the Nordströmsgrund lighthouse. Submitted to Computers and structures, under revision.

Ice force identification on the Nordströmsgrund lighthouse

Torodd S. Nord [1,2], Ole Øiseth [3], Eliz-Mari Lourens [4]

[1] *Sustainable Arctic Marine and Coastal Technology (SAMCoT), Centre for Research-based Innovation (CRI), Norwegian University of Science and Technology, Trondheim, Norway*

[2] *The University Centre in Svalbard (UNIS), Longyearbyen, Spitsbergen*

[3] *Department of Structural Engineering, Norwegian University of Science and Technology, Trondheim, Norway.*

[4] *Faculty of Civil Engineering and Geosciences, Delft University of Technology, Delft, the Netherlands.*

Abstract

Ice forces on bottom-founded structures can be measured by load panels or identified from response measurements. This paper presents a comparison between the measured and identified dynamic ice forces acting on the Nordströmsgrund lighthouse. The dynamic ice forces are identified from the measured responses using a recently developed joint input-state estimation algorithm in conjunction with a reduced-order finite element model. A convincing agreement between the measured and identified forces was found. The response predictive ability of the algorithm is further used to estimate the response of the structure at unmeasured locations including at the ice-action point.

Keywords:

Ice-induced vibrations

Bottom-founded structure

Force identification

Force measurements

[1] Corresponding author
E-mail address: torodd.nord@ntnu.no (Torodd S. Nord)

1 Introduction

Level ice crushing on bottom-founded offshore structures may cause severe ice-induced vibrations. Several measurement campaigns have been performed on many types of Arctic structures to understand the nature of different ice-structure interaction scenarios, including ice-induced vibrations. The ice forces are measured either directly or reconstructed using inverse techniques. Both of these methods have their operational difficulties, and the global forces cannot be derived without assumptions. A global force derived from load panels often relies on assumptions of friction and sensor calibration, whereas the panels may furthermore not cover the full ice-structure interface. Response sensors cost less, in terms of both installation and operation, and are easier to install than load panels. A reconstructed global force from a model-based force identification technique depends again on model assumptions, sensor locations and the quality of the response information. Sensor networks may be difficult to design because the ice-action point is often unknown and time-variant. In addition, other sources of ambient vibrations may be present in the response data [1].

Both direct force panel measurements and inverse force identification techniques may suffer from the ice conditions. Examples include problems caused by icing, ice bustles, jamming of broken ice that reconsolidates between the legs of multi-leg structures [2], or large amounts of broken ice that pile up towards the structure and disturb the load or response measurements. Because the extreme ice-induced vibration events are not fully understood, the in-situ observation of the ice conditions, the collection of ice properties and the collection of other environmental data are required, alongside the load and response measurements. Past measurement campaigns that facilitated the collection of this volume of information were extensive, for example, the Molikpaq platform [3], the Confederation Bridge [1, 4], the Nordströmsgrund lighthouse [5, 6], the Kemi 1 Lighthouse [7, 8] and the YZ-20-1 Platform in the Bohai Sea [9].

When the dominant frequency in the global ice force and response is near a natural frequency of the structure, the vibrations are commonly referred to as frequency lock-in vibrations. Because of their violent nature, they have been given significant attention in the ice-research community [3, 6, 10-14]. To better understand the frequency lock-in phenomena, it is desired to identify the global response of the structure in conjunction with the ice forces driving this response, from a limited number of response measurements.

To reconstruct ice forces, force identification has been debated for decades within the ice-research community [13, 15, 16]. In this study, we present a full-scale comparison between the measured and identified dynamic ice forces using state of the art techniques for force identification. A joint input-state estimation

algorithm [17] is used to identify the dynamic ice forces acting on the Nordströmsgrund lighthouse during two events that occurred on the 30th of March 2003. The first event is governed by (measured) local peak forces that occur simultaneously (synchronized local forces) and displays a dominant frequency component near the first natural frequency of the structure, whereas the other event is characterized by local peak forces occurring nonsimultaneously. The algorithm was originally developed for use within the field of optimal control, but was extended for applications to modally reduced order models as often used in structural dynamics by Lourens et al. [18]. This modified algorithm allows for the forces and states to be identified also when the number of sensors and/or forces exceeds the number of structural modes used to construct the model. In this paper, we use the original algorithm. It allows for uncertainty in the system equations and holds no prior assumptions on the dynamic evolution of the identified force. The algorithm was recently used to identify the ice forces exerted on a scaled structure in a model basin by Nord et al. [19]. In this study, the load identification and response predictive ability of the algorithm is validated on a full-scale structure. The ability to extract response estimates at unmeasured locations provides novel insights into the global structural behavior during dynamic ice-structure interaction.

2 System equations for model-based force and state estimation

The forces are treated as unknown concentrated loads acting on a linear time-invariant structure that is represented by selected vibration modes obtained from a finite element model:

$$\ddot{\mathbf{z}}(t)+\mathbf{\Gamma}\dot{\mathbf{z}}(t)+\mathbf{\Omega}^2\mathbf{z}(t)=\mathbf{\Phi}^{\mathrm{T}}\mathbf{S}_{\mathrm{p}}\mathbf{p}(t) \tag{1}$$

Here, $\mathbf{z}(t)\in\mathbb{R}^{n_{\mathrm{m}}}$ is the vector of modal coordinates, and n_{m} is the number of modes used to assemble the model. The excitation vector, $\mathbf{p}(t)\in\mathbb{R}^{n_{\mathrm{p}}}$, is specified to act on the desired locations through the force influence matrix $\mathbf{S}_{\mathrm{p}}\in\mathbb{R}^{n_{\mathrm{DOF}}\times n_{\mathrm{p}}}$, where n_{p} is the number of force time histories and n_{DOF} is the number of degrees of freedom. $\mathbf{\Gamma}\in\mathbb{R}^{n_{\mathrm{m}}\times n_{\mathrm{m}}}$ is the diagonal damping matrix populated on the diagonal with the terms $2\xi_j\omega_j$, where ω_j and ξ_j are the natural frequency and damping ratio corresponding to mode j, respectively. $\mathbf{\Omega}\in\mathbb{R}^{n_{\mathrm{m}}\times n_{\mathrm{m}}}$ is a diagonal matrix containing the natural frequencies ω_j, and $\mathbf{\Phi}\in\mathbb{R}^{n_{\mathrm{DOF}}\times n_{\mathrm{m}}}$ is a matrix collecting the mass-normalized mode shapes.

2.1 State-space model

78 The modally reduced continuous-time state vector $\mathbf{x}(t) \in \mathbb{R}^{n_s}$, $n_s = 2n_m$ is defined as follows:

79 $$\mathbf{x}(t) = \begin{pmatrix} \mathbf{z}(t) \\ \dot{\mathbf{z}}(t) \end{pmatrix} \tag{2}$$

80 whereby the equation of motion of second order in Eq. (1) can be organized as a first-order continuous-time state
81 equation:

82 $$\dot{\mathbf{x}}(t) = \mathbf{A}_c \mathbf{x}(t) + \mathbf{B}_c \mathbf{p}(t) \tag{3}$$

83 where the system matrices $\mathbf{A}_c \in \mathbb{R}^{n_s \times n_s}$ and $\mathbf{B}_c \in \mathbb{R}^{n_s \times n_p}$ are defined as follows:

84 $$\mathbf{A}_c = \begin{bmatrix} \mathbf{0} & \mathbf{I} \\ -\boldsymbol{\Omega}^2 & -\boldsymbol{\Gamma} \end{bmatrix}, \mathbf{B}_c = \begin{bmatrix} \mathbf{0} \\ \boldsymbol{\Phi}^T \mathbf{S}_p \end{bmatrix}. \tag{4}$$

85 The measurements are arranged in a data vector $\mathbf{d}(t) \in \mathbb{R}^{n_d}$, in which the observations can be a linear
86 combination of the displacement, velocity and acceleration with n_d response measurements. The data vector is
87 constructed as follows:

88 $$\mathbf{d}(t) = \mathbf{S}_a \boldsymbol{\Phi}\, \ddot{\mathbf{z}}(t) + \mathbf{S}_v \boldsymbol{\Phi}\, \dot{\mathbf{z}}(t) + \mathbf{S}_d \boldsymbol{\Phi}\, \mathbf{z}(t) \tag{5}$$

89 where the selection matrices $\mathbf{S}_a, \mathbf{S}_v$ and $\mathbf{S}_d \in \mathbb{R}^{n_d \times n_{DOF}}$ are populated according to the spatial location at which the
90 acceleration, velocity, displacement, strain or inclination are measured. Eq. (5) can be transformed into state-
91 space form using Eqs. (1) and (2):

92 $$\mathbf{d}(t) = \mathbf{G}_c \mathbf{x}(t) + \mathbf{J}_c \mathbf{p}(t) \tag{6}$$

93 where the matrices $\mathbf{G}_c \in \mathbb{R}^{n_d \times n_s}$ and $\mathbf{J}_c \in \mathbb{R}^{n_d \times n_p}$ represent the output influence matrix and direct transmission
94 matrix, respectively, defined as:

95 $$\begin{aligned} \mathbf{G}_c &= [\mathbf{S}_d \boldsymbol{\Phi} - \mathbf{S}_a \boldsymbol{\Phi} \boldsymbol{\Omega}^2 \quad \mathbf{S}_v \boldsymbol{\Phi} - \mathbf{S}_a \boldsymbol{\Phi} \boldsymbol{\Gamma}] \\ \mathbf{J}_c &= [\mathbf{S}_a \boldsymbol{\Phi} \boldsymbol{\Phi}^T \mathbf{S}_p] \end{aligned} \tag{7}$$

96 In discrete time under a zero-order hold assumption and given a sampling rate of $1/\Delta t$, Eqs. (3) and (6) can be
97 defined as follows:

$$\mathbf{x}_{k+1} = \mathbf{A}\mathbf{x}_k + \mathbf{B}\mathbf{p}_k \tag{8}$$

$$\mathbf{d}_k = \mathbf{G}\mathbf{x}_k + \mathbf{J}\mathbf{p}_k \tag{9}$$

where

$$\mathbf{x}_k = \mathbf{x}(k\Delta t),\ \mathbf{d}_k = \mathbf{d}(k\Delta t),\ \mathbf{p}_k = \mathbf{p}(k\Delta t),\ k = 1,...,N$$

and

$$\mathbf{A} = e^{\mathbf{A}_c \Delta t},\ \mathbf{B} = [\mathbf{A} - \mathbf{I}]\mathbf{A}_c^{-1}\mathbf{B}_c$$

$$\mathbf{G}_c = \mathbf{G},\ \mathbf{J}_c = \mathbf{J}.$$

2.2 Joint input-state estimation algorithm

Assuming that the system matrices $\mathbf{A}, \mathbf{B}, \mathbf{G}$ and $\mathbf{J}$ are known, the recursive joint input-state estimation algorithm can be used to jointly estimate the forces and states. By introducing the random variables $\mathbf{w}_k$ and $\mathbf{v}_k$, which represent the stochastic system and measurement noise, respectively, the deterministic-stochastic discrete-time state-space equations become the following:

$$\mathbf{x}_{k+1} = \mathbf{A}\mathbf{x}_k + \mathbf{B}\mathbf{p}_k + \mathbf{w}_k \tag{10}$$

$$\mathbf{d}_k = \mathbf{G}\mathbf{x}_k + \mathbf{J}\mathbf{p}_k + \mathbf{v}_k \tag{11}$$

Here, the vectors $\mathbf{w}_k$ and $\mathbf{v}_k$ are assumed to be mutually uncorrelated, zero-mean, white-noise signals with known covariance matrices $\mathbf{Q} = E\{\mathbf{w}_k \mathbf{w}_k^{\mathrm{T}}\}$ and $\mathbf{R} = E\{\mathbf{v}_k \mathbf{v}_k^{\mathrm{T}}\}$. Maes et al. [20] extended the algorithm to handle situations in which the system noise $\mathbf{w}_k$ and measurement noise $\mathbf{v}_k$ are correlated. This correlation is inherently present when accelerations are measured and the system and measurement noise are both effected by errors in the forcing (e.g., in the assumed positions of the forces). Although this is the case for the current application, the cross-correlation terms are assumed to be small in comparison to the autocorrelations and are therefore neglected.

The algorithm predicts the forces and states in three steps summarized below: the unbiased minimum-variance input estimation (MVU), the measurement update, and the time update.

Input estimation:

$$\tilde{\mathbf{R}}_k = \mathbf{G}\mathbf{P}_{k|k-1}\mathbf{G}^{\mathrm{T}} + \mathbf{R} \tag{12}$$

$$\mathcal{M}_k = (\mathbf{J}^{\mathrm{T}}\tilde{\mathbf{R}}_k^{-1}\mathbf{J})^{-1}\mathbf{J}^{\mathrm{T}}\tilde{\mathbf{R}}_k^{-1} \tag{13}$$

$$\hat{\mathbf{p}}_{k|k} = \mathcal{M}_k(\mathbf{d}_k - \mathbf{G}\hat{\mathbf{x}}_{k|k-1}) \tag{14}$$

$$\mathbf{P}_{\mathrm{p}[k|k]} = (\mathbf{J}^{\mathrm{T}}\tilde{\mathbf{R}}_k^{-1}\mathbf{J})^{-1} \tag{15}$$

Measurement update:

$$\mathbf{L}_k = \mathbf{P}_{k|k-1}\mathbf{G}^{\mathrm{T}}\tilde{\mathbf{R}}_k^{-1} \tag{16}$$

$$\hat{\mathbf{x}}_{k|k} = \hat{\mathbf{x}}_{k|k-1} + \mathbf{L}_k(\mathbf{d}_k - \mathbf{G}\hat{\mathbf{x}}_{k|k-1} - \mathbf{J}\hat{\mathbf{p}}_{k|k}) \tag{17}$$

$$\mathbf{P}_{k|k} = \mathbf{P}_{k|k-1} - \mathbf{L}_k(\tilde{\mathbf{R}}_k - \mathbf{J}\,\mathbf{P}_{\mathrm{p}[k|k]}\mathbf{J}^{\mathrm{T}})\mathbf{L}_k^{\mathrm{T}} \tag{18}$$

$$\mathbf{P}_{\mathrm{xp}[k|k]} = \mathbf{P}_{\mathrm{px}[k|k]}^{\mathrm{T}} = -\mathbf{L}_k\mathbf{J}\,\mathbf{P}_{\mathrm{p}[k|k]} \tag{19}$$

Time update:

$$\mathbf{x}_{k+1|k} = \mathbf{A}\hat{\mathbf{x}}_{k|k} + \mathbf{B}\hat{\mathbf{p}}_{k|k} \tag{20}$$

$$\mathbf{P}_{k+1|k} = \begin{bmatrix}\mathbf{A} & \mathbf{B}\end{bmatrix}\begin{bmatrix}\mathbf{P}_{k|k} & \mathbf{P}_{\mathrm{xp}[k|k]} \\ \mathbf{P}_{\mathrm{px}[k|k]} & \mathbf{P}_{\mathrm{p}[k|k]}\end{bmatrix}\begin{bmatrix}\mathbf{A}^{\mathrm{T}} \\ \mathbf{B}^{\mathrm{T}}\end{bmatrix} + \mathbf{Q} \tag{21}$$

For more details on the algorithm and the assumptions it is based upon, the reader is referred to Lourens et al. [18].

2.3 ICE-INDUCED VIBRATIONS, FULL-SCALE MEASUREMENTS

The Nordströmsgrund lighthouse is located in the Gulf of Bothnia, 60 km South-East of Luleå, Sweden. The measurement project STRICE (STRuctures in ICE) was launched to monitor the structural response and ice forces during the winter seasons from 2001 to 2003. A summary of the measurement campaigns on Nordströmsgrundis available in Bjerkås [21]. The lighthouse (Fig. 1a) is a gravity-based concrete structure with a wall thickness varying between 0.2 m at the top and 1.4 m at the mean water level. Below the mean water level,

142 the main structure and foundation caisson are filled with sand. Eight concrete bulkheads stiffen the foundation
143 frame, and a 0.7 m thick concrete foundation plate rests on a top layer of cement grouted crushed stones and a
144 lower layer of morainic soil [22].

145 **2.4 Sensor types, positions, and data acquisition**

146 To measure the ice forces, nine panels (Fig. 1b) were installed across the outer surface at + 14.2 m elevation.
147 Two types of panels were used. One panel was segmented, in which eight segments [23] measured local forces
148 through the ice thickness. The panel force was calculated as the sum of the local forces measured by the different
149 segments. The other eight panels each measured a single force. In total, the nine panels covered 162 degrees of
150 the outer perimeter. The lighthouse was further instrumented with two biaxial inclinometers and two biaxial
151 accelerometers. One accelerometer was located close to the ice-action point at +16.5 m elevation while the
152 second was installed close to the top of the lighthouse at +37.1 m elevation (Fig. 1a). The two inclinometers
153 were installed at +37.1 m and +22.8 m. The signal from the uppermost inclinometer was low-pass filtered during
154 the data acquisition such that the dynamic content is absent in the data, and therefore the sensor will not be used
155 in this analysis. Frederking [24] detailed how the signals from the tilt may be used to derive the static force.
156 Because the dynamic response of the lowermost inclinometer was claimed to provide accurate measurements
157 only up to 0.5 Hz, the data from this sensor was also omitted in this analysis. Depending on the level of
158 dynamics involved in the ice-structure interaction, the sampling frequency of the measurement system varied
159 between 1 and 100 Hz.

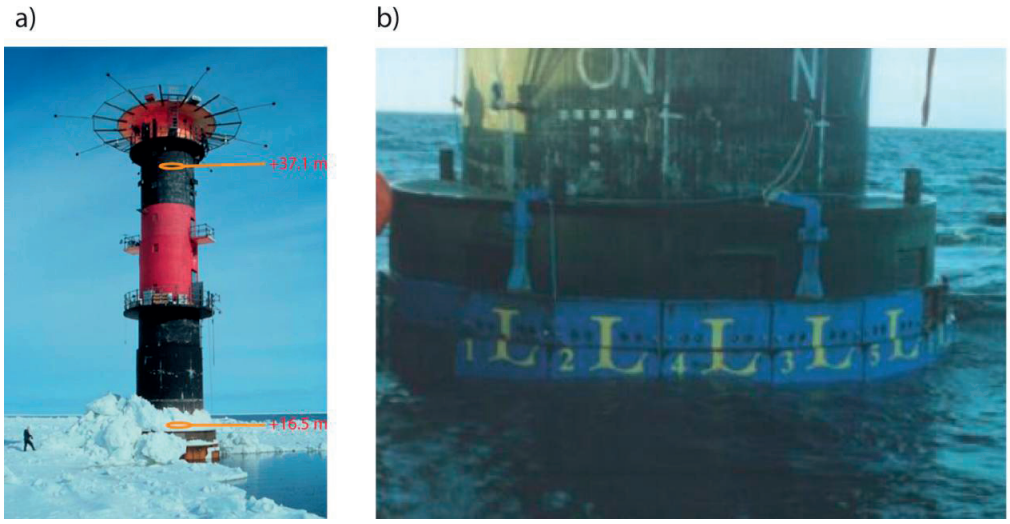

Figure 1. Nordströmsgrund lighthouse: a) Picture of the concrete structure in ice-infested water and accelerometer locations; b) force panels mounted to the outer face.

2.5 Measured forces and event characterizations

Two events of ice-induced vibrations were selected to compare measured and identified forces. One of the events can be characterized by simultaneously occurring peak forces, whereas during the other event, peak forces occur nonsimultaneously. During both events, the force panels covered a substantial amount of the ice-structure interface, and the dynamic forces and structural response were rather violent. Both events were recorded on the same day with a sampling rate of 84 Hz. In what follows, the measured forces are presented together with a more elaborate description of the events. The global forces acting North-South (N-S) and East-West (E-W) were derived from the panel forces by assuming a friction coefficient to include the shear (tangential) forces. Frederking and Barker [25] found the average friction coefficient for sea ice in contact with rough concrete surfaces and corroded steel to be 0.2 and 0.1 for a velocity of 0.01 m/s and for a velocity greater than 0.1 m/s, respectively. Wessels et al. [26] measured the forces on Nordströmsgrund with panels that were equipped with biaxial load cells. A recent study of those normal and tangential forces found an average ratio of 0.2 [27]. To calculate the shear forces in this article, a friction coefficient of $\mu = 0.15$ is used.

2.5.1 Event 1, 12.25 pm, March 30th 2003 (Event ID 3003_0300)

The ice drift direction was 45° (North-East (N-E) direction), and the approximately 0.7 m thick level ice interacted with the structure at a velocity of 0.06-0.065 m/s [5]. The event was initiated at one load panel and spread to the sides. Subsequent ice failures were initiated simultaneously and quasi-simultaneously across the interface, causing large global forces and vibrational responses lasting for approximately 80 s. The panel forces for the first 25 s are shown in Fig. 2a-b, in which a) shows the forces including the quasi-static and dynamic frequency content, whereas b) shows the dynamic forces obtained using a Butterworth high-pass filter with a 0.5 Hz cutoff frequency. Each line color corresponds to a local force measured by a panel oriented from 0 degrees (direct North) to 144 degrees (South-East). The full time histories of the panel forces and their frequency contents are displayed in Fig. 2c and d. The dominant frequency components of the forces for the full event were at 2.082 and 2.23 Hz (Fig. 2d). The onset of the event was studied by Bjerkås and Skiple [28] and Bjerkås et al. [5]. The violent dynamic response heightens our interest in investigating this ice-induced vibration event.

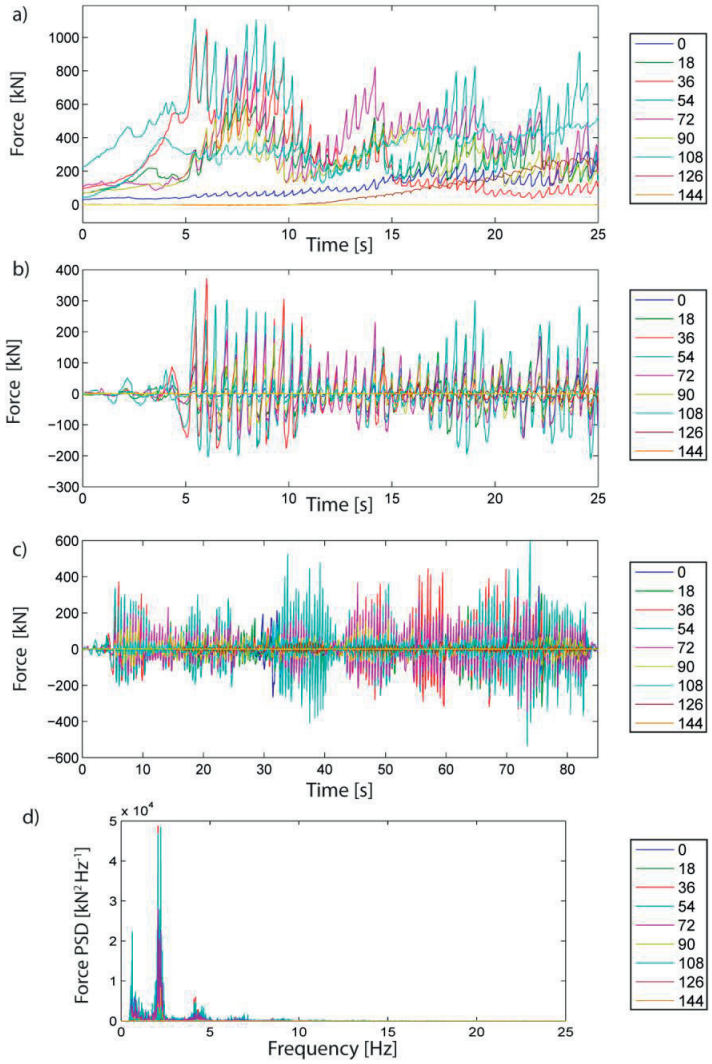

187

188 Figure 2. Local forces during event 1: a) static and dynamic force contents for the first 25 s; b) dynamic content
189 for the first 25 s; and c) frequency contents of the full event (83 s).

190 For the given ice-drift direction angle of 45 degrees, the sums of forces in the N-S and E-W directions were
191 calculated according to Eq. (22) (the directions and symbols are presented in Fig. 3). The shear force
192 components are assumed to change sign when the orientation angle ψ_j of panel number j exceeds the ice-drift
193 direction as shown in Fig. 3. The summation of local forces in the E-W and N-S direction change when the panel
194 orientation exceeds 45 degrees and 90 degrees; therefore, three subsets of force expressions in the global
195 directions ($F_{\mathrm{EW1}}, F_{\mathrm{EW2}}, F_{\mathrm{EW3}}, F_{\mathrm{NS1}}, F_{\mathrm{NS2}}, F_{\mathrm{NS3}}$) were formulated. The global forces F_{EW} and F_{NS} were calculated as

196 the sum of the three subsets in the N-S and E-W directions, respectively, similar to the global forces derived by
197 Kärnä and Yan [29]. The global forces in the N-S and E-W direction vary with the selection of the friction
198 coefficient, increasing on average by 4.8 % and 2.3 % with $\mu = 0.20$ as the friction coefficient, respectively.
199 This will however, also depend on the ice drift direction. Because the ice floe approached from the North-East
200 during the current event, a small portion of the ice-structure interface was unfurnished with panels. The local
201 force acting on the panel facing directly North (panel P0) shows increasing contributions with time (Fig. 2, blue
202 line), indicating that one could expect an unmeasured interaction zone. Bjerkås et al. [5] reported that water was
203 entrapped inside two of the panels, causing uncertainty in the measured forces which is difficult to quantify. No
204 compensating adjustments for the forces resulting from possible water filling and unmeasured areas are
205 incorporated in this paper.

206
$$
\begin{aligned}
F_{EW1}(t) &= \sum_{j=1}^{3} F_j(\mathrm{t})\sin(\psi) + \mu F_j(\mathrm{t})\cos(\psi)\ , \quad 0 \le \psi < 45 \\
F_{EW2}(t) &= \sum_{j=4}^{6} F_j(\mathrm{t})\sin(\psi) - \mu F_j(\mathrm{t})\cos(\psi)\ , \quad 45 \le \psi < 90 \\
F_{EW3}(t) &= \sum_{j=7}^{9} F_j(\mathrm{t})\cos(\psi - 90) + \mu F_j(\mathrm{t})\sin(\psi - 90)\ , \quad 90 \le \psi \\
F_{NS1}(t) &= \sum_{j=1}^{3} F_j(\mathrm{t})\cos(\psi) - \mu F_j(\mathrm{t})\sin(\psi)\ , \quad 0 \le \psi < 45 \\
F_{NS2}(t) &= \sum_{j=4}^{6} F_j(\mathrm{t})\cos(\psi) + \mu F_j(\mathrm{t})\sin(\psi)\ , \quad 45 \le \psi < 90 \\
F_{NS3}(t) &= \sum_{j=7}^{9} -F_j(\mathrm{t})\sin(\psi - 90) + \mu F_j(\mathrm{t})\cos(\psi - 90)\ , \quad 90 \le \psi \\
F_{EW}(t) &= F_{EW1}(t) + F_{EW2}(t) + F_{EW3}(t) \\
F_{NS}(t) &= F_{NS1}(t) + F_{NS2}(t) + F_{NS3}(t)
\end{aligned}
\tag{22}
$$

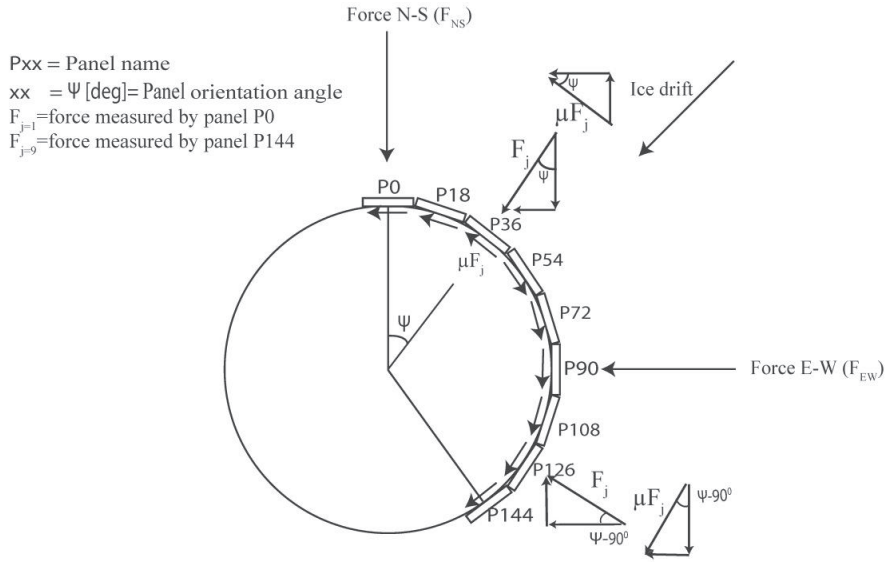

Figure 3. Illustration of the panels, local forces and assumed shear force directions.

2.5.2 Event 2, 30th March, 2003, 22.21.45 pm (Event ID, 3003_1300)

During the evening of March 30th, the ice drift changed direction from the North-East (N-E) to North of North-East (NN-E). The ice conditions were primarily deformed ice created by the reconsolidation of an ice-breaker managed ice floe and naturally deformed ice. These characteristics caused the ice thickness profile to range between 1.3 and 1.75 m, as measured with an electromagnetic system [30]. The electromagnetic antenna was installed approximately 10 m away from the lighthouse at an elevation 2 m above the ice (Fig. 4). Because of the heterogeneity of the deformed ice, the thickness underneath the electromagnetic antenna may differ from the ice thickness at the ice-structure interface. Therefore, determining the precise ice thickness value is difficult. The interaction was governed by a continuous crushing failure at an ice velocity of 0.18 m/s. The personnel stationed at the lighthouse reported that the ice-structure interaction was highly dynamic and that the lighthouse was noticeably shaking [31]. Apart from the interaction that caused high measured forces on the North-East face, an interaction also occurred on the North-West side of the lighthouse. The unfiltered and filtered forces measured by the panels are displayed in Fig. 5a and b, respectively, showing the nonsimultaneous occurrence of peak forces. Unlike the previous event, the local forces are spread over different frequencies (Fig. 5c). Because the ice conditions changed rapidly, this length of this event was limited to 35 seconds. The recorded videos showed that the ice drift direction changed slightly after 35 seconds. The largest local forces are found at 0, 18, 54 and 72 degrees. A low dynamic force contribution is measured from the panel facing 36 degrees, potentially indicating

226 that the panel was filled with water. The pair of global forces acting in the N-S and E-W directions was
227 calculated as described in the previous section, but now with the shear force direction changing at the ice drift
228 direction of 23 degrees.

Figure 4. Snapshot of the video taken during event 2. The light source aiming ahead of the interface with accumulating crushed ice on the deformed ice floe. The EM-antenna hangs 2 m above the ice.

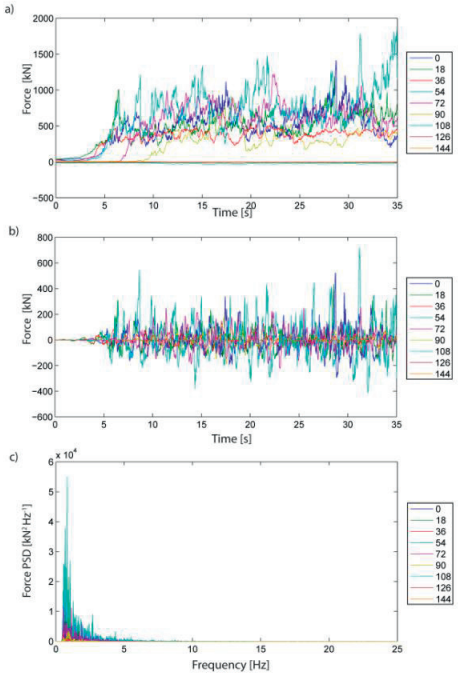

229

Figure 5. Local forces during event 2: a) static and dynamic force contents; b) dynamic content; and c) frequency contents of the full event.

3 Finite element model and model validation

The finite element model displayed in Fig. 6 was modelled with quadrilateral finite membrane-strain shell elements with reduced integration (S4R) using the software ABAQUS. The structural dimensions and material properties are obtained from Heinonen et al. [22]. The concrete density is increased to account for the additional mass from the insulation in the superstructure walls. The foundation plate is modelled as a rigid body, and the soil stiffness and added soil mass are assigned to the center node of the foundation. Volume-proportional added mass is used to account for the mass of the sand inside the foundation caisson, the displaced water and the mass of the load panels. The soil stiffness and material parameters corresponds to the Model "E400" in [22], while the combined mass of the sand fill, panels and displaced water was calculated to be 8201.2 tons. The stiffness of the sand-fill inside the caisson and the embankment of cement-grouted crushed stones on top of the foundation sand fill are neglected in the model, which are assumptions consistent with the models of Heinonen et al. [22] and Popko [32]. The parameters used in the finite element model are given in Table 1. The eight first-vibration modes (except for a torsion mode) with the corresponding natural frequencies are displayed in Fig. 7. The modes are almost symmetric in the x-y direction, explaining why the natural frequencies are almost identical and differ with a maximum of +/- 0.01 Hz. The selection of modes for the reduced-order model according to Eqs. (4) and (7) will be further demonstrated in section 3.1.

Table 1. FE Model properties

Model Parameters							
Soil stiffness k_x and k_y [kN/m]	Soil stiffness k_θ	Soil berm mass M_x M_y [kg]	Soil berm moment of inertia J_{xx}, J_{yy} [kg m^2]	Added mass of the sand and displaced water [kg]	Concrete density [kg/m^3]	Concrete Young's Modulus [Pa]	Sand density [kg/m^3]
$7.75 \cdot 10^9$	$9.60 \cdot 10^{11}$	$1.52 \cdot 10^6$	$4.51 \cdot 10^8$	$8.20 \cdot 10^6$	$2500 - 2776$	$28.53 \cdot 10^6$	2000

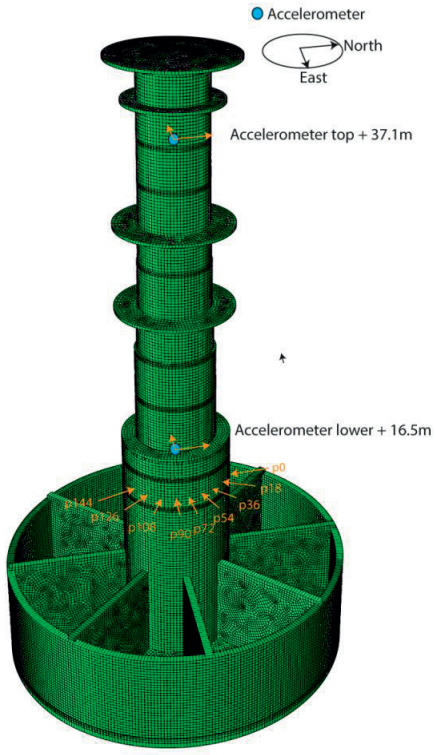

Figure 6. Finite element model and sensor locations.

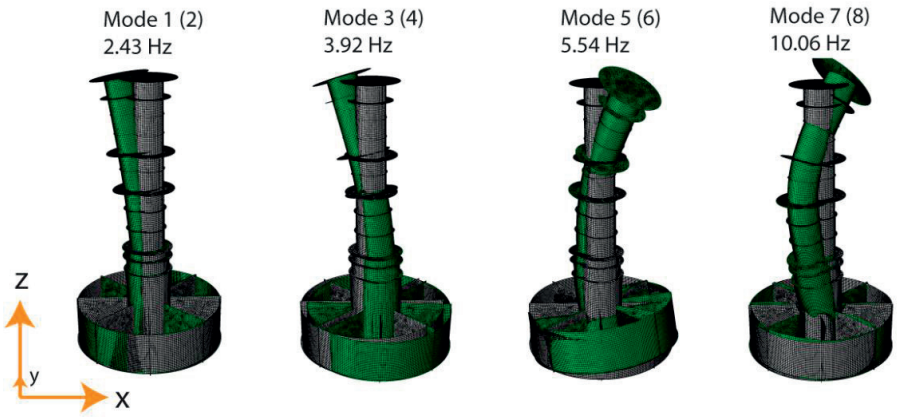

Figure 7. The first eight retained structural modes in the reduced-order model.

3.1 Model reduction and model validation

Modelling errors in terms of natural frequencies, modal damping ratios and time discretization are accounted for in the identification algorithm (section 2.3) by the state error-covariance matrix, $\mathbf{Q}$. The first natural frequency of the lighthouse has been reported to range between 2.3 [10] and 2.8 Hz [5]. The 2.8 Hz value was based on measured oscillations at the lantern deck during the late winter in 1972 [33], when drifting ice sheets were stopped by the lighthouse. The 2.3 Hz value was based on measured accelerations during ice action and calculations that considered the actual foundation. In a later report [34], the vibrations measured at the end of events of "resonant vibrations" caused by ice action were considered to be sequences of free vibrations, from which the first natural frequency was estimated to be 2.3-2.4 Hz. The frequency lock-in vibrations occur often at a frequency 5 to 15 % lower than the natural frequency [35].

Possible degradation of the structural health because of years of service in heavily ice-concentrated waters also represents an uncertainty. For instance, cracks have been observed in the concrete at locations prone to large dynamic stresses [36]. This motivates a verification of the modally reduced order finite element model to ensure accurate model-based force identifications in the next chapter.

After extracting all the (217) modes in the frequency range up to 70 Hz, the selection of vibration modes for the modally reduced order model is performed. This selection studies which modes are influenced by the assumed force location and which modes can contribute to the accelerometer response. Thereafter the acceleration responses are simulated using the measured global forces from section 2.5.1 (event 1) and the two different models: one constructed with all modes up to 70 Hz (217 modes), and one constructed with the selected, reduced number of vibration modes. The reduced-order state-space models were obtained according to Eqs. (4) and (7) using the modal properties from the finite element model and assuming a damping ratio of 3 % for all modes. To study which modes are influenced by the assumed force locations P0 and P90 (cf. Fig. 6), the modal projections of the forces $\mathbf{S}_p^T\mathbf{\Phi}$ were calculated. To study which modes potentially contribute to the acceleration response at the two accelerometer locations, the projection matrix $\mathbf{S}_a\mathbf{\Phi}$ was calculated. The force influence map $\mathbf{S}_p^T\mathbf{\Phi}$ and modal response contribution map $\mathbf{S}_a\mathbf{\Phi}$ for a selection of 24 modes are displayed in Fig. 8. These modes were selected because they show a significant force influence and a significant response contribution to the top and/or lower accelerometer. All modes are excited by either the N-S or E-W force. The top accelerometer location shows a significant contribution from all modes. The lower accelerometer location shows only a small contribution from the modes 15, 16, 19, 20, 23 and 24, but because they contribute significantly to the top accelerometer location, they are also retained.

The state-space model presented in Eqs. (8) and (9) is now used to simulate the response at the sensor locations using the measured forces for event 1, thus providing information on the accuracy of the finite element model, the assumption of the two concentrated forces, and the sensor locations. The N-S and E-W forces were applied in the nodal locations corresponding to P0 and P90 in Fig. 6, respectively. Because errors in the measured forces will propagate through the system equations and affect the simulated results, the simulated response should only be interpreted as a means to detect large discrepancies. The applied force and comparisons between the frequency contents of the measured and simulated accelerations in the E-W direction using, respectively 217 and 24 modes are shown in Fig. 9a-c. The frequency spectrum obtained with the selected 24 modes is almost identical to the frequency spectrum obtained using 217 modes. The model constructed with 217 modes can represent dynamic behaviors up to frequencies of 70 Hz, whereas the model constructed with 24 modes cover (selected) natural frequencies up to 60 Hz (Table 2). A similar correspondence is found for the accelerations in the N-S direction.

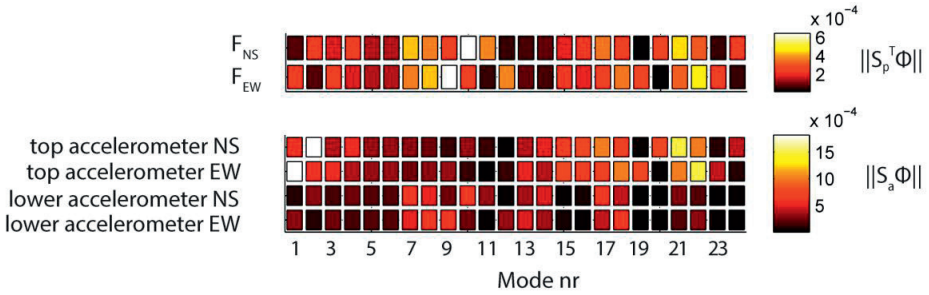

Figure 8. Force influence map $\mathbf{S}_p^T\mathbf{\Phi}$ (top map) and modal contribution map (bottom map) of the accelerometer locations $\mathbf{S}_a\mathbf{\Phi}$.

Table 2. Natural frequencies of the reduced-order model.

Mode	1,2	3,4	5,6	7,8	9,10	11,12	13,14	15,16	17,18	19,20	21,22	23,24
Frequency [Hz]	2.43	3.92	5.54	10.06	16.75	20.09	28.23	37.16	42.31	57.01	58,90	59,74

The frequency contents of the simulated accelerations (Fig. 9b-c) show that both models can accurately represent vibrations at the frequency dominant in the measured response and force signals, i.e., at 2.23 Hz. A mismatch between the simulated and measured frequency contents is observed beyond the dominant frequency at 2.23 Hz.

303 The peaks in the simulated accelerations at approximately 3.98, 10.08 and 16.78 Hz are absent in the measured
304 accelerations. They correspond to the natural frequencies for mode 3, 4, 7, 8, 9 and 10 (Table 2). The occurrence
305 of these peaks may be explained by an inaccurate model, but they can also occur because of the response of the
306 force panels, noise in the force panels, nonlinear effects not accounted for or a combination of these four factors.
307 The time histories of the measured and simulated accelerations are displayed in Fig. 10a and b. A much larger
308 discrepancy between the simulated and measured accelerations occurs at the end of the event when a crack
309 propagated across the ice sheet (described in Bjerkås et. al [5]). The accumulated ice blocks and crushed ice
310 were flooded with water, and the dynamic interaction vanished. In summary, the dynamic behavior at and around
311 the dominant frequency is simulated well with both reduced-order models, while the simulated higher frequency
312 contents deviate from the measured values. Despite that, similar amplitudes are obtained, and the use of a pair of
313 global forces in conjunction with a reduced-order model appears to be reasonable. The reduced-order model with
314 24 modes is used throughout this paper. This model rendered almost identical simulated accelerations to the 217
315 mode model, and it saves significant computational time during the force identification in the subsequent
316 sections.

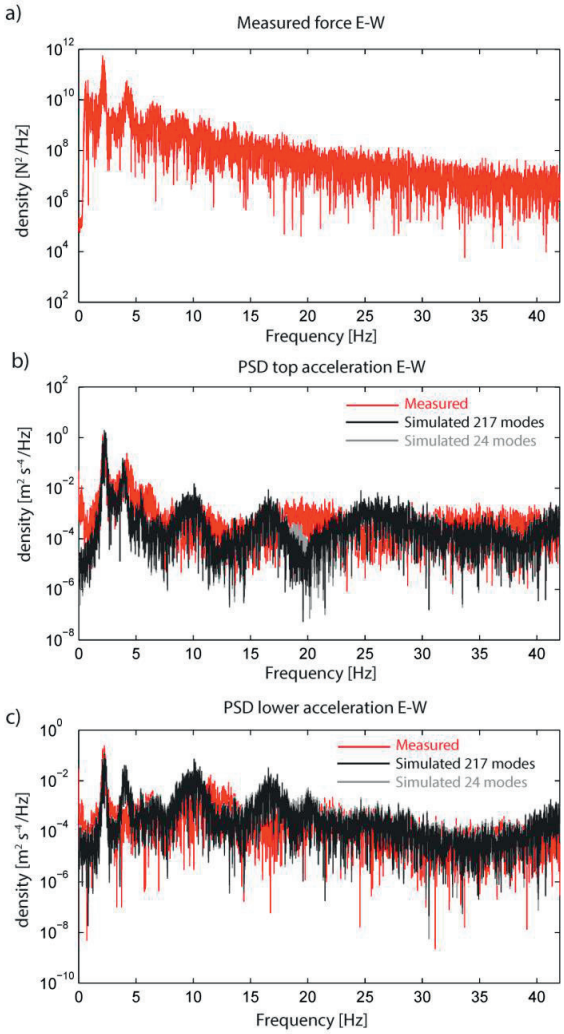

317

318 Figure 9. Frequency content of the applied forces (a) and simulated versus measured acceleration signals at the
319 top (b) and at the lower accelerometer location (c).

320

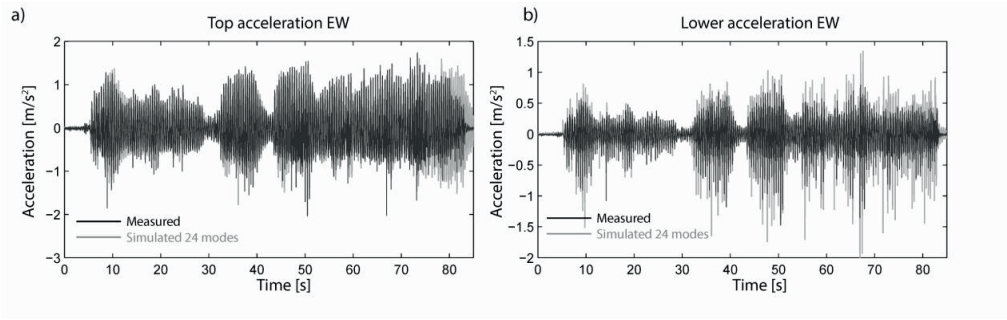

Figure 10. Simulated versus measured accelerations at the top (a) and at the lower accelerometer location (b).

4 Force identification

4.1 Force identification event 1.

For the force identification and response prediction in the next sections, the modelling errors are considered by the state error covariance matrix $\mathbf{Q}$. In accordance with its definition, the diagonal elements of this matrix were assigned values corresponding to the square of a small percentage of the standard deviation of the simulated states or, more specifically, the square of 10 % of the standard deviation of the simulated first modal displacement. The measurement noise represented by the error covariance matrix, $\mathbf{R}$, accounts for the sensor noise. Another source of measurement noise that applies to the lowermost sensors is the diesel generators, located on the +22.5 m deck that supplied electricity to the lighthouse. An indication of the measurement noise level could be obtained by calculating the variance of the measurement data in ice-free conditions. Such data was, however, not found, and would most likely not be at the same high sampling frequency. Therefore, the square of a small percentage of the standard deviation of the acceleration response (5 % of the standard deviation of the top acceleration in the E-W direction) was assigned to the diagonal of the measurement noise covariance matrix. In all of the following analyses, the matrices $\mathbf{Q}, \mathbf{R}$ and $\mathbf{P}_{0|-1}$ are assigned the values $2.3\cdot10^{-2}, 6.6\cdot10^{-4}$ and $2.3\cdot10^{-2}$ on the diagonal, respectively.

The forces were identified from the data measured by the two biaxial accelerometers shown in Fig. 6 using the JIS-algorithm presented in Eqs. (12)-(21). Because no displacement or strain measurements were available, the inversion is characterized by marginally stable transmission zeros at 0 Hz [37], implying an inability to identify the static component of the forces. These marginally stable transmission zeros cause a low-frequency drift in the identified forces and states, which can be removed using a high pass filter. Recently, Eftekhar et. al [38] proposed a new Kalman filter approach to overcome low-frequency drift problems when only accelerometer

344 measurements are used for the identification. A comparison with the results obtained using this algorithm is,
345 however, considered to lie outside the scope of this paper.

346 The raw data are used for the identification, while the identified forces and states are filtered with a Butterworth
347 high pass filter with a cut-off frequency of 0.5 Hz, well below the dominant response frequency and the first
348 natural frequency of the structure. The measured forces are also filtered with the identical high pass filter to
349 simplify the comparison (see Fig. 2 for the filtered and unfiltered forces). The identified forces in the E-W and
350 N-S directions show somewhat larger amplitudes than the measured forces (Fig. 11a-b and Fig. 12a-b). The
351 identified major frequency contents coincide well with those measured (Fig. 11c-d). With the combined
352 uncertainty in the force measurements and the modelling errors, the overall agreement is satisfactory. The
353 identified forces were therefore demonstrated to represent the rapid changes throughout the event, and the
354 amplitudes and frequency contents of the forces during a frequency lock-in event are captured well.

355

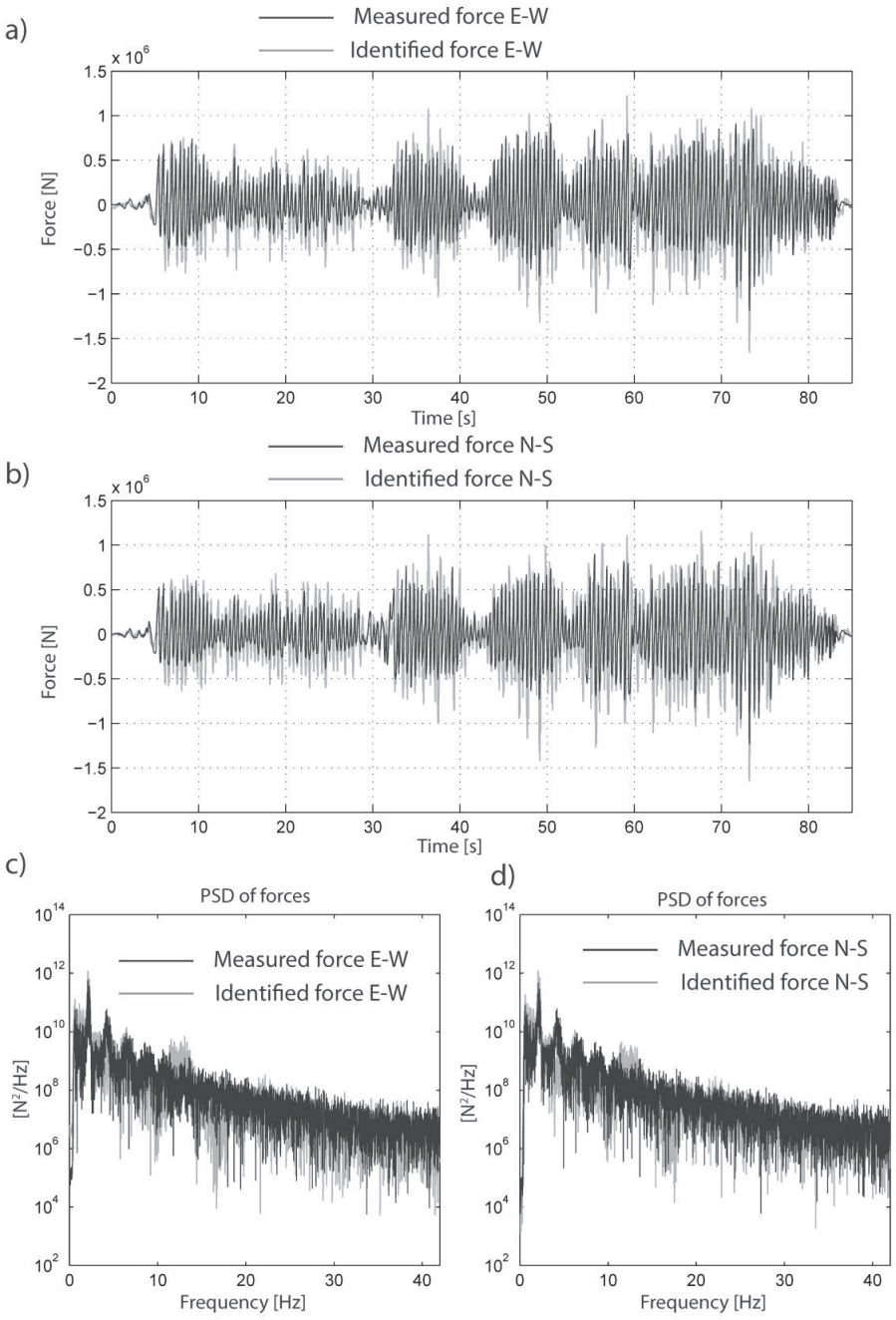

356

357 Figure 11. Identified versus measured forces: a) Time history in the E-W direction; b) Time history in the N-S
358 direction; c) Frequency contents of the forces in the E-W direction; and d) Frequency contents of the forces in
359 the N-S direction.

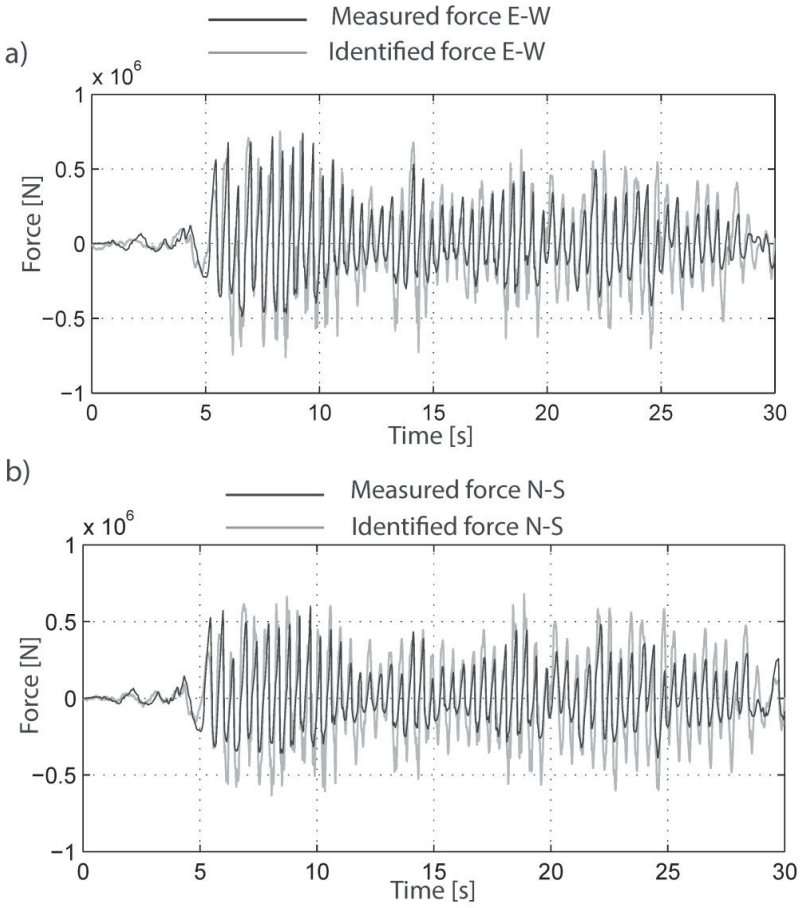

Figure 12. Zoomed time histories of the measured versus identified forces: a) forces in the E-W direction; and b) forces in the N-S direction.

4.2 Force identification event 2.

The forces were identified using the same sensors, covariance matrices, $\mathbf{Q}, \mathbf{R}$ and $\mathbf{P}_{0|-1}$, and filtered with the identical high pass filter as in the previous section. Select peaks of the identified force in the E-W direction agree with the measured force, whereas others differ (Fig. 13a) considerably. A similar agreement is obtained in the N-S direction (Fig. 13b). Examples of the identified peaks which are not measured can be found after 5 s, 11 s and 16 s in Fig. 13a and after 8 s, 16 s and 22 s in Fig. 13b. The identified forces coincide well with the measured forces in select intervals, for instance between 21-23 s in Fig. 13a and between 23-26 s in Fig. 13b. The frequency contents of the identified forces (Fig. 13c-d) deviate somewhat from the measured forces. A similar, decaying trend is noted in the frequency range up to 10 Hz. As shown in Fig. 5, the major local force peaks are found in the panels P0, P18, P54 and a few in P72. The difference between the measured and identified forces

373 can partly be explained by the nonsimultaneous occurrence of peak forces in combination with an incomplete
374 portion of the ice-structure interface being measured. Dynamic local forces acting nonsimultaneously can either
375 decrease or amplify the global force summation. The unmeasured peaks in the force-time histories may be
376 explained by significant local forces acting outside the area covered by the force panels. The peaks which appear
377 in the measured forces, but which are absent in the identified forces, may be explained by unmeasured local
378 forces that cancel the measured forces out. Because of the uncertain ice thickness, the ice-structure interface may
379 also include areas below the load panels. Panel P36 (c.f. Fig. 5) measured surprisingly low dynamic
380 contributions, which may indicate that water was trapped inside the panel. Because the nonsimultaneous
381 occurring peak forces contribute to the response at different discrete time incidents, the data must be recorded
382 with a high sampling frequency. The number of identified forces is likely less important because of the rigidity
383 of the 1.4 meter thick concrete on which the panels are installed as long as they are reconstructed from response
384 measurements that capture the driving information from the nonsimultaneous ice failures. The time-variant
385 attack point(s) because of the uneven ice-thickness may also influence the distance between the accelerometer
386 and the attack point(s) and hence the quality of the identified forces. However, the overall agreement between
387 the measured and identified forces is deemed satisfactory, therewith also the assumed force locations.

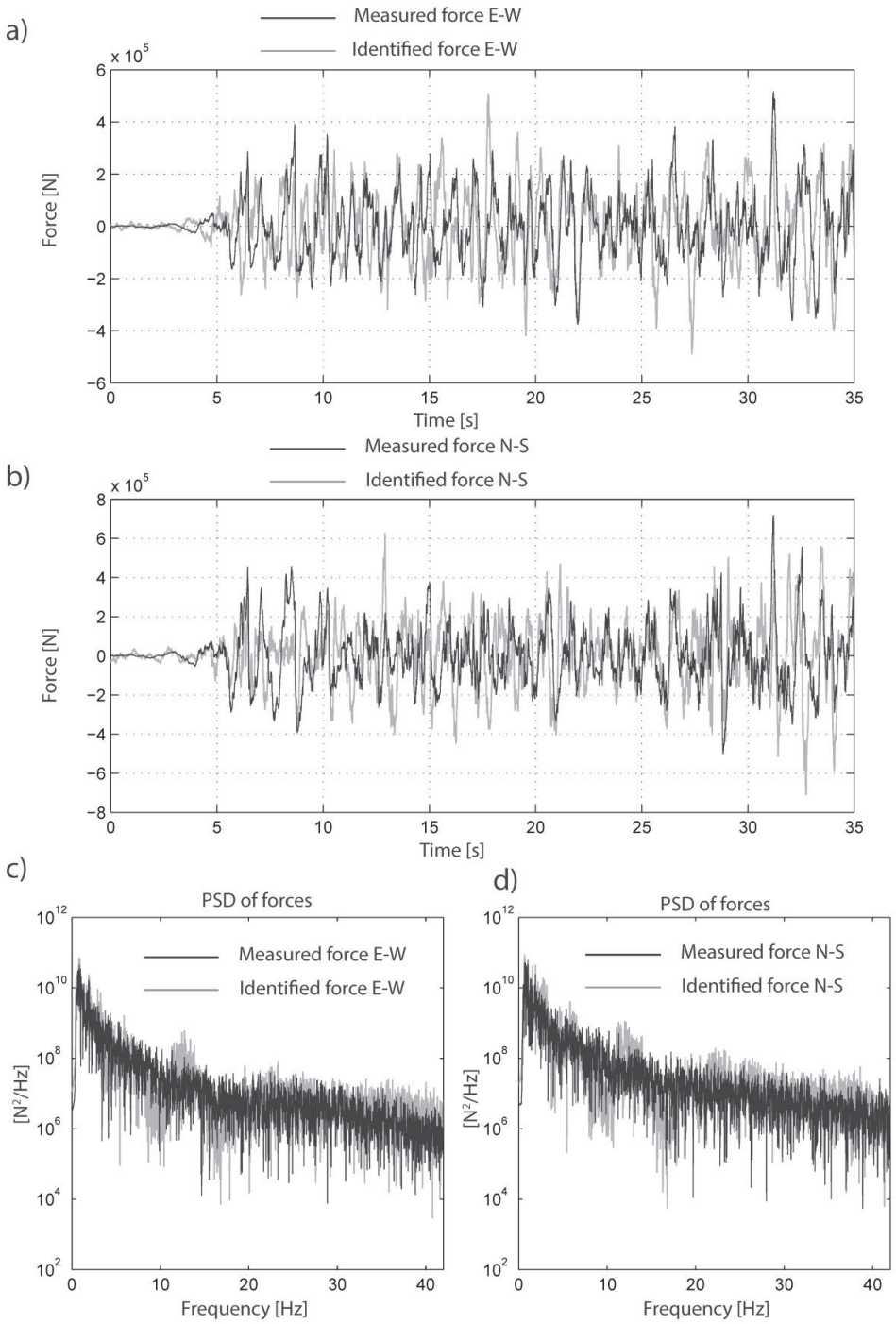

Figure 13. Identified (grey color) versus measured (black color) forces: a) Time history in the E-W direction; b) Time history in the N-S direction; c) Frequency contents of the forces in the E-W direction; and d) Frequency contents of the forces in the N-S direction.

4.3 Structural response estimation

The frequency content of the structural response of Baltic lighthouses because of ice-induced vibrations has been reported to be dominated by both the first and the second vibration mode of these structures [7]. For a survey of frequency lock-in vibrations on lighthouses, see Määttänen [12]. The spatially complete response can be used to assess the structural behavior as the ice conditions change but also to detect locations that are suitable or unsuitable for operations and installations. For operational purposes, the vibratory response can be of interest at locations vulnerable to fatigue damage or at locations at which secondary components are installed.

Kärnä and Turunen [39] showed that during several laboratory experiments and full-scale events, the structural velocity amplitudes at the ice-action point were 10-40 % higher than the ice velocity during the frequency lock-in vibrations. The compliance of the ice-field was suggested to allow the structure to move slightly faster than the ice. Therefore, the ratio between the structural velocity amplitude at the ice-action point and the ice velocity, $\beta = \frac{\dot{u}_{\mathrm{ca}}}{\dot{u}_{\mathrm{ice}}}$, is expected to be in the range 1.1 to 1.4. The velocity and displacements at the ice-action point cannot be obtained by integration of the non-collocated accelerometer time histories. The joint input-state estimation algorithm can, however, be used to identify the response at all unmeasured locations.

4.3.1 Velocity and displacement during frequency lock-in

Because the dynamic response during frequency lock-in vibrations are the least understood and potentially the most damaging, this section focuses chiefly on the dynamic response during event 1. The ice drift velocity is assumed constant during the event, being approximately $0.06/\sqrt{2}$ m/s in the N-S and E-W directions, and displayed as a straight line in Fig. 14a. The velocity at the ice-action point which was jointly estimated with the forces in section 4.1 (Fig. 14a) infrequently exceeds the ice velocity during the load build up. Subsequent to the initiation of ice failure, the continuous crushing process pulverizes and clears the ejecta from the ice-structure interface. Each ice failure causes the structure to rebound dynamically in the range of 1 to 3 mm in the N-S and E-W direction (Fig. 14b), and the dominant frequencies of the estimated displacements at the ice-action point are at 2.08 and 2.23 Hz (Fig. 15).

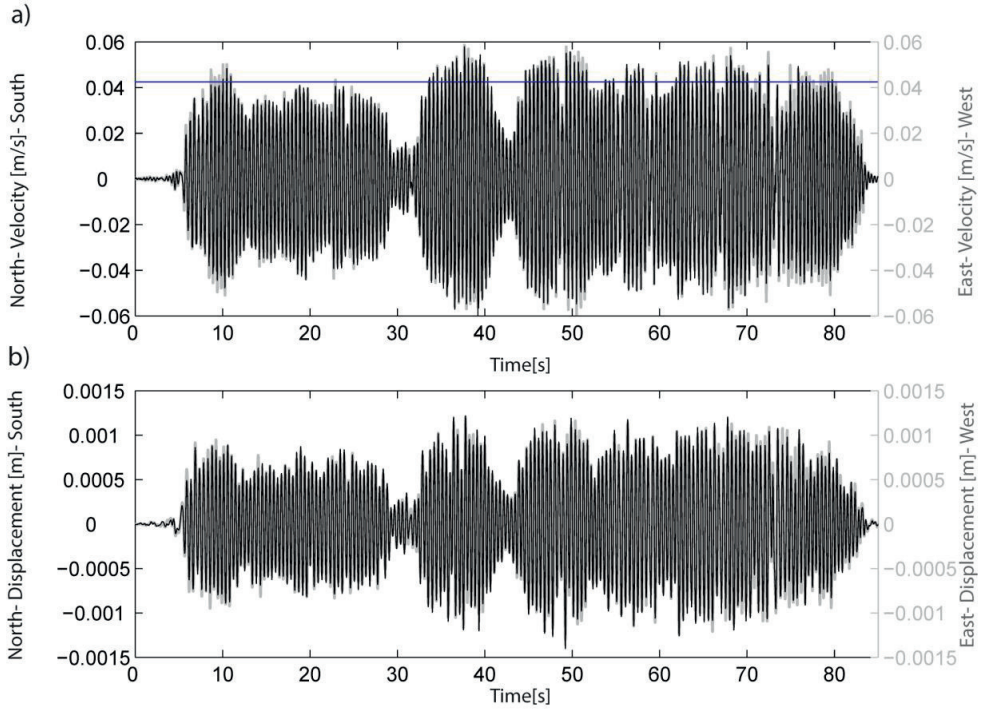

412

413 Figure 14. Estimated responses in the North-South (black lines) and in the East-West (grey lines) direction at the
414 ice action point: a) estimated velocity; and b) estimated displacement.

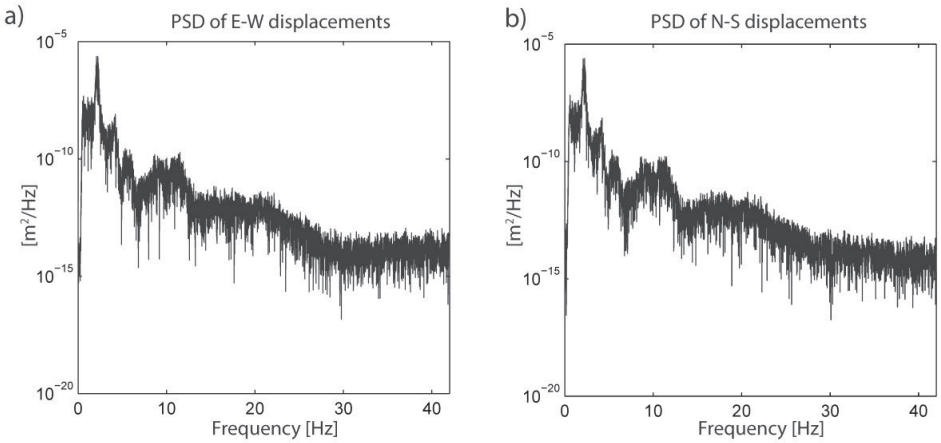

415

416 Figure 15. Frequency contents of the estimated structural displacement at the ice action point: a) displacements
417 in the E-W direction; and b) displacements in the N-S direction.

418 The structural motion often primarily corresponds to the direction of the ice drift. However, by estimating the
419 time history of the displacement response on each floor, the horizontal motion was found to deviate slightly from

a perfect line and to enter an elliptic motion (Fig. 16). It is likely that the magnitude, direction and sequence of the local forces can cause this elliptic motion (in addition to being caused by an eccentric mass centroid and inhomogeneous foundation properties). The vibrations that showed elliptic behavior in the horizontal plane were more pronounced during event 2 (Fig. 16c-d) than event 1 (Fig. 16a-b). However, the vibrations were sustained for a few cycles only during event 1 with approximately the identical shape and amplitude. The only difference from event 1 to event 2 is the ice conditions. Therefore, the ice conditions likely provoke individual vibration cycles to enter this elliptic motion. Recent ice-induced vibration model-scale experiments by Ziemer and Evers [40] showed similar in-plane vibratory displacements. They found that circular in-plane vibrations occurred with lower ice thicknesses and higher ice velocities than straight in-plane frequency lock-in vibrations.

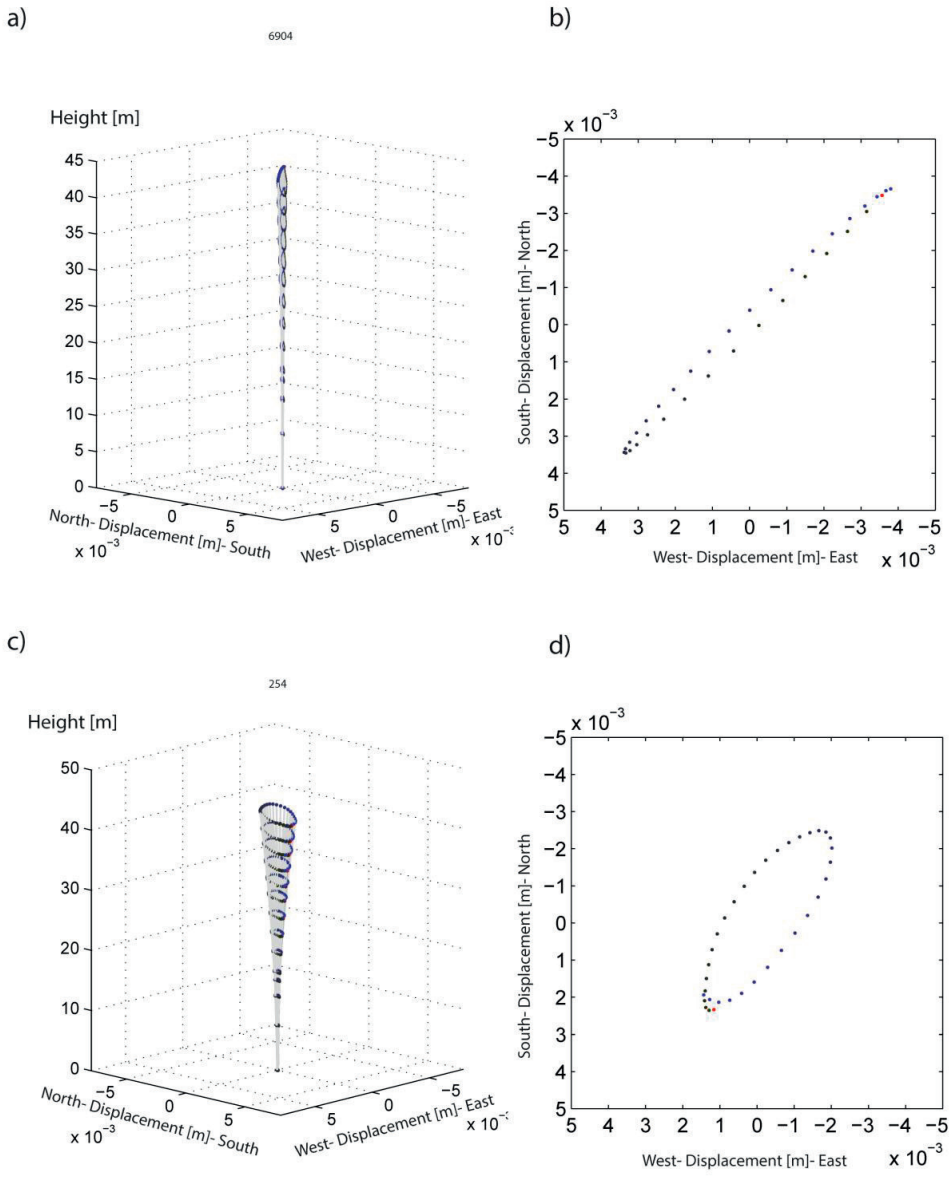

429

430 Figure 16. Time history of the structural response during one cycle of elliptic vibrations: a) estimated
431 displacement at each building floor during event 1; b) Horizontal displacements of the top floor during event 1; c)
432 estimated displacement at each building floor during event 2; and d) Horizontal displacements of the top floor
433 during event 2.

434

5 Conclusions/Discussion

A comparison between the measured and identified dynamic ice forces on a full-scale structure is presented. A framework for force identification, a description of the finite element model used and a summary of the assumptions utilized to obtain global ice forces from load panel measurements are presented.

The global dynamic forces acting on the Nordströmsgrund lighthouse are successfully identified using a joint input-state estimation algorithm in conjunction with a limited number of accelerometer measurements and a modally reduced order model. This model was based on limited quantitative information covering the dynamic properties. Convincing agreements between the measured and identified forces are found for the two ice-structure interaction events considered. During frequency lock-in, the amplitudes of the identified forces are found to be slightly higher than the measured forces. This result was expected because a portion of the ice-structure interface was not covered by load panels. A satisfactory agreement is also obtained during continuous brittle crushing despite the fact that select peaks are missing in both the measured and identified forces.

The maximum structural velocity during frequency lock-in was often slightly higher than the ice velocity, agreeing with previous observations. The dynamic ice forces during both events caused the lighthouse to occasionally enter an elliptical motion in the horizontal plane.

The presented results present a solid motivation to employ the joint input-state estimation algorithm to identify dynamic ice forces on full-scale structures. This process enables an assessment of the dynamic ice forces during many events that resulted in heavy vibrations of the lighthouse that the force panels did not cover. However, the results depend on the accuracy of the model. New studies of similar structures would benefit from dynamic calibrations of the structure to allow for the utilization of updated finite element models based on the measured dynamic properties.

6 Acknowledgements

The authors wish to acknowledge the support from the Research Council of Norway through the Center for Research-based Innovation SAMCoT and the support from all SAMCoT partners. The authors are grateful for the extensive help from Morten Bjerkås (Reinertsen AS) and Peter Jochmann (HSVA GmbH). The full-scale measurements were funded by the European Commission DG RESEARCH under the Fifth Framework Program for Research and Development within the Energy, Environment and Sustainable Development (EESD) Program under the Key Action RTD activities of a generic nature (Contract No. EVG1-CT-2000-00024)

Reference

[1] Brown TG. Analysis of ice event loads derived from structural response. Cold Regions Science and Technology. 2007;47:224-32.

[2] Timco GW. ICE FORCES ON MULTI-LEGGED STRUCTURES. Proceedings of Ice research for a sustainable environment (IAHR). Iowa City, United States1986.

[3] Jefferies MG, Wright WH. DYNAMIC RESPONSE OF "MOLIQPAQ" to ice-structure interaction. Proceedings of Proc 7th International conference on Offshore Mechanics and Arctic Engineering (OMAE 88). Houston, Texas, United States1988.

[4] Bruce JR, Brown TG. OPERATING AN ICE FORCE MONITORING SYSTEM ON THE CONFEDERATION BRIDGE. Proceedings of Proceedings POAC '01. Ottawa, Canada2001.

[5] Bjerkås M, Meese A, Alsos HS. Ice Induced Vibrations- Observations of a Full-Scale Lock-in Event. Proceedings of Proceedings of the Twenty-third International Offshore and Polar Engineering Anchorage, Alaska: International Society of Offshore and Polar Engineers (ISOPE); 2013.

[6] Bjerkås M. Wavelet transforms and ice actions on structures. Cold Regions Science and Technology. 2006;44:159-69.

[7] Määttänen M. EXPERIENCES OF ICE FORCES AGAINST A STEEL LIGHTHOUSE MOUNTED ON THE SEABED, AND PROPOSED CONSTRUCTIONAL REFINEMENTS. Proceedings of Port and Ocean Engineering under Arctic conditions (POAC). Fairbanks, Alaska1975.

[8] Määttänen M. True ice force by deconvolution. Proceedings of 1st International Modal Analysis Conference (IMAC). Orlando, FL, USA1982.

[9] Yue Q, Qu Y, Bi X, Tuomo K. Ice force spectrum on narrow conical structures. Cold Regions Science and Technology. 2007;49:161-9.

[10] Engelbrektson A. Dynamic ice loads on a lighthouse structure. Proceedings of Fourth international conference on Port and Ocean engineering under Arctic Conditions (POAC). St. John's, Newfoundland, Canada1977.

[11] Blankarn KA. Measurment and analysis of ice forces on Cook Inlet structure. Offshore Technology Conference. Houston, TX1970. p. 365-78.

[12] Määttänen M. Ice velocity limit to frequency lock-in vibrations. International symposium on Ice, IAHR. Vancouver, Canada2008. p. 1265-76.

[13] Kärnä T, Turunen R. Dynamic response of narrow structures to ice crushing. Cold Regions Science and Technology. 1989;17:173-87.

[14] Yue Q, Guo F, Kärnä T. Dynamic ice forces of slender vertical structures due to ice crushing. Cold Regions Science and Technology. 2009;56:77-83.

[15] Montgomery CJ, Lipsett AW. ESTIMATION OF ICE FORCES FROM DYNAMIC RESPONSE. Proceedings of International Symposium on Ice (IAHR). Quebec, P.Q. Canada1981.

[16] Timco GW, Frederking R, Singh SK. THE TRANSFER FUNCTION APPROACH FOR A STRUCTURE SUBJECTED TO ICE CRUSHING. POAC. Luleå, Sweden1989. p. 420-30.

[17] Gillijns S, De Moor B. Unbiased minimum-variance input and state estimation for linear discrete-time systems with direct feedthrough. Automatica. 2007;43:pp. 934-7.

[18] Lourens E, Papadimitriou C, Gillijns S, Reynders E, De Roeck G, Lombaert G. Joint input-response estimation for structural systems based on reduced-order models and vibration data from a limited number of sensors. Mechanical Systems and Signal Processing. 2012;29:pp. 310-27.

[19] Nord TS, Lourens E-M, Øiseth O, Metrikine A. Model-based force and state estimation in experimental ice-induced vibrations by means of Kalman filtering. Cold Regions Science and Technology. 2015;111:pp. 13-26.

[20] Maes K, Lourens E, Van Nimmen K, Van den Broeck P, Guillaume P, De Roeck G, et al. Verification of joint input-state estimation by in situ measurements on a footbridge. Proceedings of Proceedings of the 9th International Workshop on Structural Health Monitoring, IWSHM. Stanford, CA, USA 2013.

[21] Bjerkås M. Ice action on offshore structures [PhD]: NTNU, ISBN 82-471-7756-0; 2006.

[22] Heinonen J, Kärnä T, Luo C. Dynamic Behavior of the Nordströmsgrund Lighthouse, STRICE- REPORT. VTT Technical Research Centre of Finland and Luleå University of Technology; 2003. p. 30.

[23] Jochmann P, Schwarz J. Ice force measurements at lighthouse Nordströmsgrund- winter 1999, LOLEIF Report No. 5, MAS3-CT-97-0098. Hamburgische shiffbau-versuchsantalt GmbH; 1999. p. 48.

[24] Frederking R. Tiltmeter application at Nordströmsgrund lighthouse- Strice Project. Proceedings of 18th International Conference on Port and Ocean Engineering Under Arctic Conditions 2005.

[25] Frederking R, Barker A. Friction of Sea Ice on Various Construction Materials, Technical report, HYD-TR-67, PERD/CHC 3-49. Ottawa, Canada: National Research Council of Canada; 2001.

519 [26] Wessels E, Jochmann P, Hoffmann L. FIRST RESULTS OF ICE FORCE MEASUREMENTS WITH TIP -
520 PANELS AT NORSTRÖMSGRUND LIGHTHOUSE. Proceedings of 10th International Conference on Port
521 and Ocean Engineering under Arctic Conditions. Luleå, Sweden1989.
522 [27] Slidring-Larsen. Numerical modelling of ice induced vibrations of lock-in type [Master]. NTNU: NTNU;
523 2014.
524 [28] Bjerkås M, Skiple A. Occurrence of intermittent and continuous crushing during ice-structure interaction.
525 Proceedings of Proceedings of the 18th international Conference on Port and Ocean Engineering under Arctic
526 conditions (POAC). Potsdam, NY, USA2005.
527 [29] Kärnä T, Yan Q. Analysis of the size effect in ice crushing- edition 2, VTT INTERNAL REPORT, RTE50-
528 IR-6 , Ver. 1.3. 2009. p. 205.
529 [30] Haas C, Jochmann P, Gehrish S, Kärnä T, Kolari K, Bjerkås M, et al. Full scale measurements at
530 Lighthouse Norströmsgrund –winter 2003-Annex H2 EM ice thickness measurements. STRICE report2003.
531 [31] Kärnä T, Bonnemaire B, Bjerkås M, Jochmann P. NSG, LOGBOOK, 30. March 2003. 2003.
532 [32] Popko W. Comparison of full-scale and numerical model dynamic responses of Nordströmsgrund
533 lighthouse. Proceedings of Proceedings of the ASME 2014 33rd International Conference on Ocean, Offshore
534 and Arctic Engineering (OMAE). San Francisco, Californica, USA2014.
535 [33] Bjørk B. Ice-induced Vibration of Fixed Offshore Structures. Part 2: Experience with Baltic Lighthouses:
536 Ship Research Institute of Norway, Information Department; 1981.
537 [34] Engelbrektson A. Methods for Structural Response Measurements and their Transformation to Ice Forces,
538 Report No. 3. VBB; 1987.
539 [35] Kärnä T. Mitigation of Steady-State Vibrations Induced by Ice. Proceedings of International Offshore and
540 Polar Engineering Conference. Osaka, Japan, ISBN 1-880653-12-51994.
541 [36] Bjerkås M, Albrektsen A, Gürtner A. STATIC AND DYNAMIC ICE ACTIONS IN THE LIGHT OF NEW
542 DESIGN CODES, paper no 20036. 29th International Conference on Ocean, Offshore and Arctic Engineering.
543 Shanghai, China2010.
544 [37] Maes K, Lourens E, Van Nimmen K, Reynders E, De Roeck G, Lombaert G. Design of sensor networks for
545 instantaneous inversion of modally reduced order models in structural dynamics. Mechanical Systems and Signal
546 Processing. 2014.
547 [38] Eftekhar Azam S, Chatzi E, Papadimitriou C. A dual Kalman filter approach for state estimation via output-
548 only acceleration measurements. Mechanical Systems and Signal Processing. 2015;60–61:866-86.
549 [39] Kärnä T, Turunen R. A straightforward technique for analysing structural response to dynamic ice-action. In:
550 Ayorinde OA, Sinha NK, Sodhi DS, editors. International Conference of Offshore Mechanics and Arctic
551 Engineering1990.
552 [40] Ziemer G, Evers K-U. ICE MODEL TESTS WITH A COMPLIANT CYLINDRICAL STRUCTURE TO
553 INVESTIGATE ICE-INDUCED VIBRATIONS. Proceedings of Proceedings of the ASME 2014 33rd
554 International Conference on Ocean, Offshore and Arctic Engineering, OMAE. San Francisco, California, USA,
555 paper no. 240112014.

556

Appendix 5 Sensor network for dynamic ice-force identification: The Hanko-1 channel marker case study

This appendix includes the conference paper presented at the 23rd International Conference on Port and Ocean Engineering under Arctic Conditions (see below).

- Nord, T.S., Øiseth, O. Petersen, Ø.W., Lourens, E., 2015b. Sensor network for dynamic ice-force identification: The Hanko-1 Channel Marker case study, Proceedings of the 23rd International Conference on Port and Ocean Engineering under Arctic Conditions (POAC), Trondheim, Norway, Paper no. 160.


POAC'15
Trondheim, Norway

Proceedings of the 23rd International Conference on
Port and Ocean Engineering under Arctic Conditions
June 14-18, 2015
Trondheim, Norway

Sensor network for dynamic ice-force identification: The Hanko-1 channel marker case study

Torodd S. Nord[1,2], Ole Øiseth[3], Øyvind Wiig Petersen[3], Eliz-Mari Lourens[4]
[1] Centre for Sustainable Arctic Marine and Coastal Technology (SAMCoT), Norwegian University of Science and Technology, Trondheim, Norway
[2] The University Centre in Svalbard (UNIS), Longyearbyen, Spitsbergen
[3] Department of Structural Engineering, Norwegian University of Science and Technology, Trondheim, Norway.
[4] Faculty of Civil Engineering and Geosciences, Delft University of Technology, Delft, the Netherlands.

ABSTRACT
A measurement campaign at the Hanko-1 channel marker in the Gulf of Finland is planned in order to monitor the forces leading to ice-induced vibrations by means of force identification. It is planned to identify the ice forces using a joint input-state estimation algorithm in conjunction with a modally reduced order model. The methodology is presented together with a finite element model and a detailed analysis that determines the optimal sensor network. The novel approach used to determine the optimal response measurement types and locations ensures the identifiability of the dynamic ice forces from only a limited number of sensors and a selection of vibration modes. The optimal sensor locations are discussed in view of specific challenges posed by the arctic environment.

INTRODUCTION
Channel markers and lighthouses are examples of structures that occasionally experience ice-induced vibrations. In order to understand the nature of these vibrations, several full-scale and laboratory campaigns have been performed over the last decades. Frequency lock-in vibrations was reported by Nordlund et al. (1988), Kärnä and Turunen (1989) and Määttänen (2008) at the lowest natural frequency of the channel markers. Several other structures in the Baltic Sea have been monitored using response measurements and in some cases load panels. For a literature survey, see Bjerkås (2006).

The ice forces are measured either directly or reconstructed by means of inverse techniques. Both have their difficulties and the global forces cannot be derived without assumptions: a global force derived from load panels often relies on assumptions of friction and calibration. Furthermore the panels may not cover the full ice-structure interface. Response sensors cost less, both during the installation and the operating phase. The installation is also easier than for the load panels. A set of global forces derived from a model-based inverse technique depends on model assumptions, sensor locations and on the response information. Sensor networks can be difficult to design because the ice-action point may be unknown and time variant. In addition, other sources of ambient vibrations than the ice content may be present in the response data (Brown, 2007).

In-situ observation of the ice conditions, ice properties and other environmental data are often collected to understand more of the extreme ice-load events. The past measurement campaigns in which such amounts of information were collected, were extensive.

In this paper, we recapitulate an existing approach for real-time monitoring of level-ice forces and responses, and apply it to the Hanko-1 Channel edge marker. The objective is to identify the dynamic forces with only a limited number of response measurements.

Both the states (ensemble of displacements and velocities) and the forces will be treated as unknowns and jointly estimated using a finite element model and a joint input-state estimation algorithm. For modally reduced order models, Maes et al. (2014) recently demonstrated sensor network requirements and considerations ensuring force identifiability when using the joint input-state estimation algorithm. In this contribution, these requirements are used to design a sensor network for the Hanko-1 Channel marker.

DUAL FORCE AND STATE ESTIMATION

In this section we describe the system equations, the state-space transform, the joint input-state algorithm, and the requirements for the force identification to succeed.

System equations

The ice force is treated as an unknown concentrated load acting on a linear time-invariant structure that is represented by a finite element model consisting of a limited number of vibrational modes:

$$\ddot{\mathbf{z}}(t) + \mathbf{\Gamma}\dot{\mathbf{z}}(t) + \mathbf{\Omega}^2\mathbf{z}(t) = \mathbf{\Phi}^{\mathrm{T}}\mathbf{S}_p\mathbf{p}(t) \tag{1}$$

where $\mathbf{z}(t) \in \mathbb{R}^{n_\mathrm{m}}$ is the vector of modal coordinates and n_m the number of modes used to assemble the model. The force vector $\mathbf{p}(t) \in \mathbb{R}^{n_\mathrm{p}}$ is specified to act at the desired locations through the force influence matrix $\mathbf{S}_\mathrm{p} \in \mathbb{R}^{n_\mathrm{DOF} \times n_\mathrm{p}}$, where n_p is the number of force time histories and n_DOF is the number of degrees of freedom. $\mathbf{\Gamma} \in \mathbb{R}^{n_\mathrm{m} \times n_\mathrm{m}}$ is the diagonal damping matrix populated diagonally with the terms $2\xi_j\omega_j$ where ω_j and ξ_j are the natural frequency and damping ratio corresponding to mode *j*, respectively. $\mathbf{\Omega} \in \mathbb{R}^{n_\mathrm{m} \times n_\mathrm{m}}$ is a diagonal matrix containing the natural frequencies ω_j and $\mathbf{\Phi} \in \mathbb{R}^{n_\mathrm{DOF} \times n_\mathrm{m}}$ is a matrix collecting the mass-normalized mode shapes.

State-space model

The continuous-time state vector $\mathbf{x}(t) \in \mathbb{R}^{n_\mathrm{s}}$, $n_\mathrm{s} = 2n_\mathrm{m}$, is defined as follows:

$$\mathbf{x}(t) = \begin{pmatrix} \mathbf{z}(t) \\ \dot{\mathbf{z}}(t) \end{pmatrix} \tag{2}$$

whereby the equation of motion of second order in Eq. (1) can be organized as a first-order continuous-time state equation

$$\dot{\mathbf{x}}(t) = \mathbf{A}_\mathrm{c}\mathbf{x}(t) + \mathbf{B}_\mathrm{c}\mathbf{p}(t) \tag{3}$$

where the system matrices $\mathbf{A}_\mathrm{c} \in \mathbb{R}^{n_\mathrm{s} \times n_\mathrm{s}}$ and $\mathbf{B}_\mathrm{c} \in \mathbb{R}^{n_\mathrm{s} \times n_\mathrm{p}}$ are defined as

$$\mathbf{A}_\mathrm{c} = \begin{bmatrix} \mathbf{0} & \mathbf{I} \\ -\mathbf{\Omega}^2 & -\mathbf{\Gamma} \end{bmatrix}, \mathbf{B}_\mathrm{c} = \begin{bmatrix} \mathbf{0} \\ \mathbf{\Phi}^{\mathrm{T}}\mathbf{S}_\mathrm{p} \end{bmatrix} \tag{4}$$

The measurements are collected in a data vector $\mathbf{d}(t) \in \mathbb{R}^{n_d}$, in which the observations can be a linear combination of displacement, velocity and acceleration, with n_d the number of data measurements. The data vector is constructed as follows:

$$\mathbf{d}(t) = \mathbf{S}_a \boldsymbol{\Phi}\, \ddot{\mathbf{z}}(t) + \mathbf{S}_v \boldsymbol{\Phi}\, \dot{\mathbf{z}}(t) + \mathbf{S}_d \boldsymbol{\Phi}\, \mathbf{z}(t) \tag{5}$$

where the selection matrices $\mathbf{S}_a, \mathbf{S}_v$ and $\mathbf{S}_d \in \mathbb{R}^{n_d \times n_{DOF}}$ are populated according to the spatial location at which acceleration, velocity, displacement and/or strain are measured. Eq. (5) can be transformed into state-space form using Eqs. (1) and (2):

$$\mathbf{d}(t) = \mathbf{G}_c \mathbf{x}(t) + \mathbf{J}_c \mathbf{p}(t) \tag{6}$$

where the matrices $\mathbf{G}_c \in \mathbb{R}^{n_d \times n_s}$ and $\mathbf{J}_c \in \mathbb{R}^{n_d \times n_p}$ represent the output influence matrix and direct transmission matrix, respectively, defined as follows:

$$\begin{aligned} \mathbf{G}_c &= [\mathbf{S}_d \boldsymbol{\Phi} - \mathbf{S}_a \boldsymbol{\Phi} \boldsymbol{\Omega}^2 \quad \mathbf{S}_v \boldsymbol{\Phi} - \mathbf{S}_a \boldsymbol{\Phi} \boldsymbol{\Gamma}] \\ \mathbf{J}_c &= [\mathbf{S}_a \boldsymbol{\Phi} \boldsymbol{\Phi}^T \mathbf{S}_p] \end{aligned} \tag{7}$$

In discrete time under a zero-order hold assumption and given a sampling rate of $1/\Delta t$, Eqs. (3) and (6) become:

$$\mathbf{x}_{k+1} = \mathbf{A}\mathbf{x}_k + \mathbf{B}\mathbf{p}_k \tag{8}$$

$$\mathbf{d}_k = \mathbf{G}\mathbf{x}_k + \mathbf{J}\mathbf{p}_k \tag{9}$$

where

$$\mathbf{x}_k = \mathbf{x}(k\Delta t),\ \mathbf{d}_k = \mathbf{d}(k\Delta t),\ \mathbf{p}_k = \mathbf{p}(k\Delta t),\ k = 1, \ldots, N$$

and

$$\mathbf{A} = e^{\mathbf{A}_c \Delta t},\ \mathbf{B} = [\mathbf{A} - \mathbf{I}]\mathbf{A}_c^{-1}\mathbf{B}_c$$

$$\mathbf{G}_c = \mathbf{G},\ \mathbf{J}_c = \mathbf{J}$$

Joint input-state estimation algorithm

With the system matrices $\mathbf{A}, \mathbf{B}, \mathbf{G}$ and $\mathbf{J}$ known, the algorithm developed by Gilljins and De Moor (2007) is used to jointly estimate the forces and states. It has the structure of a Kalman filter, but with the true force replaced with an optimal estimate. Unlike force identification using the traditional Kalman filter (see Lourens et al. (2012b)), no regularization parameter has to be calculated. By introducing the random variables $\mathbf{w}_k$ and $\mathbf{v}_k$, which represent the stochastic system and measurement noise, respectively, the discrete-time state-space equations become the following:

$$\mathbf{x}_{k+1} = \mathbf{A}\mathbf{x}_k + \mathbf{B}\mathbf{p}_k + \mathbf{w}_k \tag{10}$$

$$\mathbf{d}_k = \mathbf{G}\mathbf{x}_k + \mathbf{J}\mathbf{p}_k + \mathbf{v}_k \tag{11}$$

where it is assumed that the vectors $\mathbf{w}_k$ and $\mathbf{v}_k$ are mutually uncorrelated, zero-mean, white-noise signals with known time invariant covariance matrices $\mathbf{Q} = E\{\mathbf{w}_k \mathbf{w}_k^T\}$ and $\mathbf{R} = E\{\mathbf{v}_k \mathbf{v}_k^T\}$. The algorithm predicts the forces and states in three steps summarized below: the unbiased minimum-variance input estimation (MVU), the measurement update, and the time update.

Input estimation:

$$\tilde{\mathbf{R}}_k = \mathbf{G}\mathbf{P}_{k|k-1}\mathbf{G}^{\mathrm{T}} + \mathbf{R} \tag{12}$$

$$\mathcal{M}_k = (\mathbf{J}^{\mathrm{T}}\tilde{\mathbf{R}}_k^{-1}\mathbf{J})^{-1}\mathbf{J}^{\mathrm{T}}\tilde{\mathbf{R}}_k^{-1} \tag{13}$$

$$\hat{\mathbf{p}}_{k|k} = \mathcal{M}_k(\mathbf{d}_k - \mathbf{G}\hat{\mathbf{x}}_{k|k-1}) \tag{14}$$

$$\mathbf{P}_{\mathrm{p}[k|k]} = (\mathbf{J}^{\mathrm{T}}\tilde{\mathbf{R}}_k^{-1}\mathbf{J})^{-1} \tag{15}$$

Measurement update:

$$\mathbf{L}_k = \mathbf{P}_{k|k-1}\mathbf{G}^{\mathrm{T}}\tilde{\mathbf{R}}_k^{-1} \tag{16}$$

$$\hat{\mathbf{x}}_{k|k} = \hat{\mathbf{x}}_{k|k-1} + \mathbf{L}_k(\mathbf{d}_k - \mathbf{G}\hat{\mathbf{x}}_{k|k-1} - \mathbf{J}\hat{\mathbf{p}}_{k|k}) \tag{17}$$

$$\mathbf{P}_{k|k} = \mathbf{P}_{k|k-1} - \mathbf{L}_k(\tilde{\mathbf{R}}_k - \mathbf{J}\ \mathbf{P}_{\mathrm{p}[k|k]}\mathbf{J}^{\mathrm{T}})\mathbf{L}_k^{\mathrm{T}} \tag{18}$$

$$\mathbf{P}_{\mathrm{xp}[k|k]} = \mathbf{P}_{\mathrm{px}[k|k]}^{\mathrm{T}} = -\mathbf{L}_k\mathbf{J}\ \mathbf{P}_{\mathrm{p}[k|k]} \tag{19}$$

Time update:

$$\mathbf{x}_{k+1|k} = \mathbf{A}\hat{\mathbf{x}}_{k|k} + \mathbf{B}\hat{\mathbf{p}}_{k|k} \tag{20}$$

$$\mathbf{P}_{k+1|k} = \begin{bmatrix}\mathbf{A} & \mathbf{B}\end{bmatrix}\begin{bmatrix}\mathbf{P}_{k|k} & \mathbf{P}_{\mathrm{xp}[k|k]} \\ \mathbf{P}_{\mathrm{px}[k|k]} & \mathbf{P}_{\mathrm{p}[k|k]}\end{bmatrix}\begin{bmatrix}\mathbf{A}^{\mathrm{T}} \\ \mathbf{B}^{\mathrm{T}}\end{bmatrix} + \mathbf{Q} \tag{21}$$

Error covariance for both the estimated states and forces are obtained in every step and collected in $\mathbf{P}_{k|k} \in \mathbb{R}^{n_{\mathrm{s}} \times n_{\mathrm{s}}}$ and $\mathbf{P}_{\mathrm{p}[k|k]} \in \mathbb{R}^{n_{\mathrm{p}} \times n_{\mathrm{p}}}$, respectively. For more details on the algorithm and the assumptions it is based upon, the reader is referred to Lourens et al. (2012a).
A step action table is provided to help implementation of this framework:

1. Model assembly and tuning; extract mass normalized eigenvectors and natural frequencies ($\mathbf{\Phi} \in \mathbb{R}^{n_{\mathrm{DOF}} \times n_{\mathrm{m}}}$, $\mathbf{\Omega} \in \mathbb{R}^{n_{\mathrm{m}} \times n_{\mathrm{m}}}$).
2. Define force influence locations ($\mathbf{S}_{\mathrm{p}} \in \mathbb{R}^{n_{\mathrm{DOF}} \times n_{\mathrm{p}}}$).
3. Define sensor locations and assemble the data vector.
4. State-space transform.
5. Perform joint state and input estimation.

Requirements for force identification using the JSI algorithm

The correct types and locations of response measurements are essential to successfully identify the forces. Maes et al. (2014) formulated a set of mathematical criteria that can be used to design sensor networks. The criteria ensure that the dynamic forces can be identified using the joint input-state estimation algorithm (Eqs. (10) – (21)) in conjunction with a modally reduced order model (Eqs.(8) – (9)). The first criterion ensures that the ice force can be estimated from the response measurements without a time delay. The second ensures that the stability of the system inversion is maintained. It is recommended for the reader to look into the reference for additional criteria that ensure the complete dynamic response to be identified.

Direct invertibility

It is required that the system input (the ice force) can be estimated from the output without a time delay. This is proven to hold if $\mathrm{rank}(\mathbf{J}) = \mathrm{rank}(\mathbf{S}_{\mathrm{a}}\mathbf{\Phi}\mathbf{\Phi}^{\mathrm{T}}\mathbf{S}_{\mathrm{p}}) = n_{\mathrm{p}}$. In order to ensure this, first the number of excited modes should be larger or equal to the number of forces, $\mathrm{rank}(\mathbf{S}_{\mathrm{p}}^{\mathrm{T}}\mathbf{\Phi}) = n_{\mathrm{p}}$. Second, it is required that at least n_{p} accelerations are measured to secure a direct coupling between the acceleration responses and the estimated forces. Furthermore, the acceleration measurements should pertain significant contributions from the modes excited by the forces.

Stability requirements

The stability of the system inversion can be checked by investigating the so-called transmission zeros. These depend on the matrices $\mathbf{A}, \mathbf{B}, \mathbf{G}$ and $\mathbf{J}$, and are found by solving the following eigenvalue problem (Emami-Naeini and Van Dooren, 1982)

$$\begin{bmatrix} \mathbf{A} - \lambda_j \mathbf{I} & \mathbf{B} \\ \mathbf{G} & \mathbf{J} \end{bmatrix} \begin{bmatrix} \mathbf{x}_{[0]} \\ \mathbf{p}_{[0]} \end{bmatrix} = \begin{bmatrix} \mathbf{0} \\ \mathbf{0} \end{bmatrix} \tag{22}$$

where $\lambda_j \in \mathbb{C}$ a finite transmission zero for any selection for the corresponding initial conditions $\mathbf{x}_{[0]} \in \mathbb{C}^{n_s}$ and $\mathbf{p}_{[0]} \in \mathbb{C}^{n_p}$ for the state and force, respectively. If $|\lambda_j| < 1$, the system inversion is stable, while if $|\lambda_j| > 1$ the system inversion is unstable. When $|\lambda_j| = 1$, the system inversion is marginally stable. Maes et al. (2014) explained the 0 Hz marginally stable transmission zero to occur because the acceleration and velocity measurements are insensitive to an excitation which is constant with time. The latter one occurs if only acceleration data is included in the measurement setup. By including displacement/strain measurements one can omit the marginally stable transmission zero at 0 Hz, and the inversion stability can be further checked from $\text{rank}(\mathbf{J} - \mathbf{G}(\mathbf{A} - \mathbf{I})^{-1}\mathbf{B}) = \min(n_p, n_d)$.

FORCE IDENTIFICATION ON THE HANKO-1 CHANNEL MARKER

The Hanko-1 channel marker is located at N59 44.11 and E23 02.36 (WGS-84) offshore the city Hanko in Finland. The structure was chosen because of its location close to the mainland and the fact that earlier measurements showed frequency lock-in vibrations. The foundation pile is molded into the bedrock well by concrete casting (Fig.1). A steel cone supports the 0.8 m diameter circular-sectioned steel superstructure which has varying wall thickness from the mean water level up to the lantern at the top (Fig.2). The structure exhibited frequency lock-in vibrations at the first natural frequency of 4.6 Hz on several occasions. For more information about frequency lock-in vibrations on this channel marker and others, see Määttänen (2008), Kärnä and Turunen (1989) and Nordlund et al. (1988).

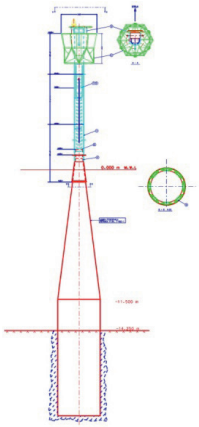

Figure 1. Hanko-1 Channel marker design.

Figure 2. Picture of a typical Channel marker, from Määttänen (2008).

Finite element model

The structure is modelled using quadrilateral finite-membrane-strain shell elements with reduced integration (S4R) in the software ABAQUS. Construction blueprints were used to define the model properties. All the shell degrees of freedom of the model are constrained in the rock well (cf. Fig. 1). The lantern plates were simplified from the true geometry with the total mass kept similar to the real value, ~ 1400 kilograms. The added mass of the displaced water is accounted for through the density of the steel below the mean water level. Several of the vibration modes are symmetric in the x-z direction, with the corresponding natural frequencies up to 40Hz given in Table 1. Circumferential modes are found in the substructure due to the high material density used to account for the displaced water. The bending modes are displayed in Fig. 3, in which the next section will demonstrate why these are important for the assembly of a modally reduced order model.

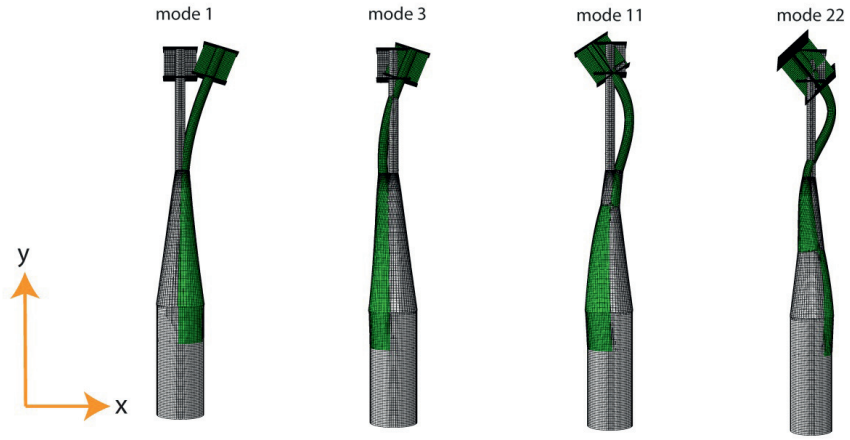

Figure 3. Bending vibration modes of Hanko-1.

Table 1. Finite element model natural frequencies and vibration modes

Mode	$f_j = \frac{\omega_j}{2\pi}$ [Hz]	Mode shape description (*displayed modes)*
1,2	*4.68*	*Bending mode in x direction (mode 1) and z direction (mode 2)*
3,4	*9.91*	*Bending mode in x direction (mode 3) and z direction (mode 4)*
5,6	10.55	Circumferential mode in the substructure
7,8	13.68	Circumferential mode in the substructure
9,10	20.15	Circumferential mode in the substructure
11,12	*22.12*	*Bending mode in x direction (mode 11) and z direction (mode 12)*
13,14	27.96	Circumferential mode in the substructure
15-18	28.4-29.2	Circumferential mode in the substructure
19	32.95	Torsion
20,21	33.45	Circumferential mode in the substructure
22,23	*35.16*	*Bending modes 45 degree to the principal axes*
24	40.72	Circumferential mode in the substructure

Direct invertibility

The locations at which each accelerometers are placed have an effect on the direct invertibility. 13 possible accelerometer locations and two assumed attack points for the ice forces are displayed in Fig. 4 (a). The modal influences, $\mathbf{S}_\mathrm{p}^\mathrm{T}\mathbf{\Phi}$, of the two assumed force locations in Fig.4 (a) are shown in Fig. 4 (b) (top). The force locations have a significant influence on the modes 1, 2, 3, 4, 11, 12, 22 and 23, which means that if the global forces in x and z directions are sought, respectively, $n_\mathrm{p} = 2$ and $\mathbf{S}_\mathrm{p}^\mathrm{T}\mathbf{\Phi}$ will be of full rank.

The contribution from the modes to each of the possible accelerometer locations, $\mathbf{S}_\mathrm{a}\mathbf{\Phi}$, are displayed in Fig. 4 (b) (bottom). At least two accelerometers are required in order to assure that $\mathrm{rank}(\mathbf{J}) = n_\mathrm{p} = 2$. In addition, it is assumed that four extra accelerometers are available providing extra safety for the measurements in case some accelerometers malfunction. The d_1, d_2, d_3, d_6, d_7 and d_8 locations capture a significant influence through all the bending modes (cf. Fig. 3) which also have a significant influence from the input.

At some locations the major modal contributions cancel each other out: d_5 is a location at which an appropriate force influence and modal contribution from several modes are obtained (Fig. 4b), but with a low direct transmission value, $\mathbf{S}_\mathrm{a}\mathbf{\Phi}\mathbf{\Phi}^\mathrm{T}\mathbf{S}_\mathrm{p}$ (Fig 5). The low transmission value means that the point has a weak input-output coupling, therewith not a preferred location for an accelerometer. The strongest input-output coupling is found slightly above the ice-action point.

Assuming that the inside of the structure is inaccessible, the sensors must be located on the outer surface. If the sensors are deployed too close to the ice-action point, they also become vulnerable to the ice floe. Therefore it is assumed that the sensors cannot be mounted closer than 1 meter from the ice-action point. Variation in the ice-action point can occur due to water-level fluctuations, interaction with deformed ice, such as rafted ice, ridged ice etc. In order to find the optimal accelerometer locations and account for varying attack-point, one can also effectively assemble in a similar manner as was done above for only two locations, a larger vector, $\mathbf{S}_\mathrm{p}$, of all possible force locations and vary the sensor positions, $\mathbf{S}_\mathrm{a}$.

The location d_10 is the lowermost possible accelerometer location which gives the best input-output coupling, and the locations below that level are not practical alternatives despite of their strong input-output coupling. The third and fourth accelerometer could for instance be installed at locations d_8, such that if the lowermost fails, a strong input-output coupling is still maintained. Location d_3 is a suitable location for the fifth and sixth accelerometer.

The modes which insignificantly contribute to the response, or have an insignificant force influence, are primarily circumferential modes of the substructure. These may be inaccurately described by the added mass and therefore they may bring large modelling errors into the system. Because of their small contribution to the response, these may also lead to a numerically rank-deficient modal projection sensor selection matrix, $\mathbf{S}_\mathrm{a}\mathbf{\Phi}$, (van der Male and Lourens, 2015). Hence, the modally reduced order model that will be used throughout this paper retains only the modes 1, 2, 3, 4, 11, 12, 22 and 23. A set of system matrices $\mathbf{A, B, G}$ and $\mathbf{J}$ are obtained using these eight modes and the six chosen accelerometer locations above. To ensure that sufficient numerical rank is obtained, the singular values of $\mathbf{J}$ are calculated. Two positive singular values of $7.333 \cdot 10^{-5}$ and $7.3184 \cdot 10^{-5}$ were found, hence $\mathrm{rank}(\mathbf{J}) = n_\mathrm{p} = 2$.

Note that because the excluded modes only contributed marginally to the input-output coupling, Fig. 5 remained almost unchanged with the modally reduced order model with $n_\mathrm{m} = 8$.

Stability requirements

The chosen accelerometer installations, the modally reduced order model with $n_m = 8$ and a sampling frequency of 100Hz rendered no unstable transmission zeros. However, the system inversion will only be marginally stable due to the lack of information at 0 Hz and the singular values of the matrix $\mathbf{J} - \mathbf{G}(\mathbf{A} - \mathbf{I})^{-1}\mathbf{B}$ were $2.3050 \cdot 10^{-20}$ and $1.3968 \cdot 10^{-20}$. In practice, to ensure that the solution is stabilized the singular values should be larger, otherwise the numerical rank falsely suggests sufficient stability is fulfilled.

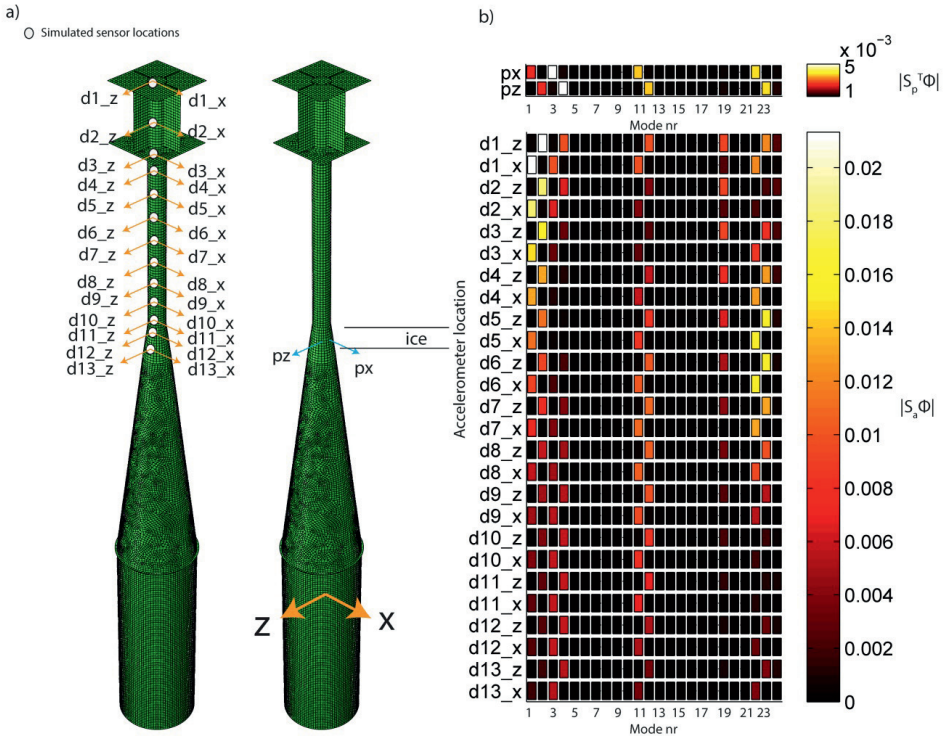

Figure 4. a) simulated sensor locations b) modal influences of forces and accelerations at simulated locations.

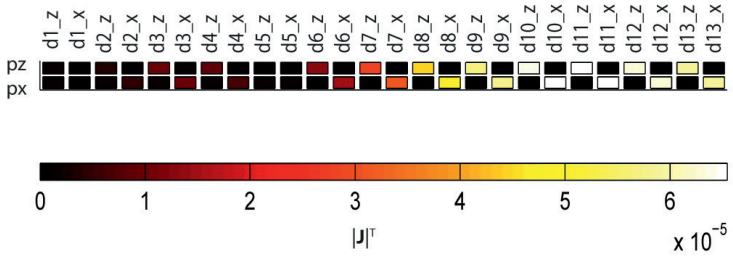

Figure 5. Direct transmission value, $\mathbf{J}$, as function of accelerometer location.

Strain measurements are one way to eliminate the marginally stable transmission zeros. The strain gauges should be installed such that the measurement data have contributions from at least $n_p = 2$ modes excited by the unknown forces. Using the modally reduced order model, the modal influences of the bending strains along the locations in Fig 4 (a) are shown in Fig. 6. The corresponding finite elements at each location are taken close to the principal axes on the cross section (Fig. 7), where the bending strains have either full or zero influence for vibration modes parallel or perpendicular to the principal axes. Locations e_3, down to e_7 show good strain influence through several modes. Because each location should capture bending strain in both the xy and zy plane, two active strain gauges at for instance the level e_4 would ensure both to be captured.

Since the system matrices depend on the modal properties, the time discretization, the type of sensors and their locations $\mathbf{S}_a, \mathbf{S}_v$ and $\mathbf{S}_d \in \mathbb{R}^{n_d \times n_{DOF}}$, each alternative for a complete sensor network has to be checked. The inversion stability is now checked for a sensor network that includes the two strain gauges at e_4 and the six accelerometers at locations d_3, d_8 and d_10. Two positive singular values were found from the matrix $\mathbf{J} - \mathbf{G}(\mathbf{A} - \mathbf{I})^{-1}\mathbf{B}$ to be $1.5773 \cdot 10^{-11}$ and $8.4806 \cdot 10^{-12}$, which means that $\text{rank}(\mathbf{J} - \mathbf{G}(\mathbf{A} - \mathbf{I})^{-1}\mathbf{B}) = 2 = n_p$. Hence the marginally stable transmission zeros are eliminated and since the system had no unstable transmission zeros, stable inversion is provided.

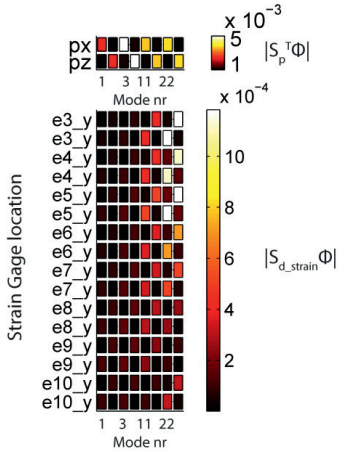

Figure 6. Modal influence on strains at different spatial locations.

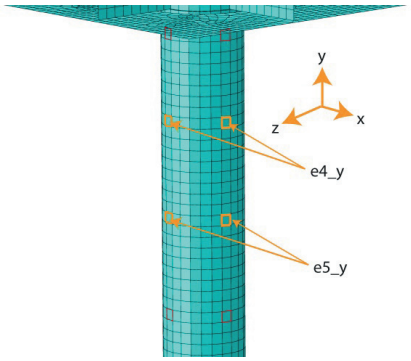

Figure 7. Two elements at each spatial level used to simulate the modal strain influence.

Static force component

Continuous ice crushing causes both static and dynamic forces, and the sensor network described above is valid only for identification the dynamic forces. Because the simulated strain gauge locations are above the ice-action point, they provide no information about the static content of the ice force. An optimal solution includes strain gauges installed below the mean water-level, similar to the instrumentation Turunen and Nordlund (1988) presented on a channel marker. Biaxial inclinometer/tiltmeter could also provide the static response. Such response sensors were installed to reconstruct the forces on the Confederation Bridge (Brown, 2007) and the Nordströmsgrund lighthouse (Frederking, 2005). Whereas both the static and

dynamic part of the forces and states will be identified simultaneously with the proposed algorithm, it is essential that the inclinometer/tiltmeter can provide accurate measurements also in the dynamic range. If not, the inclinometer/tiltmeter response may distort the identified forces. In addition, some structures are prone to lateral deformations in the soil due to the ice action and hence the inclination/tilt may be an inaccurate means to obtain the static forces.

DISCUSSION

The joint input-state estimation algorithm has become a tool for force and response estimation with well-developed requirements, first the truncation to reduced order systems by Lourens et al. (2012a) and second a compilation of requirements for a stable inversion by Maes et al. (2014). Recent papers (Nord et al., 2014; Nord et al., 2015) also successfully applied this framework to identify level-ice forces on a laboratory structure.
With the conditions described in this paper met, the algorithm will render the ice forces from the measured signals. The presented results are obtained from a model that contains several assumptions, such as the superstructure mass and the boundary conditions used in the foundation. Static and dynamic calibrations can be used to tune the model properties and provide more accurate results.

CONCLUSION

A sensor network consisting of accelerometers and strain gages are suggested in order to identify ice forces on the Hanko-1 channel marker. The network ensures the identifiability of dynamic ice forces using the joint input-state estimation algorithm in conjunction with a modally reduced order model.

ACKNOWLEDGEMENTS

The authors wish to acknowledge the support of the Research Council of Norway through the Centre for Research-based Innovation SAMCoT, and the support of all SAMCoT partners. The authors also acknowledge Professor Emeritus Mauri Määttänen for providing information on sensor installations in arctic waters, the structural design and dynamic behaviour of the Finnish channel edge markers.

REFERENCES

Bjerkås, M., 2006. Ice action on offshore structures. PhD Thesis, NTNU, ISBN 82-471-7756-0, 173 pp.

Brown, T.G., 2007. Analysis of ice event loads derived from structural response. Cold Regions Science and Technology, 47(3): 224-232.

Emami-Naeini, A. and Van Dooren, P., 1982. Computation of zeros of linear multivariable systems. Automatica, 18(4): 415-430.

Frederking, R., 2005. Tiltmeter application at Nordströmsgrund lighthouse- Strice Project, 18th International Conference on Port and Ocean Engineering Under Arctic Conditions pp. 399-408.

Gillijns, S. and De Moor, B., 2007. Unbiased minimum-variance input and state estimation for linear discrete-time systems with direct feedthrough. Automatica, 43(5): pp. 934-937.

Kärnä, T. and Turunen, R., 1989. Dynamic response of narrow structures to ice crushing. Cold Regions Science and Technology, 17(2): 173-187.

Lourens, E., Papadimitriou, C., Gillijns, S., Reynders, E., De Roeck, G. and Lombaert, G., 2012a. Joint input-response estimation for structural systems based on reduced-order

models and vibration data from a limited number of sensors. Mechanical Systems and Signal Processing, 29(0): pp. 310-327.

Lourens, E., Reynders, E., De Roeck, G., Degrande, G. and Lombaert, G., 2012b. An augmented Kalman filter for force identification in structural dynamics. Mechanical Systems and Signal Processing, 27(0): 446-460.

Maes, K., Lourens, E., Van Nimmen, K., Reynders, E., De Roeck, G. and Lombaert, G., 2014. Design of sensor networks for instantaneous inversion of modally reduced order models in structural dynamics. Mechanical Systems and Signal Processing(0).

Määttänen, M., 2008. Ice velocity limit to frequency lock-in vibrations, International symposium on Ice, IAHR, Vancouver, Canada, pp. 1265-1276.

Nord, T.S., Lourens, E.-M., Øiseth, O. and Metrikine, A., 2014. Model-based force identification in experimental ice-structure interaction by means of Kalman filtering, EURODYN, Porto, Portugal.

Nord, T.S., Lourens, E.-M., Øiseth, O. and Metrikine, A., 2015. Model-based force and state estimation in experimental ice-induced vibrations by means of Kalman filtering. Cold Regions Science and Technology, 111(0): pp. 13-26.

Nordlund, O.P., Tuomo, K. and Järvinen, E., 1988. Measurements of ice-induced vibrations of channel markers, IAHR Ice Symposium, Sapporo, Japan, pp. 537-548.

Turunen, R. and Nordlund, O.-P., 1988. Full-scale measurements of the dynamic properties of a channel marker, IAHR Ice Symposium, Sapporo, Japan, pp. 549-560.

van der Male, P. and Lourens, E.-M., 2015. Operational Vibration-Based Response Estimation of Offshore wind Lattice Structures, IMAC XXXIII A Conference and Exposition on Structural Dynamics, Paper no. 198, Orlando, Florida, US.